THEORETICAL FOUNDATIONS OF DIELECTRIC HALOSCOPES

A New Way to Discover Axion Dark Matter

Alexander Millar

München 2018

Theoretical Foundations of Dielectric Haloscopes

A New Way to Discover Axion Dark Matter

Dissertation
an der Fakultät für Physik
der Ludwig–Maximilians–Universität
München

vorgelegt von
Alexander Millar
aus Melbourne

München, den 27. April 2018

Dissertation

an der Fakultät für Physik
der Ludwig-Maximilians-Universität München
vorgelegt von Alexander Millar
am 27. April 2018.

Erstgutachter: PD Dr. Georg Raffelt
Zweitgutachter: Prof. Dr. Gerhard Buchalla

Tag der mündlichen Prüfung: 8. Juni 2018

Max-Planck-Institut für Physik,
München, den 27. April 2018.

Zusammenfassung

Die Natur der dunklen Materie ist eines der hartnäckigsten Rätsel der modernen Physik: Seit mehr als acht Jahrzehnten gibt es Hinweise auf eine mysteriöse unsichtbare Substanz, die "dunkle Materie", welche einen Großteil der Materie im Universum ausmacht. Es gibt viele mögliche teilchenphysikalische Kandidaten für diese schwer zu fassende Form der Materie, wobei einer der populärsten das Axion ist. Das Axion ist ein leichtes pseudoskalares Teilchen, welches im Zuge der Brechung einer globalen Symmetrie an einer hohen Energieskala entsteht und das ursprünglich eingeführt wurde, um die Abwesenheit von CP-Verletzung in der starken Kraft zu erklären (das Starke CP Problem). Axionen könnten im frühen Universum nicht-thermisch produziert werden und damit genau die Dichte der kalten dunkle Materie liefern. Aufgrund ihrer kleinen Masse haben Axionen eine einzigartige Phänomenologie und benötigen daher umfangreiche Experimente für ihre Detektion. Ein großer Teil des gut motivierten Parameterraumes muss noch erforscht werden, so dass neue Ideen benötigt werden, um die Suche nach Axionen weiter voranzutreiben.

Wir untersuchen die zugrundeliegende Theorie von dielektrischen Haloskopen, einer neuen Methode, um axionische dunkle Materie zu detektieren. Wenn sich eine Grenzfläche unterschiedlicher dielektrischer Medien in einem magnetischen Feld befindet, fungiert das oszillierende axionische Feld als eine Quelle elektromagnetischer Wellen, welche in beiden Richtungen senkrecht zur Oberfläche auftreten. Die Emissionsrate kann verstärkt werden durch mehrere sorgfältig platzierte Schichten, um konstruktive Interferenz zu erreichen, sowie durch eine große transversale Fläche. Beginnend mit den axionisch modifizierten Maxwell-Gleichungen berechnen wir die Effizienz dieses neuen dielektrischen Haloskop-Konzeptes. Wir führen eine Berechnung der Übergangswahrscheinlichkeit zwischen den Zuständen des quantisierten Axions und des Photons, der durch die Anwesenheit dielektrischen Medien deformierten ist, durch. Wir zeigen sowohl eine klassische Berechnung basierend auf Transfermatrizen als auch eine konventionelle störungstheoretische Berechnung erster Ordnung, welche auf ein Überlappungsintegral führt. Beide Methoden liefern dasselbe Ergebnis. Mit dielektrischen Haloskopen könnte potenziell der unerforschte Hochfrequenzbereich von 10–100 GHz (entsprechend einer Axionmasse von 40–400 μeV) untersucht werden, für welchen bei herkömmlichen Hohlraumresonatoren das Problem auftritt, das benötigte Volumen zu erzielen. Des Weiteren beschreiben wir Geschwindigkeitseffekte bei der Mischung von Axionen und Photonen in einem magnetischen Feld und bei dem Phänomen von Photonemission von Grenzflächen verschiedener dielektrischer Medien. Weil Geschwindigkeitseffekte nur dann von Bedeutung sind, wenn das

Haloskop größer als ca. 20% der de Broglie-Wellenlänge des Axions ist, kann diese Geschwindigkeitsabhängigkeit beim geplanten MADMAX-Experiment mit 80 dielektrischen Scheiben vernachlässigt werden. Jedoch wäre ein verbessertes MADMAX-Experiment oder ein Experiment zweiter Generation richtungsempfindlich hinsichtlich der Axion-Geschwindigkeit und damit eine sensitives Instrument zur Untersuchung der Astrophysik des Axions.

Abstract

The nature of dark matter is one of the enduring mysteries of modern physics. For more than eight decades there has been evidence for a mysterious invisible substance that constitutes most of the matter in the universe, "dark matter". While there are many possible particle physics candidates for this elusive substance, one of the most popular is the axion. Originally introduced to resolve the absence of charge-parity violation in the Strong force (the Strong CP Problem), the axion is a light pseudo-scalar arising from the breaking of a high energy global symmetry. Axions would be produced non-thermally in the early universe, providing the correct density of dark matter. Due to the lightness of axions, they have a unique phenomenology and so require dedicated experiments to detect. Much of the well motivated parameter space is yet to be explored, meaning that novel ideas are needed to push forward the search for axions.

We study the underlying theory of dielectric haloscopes, a new way to detect dark matter axions. When an interface between different dielectric media is inside a magnetic field, the oscillating axion field acts as a source of electromagnetic waves, which emerge in both directions perpendicular to the surface. The emission rate can be boosted by multiple layers judiciously placed to achieve constructive interference and by a large transverse area. Starting from the axion-modified Maxwell equations, we calculate the efficiency of this new dielectric haloscope approach. We do both a classical calculation and a quantum calculation of the produced power. The classical calculation is based on transfer matrices, solving for the electric field throughout the system. The quantum calculation uses conventional first-order perturbative calculation of the transition probability between a quantised axion state and the photon state, which is distorted in the presence of the dielectric media, resulting in an overlap integral. Both methods agree on the produced power in electromagnetic radiation. With dielectric haloscopes one could potentially search the unexplored high-frequency range of 10–100 GHz (axion mass 40–400 μeV), where traditional cavity resonators have difficulties reaching the required volume. We also describe non-zero velocity effects for axion-photon mixing in a magnetic field and for the phenomenon of photon emission from interfaces between different dielectric media. As velocity effects are only important when the haloscope is larger than about 20% of the axion de Broglie wavelength, for the planned MADMAX experiment with 80 dielectric disks the velocity dependence can safely be neglected. However, an augmented MADMAX or a second generation experiment would be directionally sensitive to the axion velocity, and thus a sensitive measure of axion astrophysics.

Publications

This thesis is based on a number of publications to which I contributed during my research conducted at the Max-Planck-Institut für Physik from August 2015 to April 2018 [1–5],

1. *Dielectric haloscopes: a new way to detect axion dark matter*
   A. Caldwell, G. Dvali, B. Majorovits, A. Millar, G. Raffelt, J. Redondo, O. Reimann, F. Simon and F. Steffen [MADMAX Working Group], Phys. Rev. Lett. **118** (2017) 091801 [arXiv:1611.05865].

2. *Dielectric haloscopes to search for axion dark matter: theoretical foundations*
   A. J. Millar, G. G. Raffelt, J. Redondo and F. D. Steffen, JCAP **01** (2017) 061 [arXiv:1612.07057].

3. *Axion-photon conversion caused by dielectric interfaces: quantum field calculation*
   A. N. Ioannisian, N. Kazarian, A. J. Millar and G. G. Raffelt, JCAP **09** (2017) 005 [arXiv:1707.00701].

4. *Dielectric haloscopes: sensitivity to the axion dark matter velocity*
   A. J. Millar, J. Redondo and F. D. Steffen, JCAP **10** (2017) 006 [arXiv:1707.04266].

5. *Directional axion detection*
   S. Knirck, A. J. Millar, C. A. J. O'Hare, J. Redondo and F. D. Steffen, 2018, in preparation [MPP-2018-56].

Many of the plots and figures throughout this thesis were taken from these publications. In addition the structure and content of arguments and sections often follows closely from the respective sections in these papers.

Acknowledgements

I am greatly indebted to many people for their help and support in writing this thesis. First and foremost I would like to thank my supervisors Frank Steffen and Georg Raffelt for endless support over the last three years. Both have always looked out for my interests, and have treated me with kindness and generosity. Frank's dedication to precision has been a great example to aspire to and I will always be grateful to him for encouraging me to study in Germany. In addition to his bottomless knowledge of physics, Georg has been a fantastic example to me of clarity of thought, intellectual rigour and good writing (even if I can never manage to get the bibliography to his standards). I would like to deeply thank him for going above and beyond.

I am also hugely indebted to Javier Redondo for his de-facto supervision and for being an endless source of ideas (even if I did not always have time to work on them). Each time he visited, a month's worth of work was done in a week. Javier has always provided an inspiring example by his passion for physics and delight in new ideas.

I am of course also very thankful for the hard work of all of my collaborators, without whom nothing would have been possible. I would particularly like to thank my current collaborators for their patience while I neglected them to write my thesis. I must also express my gratitude to the MADMAX Collaboration—seeing the formation of a new experimental collaboration has been an amazing experience.

The Institute has been a fantastic place for me to be during my studies, and I would like to thank everyone there for providing such a friendly environment. I would particularly like to thank the members of the Astroparticle group, with special mentions going to my officemate Edoardo Vitagliano and ruler-in-perpetuity Tanja Geib for their help and support. I am also very grateful to honorary member Lena Funcke for proofreading parts of my thesis and translating my abstract into German. It made a huge difference to be going through postdoc applications and thesis writing together with her. I am also very grateful for the never-ceasing helpfulness of the support staff of the Institute.

I am deeply grateful for the support of my friends across the continents for their distractions, support and understanding. I would particularly like to thank Yousra Yahia and Millie McDonald for always having time to listen.

As the cliché goes, last but certainly not least I would like to thank my family, my parents as well as my siblings Charlotte and Paul, from the bottom of my heart. Despite being so far away they have been a huge pillar of support, and encourage me even at cost to themselves. My biggest regret about being in Germany is not being able to see you all more often.

Contents

Chapter 1

Introduction

The nature of dark matter (DM) is one of the most enduring mysteries in cosmology. It has been 85 years since the first hint from the rotation curves of galaxies that the matter we are made of might only make up a small fraction of the Universe [6]. Since this fateful measurement it has grown increasingly certain that approximately 5/6 of the matter in the Universe does not interact strongly with Standard Model (SM) particles (via the Strong or Electromagnetic (EM) forces) [7]. Unfortunately, despite the overwhelming indirect evidence that DM exists, we are yet to have a clear discovery of DM via a direct measurement. This is due mainly to the seemingly feeble interactions between dark and visible matter—we only have uncontroversial evidence of gravitational interactions. Therefore it is almost impossible to narrow down the large number of DM candidates which, while being a playground for theorists trying to extend the SM, deprives us of a clear direction for explaining this invisible substance. To remedy this lack of direction, physicists generally try to incorporate DM into a larger theoretical framework, expanding the SM in order to connect DM to some other unsolved problem in particle physics. Such a program is well motivated as there are other issues which are not resolved in the SM, such as the existence of dark energy [8], the disparity of scales between the scale of the mass of the Higgs Boson and the Planck scale [9], the asymmetry between matter and anti-matter in the Universe [10], the origin of neutrino masses [11] and the quantum nature of the gravitational force [12]. One of the primary hopes behind the search for DM is that discovering its true nature will shed light on some of these other questions.

The axion is one of the best examples of a DM candidate inspired by another puzzle in physics. The axion was originally introduced to combat the Strong CP Problem. To great accuracy, the Strong force appears to be inviolate under a combined charge conjugation and parity (CP) transformation [13, 14]. However, quantum chromodynamics (QCD), the wildly successful theory for describing the Strong force, has in principle a CP violating term. Why such a term does not appear to be expressed in nature (or is at least much smaller than naively expected) is what is referred to as the Strong CP Problem. (A

fuller explanation of the Strong CP Problem will be given in section 2.1.1.) The favoured explanation is a dynamical solution called the Peccei Quinn mechanism [15–17], which leaves as a remnant a pseudo-Nambu-Goldstone boson—the axion. As will be discussed further in Section 2.1.3, axions can be produced non-thermally in great numbers, leading to a cold, feebly interacting population that would contribute to the DM of the Universe. In this thesis we look at the the case where axions make up the entirety (or at least the lion's share) of DM.

The main focus in this thesis will be how to find the axion, if the axion indeed exists. Historically, the class of DM candidates favoured by the community has been weakly interacting massive particles, or WIMPs [7]. These are relatively heavy ($\gtrsim$GeV) particles with Weak scale interactions which would act as cold DM after being produced by thermal freeze out. Note that the interactions themselves need not be via the Weak force, merely via interactions of a reasonably similar strength. The predominance of the WIMP as a DM candidate has been due to two factors. The first is the so called "WIMP miracle", where one finds that using interactions at the scale of the Weak force one would get the correct relic density of DM by thermal freeze out. Second is the popularity of low-energy supersymmetry, an extension of the SM. However, this form of supersymmetry is also falling in popularity as the LHC has so far failed to find evidence of superpartners (particles related to the SM particles via a supersymmetry transformation) [17]. Indeed, despite decades of increasingly sensitive searching, we still lack an uncontroversial detection of WIMPs.

The absence of evidence for WIMP DM has lead to interest in finding axions exploding over the last few years. A good way to see this is by looking at the citation history of Pierre Sikivie's seminal paper of axion detection [18], as shown in figure 1.1. Due to the axion's unique phenomenology, techniques which are sensitive to other DM candidates are generally completely insensitive to axions. However, lots of axion experiments and probes would actually be sensitive to another DM candidate, the hidden photon. Hidden photons are massive dark photons, which have similar EM interactions to an axion inside a magnetic field. As we will review in chapter 2, while there are a myriad of possible techniques for searching for axions, there is still a desperate need for techniques that will allow us to cover the full axion parameter space. Due to the less mature nature of axion detection when compared to, for example, WIMP searches, only a tiny part of the well motivated parameter space has been explored so far [19].

In this thesis we will introduce a new experimental concept for searching for DM axions, the dielectric haloscope. The main idea behind dielectric haloscopes is that one couples the stationary DM axion field to propagating electromagnetic (EM) waves by breaking translation invariance in the system with dielectrics or metallic mirrors. Dielectrics are simply electrical insulators which have some polarisation in an electric field. A good example to keep

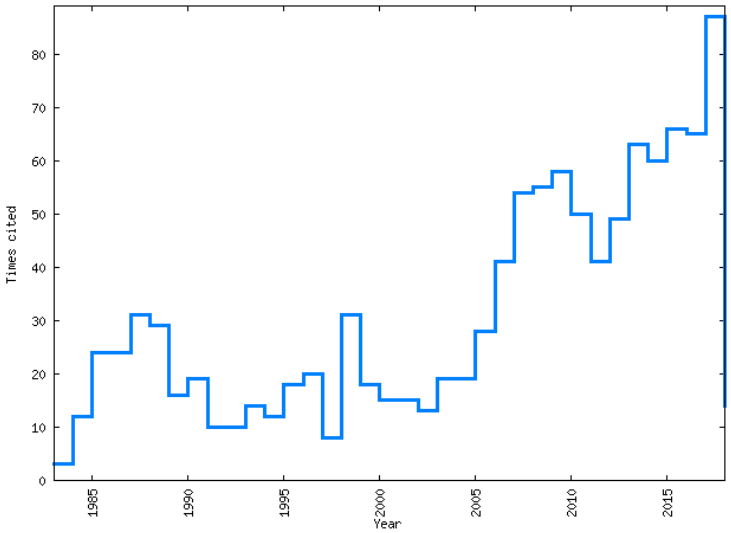

Figure 1.1: Citation history of Pierre Sikivie's paper on axion detection [18]. The last few years show a massive increase in interest in axion detection. Image taken from inSPIRE [20].

in mind is sapphire. As both metallic and dielectric materials can both be handled with a generalised dielectric constant, we will not always distinguish fully between the two. Dielectric haloscopes would use a series of up to $\mathcal{O}(100)$ dielectric disks each with m^2-scale transverse area and fixed mm-scale thicknesses and precisely adjustable spacings in a strong ($\sim$ 10 Tesla) magnetic field. In some cases a mirror may be placed on one side of the device.

Figure 1.2 shows an illustrative setup with one mirror and six dielectric disks placed in a magnetic field and one receiver in the B-field-free region. Inside the magnetic field, the axion induces an electric field $\mathbf{E}_a$ which depends on the medium. The setup produces discontinuities in the axion-induced electric field $\mathbf{E}_a$ at the various interfaces between empty space and either mirror or dielectric disk. To satisfy the usual continuity requirements of the total electric and magnetic fields in the directions parallel to the interfaces, $\mathbf{E}_\parallel$ and $\mathbf{H}_\parallel$, microwaves emerge in the perpendicular directions away from each interface with a frequency $\nu_a = m_a/2\pi$ given by the axion mass. We will be concerned axion masses in the range $m_a = 40$–$400\,\mu\mathrm{eV}$. Axions in such a range have energies corresponding to microwave frequencies (a good rule of thumb is that $4\,\mu\mathrm{eV} \sim 1\,\mathrm{GHz}$). Throughout this thesis we will use natural units with $\hbar = c = 1$ and the Lorentz-Heaviside convention $\alpha = e^2/4\pi$.

Once these microwaves emerge from the interface, they will reflect and interfere as regular EM waves, meaning that through correctly choosing the relative thicknesses and distances between the disks one can arrange for constructive interference, boosting the signal. Note that in general the disks are partially reflecting so that the stored power can be built up. With a judicious

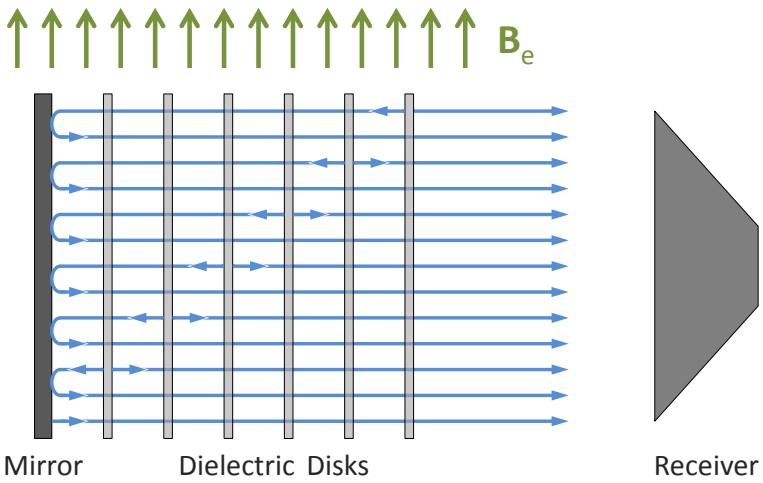

Figure 1.2: A dielectric haloscope consisting of one mirror and several dielectric disks placed in an external magnetic field $\mathbf{B}_{\rm e}$, and one receiver in the field-free region. The setup produces discontinuities in the axion-induced electric field $\mathbf{E}_a$ at the various interfaces between empty space and either mirror or dielectric disk. To satisfy the usual continuity requirements of the total electric and magnetic fields in the directions parallel to the interfaces, $\mathbf{E}_{\parallel}$ and $\mathbf{H}_{\parallel}$, microwaves emerge in the perpendicular directions away from each interface with a frequency $\nu_a = m_a/2\pi$ given by the axion mass m_a. These microwaves are illustrated by the horizontal blue arrows. The signal strength depends on the thickness of the disks and the spacings between them, which have to be varied to scan over the axion mass m_a.

adjustment of the disk separations, either the constructive interference or weak resonant behaviour or both will allow for a substantial signal boost over a sizeable search frequency range $\Delta\nu$. Moreover, by changing the disk placement, one will be able to continuously shift $\Delta\nu$ with the signal boost and thereby to scan a sizeable range of possible m_a values in a realistic total measurement time.

One key advantage of our dielectric haloscope approach is that the frequency dependent microwave emissivity can be adjusted in a flexible and varied way. This is because the total power generated over a frequency range increases linearly with the number of dielectric disks N, a finding which we call the Area Law. For example, one can achieve a very large value of the signal boost in a narrow range of frequencies, similar to a single resonator. Alternatively one can adjust the spacings to achieve a relatively uniform large signal boost over a broader range of frequencies. This freedom is very important for a practical search for axions, as at higher axion masses we will see that one requires more power to achieve the same signal strength. Using this freedom would allow one to achieve an optimal search strategy. This optimal search strategy would be to use a broadband, relatively uniform, frequency response for scanning, and a narrower resonance to confirm or reject a potential discovery.

We will show that dielectric haloscopes are extremely well suited for exploring the higher mass axion parameter space ($m_a = 40$–$400\,\mu$eV). We will show the projected sensitivity for a 80 disk experiment, using 1 m^2 disks inside a 10 T magnetic field. Such a device would be able to explore a large fraction of the high-mass parameter space, and could potentially search this entire range with appropriate upgrades. This is the configuration of the planned MADMAX experiment [21], which would be the first experimentally realised dielectric haloscope. We also show the projected sensitivity of an upgraded 200 disk experiment.

An important question is whether the small, but non-zero, axion velocity can have an effect in dielectric haloscopes. Galactic DM axions have a velocity on the scale of the virial velocity of the Galaxy, however the exact distribution is unknown. For an experiment searching for the axion, if the power emitted depends on the axion velocity then the potential sensitivity depends on the unknown velocity distribution of DM. This would stop an experiment from deriving any robust limits. However, if the axion is discovered one would wish to explore this velocity distribution in as much detail as possible. The dependence of the produced power on the velocity will come almost entirely from the velocity of the axion in the direction perpendicular to the disks, which provides a change in phase of the axion over the haloscope. We will show that the velocity of the axion is only relevant when the haloscope is a large fraction ($\sim 20\%$) of the axion's de Broglie wavelength. For an experiment searching for axions using ~ 100 disks approximately $\lambda/2$ apart such effects are negligible, allowing such an experiment to proceed unafraid of the axion's velocity dispersion. However, if the axion were to be discovered then one would swiftly obtain details of the directionally insensitive velocity distribution simply from measuring the frequency response. One could design a larger device capable of measuring the axion's velocity distribution with directional sensitivity. In some sense, this would be an "axion telescope", allowing one to pick out more detailed features form the DM halo, and verify the DM nature of the signal with, for example, daily modulation due to the Earth's rotation. We will briefly discuss strategies to probe the galactic DM velocity distribution in the event of a discovery.

Outline

As a first step, in chapter 2 we review existing and proposed axion detection techniques. We then re-examine in detail the axion-modified Maxwell equations in the presence of dielectric and permeable media (chapter 3). In chapter 4 we preform a classical analysis of the production of photons using a series of dielectric layers. To accomplish this, we first explain the basic physics of the axion-induced microwave emission process at interfaces. For greater clarity, this is done in two steps, first considering the simple case where the disk and external B-field are aligned and the axion has no velocity, followed by

the more general case. We then turn to questions arising when many dielectric disks (perhaps up to around 100, or even 1000 for velocity sensitive setups) are used. We generalise the transfer matrix approach to include axions, which allows one to calculate the frequency-dependent emission, transmission and reflection functions for a chosen placement structure of the disks. In chapter 5 we change tactics somewhat, doing the same calculation but starting from a quantum field approach. We calculate the probability of axion-photon conversion by calculating the overlap between the axion and distorted photon wave functions. Conversion is made possible in dielectric haloscopes as the photon wave function is no longer an eigenstate of momentum in the presence of spatial inhomogeneities (such as dielectrics). This result agrees perfectly with the classical calculation.

We then use the computationally efficient transfer matrix formalism to study several generic setups which highlight both resonant and non-resonant features of dielectric haloscopes (chapter 6). Following this, in chapter 7 we consider more realistic and complicated setups, showing that one can achieve a large degree of control over the response of the system through disk placement, obtaining broadband, rectangular responses. We then make projections for the potential reach of a realistic axion dark-matter search experiment in chapter 8, and discuss the possibility of directional axion detection. Finally we conclude in chapter 9. Being a crucial feature of dielectric haloscopes, a proof of the Area Law is provided in appendix A. We show that the free photon wave function in the presence of dielectrics is given by the so called "Garibian wave functions" in appendix B. We also show that the overlap integral formalism we develop agrees with that of Sikivie for a resonant cavity, and that the quantum and classical calculations always agree (appendix C). This is done by deriving the overlap integral formalism from transfer matrices. Finally, in appendix D we discuss optimal search strategies.

Chapter 2

Review of Axion Detection

Before we get to the substance of the thesis, some context is needed for the search for axions. While the axion is an old idea, for many years the technological capabilities to search for many of the most interesting models did not exist. For a more complete recent review of detection methods in axion physics, we direct the reader to reference [19], to which we follow a relatively similar path.

2.1 The axion

2.1.1 Motivation: the Strong CP Problem

The original motivation for the axion does not come from DM, but rather the curious symmetry properties of the SM. It was realised quickly by Weinberg that the classical symmetries apparent in the SU(3) theory of QCD were in contradiction with experiment [22]. There seemed to be a U(1) axial symmetry in the QCD Lagrangian which was not respected in nature. This was resolved by the realisation that this axial symmetry was in fact anomalous due to the non-trivial vacuum topology of QCD [23, 24]. However, as a secondary consequence of this result one must be very cautious of total derivatives in QCD: unlike in EM, such terms do not automatically vanish.[1] A more full discussion of CP violation can be found in, for example, references [26, 27], but for our purposes it suffices that a new term is allowed in the QCD Lagrangian, the "theta term"

$$\mathcal{L}_{\mathrm{SM}} \supset -\frac{\alpha_s}{8\pi} G^b_{\mu\nu} \widetilde{G}^{\mu\nu}_b \theta_{\mathrm{QCD}}, \tag{2.1.1}$$

where α_s is the QCD version of the fine structure constant, $G^b_{\mu\nu}$ is the QCD field-strength tensor with $\widetilde{G}^{\mu\nu}_b = \frac{1}{2}\varepsilon^{\mu\nu\alpha\beta} G^b_{\alpha\beta}$ being its dual. Here and through-

[1] That total derivatives vanish in EM does depend on the local topology. In scenarios where the environment provides non-trivial topological aspects the total derivatives cannot be neglected [25].

out this thesis we use the Levi-Civita tensor with $\varepsilon^{0123} = \varepsilon_{123} = +1$. The index b denotes the colour index of the SU(3) fields.

Such a term violates P as well as CP—this can be seen more easily by writing

$$G^b_{\mu\nu}\widetilde{G}^{\mu\nu}_b = -4\mathbf{E}^b \cdot \mathbf{B}_b, \tag{2.1.2}$$

where $\mathbf{E}^b$ and $\mathbf{B}_b$ are the QCD versions of the electric and magnetic fields [28]. By analogy with EM, we know that E-fields are odd under P and C transformations, and B-fields are even under P and odd under C.

This CP violation would have many effects, but historically has been measured very precisely by looking at the electric dipole moment of the neutron. Such a moment can only exist in the presence of CP violation. The θ induced electric dipole moment was first calculated in the chiral limit of QCD (when the pion mass goes to zero) [29,30], and more recently with QCD sum rules [31] and lattice QCD [32–35]. Here we present the QCD sum rule result, however for our purposes any of these results would be equally demonstrative. There is also a contribution to the physically observable CP violating phase coming from the quark mass matrix, which we will absorb into our definition so that θ will denote the observable phase. For more information on the exact origin and impact of CP violation in QCD there are many reviews on the topic, such as [19]. The electric dipole moment of the neutron d_n is given by

$$d_n = \theta\,(2.3 \pm 1.0) \times 10^{-3}\text{e fm}. \tag{2.1.3}$$

Note that the nuclear scale is fm—if one entirely separated the charges inside a neutron one would expect a dipole moment on the order of 0.1 e fm. Thus the dipole moment induced by a large θ is actually very significant. Experiments have become increasingly sensitive to such a dipole moment, but have only ever seen a null result. The current limit is the stringent $|d_n| < 3.0 \times 10^{-13}$e fm [13, 14], meaning that

$$|\theta| \lesssim 1.3 \times 10^{-10}. \tag{2.1.4}$$

This seems to be an extremely small value for a fundamental constant of nature to adopt, leading physicists to puzzle over why QCD seems to respect CP symmetry to such a high degree. Possible explanations have included that one of the quarks is in fact massless (which would make the phase unphysical [36, 37]), however lattice QCD disfavours massless quarks [38]. Alternatively, one could consider having the phase being "calculably small" and arriving from some higher order diagram, though this tends to be difficult. For more discussion on these issues, the reader can look to reviews such as [15,39].

There are many ways to discuss how the axion arrises from attempting to solve the Strong CP Problem. One way is to look at the high energy symmetry structure of QCD, as in the original argument by Peccei and Quinn [40]. In this paper, they showed that θ can be made unphysical without a massless quark if there is a U(1) chiral symmetry, anomalous under QCD, under which a scalar field is charged and experiences spontaneous symmetry breaking at some

temperature. In this case, a simple field redefinition shows that θ disappears. The U(1) chiral symmetry is referred to as the Peccei-Quinn (PQ) symmetry. Weinberg and Wilczek noted that such a symmetry breaking must come with a pseudo-Nambu-Goldstone mode, which was promptly named the axion (after a then popular detergent) [41, 42]. Such a Nambu-Goldstone mode interacts with the strong force via a term

$$\mathcal{L}_{\text{axion}} \supset -\frac{\alpha_s}{8\pi} G^b_{\mu\nu} \widetilde{G}^{\mu\nu}_b \frac{a}{f_a}, \tag{2.1.5}$$

where f_a is the decay constant of the axion, generally related to the scale of PQ symmetry breaking. Note that the original θ term can be absorbed by $a/f_a \to a/f_a - \theta$, leading some to say that θ has been "promoted to a field". Thus one often writes $a(x^\mu)/f_a$ as $\theta(x^\mu)$. Note that $\theta(x^\mu)$ is in fact a pseudo-scalar field, meaning it is odd under P transformations. Therefore the interaction term (2.1.5) is P and CP conserving. The potential of the axion is in general periodic, and often approximated as

$$V_{\text{QCD}}(a) \sim \Lambda^4_{\text{QCD}} \left(1 - \cos\frac{a}{f_a}\right), \tag{2.1.6}$$

where Λ_{QCD} is the QCD scale. From (2.1.6) one sees the low energy version of the argument of Peccei and Quinn: θ is made into a dynamical field, whose potential's ground state respects the CP symmetry. Hence the axion is called a dynamical solution to the Strong CP Problem. In the early Universe the axion generally starts off away from this minimum, but evolves to the minimum of its potential at $\theta(x^\mu) = 0$ at late times in the Universe. The course of this evolution can have interesting cosmological consequences, which will be discussed below.

2.1.2 Axion models

Requiring that the axion resolves the Strong CP Problem is a strong constraint. The mass of the axion is given by the potential in equation (2.1.6) and so fixed simply by f_a and the QCD scale. Further, there are significant restrictions on the possible couplings. Such restrictions makes for a very predictive theory, though the exact phenomenology of the axion will change depending on how exactly the PQ symmetry is constructed. One will in general introduce some number of scalars and coloured fermions to obtain such a symmetry. At least one scalar must be introduced, however it is not necessary to introduce new fermions (as in the DFSZ axion [43,44]). For our purposes, it is sufficient to just specify the EM $\mathcal{E}$ and colour $\mathcal{N}$ anomalies of the theory, which are calculable simply from the charge assignments of these new fermions and scalars [19].

We will be mostly concerned with the axion coupling to photons, described by the Lagrangian density

$$\mathcal{L} = -\frac{1}{4} F_{\mu\nu} F^{\mu\nu} - J^\mu A_\mu + \frac{1}{2}\partial_\mu a \partial^\mu a - \frac{1}{2} m_a^2 a^2 - \frac{g_{a\gamma}}{4} F_{\mu\nu} \widetilde{F}^{\mu\nu} a, \tag{2.1.7}$$

with a the axion field with mass m_a. The coupling strength between axions and photons is governed by $g_{a\gamma}$. We use $F_{\mu\nu} = \partial_\mu A_\nu - \partial_\nu A_\mu$ to denote the EM field-strength tensor in terms of the vector potential $A^\mu = (A_0, \mathbf{A})$ and $J^\mu = (\rho, \mathbf{J})$ is the electric 4-current involving the charge density ρ and the current density $\mathbf{J}$. The dual tensor is given by $\widetilde{F}^{\mu\nu} = \frac{1}{2}\varepsilon^{\mu\nu\alpha\beta}F_{\alpha\beta}$. The electric and magnetic fields are given by

$$\mathbf{E} = -\boldsymbol{\nabla} A_0 - \dot{\mathbf{A}} \qquad \text{and} \qquad \mathbf{B} = \boldsymbol{\nabla} \times \mathbf{A}\,. \tag{2.1.8}$$

Note that in our units 1 V/m $= 6.5163 \times 10^{-7}$ eV^2 and 1 T = 1 Tesla $=$ 195.35 eV^2. The energy density of the EM field is $\frac{1}{2}(\mathbf{E}^2 + \mathbf{B}^2)$.

One could also consider cases where there is no fixed relationship between the mass and couplings. Such a particle is called an axion-like particle (ALP), but we are mostly interested in QCD axions. In this case, both parameters are largely decided by the PQ scale, or axion decay constant, f_a by $m_a f_a \sim m_\pi f_\pi$ and $g_{a\gamma} \sim \alpha/(2\pi f_a)$, where m_π and f_π are the pion mass and decay constant, respectively. The most recent study gives the numerical values [38]

$$m_a = 5.70(6)(4)\,\mu\text{eV}\left(\frac{10^{12}\,\text{GeV}}{f_a}\right), \tag{2.1.9a}$$

$$g_{a\gamma} = -\frac{\alpha}{2\pi f_a}C_{a\gamma} = -2.04(3)\times 10^{-16}\ \text{GeV}^{-1}\left(\frac{m_a}{1\,\mu\text{eV}}\right)C_{a\gamma}, \tag{2.1.9b}$$

$$C_{a\gamma} = \frac{\mathcal{E}}{\mathcal{N}} - 1.92(4), \tag{2.1.9c}$$

where the numbers in brackets denote the uncertainty in the last digit, with the first and second error given for m_a referring to quark-mass uncertainties and higher order corrections, respectively. $C_{a\gamma}$ is a model dependent number of $\mathcal{O}(1)$, which is given by the EM and colour anomalies ($\mathcal{E}$ and $\mathcal{N}$, respectively). In models where ordinary quarks and leptons do not carry PQ charges, the axion-photon interaction arises entirely from a-π^0-η mixing and $\mathcal{E}/\mathcal{N} = 0$, the KSVZ model [45, 46] being the traditional example. In more general models, $\mathcal{E}/\mathcal{N}$ is a ratio of small integers, the DFSZ model with $\mathcal{E}/\mathcal{N} = 8/3$ being an often-cited example, although there exist many other cases [47]. Recent studies have explored the range of $C_{a\gamma}$, finding that for the QCD axion $0 \lesssim C_{a\gamma} \lesssim 55$, though the extreme cases require judicious parameter choices [48, 49]. Note that if $\mathcal{E}/\mathcal{N} = 23/12 \sim 1.92$ then the total coupling is within theoretical uncertainty of zero. However, $C_{a\gamma}$ far more likely simply be suppressed by two orders of magnitude than exactly zero, which would require the true value of the a-π^0-η mixing contribution to match 23/12 exactly. ALPs can have any value of $C_{a\gamma}$ not ruled out by experiments or observations (as will be discussed below).

2.1.3 Axion dark matter

In the last section we saw that introducing the axion as a pseudo-Nambu-Goldstone mode coupled anomalously to QCD would resolve the Strong CP

Problem. The exact origin of the axion, and the scale at which the PQ symmetry breaks, does not change this salient fact.[2] However, the axion is not cosmologically inert. After PQ symmetry breaking, the axion acts as a coherent field, and acquires some initial value in each causally connected region. If the scale of PQ symmetry breaking is high, as the axion is a pseudo-Nambu-Goldstone mode all couplings are suppressed by a factor of f_a, leading to very weak interactions with the standard model. A coherently produced, low momentum and feebly interacting scalar field would be behave exactly as DM. For a more comprehensive review of this physics, we encourage the reader to consult reference [56].

The relic abundance of DM axions depends on the axion field's initial conditions and the subsequent cosmological evolution, but it also retains a dependence on the axion mass. For a given cosmological history, we can then compute the relic abundance and find for which axion mass we would saturate the observed DM abundance. There are two main classes of cosmological histories of relevance to the DM abundance, depending on the epoch where cosmological inflation took place. We start by assuming that, at some early time, the axion field a is uncorrelated at distances greater than the causal horizon. This is the case immediately after the PQ symmetry, $a \to a + 2\pi f_a$, becomes spontaneously broken in a phase transition. We call **Scenario A** when inflation occurs after this "Peccei–Quinn epoch" and **Scenario B** when inflation occurred before it.

Scenario A

In Scenario A a sub-horizon sized patch of the Universe, where the axion field is essentially homogeneous, is blown up during inflation to a size much larger than our observable Universe. We can then take homogeneous initial conditions for the axion field $a(x) = a_{\rm I} = \theta_{\rm I} f_a$, where $0 \leq \theta_{\rm I} < 2\pi$ is the initial misalignment angle, for the purpose of comparing with the overall DM abundance measured by Planck: $\Omega_{\rm DM} h^2 = 0.120 \pm 0.003$ [57]. We denote $\Omega_{\rm DM}$ as the ratio of the DM density to the critical density and $h = H_0/100\ {\rm km\,s^{-1}Mpc^{-1}}$ with H_0 the Hubble constant. Axion DM is produced by the so called vacuum realignment mechanism (also known as the misalignment mechanism). Before the axion mass arises from non-perturbative QCD effects, any $\theta_{\rm I}$ is allowed, hence the random initial conditions, i.e., a single random $\theta_{\rm I}$. However, once the axion potential appears the axion field rolls down towards the true minimum. As the axion's interactions are negligible, the axion will continue to oscillate coherently about the minimum damped only by Hubble friction (the expansion of the Universe). For relatively small $\theta_{\rm I}$, one can assume that the axion behaves

[2] An exception is if gravitational effects spoil the PQ symmetry, as quantum gravity effects are often thought to break global symmetries at some level [50–55].

like a damped harmonic oscillator to get [58]

$$\Omega_a h^2 \sim 5 \times 10^{-1} \left(\frac{f_a}{10^{12}\ \text{GeV}} \right)^{7/6} \theta_{\text{I}}^2, \tag{2.1.10}$$

where Ω_a is the ratio of the axion density to the critical density and we have assumed that $f_a < 2 \times 10^{15}\,\text{GeV}$. At higher f_a, the axion mass turns on during or after the QCD phase transition, which changes the multiplicative constant and scaling with f_a. Expressions for higher f_a can be found in reference [56]. The cosmic axion abundance depends on both θ_{I} and f_a (and thus m_a), so the observed DM density can be matched for essentially any value of m_a allowed by astrophysical bounds [59] for a suitable θ_{I}. The required value, assuming standard radiation domination during the onset of the axion mass, has been recently calculated [60]. It spans from $\theta_{\text{I}} = 10^{-4}$ to $\theta_{\text{I}} \simeq \pi$ in the f_a range 10^9–10^{19} GeV, i.e., in the m_a range 10^{-6}–$10^3\,\mu$eV. The largest values of f_a require very small θ_{I}, while for the smallest f_a values, θ_{I} has to be exquisitely tuned to π. Note that the smaller values of θ_{I} are often justified with the anthropic principle [61–66].

Scenario B

In Scenario B inflation does not set a single homogenous θ_{I} and thus the axion abundance is given by the average over random initial conditions and the decay of accompanying cosmic strings and domain walls. Cosmic strings and domain walls are topological defects in the axion field, allowed due to the inhomogeneous nature of $\theta(x^\mu)$. For example a cosmic string occurs when $\theta(x^\mu)$ goes around (winds) a full 2π surrounding some region. This winding cannot be undone while the axion is massless, due to the residual symmetry keeping it a Nambu-Goldstone mode (not a pseudo-Nambu-Goldstone mode). The formation of these kinds of topological defects is referred to as the Kibble mechanism [67]. Domain walls are related to the number of degenerate CP conserving vacua that are in the theory. This so called domain wall number is none other than the colour anomaly $\mathcal{N}$, and determines whether the domain walls are stable (which can occur when $\mathcal{N} > 1$). While topological defects are on the order of the horizon scale in their long dimensions, they have a width which is related to the PQ scale, and so are in general extremely dense. Note that stable domain walls would generically overclose the Universe, giving a strong model building constraint. Assuming that they decay, both them and cosmic strings will decay into long wavelength axions, providing another mechanism for cold DM. A nice summary of the axion production from defects can be found in, for example, reference [68].

In Scenario B the abundance depends on the domain wall number. In the simplest $\mathcal{N} > 1$ cases (such as the DFSZ axion), the network of domain walls and cosmic strings is stable and leads to a Universe very different from the one we observe [69]. Various extensions have been discussed that avoid

this conclusion and make these scenarios viable. One possibility is that the degeneracy of the different vacua is broken by higher-dimensional operators generated by dynamics at energy scales larger than f_a [70, 71]. Generically, this breaking shifts the position of the minimum of the axion potential away from the CP conserving value, so some mechanism is required to keep this effect below the requirements of a natural solution of the Strong CP Problem. Models where the PQ symmetry is an accidental symmetry of a theory containing a discrete symmetry [72] provide a well motivated realisation of this idea. A recent phenomenological study of this scenario [73] concludes, however, that the axion mass required to saturate the observed DM abundance exceeds the meV range. (These authors do not mention the possibility of DM dilution after the axion mass turns on, which will reduce this figure.) We note that another possibility to avoid a domain-wall dominated cosmology consists of introducing other axion-like fields that connect the different vacua and lead effectively to a $\mathcal{N} = 1$ cosmology [74, 75].

Models with $\mathcal{N} = 1$ such as KSVZ [45, 46] and KSVZ-like variants like SMASH [76, 77] are remarkably predictive. The most updated calculations lead to a unique prediction for the axion mass that saturates the observed DM abundance, $m_a \sim 100\,\mu$eV [68, 78], although with some still unclear theoretical uncertainty from the efficiency of axion radiation from strings and domain walls [79]. In SMASH one estimates $50\,\mu\text{eV} \lesssim m_a \lesssim 200\,\mu\text{eV}$ [76, 77]. Note however that the heavy quarks required in this model can shift this mass range downwards if they decay/annihilate after the axion mass onset. (See reference [48] for a recent study.) The primary source of uncertainty comes from the huge hierarchy of scales between the horizon scale at the QCD epoch and the PQ scale. During the QCD phase transition the PQ symmetry is explicitly (rather than spontaneously) broken, leading to the decay of the topological defects, which have a size given by the QCD scale. The PQ scale gives the size of the core of cosmic strings and widths of the domain walls. Note also that in these estimates there is somewhat of a double counting occurring, as the fact that topological defects exist is not taken into account when calculating the axions produced by the realignment mechanism. A more recent calculation corrects the double counting and uses a modified theory with an artificially increased string tension to mimic this large discrepancy of scales [80]. This method gives [81]

$$m_a = 26.2 \pm 3.4\ \mu\text{eV}, \tag{2.1.11}$$

which would be within range of HAYSTAC [82] (to be described in the next section).

The axion-photon coupling is well studied in these scenarios too. The simplest KSVZ model features a new heavy quark with zero hypercharge that implies $\mathcal{E} = 0$ and so $C_{a\gamma} = -1.92(4)$ [38]. The heavy quark is cosmologically stable [83] and in trouble with observations [48] so one needs to consider hypercharged versions of KSVZ. With hypercharge $-1/3$ or $2/3$ (as in SMASH), the heavy quark can mix with down or up quarks and decay, leading to an uncom-

plicated cosmology. Here one finds $\mathcal{E} = 2/3$ or $8/3$ and thus $C_{a\gamma} = -1.25(4)$ or $0.74(4)$ respectively. These are the only $\mathcal{N} = 1$ models with one heavy quark and thus the simplest natural targets for dielectric haloscopes. Models with extra heavy quarks can have effectively $\mathcal{N} = 1$ and thus point to the same $100\,\mu$eV mass range, but have different values of $C_{a\gamma}$ [48].

Lastly, in Scenario B the large density contrasts due to the inhomogeneous axion field can lead to axion miniclusters or stars [84–89]. These are extremely dense objects (by DM standards), which would also contribute to DM. Unfortunately there is no reliable prediction for the fraction of DM that would be in the form of these bound objects, which would be nigh impossible to detect on the Earth [90]. If almost all of DM was contained in such objects, direct detection experiments would have almost no signal to detect. However, it may be possible to detect such dense bound objects through gravitational microlensing [91, 92].

Axion parameter space

The axion's non-trivial phenomenology has led to many and varied bounds being used to restrict the parameter space. Amongst them are cooling of stellar objects, effects on the CMB, extra-galactic background light and direct searches using axion haloscopes and helioscopes (described below). We will not go into detail here, directing the reader to reference [19], and will simply present the totality of the bounds on $g_{a\gamma}$ summarised by their figure 2.1. Of course, analogous plots exist for the other axion couplings, however one requires a specific model in order to translate them into bounds on the axion-photon coupling. Dielectric haloscopes will only be sensitive to the axion-photon coupling, so we will ignore the other couplings to reduce model dependency.

2.2 Axion detection

One can gather from the very low axion masses described in the preceeding section that the phenomenology of the axion is dramatically different from that of most other DM candidates. Further, we saw in figure 2.1 that there is still a very significant part of the axion parameter space that is left untouched. The unique phenomenology of the axion means that searching for it requires dedicated and specialised experiments. These can be broken into three broad categories: laboratory searches, searches for solar axions (helioscopes) and DM searches (haloscopes). Due to our focus on axion DM, we will only briefly cover laboratory and solar axion searches (which usually are not in competition with DM searches).

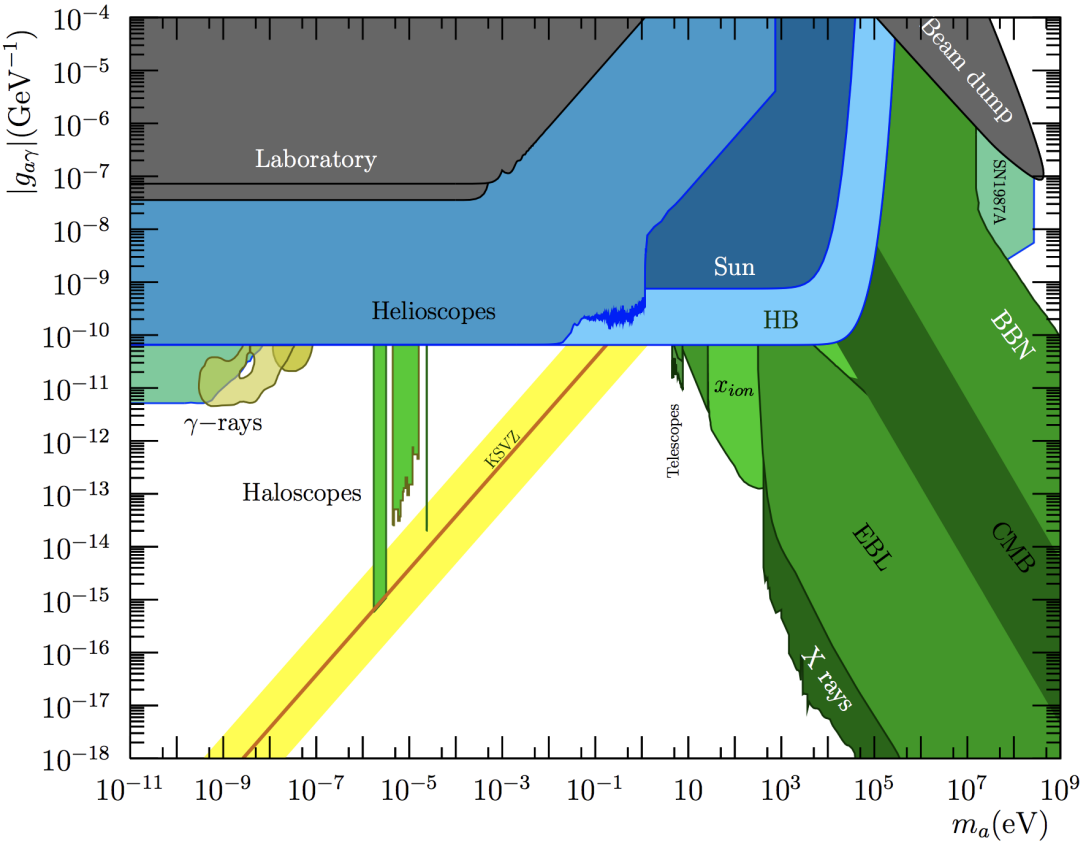

Figure 2.1: Constraints on the absolute value of the axion-photon coupling $|g_{a\gamma}|$ vs axion mass m_a. Typical QCD axion couplings are given by the yellow band, however for ALPs any combination of the mass and coupling is allowed. This figure is taken from reference [19] with permission.

2.2.1 Laboratory searches

One of the most direct ways to find axions would be to produce them inside a laboratory. This has the advantage of not requiring any assumptions about the source of the axions—everything is controlled. One can produce axions or ALPs in the lab by either the coupling to photons in equation (2.1.7), or by using couplings to fermions of the form $g_{af}\bar{f}f$ or $\bar{g}_{af}\langle\bar{f}\gamma^5 f\rangle$. The latter are the couplings of the axion to number and spin densities of the fermions, respectively. Note that axions are pseudo-scalars, so the coupling to $\bar{f}f$ would be CP violating. The coupling $g_{af}\bar{f}f$ generally does not appear in most models, leading most experiments searching for QCD axions to look for the axion coupling to spin. Thus to produce an axion field one can either use a large $\mathbf{E}\cdot\mathbf{B}$ or dense objects. However, producing the axion oneself also has a significant drawback: both the production and measurement come with a factor of the coupling squared, meaning that the overall rate is suppressed by a factor f_a^{-4}.

Laboratory experiments can be split into two main types: photon regener-

ation, also known as light shining through walls (LSW) and fifth force experiments. Most LSW are designed with a strong external magnetic field around a cavity, pumping that cavity with a strong E-field (such as a laser) with an additional empty cavity with a strong magnetic field on the other side of some barrier [93–103]. While photons cannot directly travel from one cavity to the other, they could convert to an axion, travel through the barrier, then reconvert back to a photon on the other side. This technique has so far only been used to search for ALPs, due to the large suppression by $g_{a\gamma}^4$ making reaching the QCD axion unfeasible with current designs.

On the other hand, fifth force experiments use the fact that the axion-fermion coupling induces forces with a range given by the Compton wavelength of the axion λ [104]. Such a force could be detected by deviations from Newtonian gravity [105–109] and violation of the equivalence principle [110, 111]. Alternatively, it has been suggested that one could detect the axion field sourced by some macroscopic body using nuclear magnetic resonance (NMR) techniques [112], as the interaction energy of a fermion inside an ALP field behaves like a magnetic dipole interaction. The ARIADNE Collaboration is aiming to do such an experiment [113].

2.2.2 Solar axion searches

Rather than going to the work of creating axions ourselves, the Sun provides a convenient source of axions [114–117]. Due to the lightness of axions, they can be produced in thermal processes inside stellar objects, and subsequently escape the system. This provides an additional source of energy loss and a significant flux of axions [118]. Axion helioscopes are designed to convert these relativistic axions into X-Rays using strong magnetic fields [18] (a calculation of this can be found in section 5.2). In effect, the Sun provides one side of a LSW experiment, with significantly higher flux than can be made currently in laboratories. Such a high flux at X-ray energies leads to generically stronger constraints than LSW experiments achieve. To reconvert the axions, one points a dipole magnet at the Sun [18]. Some tracking mechanism is usually employed to increase the amount of time the experiment points at the sun.

The current best helioscope is the CERN Axion Solar Telescope (CAST), using a Large Hadron Collider LHC dipole magnet [119, 120]. Limits from CAST are shown in figure 2.1. There are currently ambitious plans to supersede CAST with the International Axion Observatory (IAXO), with a specially designed multi-bore magnet, aiming to achieve a four order of magnitude improvement [116, 121]. While helioscopes are the most popular technique for searching for solar axions, there are also attempts to use Primakoff-Bragg conversion in crystals [122, 123].

2.2.3 Axion dark matter searches

Of primary relevance to our work is the detection of DM axions. As described in section 2.1.3, axions have a strong possibility of making up some or all of the DM in our Universe. The main way to discover DM axions would be to directly detect those in our own galactic halo. Being bound to our galaxy, the velocity dispersion of the DM axions on Earth is described by the galactic virial velocity $v_a \sim 10^{-3}$. The de Broglie wavelength of these galactic axions is then macroscopic

$$\lambda_{\rm dB} = \frac{2\pi}{m_a v} = 12.4 \text{ m } \left(\frac{100\,\mu\text{eV}}{m_a}\right)\left(\frac{10^{-3}}{v}\right), \tag{2.2.1}$$

Axion DM is a highly degenerate Bose gas and locally can be thought of as a classical field oscillating with frequency $\nu_a = m_a/2\pi$, i.e., in the microwave range.[3] This macroscopic coherence will lead to the overarching detection strategy: deal with small couplings by coherent enhancement!

Many of the techniques to detect DM axions will use the generic two-photon interaction described by equation (2.1.7). In a space permeated by a strong external magnetic field $\mathbf{B}_{\rm e}$, the galactic axion field $a(t)$ provides an effective oscillating electric current density $\mathbf{J}_a(t) = g_{a\gamma}\mathbf{B}_{\rm e}\dot{a}(t)$ which appears in Maxwell's equations as a source term in addition to the ordinary EM current. We will show how such a coupling appears explicitly in chapter 3. In a homogeneous situation, the solution of the modified Maxwell's equations is simply a homogeneous oscillating electric displacement field $\mathbf{D}_a(t) = \epsilon\mathbf{E}_a(t) = -g_{a\gamma}\mathbf{B}_{\rm e}\,a(t)$, where ϵ is the relative permittivity of a possible medium in the B-field region. For a plausible laboratory field of 10 Tesla, the axion-dark-matter induced oscillating electric field in vacuum is $|\mathbf{E}_a| \sim 10^{-12}$ V/m, independently of m_a, but oscillating with frequency ν_a. Instead of trying to measure this extremely small electric field directly one may use $\mathbf{J}_a(t)$ to drive dynamical modes of the EM field.

Cavity haloscopes

The traditional approach for axion DM detection is to use a microwave cavity placed in a strong laboratory B-field [18]. If the resonance is tuned to the axion mass, the cavity acts like a forced oscillator and on resonance achieves a large axion-induced excitation. As the axion field is coherent over many oscillations in the cavity the signal power is allowed to build up. The quality factor of the cavity is large ($Q \sim 10^5$) but finite so that power is constantly dissipated. This effect limits the amplitude of the excitations and implies that the oscillating axion field continuously produces microwave power. The geometric dimension of the cavity needs to be of the order of $\lambda/2 = 0.62$ cm $(100\,\mu\text{eV}/m_a)$ where λ is the photon wavelength corresponding to the microwave frequency ν_a. The

[3] Notice that $\nu_a = m_a/2\pi$ is approximately 1 GHz for $m_a = 4\,\mu$eV.

power extracted from a cavity is [124]

$$P_{\rm cav} = \kappa \mathcal{G} V \frac{Q}{m_a} \rho_a g_{a\gamma}^2 B_{\rm e}^2, \tag{2.2.2}$$

where V is the cavity volume, κ the ratio of signal power to total power loss and

$$\mathcal{G} = \frac{\left(\int dV\, \mathbf{E}_\alpha \cdot \mathbf{B}_{\rm e}\right)^2}{V B_{\rm e}^2 \int dV\, \mathbf{E}_\alpha^2} \tag{2.2.3}$$

is the geometry factor and $\mathbf{E}_\alpha$ is the cavity mode. The longest running ongoing effort, the ADMX experiment, currently begins with an axion search mass in the few-μeV range where a single cavity on resonance is big enough to produce a detectable signal [125]. If axions are the galactic DM in this mass range, ADMX will likely find them. HAYSTAC has recently started exploring higher mass ($\sim 20\,\mu$eV) axions, however it is yet to reach the most common axion benchmark models [82,126]. Development is still very much active, with squeezed-vacuum state receivers promising to significantly increase sensitivity [127]. There is also significant efforts underway at the Centre for Axion and Precision Physics (CAPP) in South Korea, with the flagship experiment being CULTASK [128], essentially a higher budget and more advanced version of ADMX.

However, dielectric haloscopes will be designed for the "high-mass range" of $m_a \gtrsim 10$ μeV where one can consider multiple resonant cavity arrangements [129,130] or resonant cavities with unusual shapes or aspect ratios [131]. In Australia the ORGAN experiment aims at the parameter range above $60\,\mu$eV, starting with traditional single cavity setups [132]. Another option is a linear resonator with a wiggled magnetic field, a first pilot study being the Orpheus experiment [133]. Recently there is increasing interest in building effective cavities operating at higher frequencies, particularly by using arrays of cavities [132, 134–136]. These try to reduce the problems of phase matching multiple resonant cavities by having some couplings between the cavities. Work in this direction comes from such groups as CAPP, ORGAN and the new RADES experiment [136], which uses multi-cavity arrays inside a CERN dipole magnet. Another interesting idea raised by the ORGAN group is to use dielectrics to form tuneable super-modes [137].

Interestingly, an axion DM search in the region with $m_a = 4$–$400\,\mu$eV was claimed to be viable a long time ago in an unpublished preprint [138]. A special cavity design with embedded dielectric plates was proposed to improve the cavity quality factor by more than one order of magnitude to $Q \gtrsim 5 \times 10^6$. The scanning over frequencies would be accomplished by varying the spacings between and the thicknesses of the plates and the width of the cavity in the direction perpendicular to the plates. Two requirements were expressed for the spacings and plate thicknesses: (i) $\lambda/4$ spacings between the cavity walls and the nearest plates with thickness $d \simeq \lambda/(4n)$ to reduce energy density at the cavity walls and (ii) $\lambda/2$ spacings between the other plates with thickness

$d \simeq \lambda/(2n)$ to optimize the phase coherence of the electric field inside the cavity volume. As a drawback we expect a significant adjustment time due to the required tuning to the cavity resonance and again due to the requirements on the plate thicknesses. This will slow down scans over a broad m_a range significantly. This idea has recently been revived in the form of the Electric Tiger by ADMX [139].

From this short summary one sees the furious effort that is going into pushing into higher (and still well motivated) axion masses. Our dielectric haloscopes will be aimed to sit just above the parameter space that is easily accessible with cavities. Of course such a range is in competition with the highest mass concepts for extending cavities. Only time will tell whether it will turn out to be more practical to build a dielectric haloscope, or whether some extension of cavity experiments will end up more easily realised. We summarise the potential reach of the proposed cavity experiments in figure 2.2.

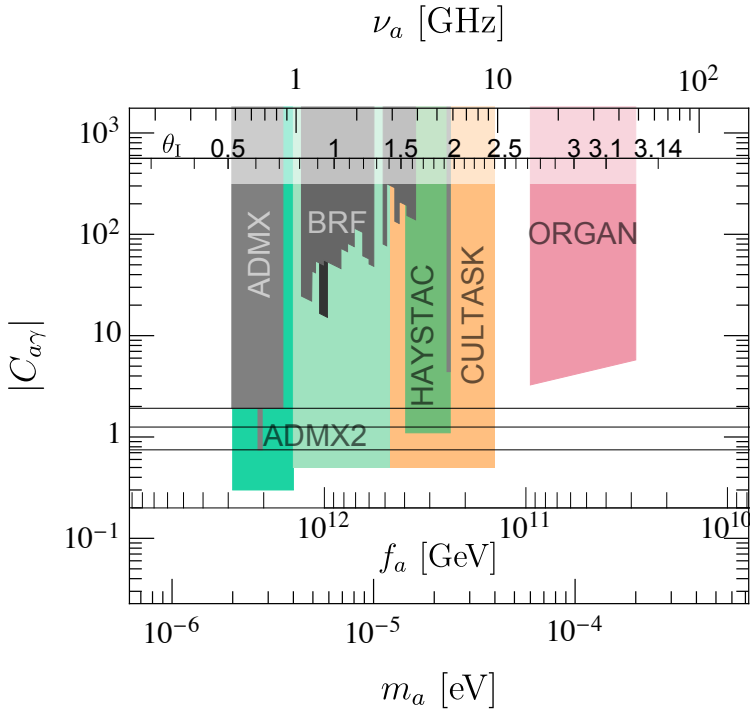

Figure 2.2: We show exclusion limits (gray) and sensitivities (coloured) of current and planned cavity haloscopes [128, 132, 140–146]. The upper inset shows the initial misalignment angle θ_I required in Scenario A [60]. The lower inset depicts the f_a value corresponding to a given m_a, and the three black lines denote $|C_{a\gamma}|$= 1.92, 1.25 and 0.746. Note that Scenario B predicts $25\,\mu\text{eV} \lesssim m_a \lesssim 200\,\mu\text{eV}$ [76, 78, 81]. Dielectric haloscopes will be ideally suited for the higher mass regime, above $\sim 20\,\mu$eV.

Dish antenna: first steps towards a dielectric haloscope

Our detection technique evolves from the dish antenna, which unlike the above mentioned cavities does not invoke resonators at all. If one places an interface that separates two dielectric media with different permittivity ϵ in a strong external magnetic field, microwave photons will be emitted in both perpendicular directions [147]. The homogeneous axion-induced electric displacement field $\mathbf{D}_a(t) = \epsilon \mathbf{E}_a(t) = -g_{a\gamma} \mathbf{B}_\mathrm{e}\, a(t)$ is no longer a self-consistent solution of Maxwell's equations because the total $\mathbf{E}$ (not $\mathbf{D}$) parallel to the interface needs to be continuous [148] and therefore requires microwave modes streaming in both directions away from the interface. Physically, these microwaves are sourced by an oscillating current $\mathbf{J}_a(t)$ in Maxwell's equations, but in a homogeneous situation no propagating wave can be excited. Once translation invariance is broken by an interface, $\mathbf{J}_a(t)$ leads to the emission of propagating waves in both perpendicular directions. A sufficiently sharp change in $\mathbf{B}_\mathrm{e}$ has the same effect, i.e., either the source density must be inhomogeneous or the medium response encoded in ϵ.

In the most extreme case of a perfect mirror in vacuum immersed in a B-field, microwaves are emitted only away from the mirror surface and the electric field strength of the propagating mode equals $\mathbf{E}_a$—the two electric fields need to cancel at the mirror surface. The signal power can be enhanced by making the mirror spherical to focus the microwaves in its centre and by placing a detector therein: the original axion dish antenna [147]. The advantage of this approach is its simplicity and broadband nature, but the signal boost that can be achieved in practice is not large enough to detect axion DM with existing technology. The dish antenna is still useful to cover a hitherto unexplored parameter range of more general axion-like particles or, without a magnetic field, of hidden photons as in the FUNK and Tokyo experiments [149, 150]. More recently, there is an ambitious project called BRASS to use a dish antenna approach to explore the higher mass range of 10–10^4 meV [151].

Another way of boosting the signal is to use multiple interfaces separating different dielectric media, which are placed at suitable distances to achieve constructive interference [152]. A minimal realization of this concept would be two near-perfect facing mirrors. However, this setup would be equivalent to a linear microwave cavity. One would need a large transverse size (large mirror area $\mathcal{S}$) and a distance of odd multiples of $\lambda/2 = 0.62$ cm for our reference value $m_a = 100\,\mu$eV. In practice, such an arrangement suffers from the same problems as any other cavity which tries to achieve a large volume for a small λ, i.e., the difficulty to extract power in detectable amounts and to achieve the resonance condition in a controlled and reproducible way.

A more encouraging realisation discussed in reference [152] is the $\lambda/2$ dielectric mirror which consists of N dielectric layers with alternating high and low refractive indices $n \simeq \sqrt{\epsilon}$ and thicknesses d given by $nd = \lambda/2$, where λ is the vacuum wavelength determined by m_a as specified above. This setting allows for constructive interference such that the signal power is boosted by

a factor of N^2 with respect to the case of a planar perfect mirror. However, an axion search will require a scan over m_a and thereby over $\lambda/2 = nd$. This seems to be very challenging if not impossible from the practical point of view because all layer thicknesses d would have to be chosen accordingly to explore each potential m_a value. We will develop the formalism to handle more complex situations, and so propose a practical version of the $\lambda/2$ dielectric mirror idea, the dielectric haloscope.

LC Circuits

If one instead wishes to consider lower axion masses, we have other options. For much smaller $m_a \sim 10^{-3}$–10^{-1} μeV, one could use an LC circuit coupled to the axion field with the help of a strong B-field [153–155]. An oscillating magnetic field can be measured by a pick up coil coupled with a (possibly resonant) LC circuit. There are two possibilities for the axion to induce such a field. One can either look at the axion induced magnetic field [154] (which comes from the small, but non-zero, velocity of the axion), or by using a secondary B-field generated by $\mathbf{E}_a$ [155, 156].

A nice realisation of the LC circuit concept is to use a toroidal magnet, giving a toroidal $\mathbf{E}_a$, with the pickup being located in the centre of the toroidal magnet [155]. This device could be operated in ether a broadband or resonant mode, though it has recently been claimed that the resonant mode is superior in general [157]. Currently there are two collaborations pursuing such a device, the first being ABRACADABRA [157], which is about to begin collecting data with a 10 cm prototype before scaling up for a full experiment. The second realisation is called DM Radio, though as of now they do not have a magnet and so are only sensitive to hidden photons [158]. Again, DM Radio has plans for an initial pathfinding experiment, which would then be ramped up to a full scale version.

NMR Techniques

To get to extremely low mass axions, it is profitable to move away from the axion-photon coupling altogether.

The gradient of the axion DM field couples to non-relativistic fermions in the same way as a magnetic field, allowing one to use NMR techniques [159–161]. While neglected for a long time, this type of experiment has resurged in the form of CASPEr Wind [162]. Alternatively, one could attempt to measure oscillations of the nuclear electric dipole moments [163]. Note that in the PQ mechanism, θ is not exactly zero as the remnant θ oscillations constitute DM. This idea is being picked up in the form of CASPEr Electric [162], and is seemingly the more practical of the two. CASPEr aims at QCD axions with $m_a \lesssim 10^{-2}\,\mu$eV.

Instead of using the axion coupling to nucleons, one could instead try to detect the coupling of axion DM to electrons [160–162, 164]. While using

electrons was initially considered extremely challenging if not impossible, the QUAX experiment [164] aims to do exactly this. Note that QUAX is aimed at much higher axion masses ($m_a \sim 200\,\mu$eV) than CASPEr, and could compete with dielectric haloscopes to some extent. Note however that as dielectric haloscopes measure a different coupling to QUAX there is no model independent way to compare the two. Indeed, discovering the axion via multiple couplings is highly desirable to learn more about the underlying physics of the axion.

2.3 Summary

The axion is a well motivated and predictive DM candidate. While introduced almost four decades ago, it is only recently that there has begun a concerted effort to explore the full range of parameter space allowed in the theory. Due to this lack of attention (as well as technological limitations) there are still significant gaps, with prime parameter space left untouched. We will focus on a new concept, dielectric haloscopes, which allow one to push into higher mass parameter space than is easily detectable in conventional cavity haloscopes.

Chapter 3

Axion-Photon Interactions in Matter

Before we can describe our experimental technique, we first need to know how the axion mixes with the photon in an external magnetic field $\mathbf{B}_\mathrm{e}$. Here we consider the linearised axion-Maxwell equations in the picture of axion-photon mixing.

3.1 Macroscopic form of Maxwell's equations

The Euler–Lagrange equations of motion for the axion and photon fields following from the Lagrangian density (2.1.7) are

$$\partial_\mu F^{\mu\nu} = J^\nu - g_{a\gamma}\widetilde{F}^{\mu\nu}\partial_\mu a\,, \tag{3.1.1a}$$

$$\left(\partial_\mu\partial^\mu + m_a^2\right) a = -\frac{g_{a\gamma}}{4} F_{\mu\nu}\widetilde{F}^{\mu\nu}\,. \tag{3.1.1b}$$

The first equation is a modification of the laws of Gauss and Ampère in the presence of axions, which leads to the extra current $J_a^\nu \equiv -g_{a\gamma}\partial_\mu(\widetilde{F}^{\mu\nu}a) = -g_{a\gamma}\widetilde{F}^{\mu\nu}\partial_\mu a$ on the right hand side (rhs) of this equation. The laws of Gauss for magnetism and of Faraday derive from a geometric property of electrodynamics, the Bianchi identity $\partial_\mu\widetilde{F}^{\mu\nu} = 0$, which does not get modified by including the axion. In terms of electric and magnetic fields, one finds [18,165]

$$\boldsymbol{\nabla}\cdot\mathbf{E} = \rho - g_{a\gamma}\mathbf{B}\cdot\boldsymbol{\nabla}a\,, \tag{3.1.2a}$$

$$\boldsymbol{\nabla}\times\mathbf{B} - \dot{\mathbf{E}} = \mathbf{J} + g_{a\gamma}\left(\mathbf{B}\,\dot{a} - \mathbf{E}\times\boldsymbol{\nabla}a\right)\,, \tag{3.1.2b}$$

$$\boldsymbol{\nabla}\cdot\mathbf{B} = 0\,, \tag{3.1.2c}$$

$$\boldsymbol{\nabla}\times\mathbf{E} + \dot{\mathbf{B}} = 0\,, \tag{3.1.2d}$$

$$\ddot{a} - \boldsymbol{\nabla}^2 a + m_a^2 a = g_{a\gamma}\mathbf{E}\cdot\mathbf{B}\,. \tag{3.1.2e}$$

While the homogeneous equations do not involve the axion field, they will be used to set the EM boundary conditions for an interface. Unsurprisingly, dielectric materials will be essential for our "dielectric haloscope". Accordingly,

we now reformulate these equations in terms of macroscopic fields to account for the EM response of the background medium.

The form of the homogeneous equations (3.1.2c) and (3.1.2d) does not change. Nevertheless, the fields $\mathbf{E}$ and $\mathbf{B}$ are here and henceforth understood to be the macroscopic ones obtained from the microscopic ones by macroscopic smoothing. This applies, in particular, to the rhs of equation (3.1.2e), which keeps its form as well. We mention in passing that there are other cases of axion electrodynamics where one would rather consider the microscopic fields. In our case of extremely small momentum transfers, the microscopic structure of the medium is not resolved.

Following a standard treatment of electrodynamics in media [148], we consider macroscopic charge and current densities and split them into a free part and a bound part: $\rho = \rho_\mathrm{f} + \rho_\mathrm{b}$ and $\mathbf{J} = \mathbf{J}_\mathrm{f} + \mathbf{J}_\mathrm{b}$. The bound parts are tied to the molecules of the medium and responsible for the EM response. They can be expressed in terms of the macroscopic polarization $\mathbf{P}$ (given by the macroscopic average over the molecular dipole moments) and the macroscopic magnetization $\mathbf{M}$ (given by the macroscopic average over the molecular magnetic moments)

$$\rho_\mathrm{b} = -\boldsymbol{\nabla}\cdot\mathbf{P} \quad \text{and} \quad \mathbf{J}_\mathrm{b} = \boldsymbol{\nabla}\times\mathbf{M} + \dot{\mathbf{P}}\,. \tag{3.1.3}$$

The free charge and current densities ρ_f and $\mathbf{J}_\mathrm{f}$ are simply the remaining parts, which satisfy the continuity equation

$$\dot{\rho}_\mathrm{f} + \boldsymbol{\nabla}\cdot\mathbf{J}_\mathrm{f} = 0\,. \tag{3.1.4}$$

Moreover, we introduce the usual macroscopic electric displacement field $\mathbf{D}$ and the macroscopic magnetic field $\mathbf{H}$ which absorb effects of the polarisation $\mathbf{P}$ and the magnetisation $\mathbf{M}$, respectively,

$$\mathbf{D} = \mathbf{E} + \mathbf{P} \quad \text{and} \quad \mathbf{H} = \mathbf{B} - \mathbf{M}\,. \tag{3.1.5}$$

(Following usual practice, we have ignored possible effects of molecular quadrupole moments.) The inhomogeneous equations (3.1.2a), (3.1.2b) and (3.1.2c) become

$$\begin{aligned}
\boldsymbol{\nabla}\cdot\mathbf{D} &= \rho_\mathrm{f} - g_{a\gamma}\mathbf{B}\cdot\boldsymbol{\nabla}a\,, && \text{(3.1.6a)}\\
\boldsymbol{\nabla}\times\mathbf{H} - \dot{\mathbf{D}} &= \mathbf{J}_\mathrm{f} + g_{a\gamma}\left(\mathbf{B}\dot{a} - \mathbf{E}\times\boldsymbol{\nabla}a\right)\,, && \text{(3.1.6b)}\\
\ddot{a} - \boldsymbol{\nabla}^2 a + m_a^2 a &= g_{a\gamma}\mathbf{E}\cdot\mathbf{B}. && \text{(3.1.6c)}
\end{aligned}$$

In our context, the important point is that on the rhs of equations (3.1.6a)–(3.1.6c) it remains $\mathbf{E}$ (not $\mathbf{D}$) and $\mathbf{B}$ (not $\mathbf{H}$) that appear in the axion–photon interaction terms, which remain unaffected by the medium response.

To solve these equations, additional constitutive relations $\mathbf{D} = \mathbf{D}[\mathbf{E},\mathbf{B}]$, $\mathbf{H} = \mathbf{H}[\mathbf{E},\mathbf{B}]$, and $\mathbf{J}_\mathrm{f} = \mathbf{J}_\mathrm{f}[\mathbf{E},\mathbf{B}]$ are needed that characterize the medium. Later we will assume simple isotropic media with a linear response. In this case, the third of these relations is Ohm's law which in our context applies, for example, to a metallic mirror.

3.2 Linearized axion-Maxwell equations

Our situation of interest is one where a strong static external magnetic field $\mathbf{B}_\mathrm{e}$ has been set up by means of an external current $\mathbf{J}_\mathrm{e}$ and is used to mix axions (in our case DM axions) with EM waves. Such a setting can be described by linearised macroscopic axion-Maxwell equations, which have plane-wave solutions. This description in terms of linear particle mixing is possible due to the significant hierarchy of scales between the static $\mathbf{B}_\mathrm{e}$ field, the background axion field and the induced EM fields, i.e., $\mathbf{B}_\mathrm{e}$ is much larger than all other fields, and the background axion field is much larger than any induced EM fields. For related linearisations, see also references [165–169]. Keeping only the leading terms in the static field $\mathbf{B}_\mathrm{e}$ on the rhs of equations (3.1.6a)–(3.1.6c) we find[4]

$$\begin{aligned}
\boldsymbol{\nabla}\cdot\mathbf{D}-\rho_\mathrm{f} &= -g_{a\gamma}\mathbf{B}_\mathrm{e}\cdot\boldsymbol{\nabla}a\,, && \text{(3.2.1a)}\\
\boldsymbol{\nabla}\times\mathbf{H}-\dot{\mathbf{D}}-\mathbf{J}_\mathrm{f} &= g_{a\gamma}\mathbf{B}_\mathrm{e}\dot{a}\,, && \text{(3.2.1b)}\\
\ddot{a}-\boldsymbol{\nabla}^2 a+m_a^2 a &= g_{a\gamma}\mathbf{E}\cdot\mathbf{B}_\mathrm{e}\,, && \text{(3.2.1c)}
\end{aligned}$$

where $\mathbf{D}$, $\mathbf{E}$, $\mathbf{H}$, ρ_f, $\mathbf{J}_\mathrm{f}$, and a all depend on t and $\mathbf{x}$.

Here $\mathbf{H}$ stands for the small time-varying part of the magnetic field, not including $\mathbf{H}_\mathrm{e}$ associated with $\mathbf{B}_\mathrm{e}$, and $\mathbf{J}_\mathrm{f}$ for the current density without $\mathbf{J}_\mathrm{e}$. Indeed, $\mathbf{H}_\mathrm{e}$ and $\mathbf{J}_\mathrm{e}$ do not appear since they fulfill equation (3.1.6b) separately. We have now written $\mathbf{J}_\mathrm{f}$ on the left hand side (lhs) of the equation because the only remaining current exists in response to the electric field. Likewise, in the modified Gauss law (3.2.1a), ρ_f is written on the lhs because we will always consider neutral media. Indeed, since we do not consider settings with a static charge density, we do not lose information by applying a time derivative on equation (3.2.1a) to obtain

$$\boldsymbol{\nabla}\cdot(\dot{\mathbf{D}}+\mathbf{J}_\mathrm{f}) = -g_{a\gamma}\mathbf{B}_\mathrm{e}\cdot\boldsymbol{\nabla}\dot{a}\,, \tag{3.2.2}$$

where the continuity equation (3.1.4) has been used. In the following we will use equation (3.2.2) instead of equation (3.2.1a) since this will allow us to include the case of conductors in a straightforward way.

The equations are now linear in all space-time dependent quantities. It is therefore convenient to expand them in plane waves proportional to $e^{-i(\omega t-\mathbf{k}\cdot\mathbf{x})}$, leading to

$$\begin{aligned}
\mathbf{k}\cdot(\omega\widetilde{\mathbf{D}}+i\widetilde{\mathbf{J}}_\mathrm{f}) &= -g_{a\gamma}\omega\mathbf{k}\cdot\mathbf{B}_\mathrm{e}\widetilde{a}\,, && \text{(3.2.3a)}\\
\mathbf{k}\times\widetilde{\mathbf{H}}+\omega\widetilde{\mathbf{D}}+i\widetilde{\mathbf{J}}_\mathrm{f} &= -g_{a\gamma}\omega\mathbf{B}_\mathrm{e}\widetilde{a}\,, && \text{(3.2.3b)}\\
\left(\omega^2-\mathbf{k}^2-m_a^2\right)\widetilde{a} &= -g_{a\gamma}\widetilde{\mathbf{E}}\cdot\mathbf{B}_\mathrm{e}\,, && \text{(3.2.3c)}
\end{aligned}$$

[4]Note that we do not consider static axion field contributions such as those associated with a static domain wall [170] on which photons can be reflected and transmitted.

where now $\widetilde{a}$, $\widetilde{\mathbf{D}} = \widetilde{\mathbf{E}} + \widetilde{\mathbf{P}}$, $\widetilde{\mathbf{H}}$, $\widetilde{\mathbf{E}}$, and $\widetilde{\mathbf{J}}_{\rm f}$ are complex amplitudes depending on ω and $\mathbf{k}$.

Let us now focus on homogeneous and isotropic materials which may be conductors and let us assume that the medium response is linear. In this case, the magnetic field and the magnetic induction are related in terms of the magnetic permeability μ in the form

$$\widetilde{\mathbf{H}} = \widetilde{\mathbf{B}}/\mu\,. \tag{3.2.4}$$

Notice that all quantities depend on ω and $\mathbf{k}$, encoding temporal and spatial dispersion. In configuration space, this relation is generally neither local in time nor in space. Thus, one cannot use the same simple form because $\mathbf{H}(t,\mathbf{x})$ is given by a convolution of $\mathbf{B}(t,\mathbf{x})$ with the $(t,\mathbf{x})$-dependent magnetic permeability. In practice, of course, the response functions may vary only slowly as functions of ω and $\mathbf{k}$ and one may not always need to worry about this issue.

If the medium is a conductor, the electric field drives a current given by Ohm's law in terms of the conductivity σ in the form $\widetilde{\mathbf{J}}_{\rm f} = \sigma\widetilde{\mathbf{E}}$. Moreover, in the linear response domain, the polarization is given as $\widetilde{\mathbf{P}} = \chi\,\widetilde{\mathbf{E}}$ where χ is the electric susceptibility. Therefore, we may combine the two terms and write on the lhs of equations (3.2.3a) and (3.2.3b) all electric effects in the form $\omega\widetilde{\mathbf{D}} + i\widetilde{\mathbf{J}}_{\rm f} = \omega\epsilon\widetilde{\mathbf{E}}$, where the total effective dielectric permittivity is

$$\epsilon = 1 + \chi + \frac{i\sigma}{\omega}\,. \tag{3.2.5}$$

In this form we can include both dielectric and conductive properties of the chosen material. Assuming that σ is real-valued for the frequency range of interest, its contribution to the imaginary part of ϵ derives from Ohm's law and accounts for absorption due to the conduction current. The additional contribution to $\mathrm{Im}(\epsilon)$ from $\mathrm{Im}(\chi)$ accounts for losses caused by the displacement current. Accordingly, the imaginary part of the permittivity is used to classify materials, e.g., as a perfect conductor for $\mathrm{Im}(\epsilon) \simeq \sigma/\omega \to \infty$ or as a perfect dielectric for $\mathrm{Im}(\epsilon) = 0$. In general, both ϵ and μ have real and imaginary parts; we comment on lossy media explicitly in section 3.4 below. Moreover, in general ϵ like μ depends on ω and $\mathbf{k}$, causing temporal and spatial dispersion.

With these definitions, the linearized macroscopic axio-electrodynamic equations in Fourier space are

$$\begin{aligned}
\epsilon\mathbf{k}\cdot\widetilde{\mathbf{E}} &= -g_{a\gamma}\mathbf{k}\cdot\mathbf{B}_{\rm e}\widetilde{a}\,, && \text{(3.2.6a)}\\
\mathbf{k}\times\widetilde{\mathbf{H}} + \omega\epsilon\widetilde{\mathbf{E}} &= -g_{a\gamma}\omega\mathbf{B}_{\rm e}\widetilde{a}\,, && \text{(3.2.6b)}\\
\mathbf{k}\cdot\widetilde{\mathbf{B}} &= 0\,, && \text{(3.2.6c)}\\
\mathbf{k}\times\widetilde{\mathbf{E}} - \omega\widetilde{\mathbf{B}} &= 0\,, && \text{(3.2.6d)}\\
\left(\omega^2 - \mathbf{k}^2 - m_a^2\right)\widetilde{a} &= -g_{a\gamma}\widetilde{\mathbf{E}}\cdot\mathbf{B}_{\rm e}\,. && \text{(3.2.6e)}
\end{aligned}$$

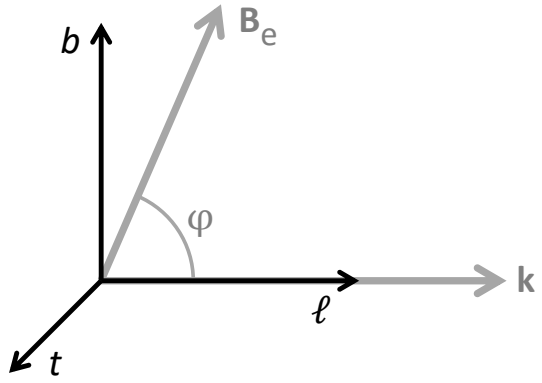

Figure 3.1: Polarization basis for a field with wavevector $\mathbf{k}$, defining the ℓ direction. Perpendicular to $\mathbf{k}$ and $\mathbf{B}_\mathrm{e}$ is the t direction, whereas the b direction is perpendicular to $\mathbf{k}$ and spans the plane containing $\mathbf{B}_\mathrm{e}$.

For completeness, we have written out the homogeneous equations in Fourier space as well, in which $\mathbf{B}_\mathrm{e}$ does not appear because it is assumed to be stationary and $\boldsymbol{\nabla} \cdot \mathbf{B}_\mathrm{e} = 0$.

We gain more insight by expressing $\mathbf{E}$ and $\mathbf{B}$ in terms of their components along $\mathbf{k}$, which we call the ℓ (longitudinal) component, and the transverse components. To describe the latter, we use a coordinate system with one vector in the plane of $\mathbf{k}$ and $\mathbf{B}_\mathrm{e}$, which we call the b direction, and one vector transverse to both $\mathbf{k}$ and $\mathbf{B}_\mathrm{e}$, which we call the t direction, (see figure 3.1). In our practical applications, typically $\mathbf{B}_\mathrm{e}$ will be very nearly perpendicular to $\mathbf{k}$ so that the "b direction" then almost coincides with $\mathbf{B}_\mathrm{e}$. We denote the angle between $\mathbf{B}_\mathrm{e}$ and $\mathbf{k}$ as φ (as in figure 3.1) so that the external B-field in the b direction is $B_\mathrm{e} \sin\varphi$ and the one in the ℓ direction is $B_\mathrm{e} \cos\varphi$.

Equation (3.2.6a) applies to the ℓ component and simply reads $k\epsilon\widetilde{E}_\ell = -g_{a\gamma} k B_\mathrm{e} \widetilde{a} \cos\varphi$, whereas the ℓ part of equation (3.2.6b) reads $\omega\epsilon\widetilde{E}_\ell = -g_{a\gamma}\omega B_\mathrm{e}\widetilde{a}\cos\varphi$. These equations are equivalent except when $\omega = 0$ or $k = 0$. We only consider solutions with $\omega \neq 0$ because by assumption the only static field is $\mathbf{B}_\mathrm{e}$. On the other hand, we also consider homogeneous situations ($k = 0$), so overall we may drop equation (3.2.6a), which is trivial when $k = 0$, and keep the ℓ part of equation (3.2.6b).

At this point, one could assume correctly that at lowest order, the DM axion field itself is unchanged when generating photons. In other words only a small number of the axions actually convert because the interaction is so weak. One could then simply think of the DM axion as the source of the axion induced E and H-fields, and proceed to solving the Maxwell equations with the axions as an external source. In other words, one would linearise the system with respect to both $\mathbf{B}_\mathrm{e}$ and a. However, to consider the full effect of the axion-photon interactions, we must calculate the axion-photon mixing. This more general approach will allow us to check such a linearisation of a

explicitly.

It is convenient to return to the vector potential as a description of the time-varying $\mathbf{E}$ and $\mathbf{B}$ fields. In Fourier space we have $\widetilde{\mathbf{B}} = i\,\mathbf{k}\times\widetilde{\mathbf{A}}$ and $\widetilde{\mathbf{E}} = i(\omega\widetilde{\mathbf{A}} - \mathbf{k}\widetilde{A}_0)$. In the longitudinal components of the equations, only the combination $\omega\widetilde{A}_\ell - k\widetilde{A}_0$ ever appears. Because in our case $\omega \neq 0$, it is consistent to set $\widetilde{A}_0 = 0$ which amounts to using the temporal gauge (also known as Weyl or Hamiltonian gauge). The subtleties of this choice do not affect our case. Alternatively, because $\omega \neq 0$, we could define $\widetilde{A}_\ell$ simply as a notation for the physical quantity $\widetilde{E}_\ell/i\omega$. In terms of $\mathbf{A}$, the remaining linear equations of motion are

$$\begin{aligned}\left(\epsilon\,\omega^2 - \mathbf{k}^2/\mu\right)\widetilde{\mathbf{A}} + (\mathbf{k}\cdot\widetilde{\mathbf{A}})\mathbf{k}/\mu &= ig_{a\gamma}\omega\mathbf{B}_\mathrm{e}\,\widetilde{a}\,, &\text{(3.2.7a)}\\ \left(\omega^2 - \mathbf{k}^2 - m_a^2\right)\widetilde{a} &= -ig_{a\gamma}\omega\mathbf{B}_\mathrm{e}\cdot\widetilde{\mathbf{A}}\,. &\text{(3.2.7b)}\end{aligned}$$

In terms of the different polarization components, our final equations of motion in Fourier space are

$$\begin{pmatrix}\omega^2 - k^2 - m_a^2 & \Delta_b\omega & \Delta_\ell\omega & 0\\ \Delta_b\omega & \epsilon\omega^2 - k^2/\mu & 0 & 0\\ \Delta_\ell\omega & 0 & \epsilon\omega^2 & 0\\ 0 & 0 & 0 & \epsilon\omega^2 - k^2/\mu\end{pmatrix}\begin{pmatrix}\widetilde{a}\\ i\widetilde{A}_b\\ i\widetilde{A}_\ell\\ i\widetilde{A}_t\end{pmatrix} = 0\,, \qquad (3.2.8)$$

where the "mixing energies" are $\Delta_b = g_{a\gamma}B_\mathrm{e}\sin\varphi$ and $\Delta_\ell = g_{a\gamma}B_\mathrm{e}\cos\varphi$. We recall that in general the response functions ϵ and μ depend on ω and $\mathbf{k}$ and that in lossy media they have imaginary parts. The factor of i in (3.2.8) reflects a phase difference of $\pi/2$ between the components of $\mathbf{A}$ and a, which disappears when $\mathbf{A}$ is expressed in terms of $\mathbf{E}$.

3.3 Eigenmodes of the interacting system

The last line of the equations of motion (3.2.8) remains unaffected by the axion-photon interaction and leads to the dispersion relation $k^2 = n^2\omega^2$, where we have introduced the usual refractive index[5]

$$n^2 = \epsilon\mu\,. \qquad (3.3.1)$$

Notice that in general n can be a complicated function of ω and k, although in our cases of practical interest, we ignore spatial dispersion (no dependence on k) and temporal dispersion (the dependence on ω), as we expect them to be weak. The same dispersion relation applies, of course, to the b polarization in the absence of axion-photon mixing. In this case the ℓ dispersion relation

[5]We assume that the imaginary part of n is much smaller than its real part and that the real part is positive. In this case we can use relations of the type $x = \sqrt{x^2}$ with impunity because we avoid the branch cut of the square-root function along the negative real axis.

is $\epsilon\omega^2 = 0$ and, because we only consider $\omega \neq 0$, would require $\epsilon(\omega, k) = 0$ to support a propagating mode. A plasma can provide such a mode, the longitudinal plasmon. A non-relativistic plasma has $\epsilon \simeq (1 - \omega_p^2/\omega^2)$, where ω_p is the plasma frequency (i.e., the frequency of the longitudinal plasmon). While in principle axions can mix resonantly with longitudinal plasmons [166], there are currently no proposed experimental efforts using such a mixing. The dielectric media we will consider later do not support such dynamical ℓ modes. The axion dispersion relation in the absence of a magnetic field is $\omega^2 - k^2 = m_a^2$.

In the presence of axion-photon interactions, the eigenmodes of our system are superpositions of the axion and photon field. Note that A_t seems to decouple in equation (3.2.8) but when we consider a boundary between different dielectric media we will see that non-trivial alignments between the interface and the magnetic field can mix A_t with A_b.

Non-trivial solutions of equation (3.2.8) require the determinant of the matrix to vanish. Because in general ϵ and μ depend on both ω and $\mathbf{k}$, the solution depends on the material properties of the medium. Here we will neglect spatial dispersion, i.e., henceforth we assume that ϵ and μ depend only on ω. Moreover, we also assume isotropic media where the response functions do not depend on the direction of $\mathbf{k}$. We then find two solutions for the dispersion relation. To lowest non-trivial order in the extremely small mixing energies they are

$$\text{Axion like:} \quad k^2 = \omega^2 - m_a^2 - \frac{\Delta_b^2 \omega^2 \mu}{n^2\omega^2 - \omega^2 + m_a^2} - \frac{\Delta_\ell^2 \omega^2 \mu}{n^2 \omega^2} + \mathcal{O}(\Delta_{b,\ell}^4) \tag{3.3.2a}$$

$$\text{Photon like:} \quad k^2 = n^2\omega^2 + \frac{\Delta_b^2 \omega^2 \mu}{n^2\omega^2 - \omega^2 + m_a^2} + \mathcal{O}(\Delta_{b,\ell}^4)\,. \tag{3.3.2b}$$

A resonance can occur when $n < 1$, i.e., when the "squared effective photon mass" $m_\gamma^2 = \omega^2 - k^2 = (1 - n^2)\omega^2$ is positive. However, as the mixing is typically exceedingly small, even tiny losses in the medium will limit the resonance enough so that higher order terms are not required. For example, for $100\,\mu$eV DM axions in a 10 T B-field $\Delta_{b,\ell} \sim 10^{-12}\,\mu$eV, so $\mathrm{Im}(n) \lesssim 10^{-26}$ is required for $\Delta_{b,\ell}^4$ effects to become relevant in equation (3.3.2). Further, to get the resonance condition one would need $n \sim 10^{-3}$, so an incredibly special material would be needed to realise this. For higher order terms to be necessary, the numerator and denominator must be of similar size, which requires very large frequencies, low losses and large mixing energies. Such resonances can occur in the often-studied case of axion-photon oscillations [171] at high energies, where one typically assumes axions and photons to be nearly degenerate, i.e., it is assumed that $\Delta_b\omega \gg m_a^2$ and $\Delta_b\omega \gg |n^2 - 1|\omega^2$. Actually at the highest astrophysically relevant energies in the 10 TeV range, intergalactic magnetic fields provide this condition as the cosmic microwave background then produces a non-negligible refractive index [172].

Motivated by our case of an ordinary dielectric medium, we have assumed a photon refractive index of $n > 1$, i.e., the photon dispersion relation is space like, ignoring a possible small imaginary part which we will discuss below. In this case the two branches of the dispersion relation do not cross for any value of ω; photons and axions are never on resonance with each other, and so the denominator in (3.3.2) never becomes zero. Note that the velocities of the particles are given by the group velocity of the waves, $\partial\omega/\partial k$. For the axion this relation then gives us that $\mathbf{v} = \mathbf{k}/\omega$.

It is now straightforward to obtain the field configurations corresponding to these propagating modes. To lowest order in the small mixing energies we find

$$\text{Axion like:} \qquad \begin{pmatrix} \widetilde{a} \\ i\widetilde{A}_b \\ i\widetilde{A}_\ell \end{pmatrix} = \begin{pmatrix} 1 \\ -\chi_{_b}\mu\sin\varphi \\ -\chi_{_\ell}\mu\cos\varphi \end{pmatrix} + \mathcal{O}(\chi_{b,\ell}^2), \tag{3.3.3a}$$

$$\text{Photon like:} \qquad \begin{pmatrix} \widetilde{a} \\ i\widetilde{A}_b \\ i\widetilde{A}_\ell \end{pmatrix} = \begin{pmatrix} \chi_{_b}\sin\varphi \\ 1 \\ 0 \end{pmatrix} + \mathcal{O}(\chi_{b,\ell}^2)\,, \tag{3.3.3b}$$

where we have defined the small dimensionless mixing parameters

$$\chi_{_b} = \frac{g_{a\gamma}B_{\rm e}\,\omega}{n^2\omega^2 - \omega^2 + m_a^2}\,, \tag{3.3.4a}$$

$$\chi_{_\ell} = \frac{g_{a\gamma}B_{\rm e}\,\omega}{n^2\omega^2}\,. \tag{3.3.4b}$$

These vectors are normalized at linear order in $\chi_{b,\ell}$ (linear order in $g_{a\gamma}$). On the other hand, the dispersion relations in equation (3.3.2) get modified only at order $g_{a\gamma}^2$. Therefore, the dominant effect of the axion-photon interaction is that the normal propagating photon and axion modes obtain a small admixture of the other flavor. Henceforth we will always work to linear order in $g_{a\gamma}$ and thus ignore the modification of the dispersion relations.

Notice that these two solutions correspond to different combinations of ω and k, i.e., those which obey the respective dispersion relations. For a fixed choice of ω, these two solutions have different k values.

Recall that in our dielectric media, there is no longitudinal photon-like solution. Regardless, through the mixing the axion-like mode carries a small electric field component along $\mathbf{k}$.[6] This small longitudinal electric field is often neglected in the literature—while for most experimental concepts the B-field is transverse by design, there are exceptions such as the AMELIE helioscope proposal [173]. As in this case the B-field is not aligned with the solar axions,

[6]Likewise, we could consider frequencies below the axion mass, $\omega < m_a$, where the axion has no propagating mode, yet the photon-like mode exists and still carries a small axion component.

it is possible that longitudinal axion induced E-fields could influence the experiment. We will show in section 4.2 that the axion induced longitudinal field can influence the generation of photon-like waves from an interface.

3.4 Lossy media

In general, dielectrics are not perfect, i.e., not all the EM energy that propagates in the form of waves is transferred or reflected but absorbed as well. For us, this means that the full signal generated by axions (described in detail below) will not be available and stacking too many lossy dielectric layers may be counter productive. To describe the effect of losses, we allow ϵ to be complex valued as discussed earlier. We quantify losses in terms of the usual dielectric loss tangent

$$\tan\delta = \frac{\mathrm{Im}\,\epsilon}{\mathrm{Re}\,\epsilon}\,. \tag{3.4.1}$$

For the dielectric layers in realistic experimental situations, we would use materials with $\tan\delta \ll 1$. Typical values may be of the order of 10^{-5} so that with excellent approximation $\tan\delta \simeq \delta$. Assuming a non-permeable material with $\mu = 1$, the refractive index can then be written as $n \simeq |n|(1 + i\delta/2)$.

EM waves are damped in lossy media. For our specific case, it is shown below that all time variations are driven by the external axion field with frequency $\omega = m_a = \omega_a = \omega_\gamma$, leading to a steady-state situation with no damping as a function of time. Therefore, when we study propagating plane-wave solutions which are proportional to $e^{-i(\omega t - \mathbf{k}\cdot\mathbf{x})}$ and which obey the dispersion relation (3.3.2b), it is the wave number k which acquires an imaginary part and not the frequency. For example, a linearly polarized electric field of a plane wave propagating in the positive x-direction is proportional to

$$e^{-i\omega(t-nx)} = e^{-\mathrm{Im}(n)\omega x}\, e^{-i\omega[t-\mathrm{Re}(n)x]}. \tag{3.4.2}$$

For $\mathrm{Im}\,n > 0$ this wave is exponentially damped as a function of x. In the opposite case, for example in an inverted medium in the context of laser physics, the wave grows exponentially.

Waves which are exponentially damped as a function of spatial coordinates cannot exist in a (semi-)infinite medium, i.e., when we discuss plane-wave solutions in a homogeneous medium, we are having in mind piecewise homogeneous situations with a plane boundary of the medium. Of course, interfaces between different media, or between a medium and empty space, is exactly what we study in our paper. Notice also that a solution of the form $e^{-i(\omega t - \mathbf{k}\cdot\mathbf{x})}$ does not represent a spatial Fourier mode of the electric-field distribution. Because $\mathbf{k}$ has now an imaginary part commensurate with the complex dispersion relation (3.3.2b), this plane wave is one component of a Laplace transform.

In the following parts of our paper, all formulas will be consistent with complex dielectric constants ϵ and with plane waves which are damped along

their direction of propagation. One should remember, however, that the electric and magnetic fields of a propagating EM wave are not in phase if the wave number k has an imaginary part.

3.5 Dark matter axions

Our case of interest is very special in that the galactic DM axions are highly non-relativistic ($v \lesssim 10^{-3}$). In view of the small axion mass and velocity, and concomitant large de Broglie wavelength, equation (2.2.1), the axion field only exhibits a slow change of phase over the laboratory scale.

First, we will consider the simple case of a monochromatic DM distribution, with a field amplitude given by a_0. As explained earlier, we ignore a frequency shift by axion-photon mixing which is quadratic in the small coupling constant $g_{a\gamma}$. The difference between the transverse and longitudinal mixing is negligible,

$$\chi_{_t} \simeq \chi_{_\ell} \equiv \chi = \frac{g_{a\gamma} B_{\rm e}}{n^2 m_a} = 3.98(5) \times 10^{-16}\, \frac{C_{a\gamma}}{n^2}\, \frac{B_{\rm e}}{10\,{\rm T}}\,. \tag{3.5.1}$$

The axion-like wave is given by

$$a(t,\mathbf{x}) = a_0 e^{i(\mathbf{p}\cdot\mathbf{x}-\omega t)} \quad ; \quad i\mathbf{A}_a(t,\mathbf{x}) = -\chi\mu\hat{\mathbf{B}}_e\, a(t,\mathbf{x}), \tag{3.5.2}$$

where $\mathbf{A}_a$ is the axion induced $\mathbf{A}$ field. We see that the axion field develops a small electric field oscillating with the axion's frequency ω,

$$\mathbf{E}_a(t,\mathbf{x}) = -\dot{\mathbf{A}}_a(t,\mathbf{x}) = -\chi\mu\omega\, a(t,\mathbf{x})\hat{\mathbf{B}}_{\rm e} = -\frac{g_{a\gamma}\mathbf{B}_{\rm e}}{\epsilon}\, a(t,\mathbf{x})\,. \tag{3.5.3}$$

In addition, there is also a small induced H-field given by

$$\mathbf{H}_a(t,\mathbf{x}) = \frac{1}{\mu}\nabla\times\mathbf{A}_a(t,\mathbf{x}) = -v\sin\varphi\,\chi\,\omega a(t,\mathbf{x})\hat{\mathbf{t}}_a = -\frac{v g_{a\gamma} B_{\rm e}\sin\varphi}{\mu\epsilon} a(t,\mathbf{x})\hat{\rm t}_a, \tag{3.5.4}$$

where $\hat{\rm t}$ is the unit vector in the t direction. Note that $\mathbf{H}_a$ is suppressed by the axion velocity; the axion induced magnetic field will only have a subdominant effect in dielectric haloscopes. However, there are proposals to use this field to detect DM axions by using an LC circuit [154]. The photon-like waves are very much like ordinary transverse EM waves (transverse up to $O(\chi^2)$ corrections) accompanied by a relativistic axion field proportional to the $\hat{\mathbf{b}}$ projection of the magnetic field, i.e., $\hat{\mathbf{B}}_{\rm e}\cdot\hat{\mathbf{b}} = \sin\varphi$ (with φ defined as in figure 3.1)

$$\mathbf{A}(t,\mathbf{x}) = A_0\hat{\mathbf{b}}e^{i(\mathbf{k}\cdot\mathbf{x}-\omega t)} \quad ; \quad a_\gamma(t,\mathbf{x}) = i\chi\hat{\mathbf{B}}_{\rm e}\cdot\mathbf{A}(t,\mathbf{x}) = \frac{\chi}{\omega}\hat{\mathbf{B}}_{\rm e}\cdot\mathbf{E}(t,\mathbf{x}). \tag{3.5.5}$$

with $n^2\omega^2 = |\mathbf{k}|^2$ and A_0 the field amplitude of the photon-like wave. As we will be converting axions to photons, all photon-like waves will be produced at linear order in χ, so the axionic component is $\mathcal{O}(\chi^2)$ and thus negligible.

Note that the physical axion field is given by the real part of $a(t, \mathbf{x})$, which up to some phase $\alpha_{\mathbf{p}}$ we can write as

$$a(t, \mathbf{x})_{\text{phys}} = |a_0| \cos(\mathbf{p} \cdot \mathbf{x} - \omega t + \alpha_{\mathbf{p}}). \tag{3.5.6}$$

To calculate the DM density of a monochromatic axion field, we note that one must perform an average of the energy density over some sufficiently long time $T \gg 1/\omega$,

$$\begin{aligned} \rho_a(\mathbf{x}) &= \frac{1}{T} \int_0^T dt \, \frac{1}{2} [\partial_t a(t, \mathbf{x})]^2 + \frac{1}{2} [\nabla a(t, \mathbf{x})]^2 + \frac{1}{2} m_a^2 a(t, \mathbf{x})^2 \\ &= \frac{\omega^2 |a_0|^2}{2} \\ &= f_{\text{DM}} \, \frac{300 \text{ MeV}}{\text{cm}^3}, \end{aligned} \tag{3.5.7}$$

where f_{DM} is a fudge factor expressing the uncertainty in the local DM density[7] as well as the uncertainty of the DM fraction consisting of axions relative to possible other forms of DM or relative to the fraction gravitationally bound in axion mini clusters.

For a zero-velocity DM axion field we then find that the axion induced electric field has an amplitude E_0 given by

$$E_0 = g_{a\gamma} B_{\text{e}} a_0 = 1.3 \times 10^{-12} \text{ V/m} \, \left(\frac{B_{\text{e}}}{10 \text{ T}} \right) \, C_{a\gamma} f_{\text{DM}}^{1/2} \, . \tag{3.5.8}$$

For comparison we mention that the energy density associated with the external magnetic field is $\frac{1}{2} B_{\text{e}}^2 = 2.5 \times 10^{14} \text{ MeV/cm}^3 \, (B_{\text{e}}/10 \text{ T})^2$, i.e., around 12 orders of magnitude larger than the local DM energy density. On the other hand, the energy density associated with the axion-induced electric field $E_0^2/2$ is found to be some 31 orders of magnitudes smaller than ρ_a. Note also that for the QCD axion, this result is independent of the axion mass because $|a_0| \propto \rho_a^{1/2}/m_a$ whereas $g_{a\gamma} \propto m_a$.

The limit of a monochromatic (usually zero velocity) axion field will often be useful throughout this thesis. For an experiment searching for the axion, one would often design the experiment to avoid sensitivity to the velocity (as discussed more in chapter 8). Further, having a single velocity makes it easier to clearly study under what conditions velocity effects do become important.

Of course, we know that the axion field cannot have a perfectly monochromatic distribution, as there is spatial variation in the DM halo. More generally, we can describe the local axion field as a superposition of plane waves

$$a(t, \mathbf{x}) = \int \frac{d^3\mathbf{p}}{(2\pi)^3} a(\mathbf{p}) e^{i(\mathbf{p} \cdot \mathbf{x} - \omega t)} \, , \tag{3.5.9}$$

[7] The local DM density has been estimated by various authors using different data and assumptions [174–180]. The value 300 MeV cm^{-3} is often used as a benchmark number, although in the axion literature, 400 MeV cm^{-3} is frequently used. The particle data group [17] gives an even larger value based on Ref. [174].

where $a(\mathbf{p})$ is the momentum Fourier decomposition associated with the DM field. Averaging over some large volume V, the average energy density is given by

$$\begin{aligned}\bar{\rho}_a &= \frac{1}{V}\int_V d^3\mathbf{x}\,\frac{1}{2}[\partial_t a(t,\mathbf{x})]^2 + \frac{1}{2}[\nabla a(t,\mathbf{x})]^2 + \frac{1}{2}m_a^2 a(t,\mathbf{x})^2 \\ &= \frac{1}{V}\int \frac{d^3\mathbf{p}}{(2\pi)^3}\frac{\omega^2|a(\mathbf{p})|^2}{2} \simeq \frac{1}{V}\int \frac{d^3\mathbf{p}}{(2\pi)^3}\frac{m_a^2|a(\mathbf{p})|^2}{2}\,, \end{aligned} \tag{3.5.10}$$

which holds in the limit that V is large enough to resolve the full structure of DM. Explicitly, the spatial integration gives sinc functions, which act as Dirac delta functions as if V is sufficiently large compared to the variation in $|a(\mathbf{p})|$ and $\alpha_{\mathbf{p}}$. In reference [181] it was assumed that the phases $\alpha_{\mathbf{p}}$ are totally random as a function of $\mathbf{p}$ (i.e., a discontinuous function), meaning that the Dirac delta limit is never achieved. However, if $\alpha_{\mathbf{p}}$ is discontinuous then different, arbitrarily large, volumes have different average DM densities, which would contradict the large scale homogeneity of the Universe. Thus on some scale $\alpha_{\mathbf{p}}$ should be a continuous function.

On the other hand, a local measurement of the DM density will not necessarily provide a large enough measured volume to resolve all the structure in the axion field. We will not worry about such issues in this thesis, assuming that the DM density is homogeneous enough for one to reasonably expect a detection without significant fluctuation. In other words, we assume that this average density is the same as the local one,

$$\bar{\rho}_a = f_{\rm DM}\,\frac{300\text{ MeV}}{\text{cm}^3}\,. \tag{3.5.11}$$

If it is not, each measurement will measure a different ρ_a, giving a time dependence to the signal which could be modelled as a time dependent $f_{\rm DM}$.

We can also write down the E-field associated with each Fourier mode,

$$E_a(\mathbf{p}) = -\frac{g_{a\gamma}B_{\rm e}a(\mathbf{p})}{\epsilon}\,, \tag{3.5.12}$$

where,

$$E_a(\mathbf{x},t) = \int \frac{d^3\mathbf{p}}{(2\pi)^3}E_a(\mathbf{p})e^{i(\mathbf{p}\cdot\mathbf{x}-\omega t+\alpha_{\mathbf{p}})}\,. \tag{3.5.13}$$

We caution the reader that the dimension of $E(\mathbf{p})$, $(\text{energy})^{-1}$, is not the same as E_0, $(\text{energy})^2$. We will in general either be dealing with the Fourier component or a monochromatic wave, so the difference between them will not be relevant.

Now that we have found the mixed axion and photon fields, including a non-zero velocity, we can consider a 3D axion field interacting with an interface. From this we will build up a transfer matrix formalism that includes velocity effects, giving us a very general and powerful classical formalism.

Chapter 4

Classical Calculation: Transfer Matrix Formalism

With our new understanding of the axion-Maxwell equations, we are ready to begin considering a device that would be able to detect axions. After setting up a static magnetic field $\mathbf{B}_{\mathrm{e}}$ in the laboratory, we can measure an electric field $\mathbf{E}_a(t)$ given by equation (3.5.3) which is driven by the nonrelativistic DM axion field and oscillates with the frequency $\omega \sim m_a$ corresponding to the axion mass. In practice, to couple a detector efficiently to this EM signal requires amplification, an enhancement of the rate of axion-photon conversion.

The main idea behind this thesis is to do so with layered dielectrics, arranged to give constructive interference. To explain this concept, it is useful to consider the simplest possible case with the simplest possible language. To this end we first derive the EM response of the simplest element of our overall system: a single interface between two media, which could be a boundary between regions with either different dielectric properties, with different an applied field strength $\mathbf{B}_{\mathrm{e}}$, or both.

In this chapter we will perform a classical analysis of the production of EM waves in a series of dielectric and magnetic materials by a DM axion field, including the axion velocity. We will first do a simple version of the production of EM waves from a single interface, before expanding our analysis to include non-zero axion velocities and unaligned magnetic fields. We will then develop a transfer matrix based formalism that allows one to handle an arbitrary series of dielectric layers.

4.1 Axion-induced electromagnetic radiation at an interface

For our first and simplest example of the production of EM waves due to DM axions, we will treat the DM axion as an external field, sourcing induced EM fields but itself being unchanged by the media. By exploring this example in

detail, we will gain some intuition to help guide us in more complicated and realistic settings. As we will show explicitly in section 4.2, such a linearisation will hold true up to terms proportional to $g_{a\gamma}^2$. We will also neglect the axion's velocity in this section, and return to treat it explicitly in section 4.2.

4.1.1 Radiation from an interface

We begin with the simplest possible configuration, where the interface between two regions 1 and 2 is an infinite plane with a parallel applied magnetic field $\mathbf{B}_\mathrm{e}$ as shown in figure 4.1. At the interface, there is a jump of the dielectric constant ϵ or the magnetic field $\mathbf{B}_\mathrm{e}$ or both, and so the axion-induced electric field $\mathbf{E}_a$ jumps at the interface as well. Note that in each region Maxwell's equations in the presence of axions, equation (3.2.6), are inhomogeneous differential equations: the general solution is given by adding solutions of the homogeneous equations (regular EM waves) to an inhomogeneous solution (i.e., $\mathbf{E}_a$). The global solution to Maxwell's equations then comes from choosing EM waves in each region such that they match the boundary conditions. In other words, the presence of the interface couples the axion-induced electric field to propagating waves. We ignore possible EM waves which are causally unrelated to the axion field in this section. In particular, we exclude waves moving toward the interface from far away. Therefore, the symmetries of our configuration allow only waves moving away from the interface on either side in perpendicular directions.

The axion-induced electric field and the electric and magnetic fields associated with these propagating waves are all parallel to the interface. The usual continuity requirements at an interface between different media are [148]

$$\mathbf{E}_{\parallel,1} = \mathbf{E}_{\parallel,2} \quad \text{and} \quad \mathbf{H}_{\parallel,1} = \mathbf{H}_{\parallel,2}\,, \tag{4.1.1}$$

where the first condition follows from Faraday's law (3.1.2d), which remains unchanged by axions. The second condition follows from Ampère's law (3.1.2b) in the usual way because the presence of axions amounts to an external volume current density, which vanishes for a surface.

One consequence of these boundary conditions is that $\mathbf{B}_\mathrm{e}$, assumed to be parallel to the interface, must jump if the static (DC) permeability μ_DC is different between the two media. Recall that in our equations, usually the symbols μ and ϵ represent the material properties at angular frequency $\omega = m_a$, not the DC quantities, although in practice, the frequency dependence may be small. In our conceptual discussion here we will mostly ignore a possible $\mathbf{B}_\mathrm{e}$ discontinuity at the interface caused by a jump of μ_DC because we are primarily concerned with such dielectric media that have only a negligible magnetic response. This issue is one of many small effects to be studied in a realistic experimental design.

Turning to propagating waves, equation (3.2.6b) without the source term on the rhs and using $\mathbf{H} = \mathbf{B}/\mu$ implies the usual condition $\mathbf{k} \times \mathbf{H}_\gamma + \omega\epsilon\mathbf{E}_\gamma = 0$,

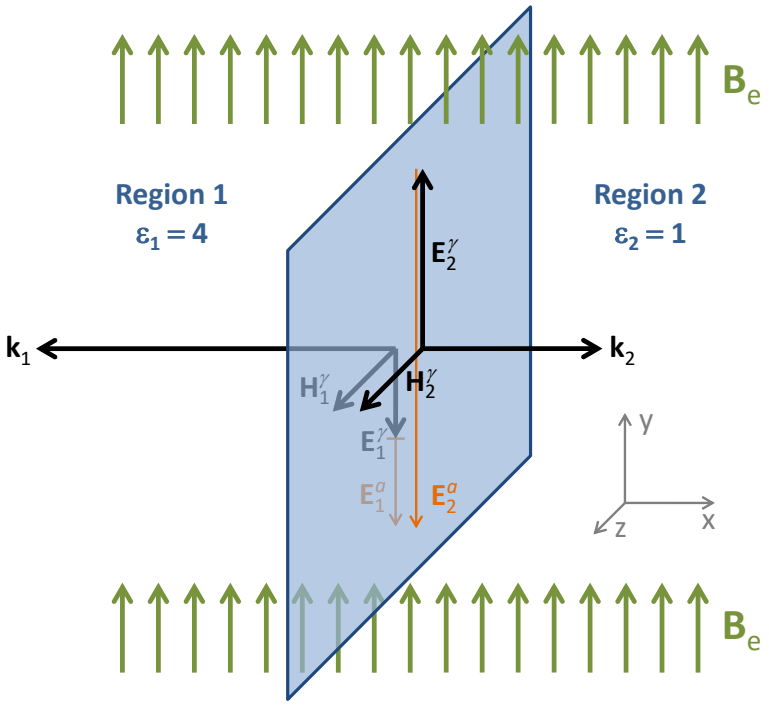

Figure 4.1: Interface between two regions 1 and 2 with equal $\mathbf{B}_\mathrm{e}$ and chosen material properties $\mu_1 = \mu_2 = 1$, $\epsilon_1 = 4$ and $\epsilon_2 = 1$, implying $n_1 = \sqrt{\epsilon_1} = 2$ and $n_2 = 1$ so that $k_1 = 2\omega$ and $k_2 = \omega$. The EM waves propagating away from both sides of the interface ensure continuity of $\mathbf{H}_\parallel$ and $\mathbf{E}_\parallel$, here implying $H_1^\gamma = H_2^\gamma = 1/2$, $E_1^a = E_1^\gamma = -1/4$, $E_2^a = -1$ and $E_2^\gamma = 1/2$, where all fields are given in units of $E_0 = |g_{a\gamma} B_\mathrm{e} a_0|$.

where the subscript γ indicates that these are the fields of a propagating EM wave. With the wave number satisfying $k = n\omega$ (refractive index n) one finds $H_\gamma = \pm(\epsilon/n)\, E_\gamma$. Notice that $n = \sqrt{\epsilon\mu}$ so that $\epsilon/n = \sqrt{\epsilon/\mu}$. However, because the medium is described by two material constants μ and ϵ we prefer to use instead the pair of parameters n and ϵ which avoids the appearance of many square-root symbols. In most practical cases, $\mu \approx 1$ so that n becomes essentially a notation for $\sqrt{\epsilon}$. For the EM waves, $\mathbf{H}_\gamma$ is perpendicular to $\mathbf{E}_\gamma$ which itself is collinear with $\mathbf{E}_a$ and thus with $\mathbf{B}_\mathrm{e}$. Therefore, the continuity of $\mathbf{H}_\parallel$ does not involve $\mathbf{B}_\mathrm{e}$ and implies[8] $\mathbf{H}_1^\gamma = \mathbf{H}_2^\gamma$. Because $\mathbf{k}_1$ and $\mathbf{k}_2$ point in opposite directions, also $\mathbf{E}_1^\gamma$ and $\mathbf{E}_2^\gamma$ must be oriented in opposite directions as shown in figure 4.1. Moreover, the continuity of $\mathbf{E}_\parallel$ must involve the axion-induced field $\mathbf{E}_a$ so that at the interface, which is defined by a jump of $\mathbf{E}_a$, the total $\mathbf{E}_\parallel$ is continuous. Therefore, the continuity conditions of equation (4.1.1)

[8]We put the symbols a and γ as subscripts or superscripts depending on typographical convenience.

imply for the field values at the interface

$$\text{Continuity of } \mathbf{H}_\parallel \qquad -\frac{\epsilon_1}{n_1}\,E_1^\gamma = \frac{\epsilon_2}{n_2}\,E_2^\gamma, \tag{4.1.2a}$$

$$\text{Continuity of } \mathbf{E}_\parallel \qquad E_1^\gamma + E_1^a = E_2^\gamma + E_2^a, \tag{4.1.2b}$$

where a positive E-field means that it is oriented along $\mathbf{B}_\text{e}$, i.e., in the positive y-direction in the geometric setup of figure 4.1. Overall we find

$$E_1^\gamma = +(E_2^a - E_1^a)\,\frac{\epsilon_2 n_1}{\epsilon_1 n_2 + \epsilon_2 n_1}\,, \tag{4.1.3a}$$

$$E_2^\gamma = -(E_2^a - E_1^a)\,\frac{\epsilon_1 n_2}{\epsilon_1 n_2 + \epsilon_2 n_1}\,, \tag{4.1.3b}$$

$$H_{1,2}^\gamma = -(E_2^a - E_1^a)\,\frac{\epsilon_1 \epsilon_2}{\epsilon_1 n_2 + \epsilon_2 n_1}\,, \tag{4.1.3c}$$

where the direction of the H fields is orthogonal to $\mathbf{B}_\text{e}$ and parallel to the interface as shown in figure 4.1, i.e., defining the z-direction.

In the lossless limit in which n_1 and n_2 are real, these values can be taken as real numbers because in this case all E and H fields at the interface are in phase. As a function of time t and distance x from the interface, the physical axion-induced electric and propagating electric and magnetic fields are respectively the real parts of the expressions

$$E_{1,2}^a\, e^{-i\omega t}\,, \quad E_{1,2}^\gamma\, e^{-i(\omega t - k_{1,2} x)}\,, \quad \text{and} \quad H_{1,2}^\gamma\, e^{-i(\omega t - k_{1,2} x)}\,, \tag{4.1.4}$$

where $\omega = m_a$, $k_1 = -n_1\omega$ (wave moving in the negative x-direction), and $k_2 = +n_2\omega$ (wave moving in the positive x-direction).

If the media are lossy, the refractive indices n_1 and n_2 are complex numbers with $\text{Im}(n_{1,2}) > 0$ and the fields at the interface are not in phase. In particular, the axion-induced fields $E_a(t)$ on both sides of the interface are no longer in phase with each other or with the driving galactic dark-matter axion field $a(t)$. In this case, $E_a(t)$ jumps at the interface even if $|n_1| = |n_2|$, but if the media have different loss tangents (3.4.1). One can convince oneself that all derivations and results of this section remain unchanged if $\epsilon_{1,2}$ and $n_{1,2}$ are complex numbers. In particular, the axion-induced electric fields $E_{1,2}^a(t)$ remain homogeneous in the two half-spaces separated by the interface, whereas the amplitudes of the propagating EM waves decrease in proportion to $e^{-\text{Im}(n_{1,2})\omega|x|}$ as a function of distance $|x|$ from the interface.

4.1.2 Simple examples

Let us now consider three simple examples in the zero velocity limit. For each we will provide the explicit expressions of $E_{1,2}^a$, $E_{1,2}^\gamma$, and $H_{1,2}^\gamma$ at the interface. The corresponding fields away from the interface and as a function of time are given by equation (4.1.4) and used to determine the energy flux density.

• ***Sudden change of external magnetic field***

As a first simple example we consider a magnetic field region which ends abruptly at the interface so that $\mathbf{B}_\mathrm{e} = 0$ in region 2. While such a situation is not strictly possible, we simply assume that $\mathbf{B}_\mathrm{e}$ falls off very quickly, i.e., on a scale much faster than the wavelength of the produced EM waves. The medium itself is taken to be vacuum everywhere so that $\epsilon_1 = \epsilon_2 = n_1 = n_2 = 1$. Moreover, as a scale for all fields we use $E_0 = g_{a\gamma} B_\mathrm{e} a_0$ as previously defined in equation (3.5.8). If the $\mathbf{B}_\mathrm{e}$ direction is taken to define the electric field direction, the y-direction in figure 4.1, the axion-induced electric field in a medium with dielectric permittivity ϵ is

$$E_a = -\frac{E_0}{\epsilon}\,. \tag{4.1.5}$$

In our example this means $E_1^a = -E_0$ and $E_2^a = 0$ so that

$$E_1^\gamma = +\tfrac{1}{2}\,E_0, \quad E_2^\gamma = -\tfrac{1}{2}\,E_0, \quad \text{and} \quad H_{1,2}^\gamma = -\tfrac{1}{2}\,E_0\,. \tag{4.1.6}$$

The propagating waves both have half the electric field strength of the homogeneous axion-induced field-strength in the magnetic field region.

• ***Dielectric interface***

Our main example, however, is a dielectric interface between two media with ϵ_1 and ϵ_2. We assume negligible magnetic responses at our frequencies, i.e., $\mu_1 = \mu_2 = 1$ so that $\epsilon_1 = n_1^2$ and $\epsilon_2 = n_2^2$ and we express the material properties in terms of the refractive indices. $\mathbf{B}_\mathrm{e}$ is taken to be homogeneous, not jumping at the interface. The E_a-field discontinuity is $E_2^a - E_1^a = -(\epsilon_2^{-1} - \epsilon_1^{-1})E_0$ and the interface-values of the wave electric fields are

$$E_1^\gamma = -\frac{E_0}{n_1}\left(\frac{1}{n_2} - \frac{1}{n_1}\right) \quad \text{and} \quad E_2^\gamma = +\frac{E_0}{n_2}\left(\frac{1}{n_2} - \frac{1}{n_1}\right), \tag{4.1.7}$$

whereas

$$H_{1,2}^\gamma = E_0\left(\frac{1}{n_2} - \frac{1}{n_1}\right) \tag{4.1.8}$$

is the magnetic field associated with both waves. Notice that the positive H direction is the z-direction in the convention of figure 4.1.

The energy flux density (energy transfer per unit area and per unit time or equivalently power per unit area) of an EM field configuration is given by Poynting's theorem as

$$\mathbf{S} = \mathbf{E} \times \mathbf{H}\,. \tag{4.1.9}$$

If these vectors are complex Fourier components, we must use the real parts of $\mathbf{E}$ and of $\mathbf{H}$ to obtain the physical energy flux. When considering $\mathbf{S}$ in lossless

media, the cycle average introduces a factor 1/2 so that our two waves carry the cycle-averaged power per unit surface

$$\bar{S}_i^\gamma = \mp \frac{E_0^2}{2n_i} \left(\frac{1}{n_2} - \frac{1}{n_1} \right)^2 , \tag{4.1.10}$$

for $i = 1$ (upper sign) or 2 (lower sign). A positive sign means energy flowing in the positive x-direction, i.e., the energy flows away in opposite directions from the interface. In absolute terms, the medium with the smaller refractive index carries the larger energy in produced EM waves.

• ***Perfect mirror***

As an extreme case, we may assume that medium 2 is vacuum ($n_2 = 1$) whereas medium 1 has a huge dielectric constant so that $|n_1| \to \infty$. In this case $E_1^\gamma = 0$ (and $H_{1,2}^\gamma = 0$), whereas the wave emitted into vacuum is $E_2^\gamma = E_0$. Notice that $E_2^a = -E_0$, so the electric field of the wave simply has to cancel the ambient axion-induced field such that the total electric field vanishes at the mirror surface.

A mirror could be a purely dielectric medium with a very large real value of ϵ, but in practice more realistically is a metallic surface with a large real-valued conductivity $\sigma \to \infty$ so that $\epsilon \sim 1 + i\sigma/\omega$. Put another way, the value of the mirror's loss tangent does not affect the production of axion-induced EM waves from its surface; in our context the only defining property of a perfect mirror is $|n_1| \to \infty$.

4.1.3 Energy flux

In our example for a dielectric interface, we have stated the power per unit area carried by the produced EM waves based on the Poynting vector $\mathbf{S}$ which we applied to the propagating solution alone. The result is somewhat paradoxical because power seems to pour from the interface in both directions, carried by the EM waves which are generated by the presence of the interface. On the other hand, the Poynting vector in equation (4.1.9) is constructed from $\mathbf{E}$ and $\mathbf{H}$ which are both parallel to the interface and so continuous. Therefore, the Poynting vector itself must be continuous as well, so the interface cannot be a source of energy.

The apparent paradox is resolved if we note that the energy flux given in terms of the fields of the generated EM wave is meaningful only at a large distance. If we assume that $\mathbf{B}_\mathrm{e}$ adiabatically decreases as a function of distance, far away the only EM fields are those of the propagating waves. However, in the "near-field region" around the interface, this interpretation is not complete. The Poynting vector involves all EM fields, and especially the axion-induced field $\mathbf{E}_a$, whereas the external field $\mathbf{B}_\mathrm{e}$ does not appear in any of the cross products because all electric fields are parallel to $\mathbf{B}_\mathrm{e}$. Overall we thus have

$\mathbf{S} = (\mathbf{E}_a + \mathbf{E}_\gamma) \times \mathbf{H}_\gamma$, correcting what looked like an inconsistency earlier. In other words, we cannot think of the "background axion-induced field" and the propagating waves as incoherent phenomena. Rather, they are phase-locked as the oscillating axion field drives them all. Both $\mathbf{E}_a(t)$ and $\mathbf{E}_\gamma(t)$ are part of the overall solution of Maxwell's equations.

Considering explicitly the overall solution of Maxwell's equations in the presence of an interface as given in equation (4.1.4), the cycle-averaged energy flux density is found to be

$$\bar{S}_i = \tfrac{1}{2}[E_i^\gamma + E_i^a \cos(k_i x)]\, H_i^\gamma \,, \tag{4.1.11}$$

where $i = 1$ or 2 and we assume real n. Notice that a positive value of $\bar{S}$ means energy flowing in the positive x-direction in the arrangement of figure 4.1. For our main example, a dielectric interface where B_e is continuous and $\mu = 1$ everywhere (no magnetic response), the explicit solutions for the fields at the interface were given in equations (4.1.7) and (4.1.8). In this case, the explicit cycle-averaged energy flux density is

$$\bar{S}_i = -\frac{E_0^2}{2n_i}\left(\frac{1}{n_2} - \frac{1}{n_1}\right)\left[\pm\left(\frac{1}{n_2} - \frac{1}{n_1}\right) + \frac{\cos(n_i\omega x)}{n_i}\right] , \tag{4.1.12}$$

where $i = 1$ (upper sign) or 2 (lower sign). The first term reproduces our previous result of equation (4.1.10) for the energy carried by the propagating EM waves alone. The second term arises from the interference of H_γ with the homogeneous but time-varying electric field E_a. The Poynting fluxes on the two sides of the interface are explicitly

$$\bar{S}_1 = -\frac{E_0^2}{2n_1^2}\left(\frac{1}{n_2} - \frac{1}{n_1}\right)\left[\frac{n_1}{n_2} - 2\sin^2\left(\frac{n_1\omega x}{2}\right)\right] , \tag{4.1.13a}$$

$$\bar{S}_2 = +\frac{E_0^2}{2n_2^2}\left(\frac{1}{n_2} - \frac{1}{n_1}\right)\left[2\sin^2\left(\frac{n_2\omega x}{2}\right) - \frac{n_2}{n_1}\right] . \tag{4.1.13b}$$

Let us assume that $n_1 \gg n_2$, having in mind that region 1 is a dielectric and region 2 vacuum or air. We immediately glean from these equations that the term in square brackets of $\bar{S}_1$ is positive for any x if $n_1 > 2n_2$, meaning that for any $x < 0$ energy flows in the negative x-direction. On the other hand, in $\bar{S}_2$ this term has a positive spatial average, but it varies between $-n_2/n_1 < 0$ and $2 - n_2/n_1 > 0$, i.e., between positive and negative values. For $n_2 = 1$ and several examples of $n_1 > 1$ we show the Poynting flux in figure 4.2.

Therefore, in the medium with smaller ϵ, there are surfaces parallel to the interface through which no energy flux passes. Of course, as B_e falls off adiabatically in the x-direction, the interference term disappears and we are left with an energy flux carried by the propagating EM wave alone. The purpose of our dielectric haloscope concept to be discussed in the next section is, of course, to boost E_γ to much larger values by multiple dielectric surfaces.

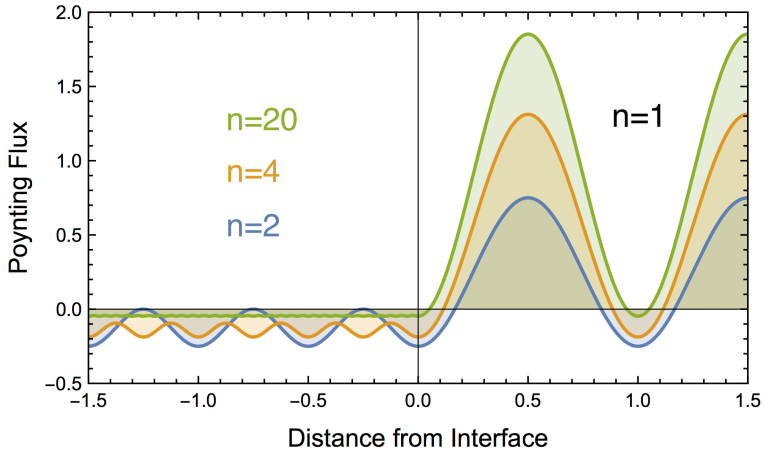

Figure 4.2: Energy flux density (cycle-averaged value of Poynting vector) in the x-direction (4.1.12) in units of $E_0^2/2$ for the setup of figure 4.1 with region 1 (region 2) at negative (positive) distance values, except that here we use $n_1 = 2$, 4, and 20 (blue, orange, and green), always keeping $n_2 = 1$.

In this case the interference term with E_a is small and we can think of the produced EM wave independently from E_a in any practically relevant sense.

However, this exercise shows that the EM power transferred from the oscillating axion field to a propagating EM wave does not pour from the interface into space in both directions. Rather, it is transferred within the magnetized volume in a spread-out region, commensurate with the picture that neither the axion nor the propagating EM wave can be exactly localized.

4.1.4 Detection

To get a first grasp of the detection requirements we consider the EM radiation emitted by a perfect mirror ($n_1 \to \infty$) into vacuum ($n_2 = 1$). From equation (4.1.10) we find for the cycle-averaged energy flux density (power per unit surface $\mathcal{S}$) in the x-direction

$$\frac{P_\gamma}{\mathcal{S}} = \bar{S}_2^\gamma = \frac{1}{2}\overline{\left[\mathrm{Re}\left(\mathbf{E}_2^\gamma\right) \times \mathrm{Re}\left(\mathbf{H}_2^\gamma\right)\right]_x} = \frac{E_0^2}{2} = 2.2 \times 10^{-27}\,\frac{\mathrm{W}}{\mathrm{m}^2}\left(\frac{B_\mathrm{e}}{10\ \mathrm{T}}\right)^2 C_{a\gamma}^2 f_\mathrm{DM}\,. \tag{4.1.14}$$

The corresponding photon flux,

$$\Phi_\gamma = \frac{P_\gamma}{\mathcal{S}\,\omega} = \frac{12}{\mathrm{m}^2\ \mathrm{day}}\left(\frac{100\,\mu\mathrm{eV}}{m_a}\right)\left(\frac{B_\mathrm{e}}{10\ \mathrm{T}}\right)^2 C_{a\gamma}^2 f_\mathrm{DM}\,, \tag{4.1.15}$$

is extremely tiny.

To illustrate the detection challenge we recall that virialised galactic axions have a velocity dispersion of around $v_a \sim 10^{-3}$. The kinetic energy of a nonrelativistic axion is $m_a v_a^2/2$ so that these axions have an energy spread around $\omega_a = m_a$ of $\Delta\omega_a \sim m_a v_a^2/2 \sim 10^{-6}\, m_a$, corresponding to a signal

bandwidth given by the frequency range $\Delta\nu_a = \Delta\omega_a/2\pi$. If the power in this frequency band is detected with a linear amplifier with system noise $T_{\rm sys}$, the Gaussian noise power fluctuations after a measurement time Δt have a standard deviation of $T_{\rm sys}\Delta\nu_a/\sqrt{\Delta\nu_a\,\Delta t}$. The signal-to-noise ratio in this band is given by the Dicke radiometer equation [182]

$$\begin{aligned}\frac{\rm S}{\rm N} &= \frac{P_\gamma}{T_{\rm sys}}\sqrt{\frac{\Delta t}{\Delta\nu_a}} \\ &= 1.0\times 10^{-4}\left(\frac{\mathcal{S}}{1\,{\rm m}^2}\right)\sqrt{\frac{100\,\mu{\rm eV}}{m_a}}\sqrt{\frac{\Delta t}{\rm week}}\left(\frac{8\,{\rm K}}{T_{\rm sys}}\right)\left(\frac{B_{\rm e}}{10\,{\rm T}}\right)^2 C_{a\gamma}^2 f_{\rm DM}\,.\end{aligned} \tag{4.1.16}$$

For plausible parameters $B_{\rm e}\sim 10$ T and $\mathcal{S}\sim 1$ m^2 this is far too small for a realistic experiment as noted earlier [152]. To be able to detect axion dark matter in a reasonable time scale, the signal power must be enhanced by a factor of 10^4 or more.

Our eventual goal will be to consider dielectric haloscopes, which will achieve such a boost via multiple dielectric layers. We will define a boost factor β for the electric-field amplitude of the produced EM wave, i.e., the power is amplified by a factor β^2,

$$\frac{P_\gamma}{\mathcal{S}} = \frac{E_0^2}{2} \quad\rightarrow\quad \frac{P_\gamma}{\mathcal{S}} = \frac{\beta^2 E_0^2}{2}\,\eta \tag{4.1.17}$$

where also η is introduced to account for the efficiency of the detector. If we require a certain signal-to-noise ratio S/N in a given search channel $\Delta\nu_a$, the scanning speed per channel is

$$\begin{aligned}\frac{\Delta t}{1.3\,{\rm days}} &\sim \left(\frac{\rm S/N}{5}\right)^2\left(\frac{400}{\beta}\right)^4\left(\frac{1\,{\rm m}^2}{\mathcal{S}}\right)^2\left(\frac{m_a}{100\,\mu{\rm eV}}\right)\left(\frac{T_{\rm sys}}{8\,{\rm K}}\right)^2 \\ &\times \left(\frac{10\,{\rm T}}{B_{\rm e}}\right)^4\left(\frac{0.8}{\eta}\right)^2 C_{a\gamma}^{-4} f_{\rm DM}^{-2}\,.\end{aligned} \tag{4.1.18}$$

Of course, the main problem is that we do not know the axion mass and thus have to scan over a range of search masses that is as broad as possible. In a given run, we are not limited to covering a single channel defined by the natural line width $\Delta\nu_a$ of the virialised axion field. Instead we may achieve a large boost factor over a broader frequency range and in this way achieve a reasonable overall scanning speed. The option of a broadband search is one of the attractions of the dielectric haloscope approach.

This simple case will help provide the intuition behind what follows. The axion field will exhibit a discontinuity in the induced E and H-fields, which will require propagating EM waves in order to provide a consistent solution of the axion-Maxwell equations. We will then try to detect these propagating EM waves.

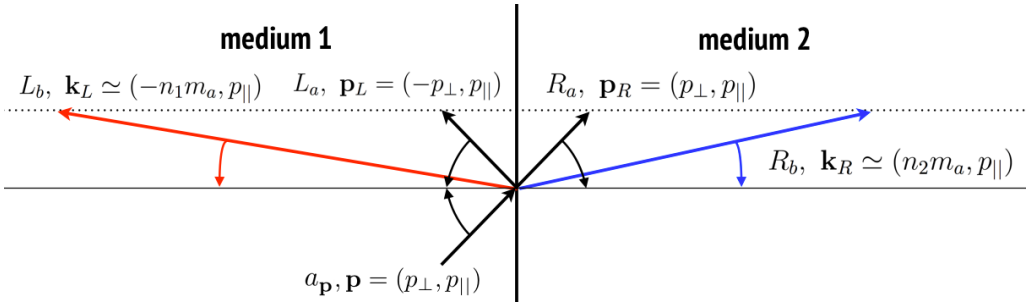

Figure 4.3: A non-relativistic axion DM wave of amplitude $a(\mathbf{p})$ and momentum $\mathbf{p}$ crosses from medium 1 to medium 2 becoming the transmitted right moving wave of amplitude $R_a \simeq a(\mathbf{p})$, with a negligible reflected left moving wave $L_a \simeq 0$. In general the change in media causes a discontinuity in the axions E and H fields that will be compensated by emission of EM waves L_b, R_b (as well as the not pictured L_t, R_t). The momentum parallel to the boundary is conserved and the perpendicular momentum is fixed by the dispersion relations, leading the EM waves to be emitted almost perpendicular to the boundary. Different media are those with different axion-photon mixing energies, so any change in the B-field intensity, direction or dielectric constant induces radiation of EM waves from both sides of the interface (red and blue arrows).

4.2 Radiation with non-zero axion velocities

The previous section gave us a good understanding of the boundary EM radiation emitted from a external, stationary axion field inside a strong magnetic field. However, in practice one might worry to what extent the axion field itself is effected, and what influence a non-zero axion velocity might have. Here we will consider a fully general 3D case, albeit with an interface of infinite extent, as depicted in figure 4.3. We allow both the axion velocity and the B-field to have a non-trivial orientation with respect to the boundary. However, while this situation is technically more complex, as in section 4.1 the solution still reduces to compensating discrepancies in the axion induced E and H fields with (mostly) regular EM waves.

Here it is beneficial to return to the vector potential language in which we derived the axion-photon mixing in section 3.3. From here on we will neglect the $\sim$ notation for Fourier components, understanding that all quantities are defined in Fourier space. The EM and axion fields in medium 1 can be represented as a combination of the incoming axion-like wave, and reflected

axion-like and photon-like waves

$$\begin{pmatrix} a \\ iA_b \\ iA_\ell \\ iA_t \end{pmatrix}_1 = a(\mathbf{p}) \begin{pmatrix} 1 \\ -\chi_1\mu_1 \sin\varphi \\ -\chi_1\mu_1 \cos\varphi \\ 0 \end{pmatrix} e^{i(\mathbf{p}\cdot\mathbf{x})} + L_a \begin{pmatrix} 1 \\ -\chi_1\mu_1 \sin\varphi_{L_a} \\ -\chi_1\mu_1 \cos\varphi_{L_a} \\ 0 \end{pmatrix} e^{i(\mathbf{p}_L\cdot\mathbf{x})}$$
$$+L_b \begin{pmatrix} \chi_1 \sin\varphi_{L_b} \\ 1 \\ 0 \\ 0 \end{pmatrix} e^{i(\mathbf{k}_L\cdot\mathbf{x})} + L_t \begin{pmatrix} 0 \\ 0 \\ 0 \\ 1 \end{pmatrix} e^{i(\mathbf{k}_L\cdot\mathbf{x})} \tag{4.2.1}$$

while in medium 2 the transmitted axion-like and created photon-like waves are

$$\begin{pmatrix} a \\ iA_b \\ iA_\ell \\ iA_t \end{pmatrix}_2 = R_a \begin{pmatrix} 1 \\ -\chi_2\mu_2 \sin\varphi_{R_a} \\ -\chi_2\mu_2 \cos\varphi_{R_a} \\ 0 \end{pmatrix} e^{i(\mathbf{p}_R\cdot\mathbf{x})} + R_b \begin{pmatrix} \chi_2 \sin\varphi_{R_b} \\ 1 \\ 0 \\ 0 \end{pmatrix} e^{i(\mathbf{k}_R\cdot\mathbf{x})}$$
$$+R_t \begin{pmatrix} 0 \\ 0 \\ 0 \\ 1 \end{pmatrix} e^{i(\mathbf{k}_R\cdot\mathbf{x})}. \tag{4.2.2}$$

Here L_b, R_b (L_t, R_t) are the amplitudes of the photon-like waves moving in the left (L) and right (R) directions and polarised in the b (t) direction. Every wave has in principle a different orientation with respect to the external magnetic fields and thus a different φ angle (as defined in section 3.2). While in this language it seems like A_t plays no role, this is only because we are not in the natural basis of the system, which would be (x, y, z) coordinates.

The boundary conditions on the EM waves are still given by equation (4.1.1) so that without any additional symmetries there are four constraints, requiring four propagating waves to satisfy. To lowest order the axion field is conserved across the boundary. This is because to the axion itself the boundary is essentially non-existent, up to the very small couplings of the axion to matter. This will mean that in general both polarisations (which we take to be A_b, A_t) will be required in each medium. Choosing $x = x_0$ as our boundary, we first impose

$$\begin{pmatrix} a \\ iA_{b,||} \\ iA_{t,||} \end{pmatrix}_1 (t, x_0, y, z) = \begin{pmatrix} a \\ iA_{b,||} \\ iA_{t,||} \end{pmatrix}_2 (t, x_0, y, z), \tag{4.2.3}$$

where $A_{b,||}, A_{t,||}$ are the projections of the A_b, A_t components in the parallel plane at $x = x_0$. These equations can be only satisfied for all points (y, z) in the boundary if all the phases vary with the same wavenumber along the boundary, i.e.,

$$\mathbf{p}_{||} = \mathbf{p}_{||,L} = \mathbf{p}_{||,R} = \mathbf{k}_{||,L} = \mathbf{k}_{||,R}. \tag{4.2.4}$$

We can then divide out a common $e^{i\mathbf{p}_{||}\cdot\mathbf{x}}$ factor from the boundary condition given by equation (4.2.3). This implies that the angle of the reflected and transmitted photon-like waves with respect to the normal to the surface is suppressed by the small axion DM velocity,

$$\sin\kappa = \frac{|\mathbf{k}_{||}|}{|\mathbf{k}|} = \frac{|\mathbf{p}_{||}|}{n\omega} = \frac{|\mathbf{v}_{||}|}{n}, \tag{4.2.5}$$

i.e., photon-like waves are emitted *perpendicularly* to the surface up to $\mathcal{O}(v/n) \sim 10^{-3}$ corrections. A kin of Snell's law relates the angles of the transmitted and reflected photon-like waves $n_1 \sin\kappa_1 = n_2 \sin\kappa_2$. For the axion-like waves, the transmission and reflection angles are the same because their dispersion relation is the same in both sides of the boundary, up to χ^2 corrections.

Finally, note that the conservation of momentum and of energy for every wave defines the magnitude of the perpendicular momenta through the dispersion relations. This is particularly important for the photon-like waves, for which $|\mathbf{k}|^2 = n^2\omega^2$. This imparts a large perpendicular momentum

$$|\mathbf{k}_\perp| = \sqrt{n^2\omega^2 - |\mathbf{k}_{||}|^2} = \sqrt{n^2\omega^2 - |\mathbf{p}_{||}|^2} = n\omega + \frac{|\mathbf{p}_{||}|^2}{2n\omega} + ... = n\omega[1 + \mathcal{O}(v^2)]. \tag{4.2.6}$$

In order to continue we make the assumption that the B-field *direction* is constant across the boundary. This is not necessary but serves for all the cases we want to cover and simplifies our derivations. We still allow for changes in the magnetic field strength across the boundary. We use $\hat{\mathbf{B}}_\mathrm{e} = (\cos\beta, \sin\beta, 0)$ with $\sin\beta > 0$ in the (x, y, z) basis. That is, $\hat{\mathbf{B}}_\mathrm{e}$ is in the x, y plane with z being the transverse direction. The B-field aligns with the boundary when $\beta = \pi/2$. Note that this assumption of a constant, arbitrary B-field direction requires that the μ of each media is the same. This is also desired for practical reasons, as moving magnetic materials inside strong B-fields is practically very difficult. Thus we set $\mu_r = 1$ from here on.

We also make the stronger assumption that $\mathbf{B}_\mathrm{e}$ is homogeneous. Inhomogeneities in the B-field also would act as a source of momentum for the generated photons [183]. We will leave such considerations for future work looking in more depth at this kind of three dimensional effects. In general we will have six boundary conditions, which will require six fields to satisfy them. To provide enough fields we must include the transversely polarised photons A_t. We can use a change of basis to write the $\mathbf{A}$ fields associated to the different waves in (x, y, z) coordinates. For the axion-like waves we get

$$i\mathbf{A}_a = -\chi_1 a(\mathbf{p})(\cos\beta, \sin\beta, 0)\,, \tag{4.2.7a}$$

$$i\mathbf{A}_{L_a} = -\chi_1 L_a(\cos\beta, \sin\beta, 0)\,, \tag{4.2.7b}$$

$$i\mathbf{A}_{R_a} = -\chi_2 R_a(\cos\beta, \sin\beta, 0)\,. \tag{4.2.7c}$$

Note that A_ℓ is a component of $\mathbf{A}_a$; mismatches in the longitudinal field must

also be compensated. For the photon-like waves we find

$$i\mathbf{A}_{L_b} = \frac{L_b}{\sin\beta + v_y\cos\beta/n_1}\left[(0,\sin\beta,0) + \frac{1}{n_1}(v_y\sin\beta, v_y\cos\beta, v_z\cos\beta) + ...\right], \tag{4.2.8a}$$

$$i\mathbf{A}_{R_b} = \frac{R_b}{\sin\beta - v_y\cos\beta/n_2}\left[(0,\sin\beta,0) - \frac{1}{n_2}(v_y\sin\beta, v_y\cos\beta, v_z\cos\beta) + ...\right], \tag{4.2.8b}$$

$$i\mathbf{A}_{L_t} = \frac{L_t}{\sin\beta + v_y\cos\beta/n_1}\left[(0,0,-\sin\beta) - \frac{1}{n_1}(v_z\sin\beta, -v_z\cos\beta, v_y\cos\beta) + ...\right], \tag{4.2.8c}$$

$$i\mathbf{A}_{R_t} = \frac{R_t}{\sin\beta - v_y\cos\beta/n_2}\left[(0,0,\sin\beta) - \frac{1}{n_2}(v_z\sin\beta, -v_z\cos\beta, v_y\cos\beta) + ...\right]. \tag{4.2.8d}$$

In writing the last four equations we have used that

$$\hat{\mathbf{b}}_\gamma = \hat{\mathbf{t}}_\gamma \times \hat{\ell}_\gamma, \tag{4.2.9a}$$

$$\hat{\mathbf{t}}_\gamma = -\frac{1}{\sin\varphi_\gamma}\hat{\mathbf{B}}_{\rm e} \times \hat{\ell}_\gamma, \tag{4.2.9b}$$

with $\hat{\ell}_\gamma = ((-1)^j, v_y/n_j, v_z/n_j)$ for each media j. Both photon polarisations have the same $\mathbf{k}$. Note $\hat{\mathbf{b}}$ is approximately the same for right and left moving waves, whereas from our definition the $\hat{\mathbf{t}}$ are almost equal and opposite. To simplify matters, we can express the φ angles (that enter into the axion-photon mixing) as

$$\sin\varphi_{R_a} = \sin\varphi = ..., \tag{4.2.10a}$$

$$\cos\varphi_{R_a} = \cos\varphi = ..., \tag{4.2.10b}$$

$$\sin\varphi_{L_b} = \sin\varphi_{L_t} = \sin\beta + \cos\beta\frac{v_y}{n_1} + O(v^2) \equiv \sin\varphi_L\,, \tag{4.2.10c}$$

$$\sin\varphi_{R_b} = \sin\varphi_{R_t} = \sin\beta - \cos\beta\frac{v_y}{n_2} + O(v^2) \equiv \sin\varphi_R\,. \tag{4.2.10d}$$

We just need to solve for the values of $L_a, R_a, L_b, R_b, L_t, R_t$ as a function of $a(\mathbf{p})$. Explicitly, the boundary conditions in equation (4.1.1) are

$$\begin{aligned}
a(x_0)_1 &= a(x_0)_2, \qquad (4.2.11a)\\
\partial_x a(x_0)_1 &= \partial_x a(x_0)_2,\\
\mathbf{A}_y(x_0)_1 &= \mathbf{A}_y(x_0)_2,\\
(\partial_x\mathbf{A}_y - \partial_y\mathbf{A}_x)(x_0)_1 &= (\partial_x\mathbf{A}_y - \partial_y\mathbf{A}_x)(x_0)_2,\\
\mathbf{A}_z(x_0)_1 &= \mathbf{A}_z(x_0)_2,\\
(\partial_x\mathbf{A}_z - \partial_z\mathbf{A}_x)(x_0)_1 &= (\partial_x\mathbf{A}_z - \partial_z\mathbf{A}_x)(x_0)_2,
\end{aligned}$$

which translate into the following equations at first order in v

$$\begin{pmatrix} 1 & 1 & -1 & \chi_1 \sin\varphi_{L_b} & -\chi_2 \sin\varphi_{R_b} & 0 & 0 \\ v_x & -v_x & -v_x & -n_1\chi_1 \sin\varphi_{L_b} & -n_2\chi_2 \sin\varphi_{R_b} & 0 & 0 \\ -\chi_1 \sin\beta & -\chi_1 \sin\beta & \chi_2 \sin\beta & 1 & -1 & \frac{v_z}{n_1}\cot\beta & -\frac{v_z}{n_2}\cot\beta \\ \chi_1 g_- & \chi_1 g_+ & -\chi_2 g_- & -n_1 & -n_2 & -v_z\cot\beta & -v_z\cot\beta \\ 0 & 0 & 0 & \frac{v_z}{n_1}\cot\beta & \frac{v_z}{n_2}\cot\beta & -1 & -1 \\ v_z\chi_1\cos\beta & v_z\chi_1\cos\beta & -v_z\chi_2\cos\beta & -v_z\cot\beta & v_z\cot\beta & n_1 & -n_2 \end{pmatrix} \begin{pmatrix} a(\mathbf{p}) \\ L_a \\ R_a \\ L_b \\ R_b \\ L_t \\ R_t \end{pmatrix} = 0, \tag{4.2.12}$$

where we have taken $x_0 = 0$ and used $\mathbf{v} = \mathbf{p}/\omega$. We have defined $g_\pm = v_y \cos\beta \pm v_x \sin\beta$.

It is interesting to see that even neglecting the axion components there is an interaction term between the polarisations b, t due to the non-trivial geometry. When these cross terms are non-zero this indicates that both A_b and A_t are required for a consistent solution to the axion-Maxwell equations. One can think of this as coming from the mismatch between the b, t directions and the y, z directions. The full solution is quite involved, but at first order in the tiny quantities χ_1, χ_2 and in the DM velocity v it simplifies to:

$$L_a = 0, \tag{4.2.13a}$$

$$R_a = a(\mathbf{p}), \tag{4.2.13b}$$

$$L_b = a(\mathbf{p})\,(\chi_1 - \chi_2)\sin\beta\frac{n_2}{n_1+n_2} - a(\mathbf{p})\,(\chi_1-\chi_2)\,\frac{v_x\sin\beta - v_y\cos\beta}{n_1+n_2}, \tag{4.2.13c}$$

$$R_b = -a(\mathbf{p})\,(\chi_1 - \chi_2)\sin\beta\frac{n_1}{n_1+n_2} - a(\mathbf{p})\,(\chi_1-\chi_2)\,\frac{v_x\sin\beta - v_y\cos\beta}{n_1+n_2}, \tag{4.2.13d}$$

$$L_t = L_b\frac{v_z}{n_1}\cot\beta - a(\mathbf{p})\,(\chi_1-\chi_2)\,\frac{v_z\cos\beta}{n_1+n_2}, \tag{4.2.13e}$$

$$R_t = R_b\frac{v_z}{n_2}\cot\beta + a(\mathbf{p})\,(\chi_1-\chi_2)\,\frac{v_z\cos\beta}{n_1+n_2}, \tag{4.2.13f}$$

which agrees with the results of section 4.1 when $v \to 0$ and $\sin\beta = 1$. Note that at lowest order the axion field is unchanged, meaning that treating the axion as an external field was justified in section 4.1. Note also that the energy contained in the photon field appears at quadratic order in χ as it is given by $E^2/2$. One would similarly consider the square of the $a(\mathbf{p})$, which then would also give a quadratic dependence. As one would expect, while the photons seem to appear out of nothing the energy is indeed provided by the axion field. This will be even more apparent in the quantum calculation appearing in the next chapter; each photon comes from a single axion being converted with the same energy. While these solutions are not as elegant as in the $v = 0$ case, the interpretations are just as straightforward. The first term in L_b and R_b is due to the mismatch in the axion-like E-field, whereas the second terms in of L_b, R_b, as well as both terms in L_t and R_t come from a mismatch in the axion-like H-field. This can be seen more explicitly by rewriting the last four equations

in terms of E and H:

$$E_L^b = (\mathbf{E}_2^a - \mathbf{E}_1^a)_y \frac{n_2}{n_1+n_2} - (\mathbf{H}_2^a - \mathbf{H}_1^a)_z \frac{1}{(n_1+n_2)}, \tag{4.2.14a}$$

$$E_R^b = -(\mathbf{E}_2^a - \mathbf{E}_1^a)_y \frac{n_1}{n_1+n_2} - (\mathbf{H}_2^a - \mathbf{H}_1^a)_z \frac{1}{(n_1+n_2)}, \tag{4.2.14b}$$

$$E_L^t = (\mathbf{H}_2^a - \mathbf{H}_1^a)_y \frac{n_2-n_1}{n_1(n_1+n_2)}, \tag{4.2.14c}$$

$$E_R^t = (\mathbf{H}_2^a - \mathbf{H}_1^a)_y \frac{n_2-n_1}{n_2(n_1+n_2)}, \tag{4.2.14d}$$

where $E_{L,R}^{b,t}$ is the E-field traveling in the left and right direction polarised in the b, t direction, respectively. As $\mathbf{B}_\mathrm{e}$ is defined to lie in the x, y plane there is no mismatch in $\mathbf{E}_{a,z}$ so the axion field does not directly require $A_t \neq 0$ as $B_{\mathrm{e},z} = 0$. However, the cross terms between the two photon polarisations b and t do require A_t to be present as well. The symmetry between the two is broken as the axions only interact with A_b (and so the corrections to A_b come at v^2 order). Maximum emission of the b polarisation waves happens when the B-field is exactly along the boundary direction $\hat{\mathbf{y}}$ ($\sin\beta = 1$), as noted in reference [147]. The amplitude of the waves polarised along A_t, i.e., orthogonal to the external B-field, are suppressed by $v_z \sim O(10^{-3})$. While the longitudinal modes A_ℓ are not dynamical, the mismatch in the axion field induced $A_{\ell,||}^a$ does contribute to the production of photon-like waves. We now have the solution to the 3D boundary case.

4.3 Multilayer analysis: dielectric haloscopes

To gain the 4–5 orders of magnitude increase in power discussed in section 4.1.4, we are interested not only in the production of photons from a single interface, but rather in the cumulative effects of many dielectric layers (as depicted in figure 1.2). In the presence of several media with numerous interfaces we can arrange them to radiate coherently, enhancing the signal—a dielectric haloscope. A nice computational tool for for such a calculation is given by transfer matrices, which will allow us to rewrite the boundary condition requirements and propagation of photons as a series of matrices.

4.3.1 Transfer matrix formalism

We consider the idealised case of a plane parallel sequence of dielectric regions labelled $0, 1...m$, where 0 and m are semi-infinite regions for the output/input, see figure 4.4. The thickness of each layer is $d_1, d_2, ..., d_{m-1}$ and we allow the indices of refraction to be different $(n_0, ..., n_m)$ so that the optical thicknesses are $\delta_1 = \omega n_1 d_1, ...$ We consider $\mu = 1$ throughout the system, i.e., we assume non-magnetic media. We consider the external B-field aligned with

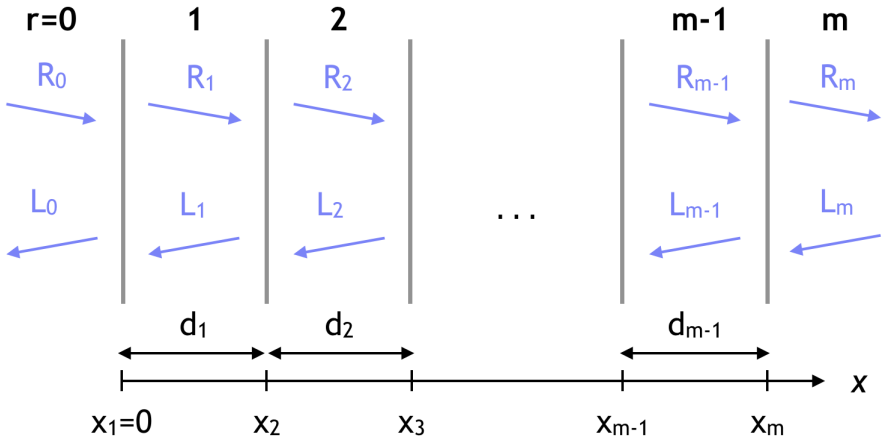

Figure 4.4: Several dielectric regions. The amplitudes L_r and R_r denote the electric-field amplitudes of left and right moving EM waves in each homogeneous region r. The regions end at x_{r+1}, covering a distance d_r. The angle of photon emission has been exaggerated for visual effect.

the boundaries, which corresponds to maximal photon emission as noted in reference [147] and can be seen from taking $\sin\beta = 1$ in equation (4.2.14).

Consider an axion DM wave travelling through such a set of dielectric regions. We have learned in section 4.2 that the axion wave gets transmitted completely through the surfaces, up to higher order effects, and that the momentum of each wave in the direction parallel to the surfaces is conserved in each crossing. As we need to solve for the propagation of the waves generated at each interface via axions, we will need to develop a transfer matrix formalism. The solution of the axion-Maxwell equations is a combination of two plane waves inside each dielectric region together with the axion wave. We have for each region r at first order in the DM velocity $\mathbf{v} = \mathbf{p}/\omega$ and in χ_r

$$\begin{pmatrix} a \\ iA_x \\ iA_y \\ iA_z \end{pmatrix} = a(\mathbf{p}) \begin{pmatrix} 1 \\ 0 \\ -\chi_r \\ 0 \end{pmatrix} e^{iv_x\omega x} + R_r \begin{pmatrix} \chi_r \\ -v_y \\ 1 \\ 0 \end{pmatrix} e^{in_r\omega(x-x_r)} + L_r \begin{pmatrix} \chi_r \\ v_y \\ 1 \\ 0 \end{pmatrix} e^{-in_r\omega(x-x_r)}, \tag{4.3.1}$$

where we have divided out a common factor of $e^{i(p_y y + p_z z - \omega t)} = e^{i\omega(v_y y + v_z z - t)}$, which does not affect the derived quantities. However, these terms will offset the angle of emitted EM waves. The continuity of the axion and $\mathbf{E}_{||}$-field and its derivatives across the boundary $r, r+1$ imposes in principle four restrictions onto the amplitude of the right and left moving waves. At first order in $\chi \equiv \mathrm{Max}(\chi_r)$ only the continuity of the E_y-component and its derivative is relevant

as E_z vanishes, giving

$$\begin{aligned} -a(\mathbf{p})e^{iv_x\omega x_{r+1}}\chi_r + R_r e^{i\delta_r} + L_r e^{-i\delta_r} &= -a(\mathbf{p})e^{iv_x\omega x_{r+1}}\chi_{r+1} && \text{(4.3.2a)} \\ &\quad + R_{r+1} + L_{r+1}, && \text{(4.3.2b)} \\ -a(\mathbf{p})e^{iv_x\omega x_{r+1}}v_x\chi_r + n_r R_r e^{i\delta_r} - n_r L_r e^{-i\delta_r} &= -a(\mathbf{p})e^{iv_x\omega x_{r+1}}v_x\chi_{r+1} \\ &\quad + n_{r+1}R_{r+1} - n_{r+1}L_{r+1}. && \text{(4.3.2c)} \end{aligned}$$

Recalling that $\delta_r = \omega n_r(x_{r+1} - x_r)$, which can be complex if the medium is conducting or absorbing, the system solves to

$$\begin{aligned} \begin{pmatrix} R_{r+1} \\ L_{r+1} \end{pmatrix} &= \frac{1}{2n_{r+1}} \begin{pmatrix} n_{r+1}+n_r & n_{r+1}-n_r \\ n_{r+1}-n_r & n_{r+1}+n_r \end{pmatrix} \begin{pmatrix} e^{i\delta_r}R_r \\ e^{-i\delta_r}L_r \end{pmatrix} \\ &+ a(\mathbf{p})e^{iv_x\omega x_{r+1}}\frac{\chi_{r+1}-\chi_r}{2}\begin{pmatrix} 1+v_x/n_{r+1} \\ 1-v_x/n_{r+1} \end{pmatrix}, \end{aligned} \tag{4.3.3}$$

which we can write as

$$\begin{pmatrix} R_{r+1} \\ L_{r+1} \end{pmatrix} = \mathsf{G}_r\mathsf{P}_r \begin{pmatrix} R_r \\ L_r \end{pmatrix} + a(\mathbf{p})\chi\mathsf{S}_r \begin{pmatrix} 1 \\ 1 \end{pmatrix}, \tag{4.3.4}$$

where

$$\mathsf{G}_r = \frac{1}{2n_{r+1}} \begin{pmatrix} n_{r+1}+n_r & n_{r+1}-n_r \\ n_{r+1}-n_r & n_{r+1}+n_r \end{pmatrix}, \tag{4.3.5a}$$

$$\mathsf{P}_r = \begin{pmatrix} e^{i\delta_r} & 0 \\ 0 & e^{-i\delta_r} \end{pmatrix}, \tag{4.3.5b}$$

$$\mathsf{S}_r = e^{iv_x\omega x_{r+1}}\frac{\chi_{r+1}-\chi_r}{2\chi}\begin{pmatrix} 1+v_x/n_{r+1} & 0 \\ 0 & 1-v_x/n_{r+1} \end{pmatrix}. \tag{4.3.5c}$$

For multiple layers we iterate this equation to derive a relation between the amplitude of the R, L waves in the external media, 0 and m:

$$\begin{aligned} \begin{pmatrix} R \\ L \end{pmatrix}_m &= \mathsf{G}_{m-1}\mathsf{P}_{m-1}\begin{pmatrix} R \\ L \end{pmatrix}_{m-1} + a(\mathbf{p})\chi\mathsf{S}_{m-1}\begin{pmatrix} 1 \\ 1 \end{pmatrix} \\ &= \mathsf{G}_{m-1}\mathsf{P}_{m-1}\left[\mathsf{G}_{m-2}\mathsf{P}_{m-2}\begin{pmatrix} R \\ L \end{pmatrix}_{m-2} + a(\mathbf{p})\chi\mathsf{S}_{m-2}\begin{pmatrix} 1 \\ 1 \end{pmatrix}\right] \\ &\quad + a(\mathbf{p})\chi\mathsf{S}_{m-1}\begin{pmatrix} 1 \\ 1 \end{pmatrix} \\ &= \ldots \\ &= \mathsf{T}\begin{pmatrix} R \\ L \end{pmatrix}_0 + a(\mathbf{p})\chi\mathsf{M}\begin{pmatrix} 1 \\ 1 \end{pmatrix}, \end{aligned} \tag{4.3.6}$$

where $\mathsf{T} = \mathsf{T}_0^m$, with T_b^a the transfer matrix from surface b to a

$$\mathsf{T}_b^a = \mathsf{G}_{a-1}\mathsf{P}_{a-1}\mathsf{G}_{a-2}\mathsf{P}_{a-2}\mathsf{G}_{a-3}\mathsf{P}_{a-3}\ldots\mathsf{G}_b\mathsf{P}_b. \tag{4.3.7}$$

In this notation, $\mathsf{T}_a^a = \mathsf{P}_0 = \mathbb{1}$. Similarly, we have defined

$$\mathsf{M} \equiv \sum_{s=1}^{m} \mathsf{T}_s^m \mathsf{S}_{s-1}. \tag{4.3.8}$$

We have separated equation (4.3.6) into two parts. The first part encodes the normal propagation of EM waves through dielectric media. The second gives the axion-DM induced source terms S_r, one for each layer. Because each wave has to traverse different layers to reach the detector they will all come with different phases. These are the phases we shall arrange to be coherent to increase the axion DM signal. Interestingly, the main axion velocity effects only enter in S_r, and then only by v_x. Essentially, the dielectric haloscope picks out the part of the axion's velocity aligned with the haloscope. Because of this, in situations where the velocity is non-negligible a dielectric haloscope should have a directional sensitivity to the axion.

We may also solve for the left-most amplitudes in region 0 in terms of those in region m by multiplying equation (4.3.6) from the left with T^{-1}. The inverse matrix involves the determinant of T for which one finds

$$\mathrm{Det}[\mathsf{T}] = \frac{n_0}{n_m}\,. \tag{4.3.9}$$

This is because the determinant of a product of matrices is the product of the determinants and the determinants are $\mathrm{Det}[\mathsf{P}_r] = 1$ and $\mathrm{Det}[\mathsf{G}_r] = n_r/n_{r+1}$. In the special case when one external medium is a perfect mirror, e.g., $|n_0| \to \infty$, one must be careful. The correct results can be obtained by taking the limit of a large but finite n.

Lastly, we note this formalism is developed for linear equations, and so can be used with any normalisation of the A-fields. For example, the same matrices also give the same transformations with E-fields, or a differently normalised, dimensionless version of the vector potential used in the next chapter.

4.3.2 Transmissivity and reflectivity

We can use T to define the usual transmission and reflection amplitude coefficients

$$\mathcal{T}_L = \frac{R_m}{R_0}\Big|_{L_m=0} = \frac{\mathrm{Det}[\mathsf{T}]}{\mathsf{T}[2,2]}\,, \tag{4.3.10a}$$

$$\mathcal{T}_R = \frac{L_0}{L_m}\Big|_{R_0=0} = \frac{1}{\mathsf{T}[2,2]}\,, \tag{4.3.10b}$$

$$\mathcal{R}_L = \frac{L_0}{R_0}\Big|_{L_m=0} = -\frac{\mathsf{T}[2,1]}{\mathsf{T}[2,2]}\,, \tag{4.3.10c}$$

$$\mathcal{R}_R = \frac{R_m}{L_m}\Big|_{R_0=0} = \frac{\mathsf{T}[1,2]}{\mathsf{T}[2,2]}\,, \tag{4.3.10d}$$

with $\mathrm{Det}[\mathsf{T}] = n_0/n_m$. These expressions correspond to decoupling the axion by taking $\chi \to 0$, though for $\chi > 0$ the RHS of the above equations (4.3.10) then define the transmissivity and reflectivity. These can be useful quantities, as they will generally be correlated with the production of photons from axions. Note that non-zero axion velocities can make this correlation less manifest, as the transmissivity and reflectivity are unaffected by the axion. To regain the connection, one must also know the axion velocity.

4.3.3 Boost amplitude

For a dielectric haloscope we only want the EM waves generated in the presence of axions. In this case we exclude any incoming EM waves, $R_0 = L_m = 0$, and solve for the outgoing waves to define the usual boost amplitude for dielectric haloscopes

$$\mathcal{B}_L = \frac{L_0}{\chi a(\mathbf{p})} = -\frac{\mathsf{M}[2,1] + \mathsf{M}[2,2]}{\mathsf{T}[2,2]}, \tag{4.3.11a}$$

$$\mathcal{B}_R = \frac{R_m}{\chi a(\mathbf{p})} = \mathsf{M}[1,1] + \mathsf{M}[1,2] - \frac{\mathsf{M}[2,1] + \mathsf{M}[2,2]}{\mathsf{T}[2,2]}\mathsf{T}[1,2]. \tag{4.3.11b}$$

Often we will not be interested in the phase of the outgoing wave relative to the original axion field. In this case we will use the term

$$\text{Boost factor:} \qquad \beta = |\mathcal{B}| \tag{4.3.12}$$

to denote the modulus of the boost amplitude. This corresponds to an emitted power per area for a given axion momentum $\mathbf{p}$ of

$$\frac{P_{L,R}(\mathbf{p})}{\mathcal{S}} = \frac{\beta_{L,R}^2 E_a(\mathbf{p})^2}{2} = \frac{g_{a\gamma}^2 B_\mathrm{e}^2 |a(\mathbf{p})|^2}{2}, \tag{4.3.13}$$

where we will ignore any potential issues due a lack of homogeneity on the scale of the measurement. In the zero velocity limit, which will be useful when discussing an experiment searching for axions, this can be reduced to

$$\frac{P_{L,R}}{\mathcal{S}} = \rho_a \left(\frac{g_{a\gamma} B_\mathrm{e}}{m_a}\right)^2 \beta_{L,R}^2 \,. \tag{4.3.14}$$

In general, we will not need to worry about the distinction between $\mathcal{B}_L$ and $\mathcal{B}_R$, as we only consider situations that are either symmetric, so $\mathcal{B}_L = \mathcal{B}_R \equiv \mathcal{B}$, or maximally asymmetric, with the medium on one side being a mirror. In this case only one of $\mathcal{B}_L$ and $\mathcal{B}_R$ is non-zero. Note that in the case of a perfect mirror, one can either use the above equations in a limiting sense, or simply use (for $n_0 = \infty$)

$$\mathcal{B}_R = \mathsf{M}[1,1] + \mathsf{M}[1,2]. \tag{4.3.15}$$

The axion-produced EM power is proportional to $|\mathcal{B}|^2 = \beta^2$, cf. equation (4.1.17). For arrangements which are open on both ends (no mirror) and left-right-symmetric, the boost amplitude and boost factor applies only to one of the

emerging waves. The produced power refers to the one emerging from one side only.

The boost amplitude is our main quantity of interest because it describes the response of the haloscope to the axion field. By construction, $\mathcal{B}$ is a function of the refractive indices $n_0, \ldots, n_m$, the distances between the interfaces $d_1, \ldots, d_{m-1}$, and the chosen frequency ω. The latter quantities together provide us with the phase depths $\delta_r = n_r \omega d_r$ with $r = 1, \ldots, m-1$. It is really the phase depths and refractive indices which determine $\mathcal{B}$.

In practice, a given haloscope will consist of a series of dielectric plates with fixed properties that can be shifted relative to each other. In the zero velocity limit (which will often be used) and keeping all refractive indices fixed, we may think of $\mathcal{B}(\mathbf{d}, \omega)$ as a function of an $(m-1)$-dimensional "configuration vector" $\mathbf{d} = (d_1, \ldots, d_{m-1})$ of distances and of the frequency ω. If all n_r are real numbers (no losses), it is easy to show (appendix A) that

$$\langle |\mathcal{B}|^2 \rangle_{\mathbf{d}} = \langle |\mathcal{B}|^2 \rangle_{\omega} \,. \tag{4.3.16}$$

Here the average $\langle \ldots \rangle_{\mathbf{d}}$ is the average over all configurations, whereas $\langle \ldots \rangle_{\omega}$ the average over all frequencies. In particular, the configuration average does not depend on frequency and the frequency average not on configuration.

In the latter interpretation, this result means that the power emitted by the haloscope, averaged over a flat spectrum of ω, does not depend on configuration. In particular, if $|\mathcal{B}|^2$ shows a resonance as a function of ω, small modifications of the disk spacings will change the resonance structure, perhaps shift it a bit, but leave the "area" $\int d\omega \, |\mathcal{B}|^2$ unchanged. We refer to this rule as the Area Law. For a simple resonance described by a Lorentzian response, this result means that the integral over the Lorentzian does not depend on the resonance width Γ as expected.

4.3.4 General behaviour of velocity effects

To lowest order, one does not expect that the velocity of the axion will play much of a role due to the non-relativistic nature of the axion. Because of this for much of this thesis we will neglect velocity effects except in cases where they may be important. To see when this might be we should gain a general understanding of at what order and from which terms velocity effects begin to affect dielectric haloscopes. To do this, we must look closer at M [as defined in equation (4.3.8)]. We note that it is possible to rewrite any element of a transfer matrix $\mathsf{T}_a^b[i,j]$ in the form

$$\mathsf{T}_a^b[i,j] = \sum_p W_{\mathbf{k}}^{i,j} e^{i\delta_p}, \tag{4.3.17}$$

where $W_p^{i,j}$ is a constant depending only on the n_r, and δ_p is a combination of the phases with differing signs, i.e., each δ_p is of the form $\pm\delta_a \pm \ldots \pm \delta_b$ with

all 2^{b-a-1} possible combinations. From this we can write

$$\mathsf{M}[i,j] = \sum_{s=1}^{m} e^{iv_x\omega x_s} \frac{\chi_s - \chi_{s-1}}{2\chi} \left(1 \pm \frac{v_x}{n_s}\right) \sum_p W_p^{i,j} e^{i\delta_p}, \tag{4.3.18}$$

where the $\pm$ signs depends on the exact matrix element. The axion velocity enters in three places: the change in the phase of the axion, the discontinuity in the axion induced H-field and the shift to the axion frequency. To isolate the velocity effects, we can look at

$$\begin{aligned} v_x \frac{\partial \mathsf{M}[i,j]}{\partial v_x} &= v_x \sum_{s=1}^{m} i\omega x_s \frac{\chi_s - \chi_{s-1}}{2\chi} \sum_p W_p^{i,j} e^{i\delta_p}|_{v=0} \\ &\pm v_x \sum_{s=1}^{m} \frac{1}{n_s} \frac{\chi_s - \chi_{s-1}}{2\chi} \sum_p W_p^{i,j} e^{i\delta_p}|_{v=0} \\ &+ v_x^2 \sum_{s=1}^{m} \frac{\chi_s - \chi_{s-1}}{2\chi} \sum_p i\delta_p W_p^{i,j} e^{i\delta_p}|_{v=0} \\ &+ \ldots, \end{aligned} \tag{4.3.19}$$

where we have only kept the leading contribution from each of the three effects mentioned above. This assumes that the phase appearing in the exponentials is small, which breaks down for physically large haloscopes. The three effects can be understood separately:

1. *Axion phase:* The term in the first line of equation (4.3.19) is the most important, and comes from the change of phase of the axion itself. As it comes with factors of x_s, this term is roughly proportional to $m_a L v_x$, where L is the length of the haloscope in the x direction, leading it to dominate over the other terms as L increases. When L is very large, this expansion breaks down and the change in M is significant, potentially even $\mathcal{O}(1)$. Note that this is only the leading contribution coming from the phase of the axion: we neglect cross terms that may be of the same or higher order as the other two contributions, such as terms proportional to $m_a^2 L^2 v_x^2$ and $m_a L v_x^2$.

2. *H-field:* The term in the second line of equation (4.3.19) is due to the discontinuity in the axion induced H-field. Note that there is no enhancement by the length scales of the haloscope. Because of this, terms coming purely from the axion induced H-field cannot have a significant effect on M as v is very small.

3. *Frequency shift:* The contribution in the last line of equation (4.3.19) comes from the frequency shift of the axion appearing in the photon propagator. We can see from the combination of the phase δ_p and the factor of v_x^2 that this contribution is generically proportional $m_a L v^2$. As

this is a frequency shift, it can only large effect when the boost factor varies rapidly as a function of frequency, a case which is not usually considered in the dielectric haloscope context. For the cases we will study below, $\beta(m_a) \simeq \beta(\omega)$ to very good approximation. Note that the transverse velocities also result in a similar frequency shift. For simplicity, we will assume throughout this section that the disk is perfectly aligned with the axion velocity, so that $v \equiv v_x$. As the shift to the frequency makes certain analytic cases more complex, but is numerically irrelevant, for the analytic cases we will define distances in terms of ω, rather than the axion mass m_a. Note that even though the change to the boost factor is negligible, a detector with an energy resolution better than $\mathcal{O}(10\text{ kHz})$ would be able to resolve this frequency shift for $100\,\mu$eV axions.

Thus we expect that the primary influence on the boost factor will come from the change of phase of the axion. This can be contrasted with the velocity effects considered in dish antenna setups [184, 185]. Dish antennas have only a single interface, essentially giving $L = 0$ so that the dominant effects come from the axion velocities parallel to the interface.

Because of this, we only expect that velocity effects must be included when we consider devices where the length scales become a noticeable fraction (on the order of 20%) of the axion de Broglie wavelength. For many of our examples this will never be the case, but we will also consider cases where the velocity plays a role. To see exactly at what level the velocity comes into play, we must consider some more concrete examples, which will be explored in chapters 6 and 7 along with the velocity-negligible cases.

Chapter 5

Quantum Field Calculation: Overlap Integral Formalism

In the previous chapter, we derived a practical classical computational technique to find the EM waves generated by the DM axion field. Transfer matrices have the advantage of being computationally efficient, however they are not always the most transparent to use for analytic proofs, and have no obvious connection to other axion experiments such as helioscopes or cavity haloscopes. Ideally, one would like a unified framework in which one could see the connection between the different types of experiments. In particular, this would provide a simple explanation for how the overlap integral formalism used in cavity experiments would be extended to deal with dielectric haloscopes.

One also might wonder whether the classical treatment itself is appropriate for the axion field. If one was to do a quantum calculation, would there be an extra factor coming from, for example, stimulated emission? Fortunately both of these questions can be answered via a quantum field calculation of the axion-photon conversion. First we will introduce the general framework for such a calculation, applying the results to three major types of experiments using the axion-photon coupling. Finally, we will check that the quantum calculation agrees with the classical calculation where appropriate, and comment on the connection.

The quantum field approach is motivated by analogy with the calculation of transition radiation [186, 187]. A charged particle, moving uniformly on a straight line, does not radiate due to energy-momentum conservation. However, this is different in the presence of dielectrics because free photons are now solutions of Maxwell's equations in the presence of dielectrics, i.e., they are no longer eigenstates of momentum. Likewise, for a dielectric haloscope we can perform a conventional first-order perturbative calculation for the transition between DM axions and these distorted photons. The result will be given in terms of a matrix element which effectively is an overlap integral similar to the traditional cavity haloscope calculation, but now involving photon "scattering states" rather than the "bound state" excitations of a cavity.

This approach gives a new perspective on the conversion of axions to photons inside a dielectric haloscope, and clarifies the relationship between the overlap integral and classical calculations. While both are mathematically equivalent, they evoke very different physical pictures. While such an overlap integral formalism can be developed from the classical equations through cumbersome mathematical transformations (and is contained in appendix C), the overlap integral formalism emerges here very naturally from the quantum-field calculation. Further, in the classical treatment many features of the overlap integral formalism, such as the normalisation and choice of the integrated E field, emerge seemingly from nowhere. In the perturbative quantum-field calculation the integrand will be obvious: one must integrate over the free Garibian photon wave functions [188, 189], which are uniquely determined up to time-reversals. Thus we gain a deeper understanding of the underlying physics of dielectric haloscopes.

5.1 First-order perturbative transition probability

Our setup for the quantum calculation will be very general, in principle applying to essentially any axion experiment. We consider a generic situation of a plane-wave axion interacting with a configuration of external classical static electric or magnetic fields by virtue of the interaction given in equation (2.1.7). Rather than solving for some classical E and B-fields, we ask for the decay rate (inverse lifetime) $\Gamma_{a\to\gamma}$ of an axion to convert into a photon. This could be a plane wave with momentum $\mathbf{k}$ or another type of propagating state, notably of the type caused by the presence of dielectrics. In this case $\mathbf{k}$ represents some suitable set of quantum numbers describing the wave function. Generally we consider situations where translational invariance is broken by external agents. Therefore, the simplest approach is to use non-covariant perturbation theory in the laboratory frame. The inverse lifetime of a single quantized axion with energy ω_a to convert into a single photon following from elementary time-dependent perturbation theory is

$$\Gamma_{a\to\gamma} = 2\pi \sum_{\mathbf{k}} |\mathcal{M}|^2 \, \delta(\omega_a - \omega_{\mathbf{k}}) \, . \tag{5.1.1}$$

Here $\mathcal{M} = \langle \mathrm{f}|H_{a\gamma}|\mathrm{i}\rangle$ is the non-covariant matrix element of the interaction Hamiltonian between the initial and final state and as such has the dimension of energy. If $\mathcal{M}$ does not depend on $\mathbf{k}$, equation (5.1.1) is Fermi's Golden Rule in its simplest form $\Gamma = 2\pi|\mathcal{M}|^2 \, dN/d\omega$ where $dN/d\omega$ is the density of continuum final states per unit energy.

To recall the normalisation of the fields quantized in some large but finite volume V we mention that the axion field has the form

$$\phi = \sum_{\mathbf{p}} \frac{1}{\sqrt{2\omega_{\mathbf{p}} V}} \left[a_{\mathbf{p}} e^{-i(\omega_{\mathbf{p}} t - \mathbf{p}\cdot\mathbf{r})} + a^\dagger_{\mathbf{p}} e^{i(\omega_{\mathbf{p}} t - \mathbf{p}\cdot\mathbf{r})} \right] , \tag{5.1.2}$$

where $a_{\mathbf{p}}$ and $a_{\mathbf{p}}^\dagger$ are the usual destruction and creation operators for a quantum of momentum $\mathbf{p}$ and energy $\omega_{\mathbf{p}} = \sqrt{\mathbf{p}^2 + m_a^2}$. (Notice that $a_{\mathbf{p}}$ and $a_{\mathbf{p}}^\dagger$ are dimensionless and ϕ has dimension energy as it should.) In this case we say that the axion plane waves have amplitude 1. A similar expression pertains to the propagating polarization components of the quantized photon field $\mathcal{A}$. For simplicity, we will often separate the normalisation from the photon wave function, writing $\mathcal{A}_{\mathbf{k}} \equiv A_{\mathbf{k}}/\sqrt{2\omega_{\mathbf{k}}V}$, where plane-wave photons correspond to $|A_{\mathbf{k}}| = 1$. This definition agrees with our earlier notation for the classical vector potential, with corresponding E and B-fields. However, our main interest is in photon wave functions modified by dielectrics so that $\mathbf{k}$ is a more general set of quantum numbers and $A_{\mathbf{k}}$ is a nontrivial wave function that breaks translational invariance.

As a next step we assume that the external field is given as $\mathbf{B}_{\rm e}(\mathbf{r})$ or as $\mathbf{E}_{\rm e}(\mathbf{r})$ and we consider the transition of one quantum of the axion field (5.1.2) to a photon with quantum numbers $\mathbf{k}$. The matrix element of the interaction Hamiltonian between initial and final quantum states is then found to be

$$\mathcal{M} = \frac{g_{a\gamma}}{2\omega V}\int d^3\mathbf{r}\, e^{i\mathbf{p}\cdot\mathbf{r}}\, \mathbf{B}_{\rm e}(\mathbf{r})\cdot\mathbf{E}^*_{\mathbf{k}}(\mathbf{r}) \quad \text{or} \quad \mathcal{M} = \frac{g_{a\gamma}}{2\omega V}\int d^3\mathbf{r}\, e^{i\mathbf{p}\cdot\mathbf{r}}\, \mathbf{E}_{\rm e}(\mathbf{r})\cdot\mathbf{B}^*_{\mathbf{k}}(\mathbf{r})\,, \tag{5.1.3}$$

where $\omega = \omega_a = \omega_{\mathbf{k}}$. Moreover, $\mathbf{E}_{\mathbf{k}}(\mathbf{r})$ or $\mathbf{B}_{\mathbf{k}}(\mathbf{r})$ are the electric or magnetic field configuration associated with the unnormalised photon wave function $A_{\mathbf{k}}$. To check the dimensions of this expression, notice that the external electric or magnetic fields, in natural units, have dimension $(\text{energy})^2$, $g_{a\gamma}$ has dimension $(\text{energy})^{-1}$, and the amplitudes $\mathbf{E}_{\mathbf{k}}$ or $\mathbf{B}_{\mathbf{k}}$ have dimension (energy) because $A_{\mathbf{k}}$ is dimensionless and $E_{\mathbf{k}} \sim \omega A_{\mathbf{k}}$. Overall $\mathcal{M}$ therefore has dimension (energy) as it should.

The matrix element equation (5.1.3) is an overlap integral of the external EM field, sandwiched between the spatial axion and photon wave functions. In the haloscope context, the axion momentum will be taken to be vanishingly small. In this sense, the microwave production rate is proportional to an overlap integral of the external EM field configuration with the photon wave function.

5.2 Helioscope

As a first example we consider the axion helioscope [18]. As we reviewed in section 2.2.2 a helioscope is essentially a dipole magnet oriented toward the Sun such as the CAST experiment [190]. The external magnetic field is taken to be a constant value $\mathbf{B}_{\rm e}$, whereas the final-state photon is taken to be a plane wave so that $\mathbf{E}_{\mathbf{k}}(\mathbf{r}) = i\omega_{\mathbf{k}}\,\boldsymbol{\epsilon}\, e^{i\mathbf{k}\cdot\mathbf{r}}$, where $\boldsymbol{\epsilon}$ is a polarization vector. Therefore, the matrix element is

$$\mathcal{M} = i\,\frac{g_{a\gamma}\,\boldsymbol{\epsilon}\cdot\mathbf{B}_{\rm e}}{2V}\int d^3\mathbf{r}\, e^{-i\mathbf{q}\cdot\mathbf{r}}\,. \tag{5.2.1}$$

We assume $\mathbf{B}_\mathrm{e}$ to be transverse to the axion momentum $\mathbf{p}$, so only photons with polarization parallel to $\mathbf{B}_\mathrm{e}$ are produced. Moreover, our setup has translational invariance in the y-z-directions, assuming the axion momentum is in the x-direction. Therefore, the y and z components of momentum are conserved and the photon momentum must also be along the x-direction. Our large quantization volume is $V = \mathcal{S}L$ with $\mathcal{S}$ some large area in the y-z-plane and L some large distance in the x-direction. The magnetic region itself is taken to have length ℓ in the x-direction, so with $\int dydz = \mathcal{S}$ overall the matrix element is

$$\mathcal{M} = \frac{g_{a\gamma}B_\mathrm{e}}{2L}\int_{-\ell/2}^{+\ell/2} dx\, e^{-iqx} = \frac{g_{a\gamma}B_\mathrm{e}}{2L}\,\frac{2\sin(q\ell/2)}{q}\,, \tag{5.2.2}$$

where $q = k_x - p_x$. Note that there are two possibilities for q, depending on whether the photon is emitted forwards or backwards, $q_\pm = \pm\omega - \sqrt{\omega^2 - m_a^2}$, respectively. Energy conservation implies $|k_x| = \omega$.

To sum over final states, the symmetry of our setup in the y and z directions dictates that only photon momenta $\mathbf{k}$ in the x-direction appear, i.e., $\sum_\mathbf{k}\delta(\omega_a - \omega_\mathbf{k}) \to (L/2\pi)\int d|k_x|\delta(\omega_a - \omega_{k_x}) = (L/2\pi)$ with $|k_x| = \omega_{k_x}$. We find for the axion transition rate

$$\Gamma_{a\to\gamma} = \frac{1}{L}\,\mathcal{P}_{a\to\gamma} \quad \text{where} \quad \mathcal{P}_{a\to\gamma} = \sum_{q=q_\pm}\left(g_{a\gamma}B_\mathrm{e}\,\frac{\sin(q\ell/2)}{q}\right)^2\,, \tag{5.2.3}$$

where the sum is over the two cases of momentum transfer and $\mathcal{P}_{a\to\gamma}$ is the probability of converting from an axion to a photon.

For solar axions, the x-ray energies are very large compared with the Fourier components of the magnetic field region, so we neglect the fast-oscillating part from $q_- = -\omega - \sqrt{\omega^2 - m_a^2}$. In other words, "wrong direction" photons are hardly emitted because the B-field region does not end abruptly enough to provide the required large momentum transfer. On the other hand, the difference term $q_+ = \omega - \sqrt{\omega^2 - m_a^2}$ can be so small that $q_+\ell \ll 1$ and the conversion rate is then the usual expression $\mathcal{P}_{a\to\gamma} = (g_{a\gamma}B_\mathrm{e}\ell/2)^2$. Of course, if we neglect the fast-oscillating part, we are back to the usual picture of axion-photon oscillations in the spirit of neutrino flavor oscillations along the magnet pipe.

To interpret the normalisation of our result we notice that by construction we began with one axion in our normalisation volume $V = \mathcal{S}L$. We can express our result as a photon flux per unit area and unit time emerging at the ends of the magnetic field region. Therefore, we divide $\Gamma_{a\to\gamma}$ by the area $\mathcal{S}$, implying that the result is proportional to $1/V$, the number of axions per normalisation volume. So the emerging photon flux is proportional to the axion number density n_a as it should be.

In the limit $\mathbf{p} \to 0$ the helioscope becomes a haloscope, i.e., we can interpret the result as a photon flux from dark matter axion conversion emerging in two directions from a homogeneous magnetic field region (length ℓ) which ends

abruptly on both sides. The number density of axions is $n_a = \rho_a/m_a$ with ρ_a the local DM axion mass density. Thus the number of microwave photons emerging from one side of the magnetic field region per unit time and unit area is

$$\Phi_\gamma = \frac{\rho_a}{m_a} \left(g_{a\gamma} B_\mathrm{e} \frac{\sin(m_a \ell/2)}{m_a} \right)^2 . \tag{5.2.4}$$

Of course, such a device is not an ideal haloscope, with a relatively small conversion rate. However, this can inspire us to move onto a more promising setup.

5.3 Dielectric haloscope

5.3.1 Haloscope setup

Our real interest, however, is a setup where the quasi-homogeneous external magnetic field falls off adiabatically so that it does not provide any significant momentum transfer and the axion-photon transition rate vanishes with excellent approximation. However, we now introduce a system of parallel dielectric layers, oriented parallel to $\mathbf{B}_\mathrm{e}$. The simplest case of a dielectric disk is shown in figure 5.1. The dielectric disk breaks translation invariance and thus enables the transition between dark-matter axions and microwave photons.

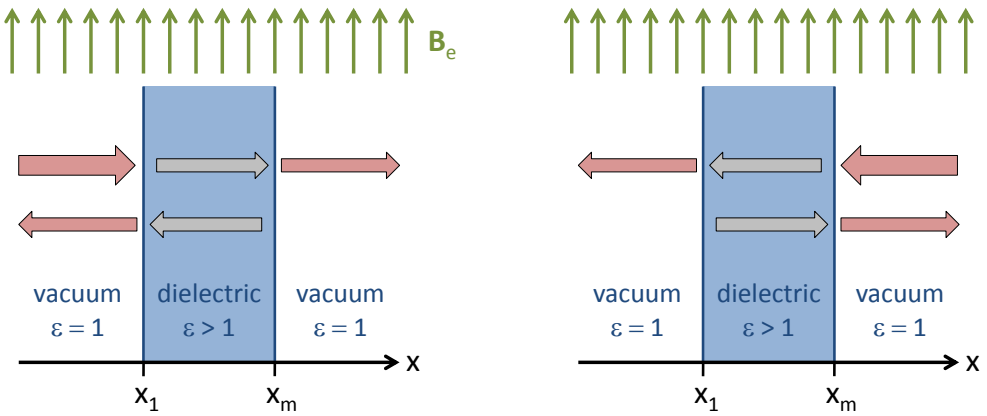

Figure 5.1: Dielectric haloscope. The dielectric region could be a single layer as shown or consist of many layers with the outermost interfaces at $x = x_1$ and $x = x_m$. For several layers there are many internal reflections which are not shown. The arrows indicate the photon wave functions with an incoming wave being split into a reflected and transmitted one. Reversing the arrows in both panels, there exists a second set of wave functions with two incoming waves coalescing to a single outgoing one. The shown set of wave functions or this second set are equivalent representations, as shown explicitly in reference [188].

It is now the photon wave function itself which is distorted by the dielectric layers and thus no longer an eigenstate of momentum. The same logic applies

to transition radiation which arises when a charged particle traverses dielectric interfaces. While transition radiation is traditionally treated on the classical level, a quantum calculation is required to treat backreaction on the emitting particle. This point was first made by Garibian [188, 189] who defined the photon wave functions for the simple case of a dielectric interface, but the same approach applies to a dielectric disk [191] or more complicated arrangements. We will only consider axions with momentum $\mathbf{p}$ perpendicular to the interfaces, so they and the photon wave functions will be translationally invariant in the transverse directions. We know from section 4.3.4 that the primary velocity effects should come from the perpendicular axion momentum, making this a reasonable simplification.

5.3.2 Garibian wave functions

In this simple geometric setup, the Garibian wave functions consist of an incoming plane wave which is split by the haloscope into a transmitted and a reflected component. There are two such wave functions, depending on the side of the haloscope on which they impinge. Without the haloscope, these would be left- and right-moving plane waves with wave vector $\mathbf{k}$. Equivalently, one can use the time-reversed wave functions with all momenta reversed, corresponding to two incoming waves which coalesce such as to produce only one outgoing wave on either side of the haloscope. One can use one or the other set to span the space of photon wave functions. The picture of an incoming beam being split into two outgoing waves as shown in figure 5.1 is somewhat more intuitive to construct the wave functions, whereas the coalescence picture is more intuitive when we ask for photon emission in one specific direction from the haloscope. Notice that in general our system is not left-right symmetric.

Explicitly we write the Garibian wave functions for the photon electric field configuration for our one-dimensional problem in the form $\mathbf{E}(\mathbf{r}) = i\omega\boldsymbol{\epsilon}A_\omega(x)$, where $\boldsymbol{\epsilon}$ is a polarization vector parallel to $\mathbf{B}_\mathrm{e}$. Outside of the haloscope ($x < x_1$ and $x > x_m$) the L wave function (left panel of figure 5.1) has the form

$$A^L_\omega(x) = \begin{cases} e^{i\omega\Delta x_1} + \mathcal{R}_L\, e^{-i\omega\Delta x_1} & \text{for } x < x_1, \\ \mathcal{T}_L\, e^{i\omega\Delta x_m} & \text{for } x > x_m, \end{cases} \tag{5.3.1}$$

corresponding to a plane wave with amplitude 1 impinging from the left side and $\Delta x_j = x - x_j$. Notice that we define these coefficients with reference to the left most interface ($x = x_1$) for the waves on the lhs of the device and rightmost interface ($x = x_m$) for those on the rhs of the device. It is reflected with the reflection coefficient $\mathcal{R}_L$ and transmitted with $\mathcal{T}_L$, where $|\mathcal{R}_L|^2 + |\mathcal{T}_L|^2 = 1$. In general, our system is not left-right symmetric, so one needs to treat separately the case where the incoming wave impinges from the right,

$$A^R_\omega(x) = \begin{cases} \mathcal{T}_R\, e^{-i\omega\Delta x_1} & \text{for } x < x_1, \\ e^{-i\omega\Delta x_m} + \mathcal{R}_R\, e^{i\omega\Delta x_m} & \text{for } x > x_m. \end{cases} \tag{5.3.2}$$

In the haloscope region $x_1 < x < x_m$, the wave functions can be very complicated due to the multiple reflections on many layers.

The main feature of these wave functions is that the normalisation is such that the incoming wave has amplitude 1, identical to an ordinary plane-wave photon, independently of the detailed behaviour within the haloscope. This is physically clear if we think of a single photon moving toward the haloscope and if we think of it as a wave packet which does not yet know about the haloscope. It is built from ordinary plane wave components which must be the same whether or not the haloscope has been put in place. Therefore, the normalisation of its Fourier components should not be affected by the presence of the haloscope. By the same token, the Garibian wave functions for different ω and ω' must be orthogonal. The haloscope, being a linear optical element, cannot mix photons with different frequencies.

The orthonormality of such wave functions was shown explicitly for the case of a single dielectric disk for a more complicated situation where the photons impinge at some angle [191]. This more general case was needed to treat transition radiation from a particle traversing the disk. Here we are considering 1D setups with many layers of dielectric material. While this situation appears more complicated, we show in appendix B that one can use the relationship between the fields on either side of an interface to rewrite the orthonormality condition to be the same as for a free photon in a vacuum. This confirms that Garibian wave functions are the correct free photon wave functions for quantisation and use in our perturbative quantum calculation.

Note that as the Garibian wave functions are given by reflecting an EM wave on either side of the device, one would expect that such a wave function can be measured in the same way. From this we would expect that as the boost factor is calculated from the Garibian wave functions the reflective behaviour of a dielectric haloscope should be correlated with boost factor.

5.3.3 Photon production rate

To obtain the photon production rate we follow the same steps as in section 5.2 for the helioscope, except that the photon plane waves need to be replaced by Garibian wave functions. In other words, the integral expression in equation (5.2.2) must be substituted with

$$\mathcal{I}_\omega = \int_{-\infty}^{+\infty} dx\, A_\omega(x)\,, \tag{5.3.3}$$

where we have already assumed zero-velocity axions, i.e., $\mathbf{p} = 0$, implying $\omega = m_a$.

The integrals outside of the haloscope can be performed explicitly if we observe that the oscillating part at infinity does not contribute, so for example

$\int_{x_m}^{\infty} dx\, e^{i\omega x} = ie^{i\omega x_m}/\omega$. Therefore the scattering amplitudes are

$$\mathcal{I}_\omega^L = \frac{1-\mathcal{R}_L-\mathcal{T}_L}{i\omega} + \int_{x_1}^{x_m} dx\, A_\omega^L(x)\,, \tag{5.3.4a}$$

$$\mathcal{I}_\omega^R = \frac{1-\mathcal{R}_R-\mathcal{T}_R}{-i\omega} + \int_{x_1}^{x_m} dx\, A_\omega^R(x)\,. \tag{5.3.4b}$$

In general, these expressions are different for L and R photons.

The photon flux per unit area and unit time emerging from the L or R side of the haloscope therefore is

$$\Phi_{L,R} = \frac{\rho_a}{m_a}\left(\frac{g_{a\gamma}B_\mathrm{e}}{2}\right)^2 \left|\mathcal{I}_\omega^{L,R}\right|^2\,, \tag{5.3.5}$$

with $\omega = m_a$. In particular, the photon flux emerging from the L side is calculated using the L photon as in the left panel of figure 5.1. Notice that we can look at this configuration as the time-reversed case with a photon emerging on the L side, using these as the appropriate "out states." This can be converted to a power per unit area

$$\frac{P_{L,R}}{\mathcal{S}} = \rho_a \left(\frac{g_{a\gamma}B_\mathrm{e}}{2}\right)^2 \left|\mathcal{I}_\omega^{L,R}\right|^2\,. \tag{5.3.6}$$

In order to connect to the previous chapter recall that the power was given by equation (4.3.13), which gave

$$\frac{P_{L,R}}{\mathcal{S}} = \rho_a \left(\frac{g_{a\gamma}B_\mathrm{e}}{m_a}\right)^2 \left|\mathcal{B}_\omega^{L,R}\right|^2\,, \tag{5.3.7}$$

One can prove explicitly (see appendix C) that

$$\mathcal{B}_\omega^{L,R} = i\frac{\omega}{2}\,\mathcal{I}_\omega^{L,R}\,. \tag{5.3.8}$$

The boost amplitude, like the transmission and reflection coefficients, is a dimensionless quantity. Note that the factor of $i\omega$ can be used to rewrite the boost factor in terms of the E-field instead of the wavefunction A,

$$\mathcal{B}_\omega^{L,R} = \frac{1}{2}\int_{-\infty}^{+\infty} dx\, E_\omega^{L,R}(x). \tag{5.3.9}$$

Thus we see that from a purely QFT starting point, we can obtain the same result of the classical analysis of chapter 4. In appendix C, we show that this holds true entirely generically by rearranging the transfer matrices to derive the overlap integral classically. However, this treatment does not give any insights to the Garibian wave functions; classically the integrated wave function just encodes boundary conditions, without any physical underpinning. One can further note that this formalism actually gives the result for a one dimensional cavity haloscope. By treating the outermost dielectric layers as highly reflective, one obtains a resonant cavity. In appendix C we show that this result agrees with Sikivie's original calculation of the axion-photon conversion inside a resonant cavity [124].

5.3.4 Perfect mirror

For the simplest example, we can calculate the boost amplitude for a flat dish antenna, i.e., an interface between a mirror and vacuum [147]. In this case, there are only two regions, and, for a perfect mirror, photon modes are only supported in the vacuum region. In this case only one of $\mathcal{I}_\omega^{L,R}$ is non-trivial and we do not have to worry about multiple interfaces. As the E-field must be zero at the mirror, $\mathcal{R} = -1$. Thus we very easily get that $\mathcal{B} = 1$, a perfect agreement with the definition in section 4.3.1.

That both this overlap integral formalism and the transfer matrices introduced in Chapter 4 give the same result is not surprising. However, each formalism comes with very different physical interpretations. In the overlap integral formalism, the conversion of axions to photons occurs throughout the volume and axions and photons are in some sense treated separately. The free photon wave function satisfies Maxwell's equations by itself, for example canceling itself at the surface of the mirror.

The transfer matrix approach brings the interfaces to the forefront: the axion acts as a source of a discontinuity at each interface, requiring propagating EM waves to be emitted from the interface to satisfy Maxwell's equations. For a mirror, the axion induced E-field must cancel at the mirror with the propagating wave, giving $|\mathcal{B}|= 1$. The volume only comes in via the distances between each interface, giving rise to interference effects (though power is generated throughout the device). This difference between the two pictures is highlighted in the present case of a mirror: a calculation that involves integrating over all space and one that only uses a single surface, with no volume or length scales, give the same result. Mathematically, this is explained by the fact that the volume integral can be rewritten as a sum over the surface terms coming from the boundaries of integration in each region as shown in appendix C.

5.3.5 Many layers

To make our result yet more explicit we assume the haloscope to consist of $m-1$ dielectric regions between x_1 and x_m, with parallel interfaces at x_r with $r = 1, \ldots, m$. (We follow the convention of chapter 4 where the region left of the haloscope is region $r = 0$ and the region to the right is $r = m$, here both taken to be essentially vacuum with $n_0 = n_m = 1$.) In each region, the refractive index is $n_r = \sqrt{\epsilon_r}$, assuming trivial magnetic permeability $\mu_r = 1$. In each region r the wave function is written in the form

$$A_r(x) = R_r e^{in_r\omega\Delta x_r} + L_r e^{-in_r\omega\Delta x_r}\,, \tag{5.3.10}$$

where R_r is the amplitude of the right-moving component and L_r the left-moving one and we take $\Delta x_0 = \Delta x_1$. We follow the same prescription as chapter 4, so that the field amplitudes R_r and L_r of the right and left moving EM waves are defined at the left boundary of every region, except for R_0

and L_0 which are defined at x_1, i.e., the leftmost interface. Note that unlike in chapter 4 the A-fields are dimensionless, due to our slightly different definition. However, this makes no real difference to the discussion of things like boundary conditions. Therefore, apart from a polarization vector parallel to $\mathbf{B}_{\rm e}$, the electric field of this EM wave is $E_r(x) = i\omega(R_r e^{in_r\omega\Delta x_r} + L_r e^{-in_r\omega\Delta x_r})$, whereas the magnetic field, orthogonal to the electric one, is $B_r(x) = i\omega\, n_r(R_r e^{in_r\omega\Delta x_r} - L_r e^{-in_r\omega\Delta x_r})$. We can then use the now familiar EM boundary conditions. From equation (4.3.7) we see

$$\begin{pmatrix} R_r \\ L_r \end{pmatrix} = \mathsf{G}_{r-1}\mathsf{P}_{r-1} \begin{pmatrix} R_{r-1} \\ L_{r-1} \end{pmatrix}. \tag{5.3.11}$$

For the case of L photons, we specify fields by $R_0 = 1$ and $L_m = 0$, whereas for R photons we have $R_0 = 0$ and $L_m = 1$.

Note that for L photons the reflection coefficient is $\mathcal{R}_L = L_0^L$ and the transmission coefficient $\mathcal{T}_L = R_m^L$, with similar expressions for R waves, so the scattering amplitudes of equation (5.3.4) are found to be

$$\mathcal{I}_\omega^L = \frac{1 - L_0^L - R_m^L}{i\omega} + \sum_{s=1}^{m-1} \frac{R_s^L\left(e^{in_s\omega d_s} - 1\right) - L_s^L\left(e^{-in_s\omega d_s} - 1\right)}{i\omega n_s}, \tag{5.3.12a}$$

$$\mathcal{I}_\omega^R = \frac{1 - R_m^R - L_0^R}{i\omega} + \sum_{s=1}^{m-1} \frac{R_s^R\left(e^{in_s\omega d_s} - 1\right) - L_s^R\left(e^{-in_s\omega d_s} - 1\right)}{i\omega n_s}, \tag{5.3.12b}$$

where $d_{r-1} = x_r - x_{r-1}$ is the thickness of each dielectric layer. In general, these expressions are different for L and R photons.

5.3.6 Single disk

As a specific example we use a single dielectric disk of thickness d as shown in figure 5.1, i.e., two interfaces at $x_1 = -d/2$ and $x_2 = d/2$. For L photons we have $R_0 = 1$ and $L_m = 0$ and otherwise find

$$L_0 = -\frac{(n^2-1)\sin\delta}{(n^2+1)\sin\delta + i\,2n\cos\delta}, \tag{5.3.13a}$$

$$R_1 = \frac{-2\,(n+1)}{(n+1)^2 - (n-1)^2 e^{i2\delta}}, \tag{5.3.13b}$$

$$L_1 = \frac{-2\,(n-1)\,e^{i\,2\delta}}{(n+1)^2 - (n-1)^2 e^{i2\delta}}, \tag{5.3.13c}$$

$$R_2 = \frac{i\,2n}{(n^2+1)\sin\delta + i\,2n\cos\delta}, \tag{5.3.13d}$$

where $\delta = n\omega d$ is the phase accrued by a photon traversing the disk. The transmission coefficient is $\mathcal{T}_L = R_2$ and the reflection coefficient is $\mathcal{R}_L = L_0$.

With these explicit results it is straightforward to evaluate the L scattering amplitude. We find for the corresponding boost factor

$$\mathcal{B}_\omega^L = \frac{(n^2-1)\,\sin(\delta/2)}{n^2\sin(\delta/2) + i\,n\cos(\delta/2)}\,. \tag{5.3.14}$$

We will explore the properties of the dielectric disk more completely in section 6.1.

5.3.7 Velocity effects

To handle a non-zero velocity effect fully, one would have to include conservation of momentum in the y and z directions. In particular, the outgoing photon must inherit the axion's transverse momenta. Such an effect does not change our calculation in any significant way. However, to first approximation we can simply note that the primary velocity effects come from the change in phase of the axion as shown in section 4.3.4. Thus we can neglect the slight changes to the free photon wave function and use the same Garibian wave functions as the zero velocity limit. Thus the photon flux for an axion with velocity $\mathbf{v}$ and a frequency ω is

$$\Phi_{L,R} = \frac{\rho_a}{m_a}\left(\frac{g_{a\gamma}B_\mathrm{e}}{2}\right)^2 \left|\int_{-\infty}^{+\infty} dx\, A_\omega(x) e^{ip_x x}\right|^2 . \tag{5.3.15}$$

One can expand the axion phase, getting

$$\Phi_{L,R} = \frac{\rho_a}{m_a}\left(\frac{g_{a\gamma}B_\mathrm{e}}{2}\right)^2 \left|\int_{-\infty}^{+\infty} dx\, A_\omega(x)\left(1 + ip_x x - \frac{(p_x x)^2}{2} + ...\right)\right|^2 . \tag{5.3.16}$$

Note that if A_ω is a standing wave then A_ω has no spatial phase variation and so can be treated as real. Due to the mod squaring no linear order terms in the velocity survive as they are purely imaginary. So for any setup where A_ω is a standing wave then at most the velocity dependence occurs at quadratic order. As Garibian wave functions are simply given by reflections off of one side of the device if the system is strongly resonant, or there is a mirror on one side they will form a standing wave.

The case of linear dependence on v is particularly interesting, as it would give the most information if one was to try to build a velocity dependent device, as will be discussed in chapter 8. For a linear velocity dependence in equation (5.3.16) one can see the free photon wave function must have some traveling wave behaviour (i.e., some spatial variance of the phase). Note that traveling wave behaviour is a necessary, but insufficient, condition for a linear response to the axion velocity. We will see examples in the next chapter where the system is transparent but has a quadratic dependence on the axion velocity.

5.4 Quantum vs. classical calculation

Thus far our calculation has assumed the transition from a single axion to a single photon, whereas galactic DM axions have huge occupation numbers. If we consider an axion plane wave with occupation number N, the axion part is of the type $|N\rangle \to |N-1\rangle$, i.e., the quantized field amplitude part of the matrix element is of the form $\langle N-1|a|N\rangle = \sqrt{N}$, where a is the destruction operator. Therefore, the transition rate now picks up a factor N, i.e., it is now proportional to N/V with V the normalisation volume. In other words, we now have begun with N axions instead of 1 and the photon production rate remains proportional to the axion number density.

A given momentum mode of the axion field is highly occupied, but not necessarily in a number eigenstate. The classical calculation uses a classical axion field that would be represented by a Glauber state, i.e., a superposition of number states such that it is an eigenstate of the destruction operator, not of the number operator, and the eigenvalue would be the classical field strength in analogy to an optical laser. Therefore, the photon production rate is proportional to the square of the classical axion field strength, a quantity that is the axion number density up to normalisation factors.

In general, the axion field is in some superposition of number states of the type $\phi_{\mathbf{p}}^{N}|N,\mathbf{p}\rangle$ for all momentum modes, where $\phi_{\mathbf{p}}^{N}$ is the amplitude for finding the momentum mode $\mathbf{p}$ occupied with N quanta. Because the states $|N,\mathbf{p}\rangle$ are orthogonal, the overall rate is simply proportional to $\sum_{N,\mathbf{p}}|\phi_{\mathbf{p}}^{N}|^2$ and thus again to the total number of axions per normalisation volume.

So far we have assumed that the final-state photon state is empty before production by axions, but hypothetically it could be occupied with N_γ quanta, and the rate would acquire a stimulation factor $N_\gamma+1$. Actually there is always an ambient bath of thermal photons unless the detector works at sufficiently cryogenic conditions. However, in this case there is also a backconversion of photons to axions which is proportional to $N_\gamma(N_a+1)$ with N_a the axion occupation number. So the net rate is proportional to $N_a(N_\gamma+1)-(N_a+1)N_\gamma = N_a - N_\gamma$. In other words, the dominant part N_aN_γ cancels and one cannot achieve an increased stimulated conversion rate.

The bottom line is that, as long as we are only asking for the average photon production rate, there is no difference between a classical calculation using classical axion and photon fields and a quantum-field calculation using quantized field amplitudes. A classical field has the boson property built in, so no additional coherence or stimulation factors appear. On the other hand, if one were not only to measure the average photon production rate but also its fluctuation spectrum or time correlations, then the detailed quantum properties of the axion field would feed through to the secondary EM radiation.

5.5 Summary

As we have seen here, a quantum field calculation elegantly derives an overlap integral formalism for dielectric haloscopes, prescribing a physically meaningful interpretation of the integrated fields. We have further shown that the classical and quantum mechanical calculations are in perfect agreement, which provides an excellent grounding in which to consider some more specific cases. In general, the formulaic nature of transfer matrices will allow for efficient computation, and so will be predominantly used throughout this thesis. That being said, we will occasionally refer to this quantum calculation in order to explain some behaviours of dielectric haloscopes. For example, it is easier to understand the requirements of a linear velocity dependence or the correlation of reflectivity and boost factor in the overlap integral picture than in the transfer matrix picture.

Chapter 6

Analytic Examples

We now start approaching the crux of dielectric haloscopes: how does one achieve a large boost factor? The EM radiation emitted by a single interface can be boosted in two generic ways. One is the coherent superposition of the radiation from many surfaces, the other is by creating a resonance between two reflecting surfaces. A realistic layered haloscope takes advantage of both effects in what can be a complicated arrangement of dielectric disks. In this chapter we consider several generic examples which illustrate these effects: a single dielectric disk, a resonator or "cavity" consisting of a dielectric disk at some distance in front of a perfect mirror, and a series of equally spaced dielectric disks.

Except where otherwise specified, we will assume the zero velocity limit throughout this chapter. For the majority of examples, the basic behaviour is very accurately, and much more simply, represented by neglecting the axion velocity. However, we will also show situations in which the velocity cannot be neglected, and may dominate the boost factor. Such a situation only occurs for configurations where the physical size approaches the axion de Broglie wavelength.

6.1 Single dielectric disk

The first example will be the basic building block of a dielectric haloscope—a single dielectric disk as sketched in figure 6.1. The single disk has already been touched on during our quantum field calculation in section 5.3.6, but here we will explore the behaviour in more detail. Specifically we assume a disk of thickness d, infinite in the transverse direction, with index of refraction $n \equiv n_1 > 1$, surrounded by vacuum with $n_0 = n_2 = 1$. Here and in all following examples we assume that the external field B_e is the same in all regions. The phase accrued by an EM wave with frequency ω traversing this disk is $\delta \equiv \delta_1 = n\omega d$.

The transfer and axion source matrices defined in equation (4.3.8) are for

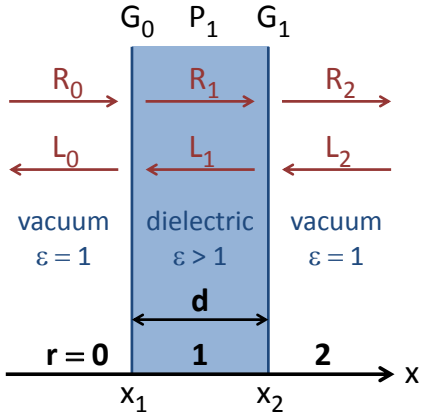

Figure 6.1: Schematic picture of a single dielectric disk.

a two-interface arrangement $\mathsf{T} = \mathsf{G}_1\mathsf{P}_1\mathsf{G}_0$ and $\mathsf{M} = \mathsf{S}_1 + \mathsf{G}_1\mathsf{P}_1\mathsf{S}_0$, respectively. Here, as in subsequent multi-disk systems, we are only dealing with a few types of interfaces, so there are significant simplifications to the notation. The matrix G_0 takes us from vacuum (v) to a dielectric (ϵ), so we may denote it as $\mathsf{G}_{\epsilon v}$, whereas G_1 does the opposite and we call it $\mathsf{G}_{v\epsilon}$. Notice that $\mathsf{G}_{v\epsilon}\mathsf{G}_{\epsilon v} = \mathbb{1}$, i.e., $\mathsf{G}_{v\epsilon} = \mathsf{G}_{\epsilon v}^{-1}$. Explicitly, we find with $n = \sqrt{\epsilon}$

$$\mathsf{G}_{\epsilon v} = \frac{1}{2n}\begin{pmatrix} n+1 & n-1 \\ n-1 & n+1 \end{pmatrix} \quad \text{and} \quad \mathsf{G}_{v\epsilon} = \frac{1}{2}\begin{pmatrix} n+1 & 1-n \\ 1-n & n+1 \end{pmatrix}, \tag{6.1.1}$$

which are indeed the inverse of each other. Likewise, the source matrix S_0 applies to an interface with vacuum on the left and a dielectric ϵ on the right, so we call it $\mathsf{S}_{\epsilon v}$ and the opposite for S_1 which we call $\mathsf{S}_{v\epsilon}$. The two matrices are related by $\mathsf{S}_{v\epsilon} = -\mathsf{S}_{\epsilon v}$ and are explicitly

$$\mathsf{S}_{\epsilon v} = \frac{1-n^2}{2n^2}\,\mathbb{1} \quad \text{and} \quad \mathsf{S}_{v\epsilon} = \frac{n^2-1}{2n^2}\,\mathbb{1}\,. \tag{6.1.2}$$

Finally, the matrix P_1 advances the phases through the dielectric disk and is generically called $\mathsf{P}_\epsilon = \mathrm{diag}(e^{+i\delta}, e^{-i\delta})$ with $\delta \equiv \delta_\epsilon = \delta_1 = n\omega d$.

Notice that the regions are labelled from left to right, but the transfer and source matrices are built up in opposite order. The matrix in the right-most position describes the left-most interface. The matrices $\mathsf{G}_{\epsilon v}$ or $\mathsf{S}_{\epsilon v}$ mean that vacuum is on the left of the dielectric. Therefore, the total transfer and axion source matrices for a dielectric disk are

$$\mathsf{T}_{\mathrm{D}} = \mathsf{G}_{v\epsilon}\mathsf{P}_\epsilon\mathsf{G}_{\epsilon v} = \begin{pmatrix} \cos\delta + i\,\frac{n^2+1}{2n}\sin\delta & i\,\frac{n^2-1}{2n}\sin\delta \\ -i\,\frac{n^2-1}{2n}\sin\delta & \cos\delta - i\,\frac{n^2+1}{2n}\sin\delta \end{pmatrix}, \tag{6.1.3a}$$

$$\mathsf{M}_{\mathrm{D}} = \mathsf{S}_{v\epsilon} + \mathsf{G}_{v\epsilon}\mathsf{P}_\epsilon\mathsf{S}_{\epsilon v} = \frac{n^2-1}{2n^2}\begin{pmatrix} 1-\frac{n+1}{2}\,e^{i\delta} & \frac{n-1}{2}\,e^{-i\delta} \\ \frac{n-1}{2}\,e^{i\delta} & 1-\frac{n+1}{2}\,e^{-i\delta} \end{pmatrix}. \tag{6.1.3b}$$

Observable quantities are the transmission and reflection coefficients as well as the boost amplitude defined in equations (4.3.10) and (4.3.11), respectively. Because the disk is perfectly left-right symmetric, the L and R quantities are the same. The explicit results are

$$\mathcal{T}_{\rm D} = \frac{i\,2n}{i\,2n\cos\delta + (n^2+1)\,\sin\delta}\,, \tag{6.1.4a}$$

$$\mathcal{R}_{\rm D} = \frac{(n^2-1)\,\sin\delta}{i\,2n\cos\delta + (n^2+1)\,\sin\delta}\,, \tag{6.1.4b}$$

$$\mathcal{B}_{\rm D} = \frac{(n^2-1)\sin(\delta/2)}{n^2\sin(\delta/2) + i\,n\cos(\delta/2)}\,. \tag{6.1.4c}$$

Their moduli are shown in figure 6.2 for several values of the refractive index n.

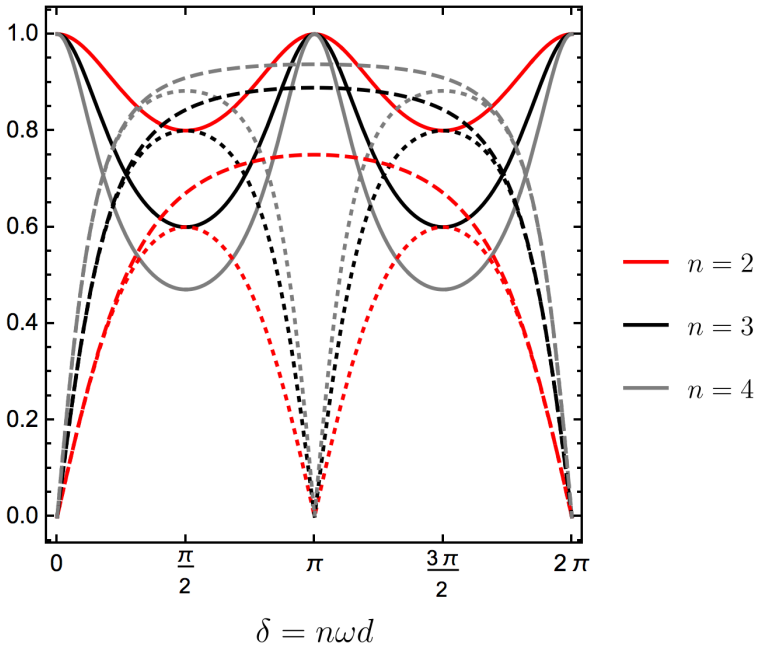

Figure 6.2: Transmission coefficient $|\mathcal{T}_{\rm D}|$ (solid), reflection coefficient $|\mathcal{R}_{\rm D}|$ (dotted), and boost factor $\beta_{\rm D} = |\mathcal{B}_{\rm D}|$ (dashed) for a dielectric disk. The refractive indices are $n = 2$, 3 and 4 (red, black and gray lines). The horizontal axis is the phase depth of the disk $\delta = n\omega d$, with d its physical thickness.

The disk becomes fully transparent ($\mathcal{T}_{\rm D} = 1$), and then does not reflect at all ($\mathcal{R}_{\rm D} = 0$), for $\sin\delta = 0$, corresponding to the frequencies

$$\omega_j = j\,\frac{\pi}{nd}\,, \quad \text{where} \quad j = 0, 1, 2, \ldots \quad \text{(transparent)}. \tag{6.1.5}$$

On the one hand, the boost factor vanishes for $\sin(\delta/2) = 0$, i.e., for even values of j in equation (6.1.5). On the other hand, it is maximal for $\sin^2(\delta/2) = 1$

and then takes the value

$$\beta_{\mathrm{D}}^{\max} = 1 - \frac{1}{n^2} \quad \text{for} \quad j = 1, 3, \ldots \quad \text{(odd)}. \tag{6.1.6}$$

We may compare this result with a single dielectric interface given in equation (4.1.7),

$$\beta_{\text{interface}} = 1 - \frac{1}{n}\,. \tag{6.1.7}$$

The maximum EM wave emerging from our disk has an amplitude enhanced by a factor $(1 + 1/n)$ relative to a single interface, caused by the constructive interference with the EM wave emitted from the second interface. In both cases, the largest emission is obtained by $n \to \infty$, corresponding to a perfect mirror.

The average squared boost factor in the spirit of equation (4.3.16) is

$$\langle |\mathcal{B}_{\mathrm{D}}|^2 \rangle = \left(1 - \frac{1}{n}\right)\left(1 - \frac{1}{n^2}\right)\,. \tag{6.1.8}$$

The average can be taken over all phase depths δ in the interval $[0, 2\pi]$ or alternatively over a flat spectrum of frequencies as explained in section 4.3.3.

Thus a single dielectric disk by itself offers no advantage compared with a mirror. It is intriguing, however, that for frequencies around maximum boost factor, the disk is completely transparent. This observation immediately suggests an arrangement of N disks spaced such that the EM waves from all disks interfere constructively, enhancing the overall amplitude by a factor of N. We will study this "transparent mode" in section 6.3.3 below.

6.2 Resonant effects: cavity setup

6.2.1 Mirror with dielectric disk

The simplest way to obtain an actual enhancement relative to a mirror is to actually use a mirror and place at some distance a dielectric disk with a thickness such that it is partially reflecting, as shown in figure 6.3. In figure 6.4 we show a schematic arrangement and its electric field distribution. Assuming a realistic dielectric constant of $\epsilon = 25$ and thus a refractive index $n = \sqrt{\epsilon} = 5$ (approximately that of LaAlO3), the emerging EM wave has an electric field boosted by a factor of around 10.

To derive the boost amplitude analytically, we need the same matrices $G_{\epsilon v}$ and $S_{\epsilon v}$ as defined in the previous section. We now write the matrix which advances the phase in the vacuum gap between mirror and disk as $\mathsf{P}_v = \mathrm{diag}(e^{+i\delta_v}, e^{-i\delta_v})$, where $\delta_v = \omega d_v$ and d_v is the physical width of the gap. For the disk we now write $\mathsf{P}_\epsilon = \mathrm{diag}(e^{+i\delta_\epsilon}, e^{-i\delta_\epsilon})$ where $\delta_\epsilon = n\omega d_\epsilon$ is the phase depth of the disk. Moreover, we need the transfer matrix for the interface from mirror to vacuum $G_{v\sigma}$ where σ symbolizes the large conductivity of the

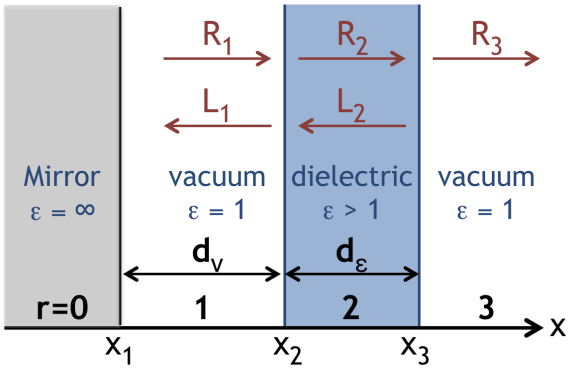

Figure 6.3: Schematic of a simple cavity consisting of a mirror and a single dielectric disk. The distances d_v and d_ϵ denote the thicknesses of the vacuum gap and dielectric disk, respectively. Note that R_0, L_0 (not shown) are both zero inside the mirror.

mirror, and we also need the source matrix $S_{v\sigma}$, which all follow from our previous expressions. Writing the compound expression, as usual from left to right, we find

$$\mathsf{T}_{\mathrm{C}} = \mathsf{G}_{v\epsilon}\mathsf{P}_{\epsilon}\mathsf{G}_{\epsilon v}\mathsf{P}_{v}\mathsf{G}_{v\sigma}\,, \tag{6.2.1a}$$

$$\mathsf{M}_{\mathrm{C}} = \mathsf{S}_{v\epsilon} + \mathsf{G}_{v\epsilon}\mathsf{P}_{\epsilon}\mathsf{S}_{\epsilon v} + \mathsf{G}_{v\epsilon}\mathsf{P}_{\epsilon}\mathsf{G}_{\epsilon v}\mathsf{P}_{v}\mathsf{S}_{v\sigma} \tag{6.2.1b}$$

for the full 1D cavity.

6.2.2 Properties of the boost amplitude

If the mirror is perfect (its refractive index is infinite), from equation (4.3.11) we then find for the boost amplitude

$$\mathcal{B}_{\mathrm{C}} = \frac{1 - \left(1 - \frac{1}{n^2}\right)\left[\cos\delta_v(1-\cos\delta_\epsilon) + n\sin\delta_\epsilon\sin\delta_v\right]}{e^{-i\delta_v}\cos\delta_\epsilon - \sin\delta_\epsilon\left(\frac{i}{n}\cos\delta_v + n\sin\delta_v\right)}\,, \tag{6.2.2}$$

which is 2π periodic in both δ_v and δ_ϵ. In figure 6.5 we show the cavity boost factor $\beta_{\mathrm{C}} = |\mathcal{B}_{\mathrm{C}}|$ as a function of δ_v and δ_ϵ. As expected, there are resonant structures for certain combinations of phase depths of the disk and vacuum gap.

As discussed earlier, we may consider β^2, averaged over all possible configurations of δ_v and δ_ϵ, or alternatively, for any fixed configuration, averaged over all frequencies, and find

$$\langle|\mathcal{B}_{\mathrm{C}}|^2\rangle = 1 + 2\left(1 - \frac{1}{n}\right)\left(1 - \frac{1}{n^2}\right)\,. \tag{6.2.3}$$

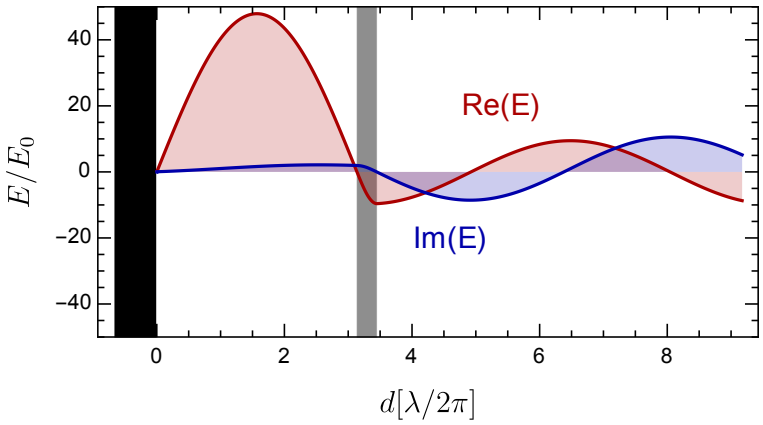

Figure 6.4: Schematic of a resonant cavity consisting of a single dielectric disk (grey) and a mirror (black), showing the real and imaginary parts of the electric field distribution (red and blue lines). For scaling purposes, we choose a realistic refractive index $n = 5$ for the disk, which is not strongly resonant (low Q). Note that the dielectric is arranged such that the distance between the mirror and dielectric is $d_v = \lambda/2$, and the thickness of the disk is $d_\epsilon = \lambda/4n$. The shown electric field amplitude is for the sum of the produced EM wave and the homogeneous axion-induced field.

This is the same as what one gets from a mirror plus two dielectric disks—the reflectivity of the mirror means that the dielectric disk must be counted twice. In other words, the emitted power, averaged over all possible values of vacuum gap and disk thickness, is the average power emitted by the mirror alone, by the outer dielectric surface alone, and by the inner dielectric surface alone, which is reflected by the mirror. As expected, in the expression for the average power, all interference terms disappear (see also appendix A).

For a fixed configuration of dielectric disk and vacuum gap, we may consider β as a function of driving frequency, which corresponds to diagonal lines in figure 6.5. The lower of these lines denoted "resonant" corresponds to $\delta_v/\delta_\epsilon = 2$, where the resonance occurs when the dielectric accommodates $\lambda/4$ of the EM wave, whereas the gap accommodates $\lambda/2$. There is a second "resonance line" where one has $\lambda/2$ in the vacuum gap, and $3\lambda/4$ within the dielectric. There is an infinite family of such resonances, corresponding to larger odd multiples of $\lambda/4$ in the dielectric. Discussion of these cases would take us too far afield and so we will neglect them. The "transparent" line corresponds to $\delta_v/\delta_\epsilon = 1$ and in the center of the plot, both the dielectric and the gap accommodate $\lambda/2$. The Area Law implies that integrating along either line gives us the same value for $\langle|\mathcal{B}|^2\rangle$ that was given in equation (6.2.3). For integrations along other lines, if taken only within the shown square of parameter space, the integral somewhat differs. For example, for lines between the "resonant" and "transparent" cases and for $n = 3$, the deviation is less then 2%. For larger n, the deviation is even smaller. The Area Law is only exact if the average is taken over a full period

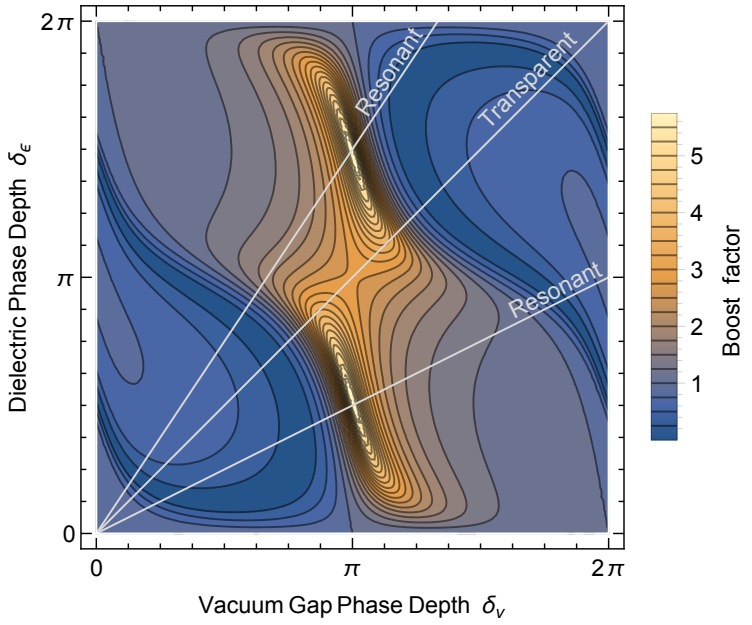

Figure 6.5: Cavity boost factor $\beta_{\mathrm{C}} = |\mathcal{B}_{\mathrm{C}}|$ of a setup consisting of a mirror and a dielectric disk as a function of the phase depths of the vacuum gap, $\delta_v = \omega d_v$, and of the dielectric disk, $\delta_\epsilon = n\omega d_\epsilon$. The refractive index is $n = 3$. For a fixed distance between mirror and disk, varying the frequency ω takes us along the diagonal lines. The "resonant" lines correspond to $\delta_\epsilon/\delta_v = n\, d_\epsilon/d_v = 1/2$ or $3/2$, whereas the "transparent" line corresponds to $\delta_v/\delta_\epsilon = 1$. These lines correspond to keeping the physical distances fixed, while scanning over frequency. Fully resonant and transparent behaviours only occur at a single point along each line in this plot.

of $|\mathcal{B}|^2$ as a function of ω.

6.2.3 Resonant mode

We briefly consider two special cases of the cavity. The most conspicuous feature of figure 6.5 is the resonance which is obtained when the phase depths are $\delta_v = \pi$ and $\delta_\epsilon = \pi/2$. There exists a frequency $\omega_{\mathrm{R}} = \pi/(2n\, d_\epsilon) = \omega_\epsilon/2$, where the cavity is on resonance, corresponding to $\lambda/4$ in the dielectric and $\lambda/2$ in the vacuum gap (ω_ϵ will correspond to the transparent mode). The resonant enhancement of the output amplitude is

$$\beta_{\mathrm{C}}^{\max} = 2n - \frac{1}{n}\,. \tag{6.2.4}$$

For the resonant setup we define the boost amplitude as a function of frequency as

$$\mathcal{B}_{\mathrm{R}}(n,\omega) = \mathcal{B}_{\mathrm{C}}\left(n, \pi\,\frac{\omega}{\omega_{\mathrm{R}}}, \frac{\pi}{2}\,\frac{\omega}{\omega_{\mathrm{R}}}\right)\,. \tag{6.2.5}$$

In figure 6.6 we show its real and imaginary parts as functions of ω. As anticipated, $\mathcal{B}_{\mathrm{R}}$ shows a resonance structure at $\omega = \omega_{\mathrm{R}}$ and odd multiples. Near resonance, the boost amplitude should correspond to the response of a driven lossy harmonic oscillator, so we expect a structure of the form $\mathcal{B}_{\mathrm{R}} \propto (\omega - \omega_{\mathrm{R}} + i\Gamma/2)^{-1}$.

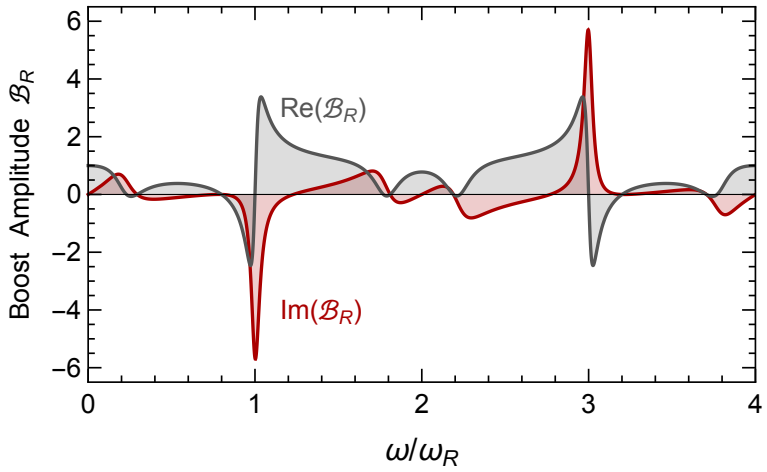

Figure 6.6: Boost amplitude $\mathcal{B}_{\mathrm{R}}$ for a cavity consisting of a mirror and a dielectric disk where $d_v = 2nd_\epsilon$ and $\omega_{\mathrm{R}}^{-1} = 2nd_\epsilon/\pi$, which forms a resonance. The real part is in gray and imaginary part is in red. The dielectric disk was chosen to have $n = 3$. For larger n, the resonance structure becomes more pronounced.

In our resonator the damping arises not from friction, but because power escapes through the disk which is an imperfect mirror. In the good-cavity-limit, $n \gg 1$, the left and right moving waves inside the cavity have to be of similar amplitude and related to the outgoing wave by the transmission coefficient $|\mathcal{T}| \sim 2/n$ of one dielectric disk (6.1.4a) at $\delta_\epsilon \sim \pi/2$. The power stored in the cavity is proportional to the squared electric-field amplitude inside, the power in the emitted wave outside proportional to the squared outside electric field strength. The ratio of the field amplitudes is $|\mathcal{T}|$ and therefore the ratio of the energy density $|\mathcal{T}|^2$. Therefore, the ratio of stored power to escaping power is $|\mathcal{T}|^{-2} \sim n^2$, thus we expect the quality factor Q of the resonator to be $Q \sim n^2$.

To find the near-resonant $\mathcal{B}_{\mathrm{R}}$ explicitly we start from equation (6.2.2) and substitute $\delta_v = (1+s)\,\pi$ and $\delta_\epsilon = (1+s)\,\pi/2$, where $s = (\omega - \omega_{\mathrm{R}})/\omega_{\mathrm{R}}$. Next we expand the numerator and denominator separately as a Taylor expansion in s to linear order and find

$$\mathcal{B}_{\mathrm{R}} = \frac{\left(2n - \frac{1}{n}\right) + \left(1 + \frac{1}{2n} - \frac{1}{n^2} - \frac{1}{2n^3}\right) n^2\pi s}{i + \left(1 + \frac{1}{2n}\right) n^2\pi s} \to \frac{2n + n^2\pi s}{i + n^2\pi s}\,, \tag{6.2.6}$$

where the second expression pertains to large n. This an excellent approximation when $n^2\pi s \lesssim 1$. The linear term in the numerator explains the slightly

skewed response around the resonance. Indeed, the maximum of $\beta_{\rm R}$ is slightly shifted relative to the nominal resonance point. For $n \gg 1$ the boost amplitude becomes

$$\mathcal{B}_{\rm R}(n\gg 1) = 1 + 2n\,\frac{\Gamma/2}{\omega - \omega_{\rm R} + i\Gamma/2} \quad \text{where} \quad \Gamma = \frac{2\,\omega_{\rm R}}{\pi n^2}\,. \tag{6.2.7}$$

The quality factor corresponds to the power damping rate as $\Gamma = \omega_{\rm R}/Q$, so our resonator has effectively $Q = \pi n^2/2$.

The cavity boost amplitude as a function of frequency shown in figure 6.6 has the squared average value given in equation (6.2.3). Using a large value of n does not enhance the power emission averaged over all frequencies, but concentrates it near the resonance. The height of resonance peak of $\beta_{\rm R}^2$ scales with n^2, its width with $1/n^2$.

In principle, one can obtain an arbitrarily large boost factor. In practice, the available dielectrics with small absorption (small loss tangent $\tan\delta$) have moderate indices of refraction, $n \sim 3$ (sapphire) and $n \sim 5$ (LaAlO3), so one would be forced to replace the dielectric with another mirror and extract a small amount of power through an antenna or a hole, tuning the frequency with the distance between the mirrors. Such an arrangement would be analogous to Sikivie's haloscope, used in the ADMX, ADMX-HF and CAPP experiments, and in the Orpheus project.

Velocity effects in resonators

One might wonder whether velocity effects can be enhanced by multiple reflections forming a resonance. The simplest way to explore the velocity effects is to write down the full version of the cavity boost amplitude. Note that a resonance will occur for a vacuum gap with a phase depth any odd multiple of π. To show the effect of increasing the size of the device, here we will loosen our requirement that $\delta_v = \pi$ to $\delta_v = (2m-1)\pi$, where m is an integer. The resulting boost amplitude is given by

$$\mathcal{B}_{{\rm C},m} = n\left(e^{\frac{i\pi v}{2n}} + e^{\frac{i\pi v[1+2n(2m-1)]}{2n}}\right) - \frac{ie^{\frac{i\pi v}{2n}}}{n} - v\left(1 - \frac{1}{n^2}\right). \tag{6.2.8}$$

There are two instructive limits of this equation: a strongly resonant setup and a physically large setup (i.e., large m).

Let us first check the strongly resonant limit of this equation. The resonance will give a sharp, high boost factor peak when the disk is as reflective as possible, i.e., when n is large. Expanding equation (6.2.8), taking the lowest order terms in mv and assuming that $n \gg 1$ we get

$$\beta_{{\rm C},m} = |\mathcal{B}_{\rm C}| \sim n\left[2 - \left(\frac{v\pi[2m-1]}{2}\right)^2\right]. \tag{6.2.9}$$

Thus enhancing the resonant conditions (by increasing n) does not change the proportional importance of velocity effects. Hence we do not expect that resonant setups will be more prone to velocity effects than non-resonant setups, such as those discussed below. Note that here we have assumed that the resonance width is much larger than the axion line width, as is expected for dielectric haloscopes for practical reasons.

On the other hand, if the device is made large by increasing the spacing between the disk and the mirror, the velocity dependent terms can dominate β_{C}. Notice that the dependence on the size of the device (given by m) enters as the phase in a complex exponential in equation (6.2.8). A similar setup was proposed in reference [192] to gain a directional sensitivity to the axion velocity. While in principle the axion velocity could enter at linear order, this does not occur due to a $\pi/2$ phase shift between the linear order v terms and the v independent terms in $\mathcal{B}_{\mathrm{C},m}$.

If the phase change of the axion is an appreciable fraction of 2π, i.e., the device is a large fraction of the de Broglie wavelength, velocity effects will be significant. In figure 6.7 we plot the boost factor against m, with the number of half wavelengths in the device given by $2m-1$. From figure 6.7 we see that these effects reach the 10% level at a scale that roughly corresponds to 15% of the de Broglie wavelength (2.2.1). Here we have assumed that $n = 5$, however this result does not depend strongly on the exact choice of n. Of course, large

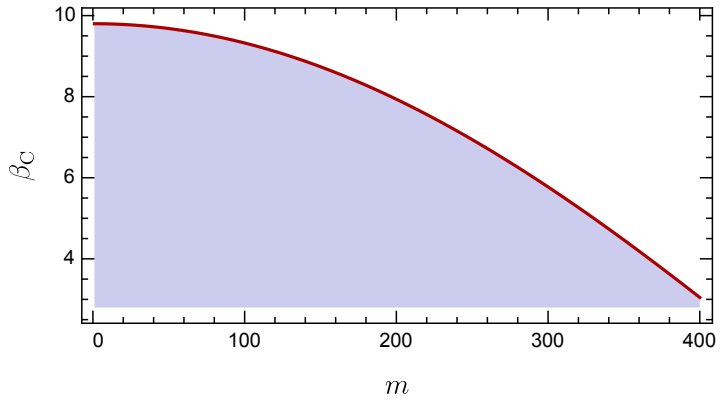

Figure 6.7: β_{C} as a function of m for a resonant cavity consisting of a mirror and a single dielectric disk of optical thickness $\pi/2$ and refractive index $n = 5$, with $2m-1$ half wavelengths between the mirror and reflective disk. Here we have used $v = 10^{-3}$; if $v = 0$ then β_{C} would be constant as we assume lossless materials.

m is not a particularly practical limit: one would never actually choose to place the disk hundreds of wavelengths away from the mirror. The losses caused by diffraction, and the narrowing of the boost factor bandwidth that accompanies higher order modes would make such an experiment very inefficient. However,

one could ameliorate the losses due to diffraction by enclosing the experiment in a metallic cavity.

6.2.4 Transparent mode

Another special case that will be of interest for our general approach is when $\delta_\epsilon = \pi$ or an odd multiple. Now the disk becomes transparent and $\mathcal{B}_\mathrm{C}$ becomes the simple sum of three waves, one emitted from the mirror and transmitted, one emitted directly from the disk outward, and the last one emitted from the disk toward the mirror, reflected, and transmitted outward, leading to a boost factor

$$\beta_\mathrm{C}(\delta_\epsilon = \pi) = \left| 1 - \left(1 - \frac{1}{n^2}\right) 2\cos\delta_v \right|. \tag{6.2.10}$$

For a gap between disk and mirror such that $\delta_v = \pi$ or an odd multiple, this is $1+2(1-1/n^2)$ and thus what one expects from a coherent superposition of the emission from a perfect mirror and twice the emission from a dielectric disk given in equation (6.1.6). For $n \to \infty$, the maximum boost factor becomes 3. Notice, however, that in this limit the disk must become infinitely thin to maintain $\delta_\epsilon = \pi$, so this is a somewhat unphysical limiting case.

We show the cavity boost amplitude $\mathcal{B}_\mathrm{T}(\omega)$ in transparent mode in figure 6.8. It is evident that it has the structure of two overlapping resonances which, for moderate n, produce a nearly box-shaped boost factor as a function of frequency. This general shape can be gleaned as well from the way the "transparent" diagonal line cuts through the resonance in figure 6.5.

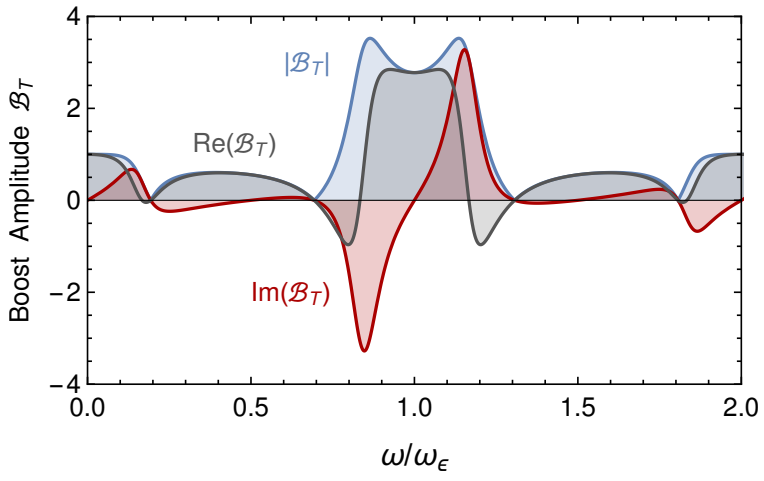

Figure 6.8: Boost amplitude $\mathcal{B}_\mathrm{T}$ for a cavity in transparent mode where $d_v = 2nd_\epsilon$ and $\omega_\mathrm{ffl}^{-1} = nd_\epsilon/\pi$. Real part in gray, imaginary part in red, and absolute value (boost factor) in light blue. The dielectric disk was chosen to have $n = 3$. For larger n, the two-peak structure becomes more pronounced.

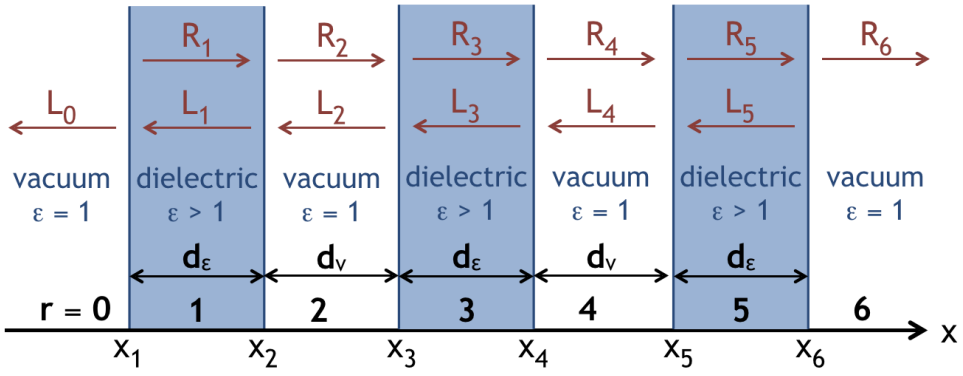

Figure 6.9: Schematic of a simple dielectric haloscope consisting of three dielectric disks, each with refractive index $n = \sqrt{\epsilon}$. The distances $d_{\rm v}$ and d_ϵ denote the thicknesses of the vacuum gaps and dielectric disks, respectively.

6.3 Equally-spaced disks

6.3.1 General homogeneous setup

An alternative approach to boost the outgoing waves is to use multiple dielectric layers. As a first simple case we consider a sequence of N equally sized, equally spaced dielectrics with index of refraction n and thickness d_ϵ (phase depth $\delta_\epsilon = n\omega d_\epsilon$). A three disk schematic is provided in figure 6.9. In terms of the transfer matrices used earlier, we now have a sequence of layers (from left to right) consisting of a disk plus a vacuum gap, i.e., each such layer has the transfer matrix $\mathsf{G}_{v\epsilon}\mathsf{P}_\epsilon\mathsf{G}_{\epsilon v}\mathsf{P}_v$, iterated N times, and un-doing one surplus vacuum gap at the end. We then have

$$\mathsf{T} = (\mathsf{G}_{v\epsilon}\mathsf{P}_\epsilon\mathsf{G}_{\epsilon v}\mathsf{P}_v)^N\,\mathsf{P}_v^{-1} = (\mathsf{T}_{\rm D}\mathsf{P}_v)^N\,\mathsf{P}_v^{-1}, \tag{6.3.1a}$$

$$\begin{aligned}\mathsf{M} &= (\mathsf{S}_{v\epsilon} + \mathsf{G}_{v\epsilon}\mathsf{P}_\epsilon\mathsf{S}_{\epsilon v}) + (\mathsf{G}_{v\epsilon}\mathsf{P}_\epsilon\mathsf{G}_{\epsilon v}\mathsf{P}_v\mathsf{S}_{v\epsilon} + \mathsf{G}_{v\epsilon}\mathsf{P}_\epsilon\mathsf{G}_{\epsilon v}\mathsf{P}_v\mathsf{G}_{v\epsilon}\mathsf{P}_\epsilon\mathsf{S}_{\epsilon v}) + \dots \\ &= (\mathsf{S}_{v\epsilon} + \mathsf{G}_{v\epsilon}\mathsf{P}_\epsilon\mathsf{S}_{\epsilon v}) + \mathsf{G}_{v\epsilon}\mathsf{P}_\epsilon\mathsf{G}_{\epsilon v}\mathsf{P}_v\,(\mathsf{S}_{v\epsilon} + \mathsf{G}_{v\epsilon}\mathsf{P}_\epsilon\mathsf{S}_{\epsilon v}) + \dots \\ &= \mathsf{M}_{\rm D} + \mathsf{T}_{\rm D}\mathsf{P}_v\mathsf{M}_{\rm D} + \mathsf{T}_{\rm D}\mathsf{P}_v\mathsf{T}_{\rm D}\mathsf{P}_v\mathsf{M}_{\rm D} + \dots \\ &= \left(\sum_{s=0}^{N-1}(\mathsf{T}_{\rm D}\mathsf{P}_v)^s\right)\mathsf{M}_{\rm D},\end{aligned} \tag{6.3.1b}$$

where from equations (6.1.3a) and (6.1.3b) we have recognised the transfer ($\mathsf{T}_{\rm D} = \mathsf{G}_{v\epsilon}\mathsf{P}_\epsilon\mathsf{G}_{\epsilon v}$) and source matrix ($\mathsf{M}_{\rm D} = \mathsf{S}_{v\epsilon} + \mathsf{G}_{v\epsilon}\mathsf{P}_\epsilon\mathsf{S}_{\epsilon v}$) of a single dielectric disk. As this system is governed by two parameters δ_ϵ and δ_v, in principle one can study the full parameter space. Moreover, one can derive an analytic solution for the boost amplitude as a function of N, n, δ_ϵ and δ_v because the matrix powers which appear in equation (6.3.1) can be solved explicitly in a basis where these matrices are diagonal. However, the resulting expressions for matrices are too complicated to be illuminating even for small N.

For a numerical example we consider $N = 3$ disks with refractive index $n = 3$ where we show the boost factor in the left panel of figure 6.10 . Near $\delta_\epsilon \sim \pi/2$ and $\delta_v \sim \pi$ and appropriate multiples there is a resonant enhancement of β over the simple sum of the emitted waves, similar to the resonator studied earlier. (Another numerical example for the boost factor in the case of $N = 5$ disks with refractive index $n = 3$ is shown in the left panel of figure 6.11.) For the now-familiar squared average, we find

$$\langle |\mathcal{B}_{\mathrm{R}}|^2 \rangle = N \left(1 - \frac{1}{n}\right) \left(1 - \frac{1}{n^2}\right) , \tag{6.3.2}$$

which is N times of what we get from a single disk as given in equation (6.1.8).

6.3.2 Resonant mode

For realistic refractive indices in the range $n = 3$–5, the overall resonance arises from the strongly coupled "cavities" formed by every neighboring pair of disks. One might expect there to be a large number of resonances. However, in a plot for $|\mathcal{B}|$ like the left panel of figure 6.10 for any N there is only one dominant resonance, except of course for repeating structures as periodic multiples of the phase depths.

More insight is gained from the transparency of the system which we show in the right panel of figure 6.10. Here we do see multiple regions of transparency. The lower diagonal line corresponds to $\delta_\epsilon = \delta_v/2$ and in particular, for $\delta_\epsilon = \pi/2$ and $\delta_v = \pi$, it corresponds to the naive resonance condition where each dielectric layer accommodates $\lambda/4$ of the EM wave, whereas each vacuum gap accommodates $\lambda/2$. For a fixed arrangement of the haloscope, and scanning over frequencies ω, we scan along such lines. Near the naive resonance point, the transparency indeed shows several "resonances" in the form of perfect transparency $|\mathcal{T}| = 1$, whereas the boost factor shows only one dominant peak. Notice also that the boost resonance does not occur at the naively expected point of $\delta_v = \pi$ and $\delta_\epsilon = \pi/2$ but somewhat displaced. This can be understood by analogy with a series of $N - 1$ identical coupled cavities. By diagonalising the Hamiltonian one sees that the couplings induce a splitting of the resonant frequency into $N - 1$ modes, as seen in figure 6.12. The axion itself couples most strongly to the mode in which the E-fields in each cavity are aligned, leading to a dominant resonant peak in β. Further, when the number of disks are odd, for half the modes the integral of the E-fields vanishes leading to $\beta = 0$.

Adding more disks makes the resonance of the boost factor more pronounced, but there remains only one dominant resonance as mentioned above. We show an example with $N = 5$ in figure 6.11. The transmission factor, on the other hand, shows more resonances. Scanning along the white line in figure 6.11 as a function of frequency, the highest-ω transmission resonance corresponds to the one boost resonance. This correlation suggests a practical

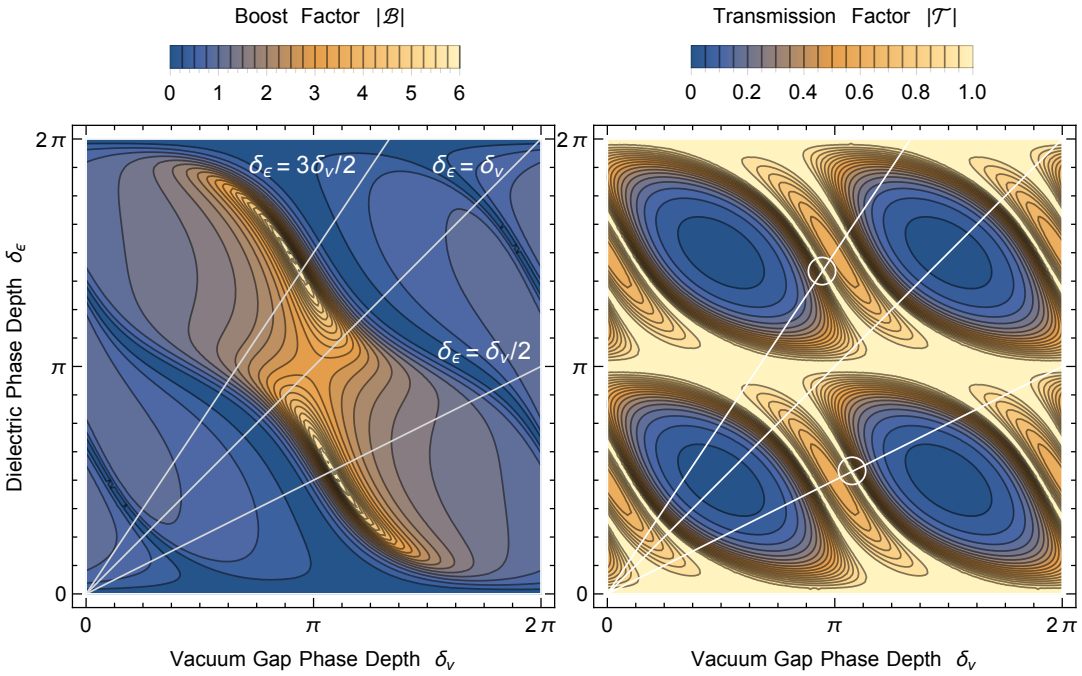

Figure 6.10: $N = 3$ equally spaced dielectric disks with refractive index $n = 3$. *Left:* Boost factor $\beta = |\mathcal{B}|$ as a function of the phase depth of the dielectric layers $\delta_\epsilon = n\omega d_\epsilon$ and of the vacuum gaps $\delta_v = \omega d_v$, with d_ϵ the thickness of the disks and d_v the disk spacing. The diagonal lines show the locus of the indicated values for δ_ϵ/δ_v. *Right:* Transmission factor $|\mathcal{T}|$. The resonant peak of the boost factor in the left panel is marked with a white circle in the right panel.

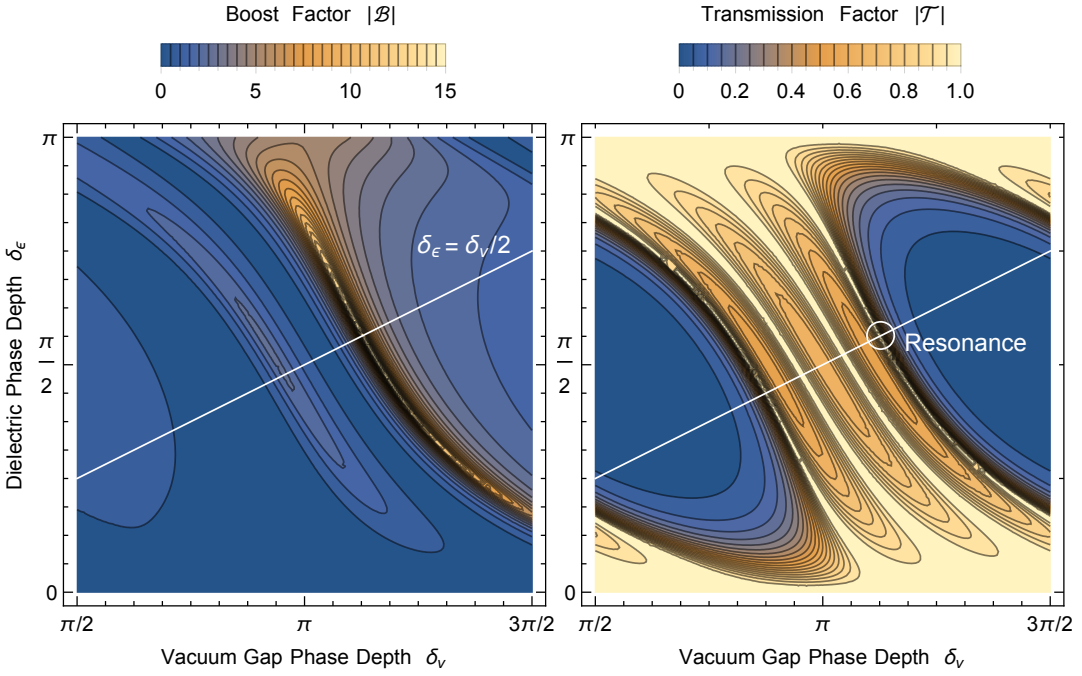

Figure 6.11: $N = 5$ equally spaced dielectric disks with refractive index $n = 3$, analogous to figure 6.10.

way to identify the resonance frequency by a transparency measurement. For different setups, there usually remains a correlation between $\mathcal{R}$, $\mathcal{T}$ and $\mathcal{B}$.

In figure 6.12 we show the same effect for $N = 11$ disks and a larger refractive index $n = 5$. Even for these moderate parameters, the boost factor on its resonance reaches around 111 and thus exceeds our nominal benchmark value of 100. For these parameters, the full width at half maximum (FWHM) of the $|\mathcal{B}|^2$ resonance is 0.7×10^{-3}, so if $\nu_0 = \omega_0/2\pi$ is 25 GHz, then the FWHM is around 18 MHz, so $\beta \sim 100$ is reached for only a very narrow range. The integrated $|\mathcal{B}|^2$ scales with N, whereas the peak of $|\mathcal{B}|^2$ scales with N^4 and its width with N^{-3} to satisfy the Area Law. So increasing N further, while quickly increasing the peak signal, very quickly makes it exceedingly narrow, in practice probably too narrow for a controlled and stable operation.

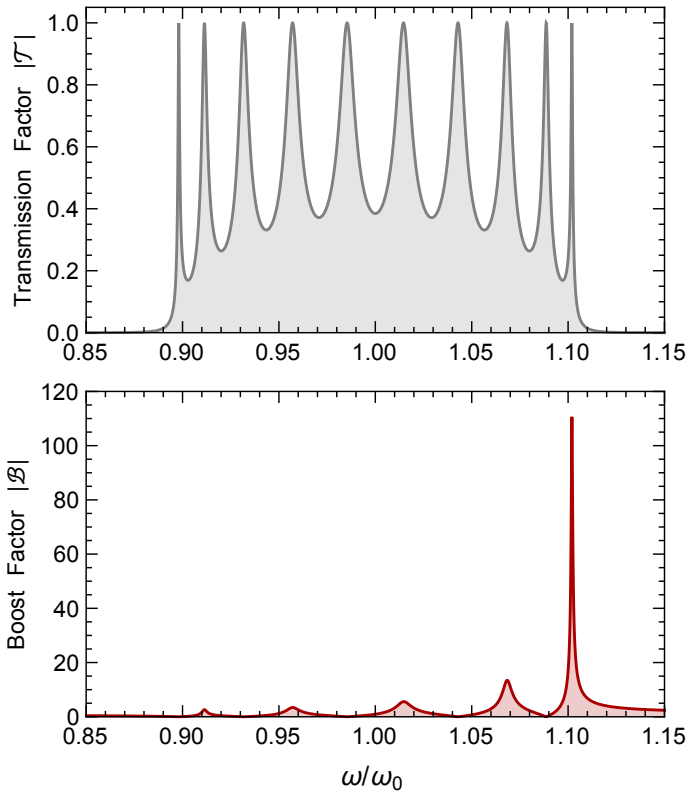

Figure 6.12: $N = 11$ equally spaced disks with refractive index $n = 5$. The phase depths are arranged as $\delta_\epsilon/\delta_v = 1/2$, the base frequency ω_0 corresponds to $\lambda/4$ in the dielectric. *Top:* Transmission factor. *Bottom:* Boost factor.

6.3.3 Transparent mode

To avoid very narrow resonances and yet get a large boost, we now consider the opposite extreme where the response functions for a given number of plates are very broad. In particular, we consider the homogeneous haloscope adjusted such that the distance between disks is $d_v = nd_\epsilon$, implying that the phase

depths are the same, $\delta_v = \omega d_v = \delta_\epsilon = n\omega d_\epsilon$, the transparent setup [152]. For the frequency $\omega_0 = \pi/d_v = \pi/(nd_\epsilon)$ both the dielectric layers and the vacuum gaps each accommodate $\lambda/2$ of the EM wave. In this case, all the dielectrics emit EM waves whose amplitude is given by the boost factor β_{D} given by equation (6.1.6). The phase depth of every gap and every disk is π, so the phase accrued by propagation through a vacuum gap plus the next disk is 2π and so all these amplitudes add up coherently, leading to a combined boost factor of

$$\beta_{\mathrm{T}} = N\beta_{\mathrm{D}} = N\left(1 - \frac{1}{n^2}\right) . \tag{6.3.3}$$

We show the electric field distribution for a four-disk example in figure 6.13.

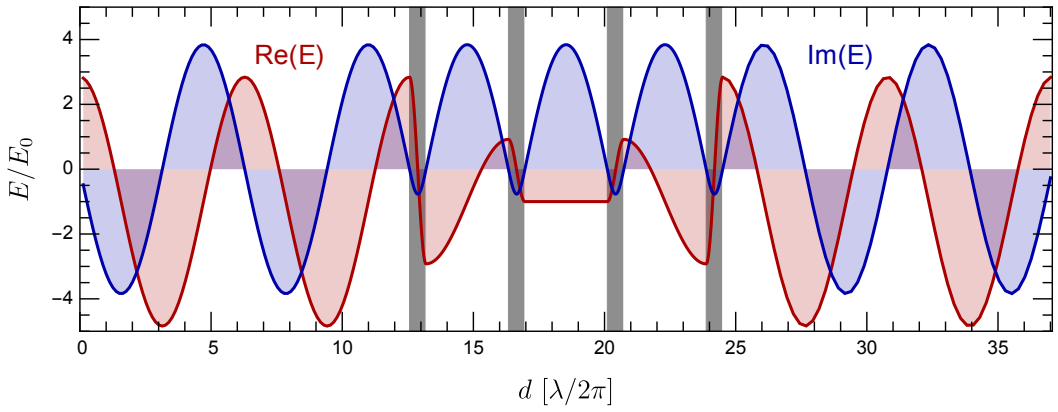

Figure 6.13: Schematic of four dielectric layers (refractive index $n = 5$) with thickness $d_\epsilon = \lambda/2n$ and separated by $d_v = \lambda/2$, i.e., in transparent mode. The red (blue) line shows the real (imaginary) electric field distribution, including left and right moving waves, as well as the axion induced electric field. Note the real and imaginary parts of the E-field outside of the system are not quite π out of phase (as one would expect for regular EM waves) because we show the coherent sum of the EM wave and the axion-induced E-field.

For frequencies de-tuned from full transparency by a small amount $\omega = \omega_0(1+s)$ with $|s| \ll 1$, after passing a disk plus a gap, the EM wave accrues an extra phase $2\pi s$, and after N disks and gaps this amounts to $2\pi sN$, leading to fully destructive interference if $s = 1/(2N)$. Therefore, we expect $\Delta\omega \sim \omega_0/N$ for the frequency range over which the boost factor is strongly enhanced. The emitted power scales as $\beta^2 \propto N^2$, meaning that the ratio of the power to the bandwidth increases linearly with N. This behaviour is in stark contrast to increasing the quality factor Q in a resonator, where $P \propto Q$ and the bandwidth $\propto Q^{-1}$. The difference to a resonant cavity is also underscored by the E-field distribution throughout the system shown in figure 6.13 as compared to that in a resonator that was shown in figure 6.4. Unlike a cavity, the E-field inside and outside the system is here of similar magnitude and indeed larger outside.

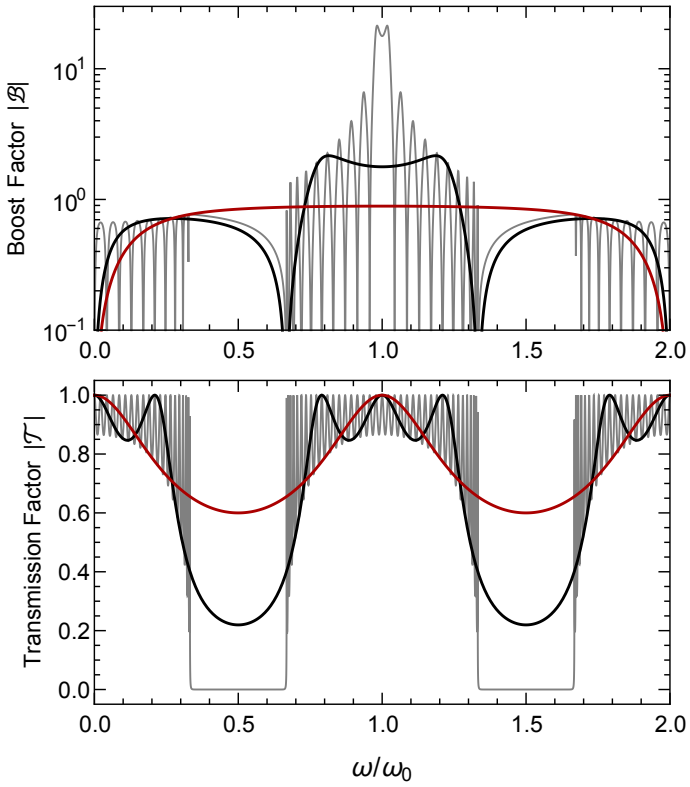

Figure 6.14: Boost factor $|\mathcal{B}|$ (top) and transmission factor $|\mathcal{T}|$ (bottom) for sets of $N = 1,\ 2,\ 20$ (red, black, gray) dielectrics ($n = 3$). The disks have thickness $d_\epsilon = \pi/n\omega_0$ separated by vacuum gaps $d_v = \pi/\omega_0$, i.e., for $\omega = \omega_0$ we have the transparent mode.

For frequencies other than ω_0 we can use the the full expressions for T and M to obtain the response of the haloscope. In figure 6.14 we show the boost factor (top) and transmission coefficient $\mathcal{T}$ (bottom) of a homogeneous setup with $N = 1,\ 2$ and 20 dielectric layers ($n = 3$). We observe that indeed the central peak of the boost factor becomes larger and narrower as N increases.

To see this scaling more explicitly we show in figure 6.15 the real and imaginary parts of $\mathcal{B}/N$ as a function of $N(\omega-\omega_0)/\omega_0$. The central peak of the scaled boost factor as a function of ω for two disks is quite similar to that for twenty disks, i.e., it is a nearly universal function. At the edge of the central peak, the boost amplitude is dominated by the imaginary part, i.e., the emerging EM wave is strongly phase shifted relative to the primary axion field. However, it is the real part of $\mathcal{B}$ which dominates over most of the frequency range. The boost factor is almost box-shaped as a function of frequency. Its frequency average was given in equation (6.3.2) for any homogeneous haloscope.

Adding more disks concentrates the response around $\omega = \omega_0$, corresponding to our earlier discussion that the height of the central peak increases with N, whereas its width decreases with $1/N$. Likewise, increasing the refractive index narrows the boost profile and enhances it. At the same time, the dips in the

transmission and boost factors get more pronounced. The central depression of the boost factor has a value given by equation (6.3.3) and does not change much with increasing n. However, the height of the two bumps increases, so the profile loses its box shape for larger n.

One may wonder if the boost factor can be empirically determined or experimentally confirmed once the haloscope has been set up. We could test the response by measuring the transmission as a function of frequency. However, for ω around ω_0 the layered dielectrics are essentially transparent, with small dips as function of frequency, covering a broad ω range as seen in figure 6.14. Increasing N increases the number of dips, but on the frequency range where the boost factor is large, the transmission factor also becomes a universal function as shown in figure 6.16. Therefore, measuring the transmission locally does not reveal the frequency ω_0 to which the boost factor has been tuned. Thinking about it from the overlap integral formalism point of view, as there are many frequencies for which the system is transparent, measuring only one of them does not give enough information to determine the free photon wave function. This situation is very different in the resonant case as discussed in the previous section.

A very recent proposal is actually considering using the transparent mode in a dielectric haloscope operating at the optical range (tentatively named LAMPOST) [193]. At such high frequencies it is easier to construct many sets of dielectric layers to scan across parameter space.

Velocity effects with many disks

As we add more and more disks, the length of the device may approach the axion de Broglie wavelength. Thus for many disks velocity effects may not be neglected. The transparent mode provides an nice example to see velocity dependence analytically. For large numbers of disks the boost factor for N disks in the transparent mode is no longer simply N times the boost factor of a single disk. The result still is given by a sum of boost factors but we must also account for the change in the phase of the axion at each interface. Note that both the right and the left side of each interface must be summed over, giving two sums

$$\begin{aligned}\mathcal{B}_{\mathrm{T}} &= (1-v)\left(1-\frac{1}{n^2}\right)\left[\sum_{j=1}^{N} e^{\frac{i\pi vj}{n}+(j-1)i\pi v} - \sum_{j=1}^{N-1} e^{\frac{i\pi vj}{n}+i\pi vj}\right] \\ &= N\frac{1-v}{2}\left(1-\frac{1}{n^2}\right)\frac{\left(1+e^{\frac{i\pi v}{n}}\right)\left(e^{\frac{i(1+n)N\pi v}{n}}-1\right)}{e^{\frac{i(1+n)\pi v}{n}}-1}. \qquad (6.3.4)\end{aligned}$$

Similar to the cavity case, as velocity effects come in from a phase enhanced now by a factor of N for large numbers of disks, corresponding to a physically large device, they will govern $\mathcal{B}_{\mathrm{T}}$. As N can be arbitrarily high in principle, to see the full behaviour we must in principle keep all orders of Nv. However, a

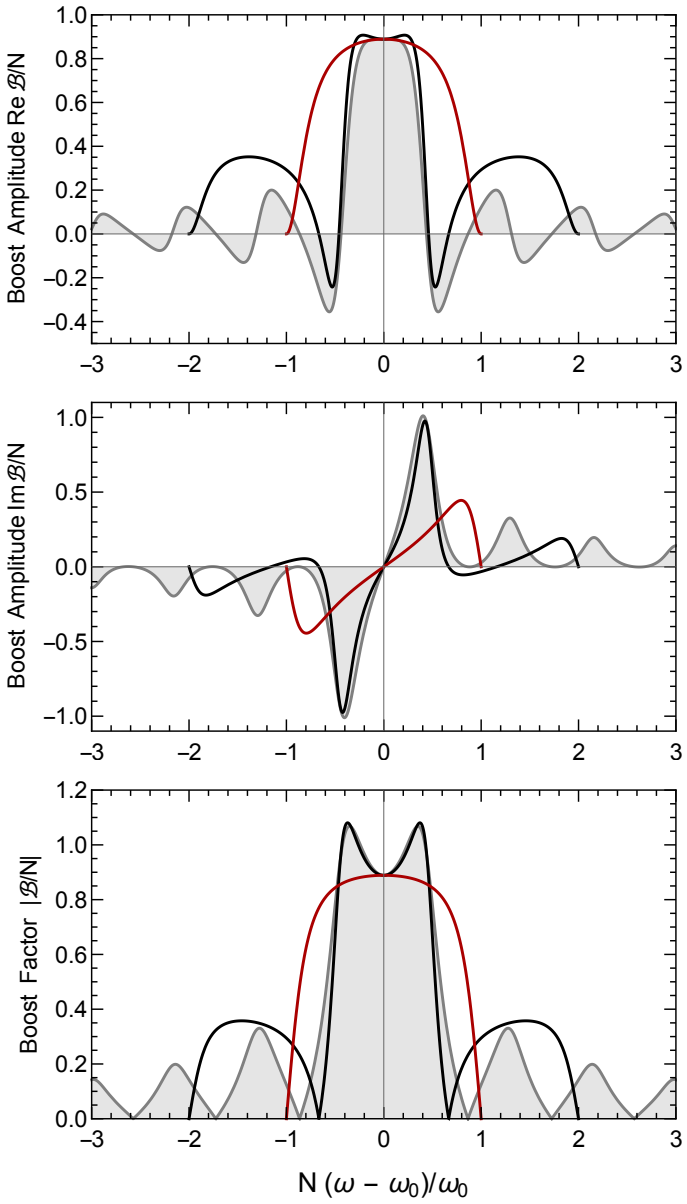

Figure 6.15: Boost amplitude (real and imaginary part) and boost factor for sets of $N = 1$, 2, 20 (red, black, gray) dielectrics as in figure 6.14. Amplitude scaled with $1/N$, frequency with N, so that the central peaks have similar size for all N values.

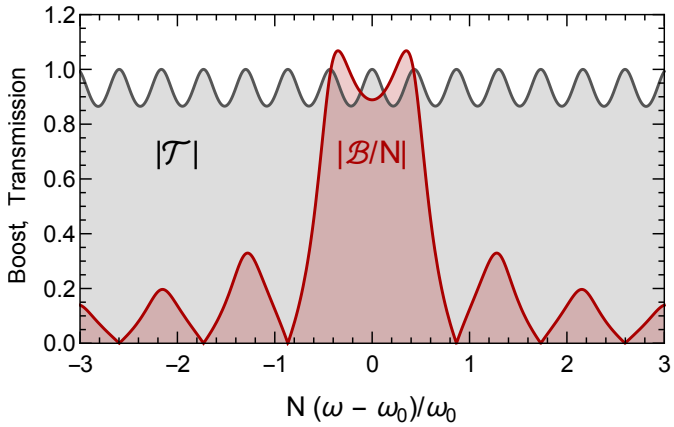

Figure 6.16: Scaled boost factor and transmission coefficient for large N.

series expansion can help us see at what N velocity effects become important. The most relevant terms at large N are

$$\beta_{\rm T}/N \sim 1 - \frac{N^2\pi^2 v^2}{12}\,. \tag{6.3.5}$$

It is clear that when N is large the velocity dependent terms will dominate, entering at quadratic order. Again, there are no linear order terms in $\beta_{\rm T}$ due to a relative phase between the relevant linear order velocity term and the velocity independent terms. To see when velocity effects become important we plot $\beta_{\rm T}$ in figure 6.17, using dielectric disks with $n = 5$. While the exact point these effects enter at occurs depends weakly on n, for $v = 10^{-3}$ velocity effects reach the 10% level for $N \gtrsim 400$. This number of disks roughly corresponds to a linear distance $L = (N-1)\lambda/2 + N\lambda/2n$ of 20% of the axion de Broglie wavelength.

Note that the transparent mode is an example of a broadband frequency response: in general one is also interested in the behaviour of frequencies adjacent to ω_0. By looking at the adjacent frequencies, as depicted in figure 6.18, we see that some frequencies are more prone to velocity effects than others. For 80 disks, which we will consider in a practical example in chapter 7, we see that velocity effects are only on the percent level. Going up to 200 disks (also considered in chapter 7) we start to see an effect, with 400 disks showing $\mathcal{O}(10\%)$ deviation from the $v = 0$ case. At 800 disks there is an $\mathcal{O}(1)$ change to β. However, these changes are not uniform: for example for 800 disks there are frequencies that go from $\beta \sim 0$ to $\beta \sim 800$, and others that exhibit almost no change. The differing response to the axion velocity at different frequencies is due to the relative phase structure of the velocity independent and dependent terms. As there is still a high degree of symmetry to the system the velocity effects show a periodic variation of maximal constructive/destructive interference.

While it appears that the primary velocity dependence is coming from adding disks, this is misleading. Note that the exponentiated factors of N

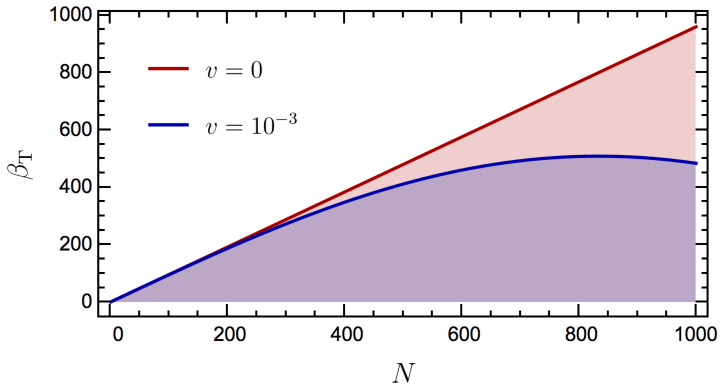

Figure 6.17: Boost factor $\beta_T(N)$ for a setup consisting of N transparent (optical thickness π) dielectric disks of refractive index $n = 5$ equally spaced with an optical thickness π between each disk. The blue curve corresponds to $v = 10^{-3}$, the red to $v = 0$.

come solely from the change of phase of the axion over the haloscope. One can see the same effects by simply increasing the spacing between the disks, as in section 6.2. As shown in figure 6.19 the same fractional deviation from the zero velocity limit occurs for 100 disks with 3π phase shifts as for 300 disks with π phase shift (though the latter will achieve a higher boost factor as it uses more disks). Note that increasing the spacing of the disks also results in a narrowing of the boost factor peak, though also allows new structures to exist (i.e., at $\omega = \omega_0/3$). So again we see that the primary influence comes simply from the size of the de Broglie wavelength of the axion when compared to the physical size of the dielectric haloscope. Velocity effects will be a significant hurdle for Phase II of LAMPOST, which aims to use 1000 alternating layers of dielectric material [193], and will thus be extremely sensitive to the (unknown) axion velocity distribution. The quadratic dependence of the velocity in β is somewhat disappointing, as one would hope from section 5.3.7 that with such strong traveling wave behaviour we would get a linear dependence on the axion velocity. The quadratic dependence is caused by the system being simply too symmetric at the transparent frequency. Instead, we can imagine placing each disk slightly out of phase with respect to the $v_x = 0$ case. Then a velocity in one direction will increase the constructive interference and a velocity in the other decease it, giving us a discrimination between the two directions. In figure 6.20 we show an example using 800 disks, demonstrating significant variation between the positive and negative directions. With such a setup we get a strong, and at lowest order linear, velocity dependence.

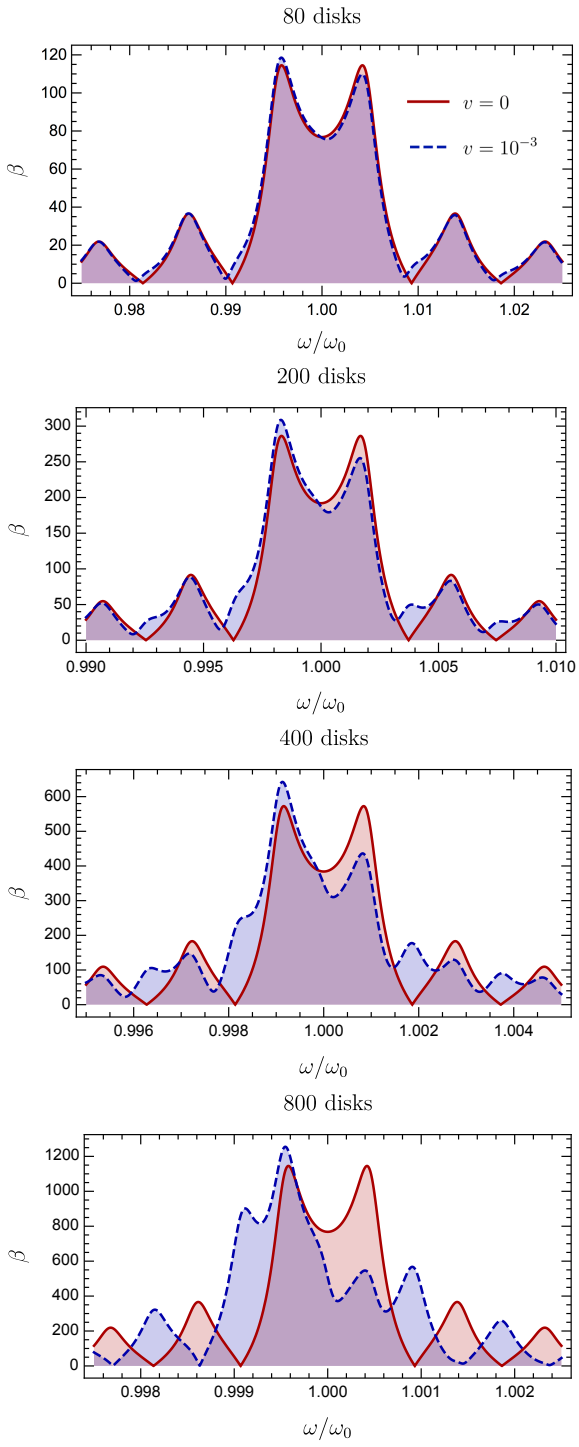

Figure 6.18: Boost factor $\beta(\omega/\omega_0)$ for 80, 200, 400 and 800 disks (labeled top to bottom panels, respectively). Note that $\omega = \omega_0$ corresponds to the transparent mode, in which all disks are transparent. In each case, the dashed blue curve corresponds to $v = 10^{-3}$, the solid red curve to $v = 0$.

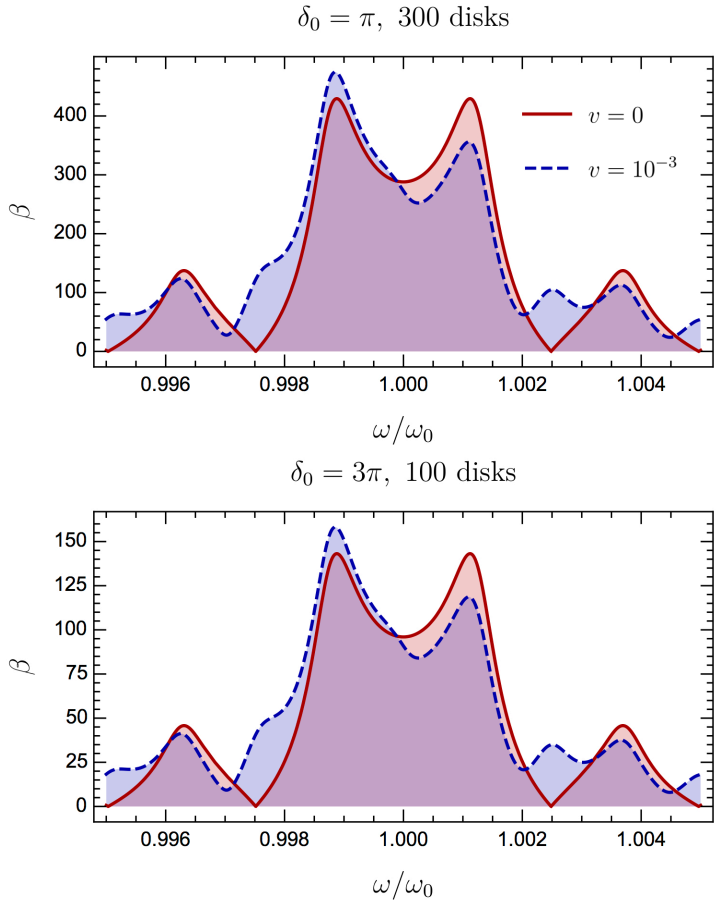

Figure 6.19: Boost factor $\beta(\omega)$ for 300 disks with $\delta_0 \equiv \delta_{\mathrm{v}} \equiv \delta_\epsilon = \pi$ for $\omega = \omega_0$ (top) and 100 disks with $\delta_0 = 3\pi$ (bottom). Note that $\omega = \omega_0$ corresponds to the transparent mode, in which all disks are transparent. In each case, the blue curve corresponds to $v = 10^{-3}$, the red to $v = 0$.

6.4 Sensitivity to inaccurate disk positioning

In a realistic setup, the distance between dielectrics cannot be made arbitrarily precise and thus cannot be precisely adjusted to $d_r = \pi/\omega_0$ for every gap $r = 1, \ldots, N-1$ (neglecting the dielectric regions). Rather, each gap distance will have an uncertainty Δd_r. If these errors are small, the boost factor for the many disk transparent mode discussed in section 6.3.3 becomes roughly

$$\beta_{\mathrm{T}} \sim \left| \sum_{r=1}^{N-1} e^{i\omega_0 \sum_{r'=1}^{r} \Delta d_{r'}} \right| . \tag{6.4.1}$$

The average shift of the power boost factor is negative and can be estimated by assuming Gaussian positioning errors with standard deviation $\langle \Delta d_r^2 \rangle = \sigma^2$

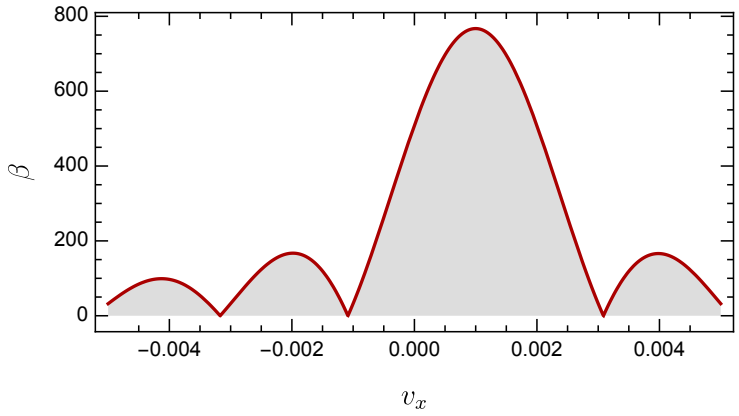

Figure 6.20: Boost factor as a function of the axion velocity for 800 transparent dielectric disks (phase thickness π) separated by a phase difference of 3.138. Here we have chosen a refractive index $n = 5$.

as

$$\left\langle \Delta\beta_{\rm T}^2 \right\rangle = -\omega_0^2\sigma^2 \frac{(N-1)(N-2)(N-3)}{6}\,. \tag{6.4.2}$$

This behaviour is to be contrasted with the simple cavity setup with large n of section 6.2, where inaccurate positioning of the singular dielectric instead gives

$$\langle \Delta\beta_{\rm C}^2 \rangle \sim -\omega_0^2\sigma^2(4n^6 - 5n^4 - n^2)\,, \tag{6.4.3}$$

where here we have assumed n real for simplicity.

Rewriting these results as a function of the boost factor itself we get $\langle \Delta\beta_{\rm T}^2 \rangle \sim -\omega_0^2\sigma^2\beta_T^3/6$, while we get a similar result for the cavity $\langle \Delta\beta_{\rm C}^2 \rangle \sim -\omega_0^2\sigma^2\beta_{\rm C}^3/2$. In order to secure the control over the boost factor we would need

$$\frac{\langle \Delta\beta^2 \rangle}{\beta^2} \sim -\omega_0^2\sigma^2\beta \ll 1 \tag{6.4.4}$$

which implies $\sigma \ll \lambda/(2\pi\sqrt{\beta})$ with λ the wavelength. Therefore, we need

$$\sigma \ll 200\,\mu{\rm m} \left(\frac{10^2}{\beta}\right)^{1/2} \left(\frac{100\,\mu{\rm eV}}{m_a}\right), \tag{6.4.5}$$

which is consistent with numerical simulations (i.e., to have the average variation be less than 10% one would need $\sim 20\,\mu$m precision for $\beta = 100$). As $\sigma \propto \beta^{-1/2}$ the sensitivity varies slowly with β.

This condition also bounds the allowed deviations of the surface from being perfectly flat. In general, the error involved in moving the disks should be more significant than manufacturing errors. A similar bound should apply to errors in the disk alignment, but a full 3D study of finite disks has not been done. Note that as the sensitivity to errors increases with β, for a practical experiment one would wish to avoid extremely large boost factors, or equivalently,

high Q in the cavity case. As the sensitivity increases linearly with the axion mass, for very high axion masses one will be unable to position the dielectrics accurately enough. While this limitation depends on the concrete mechanical setup, we expect that achieving a positioning precision better than μm will be impractical. Thus we would expect that one is restricted to $\beta \lesssim 10^{3-4}$, however the exact sensitivity to error will depend on the specific setup.

Numerically, we tend to see that small errors (those satisfying equation 6.4.5) correspond to small shifts to the boost factor in frequency space without altering the shape. Note that despite the fact that a dielectric haloscope in the transparent mode might require $\mathcal{O}(100)$ surfaces to reach the same $\beta = 100$ as a cavity with a single $n = 50$ dielectric, the sensitivity to misalignments is very much similar. This similarity is because many of the positioning errors will cancel their effects on average. However, not all setups with the same β are equally sensitive to errors: setups arranged so that the boost factor is a local maximum with respect to changing the positions of the dielectrics can be more susceptible to error as all errors necessarily reduce the boost factor. Further, as we saw in section 6.3, a setup with many dielectrics gives the possibility of a much larger bandwidth than a cavity.

As we expect to have similar sensitivity to errors in the positioning if the resonator is working in the transparent or cavity case (for equal boost factors), we expect that one can use setups which contain features of both the transparent and resonant cases with similar robustness with respect to positioning errors.

Chapter 7

Broadband Solutions

For a realistic haloscope, a resonant response function is not necessarily optimal, depending on various practical considerations. For a fixed set of dielectric disks with given uniform thickness, adjusting each vacuum spacing independently offers a large number of degrees of freedom to tailor a frequency-dependent response function within the limitations of the Area Law. We here study a few examples of constructing a nearly top-hat shaped response function. First, we will look at a 20 disk setup (along with a mirror), which is computationally more efficient, then verify these results with an 80 disk setup, as would be more plausible for a full scale experiment. For the 20 disk cases we will (justifiably) neglect the axion velocity, however we will consider a non-zero axion velocity for the 80 disk example, showing that for disk spaces that are of order $\lambda/2$ such effects are negligible.

7.1 Motivation and setup

So far we have been concerned with simple and demonstrative setups with high levels of symmetry, which however are not necessarily optimal for a practical experiment. A necessary trait is the ability to search a wide m_a range via a scanning procedure. The transparent and resonant setups discussed in chapter 6, as well as those considered in references [138, 152], require specifically chosen thicknesses for the dielectrics and would need a new set of disks for each measurement, which is clearly impractical. At higher mass ranges however, where the dielectric layers would form thin films, it is much harder to build discrete disks, but easier to create stacks of layers [193]. We will be focused on the microwave regime, as the optical frequency range considered in reference [193] is ruled out for the QCD axion.

For a realistic experiment it is desirable to have both broad rectangular (top-hat) responses and narrow resonant ones. Broadband setups reduce the sensitivity to positioning errors and compensate for the potentially non-negligible time t_{R} required to readjust the disk positions between measure-

ments.

To see this, we must consider how an experiment would be performed. The boost factor, while potentially broadband, does not cover the full frequency range we would like to search. Thus we must scan across frequencies. To do so, one must arrange the disks to enhance β over a given frequency range, measure, then adjust the positions of the disks to measure an adjacent frequency range and repeat until the full range is covered. For each measurement taking a time Δt, Dicke's radiometer equation gives the signal to noise ratio

$$\frac{S}{N} = \frac{P}{T_{\text{sys}}}\sqrt{\frac{\Delta t}{\Delta \nu_a}}, \tag{7.1.1}$$

where the T_{sys} is the system noise temperature and $\Delta\nu_a \sim 10^{-6}\nu$ is the axion line width. Throughout this chapter, we will assume that the axion's velocity is either zero, or monochromatic when non-zero. Our experiments should be velocity insensitive by design as we do not know the actual velocity distribution. In this case, the power P is given by equation (4.1.17). As the Area Law for dielectric haloscopes implies that $P\Delta\nu_\beta$ is roughly constant (where $\Delta\nu_\beta$ is the frequency width over which β is enhanced), naively one expects that a narrow resonance with high P is desirable. However, for an optimal scan rate, the measurement time should be similar to the time taken to adjust the disks (see appendix D for details). Broadband setups can compensate for the potentially lengthy time required to readjust the disk positions between each measurement. Such responses would allow one to scan a large frequency range in a single measurement; one could then use narrow resonances to confirm or reject a potential discovery at a higher signal to noise ratio. As in general the axion frequency is not simply related to the disk thickness (such as by a half wavelength as in the transparent mode above), the disk configurations must be found by a numerical optimisation procedure.

One could scan a large frequency range in one go, and then use narrow resonances to confirm or reject a potential detection. While the homogeneous setup discussed in section 6.3 can be adjusted between a wide range of frequencies, one lacks the ability to move from broadband to narrow-band responses at the same central frequency.

To show that such versatile setups are possible, we here consider dielectric disks of fixed uniform thickness, with each vacuum gap as a separate degree of freedom. Adjusting these spacings, we will see that one can control the height, width, shape, and position of the boost factor as a function of frequency.

Henceforth we will consider one side of the device to be closed by a perfect mirror. This setup ensures that the full power emerges in a single direction and can be measured by a single detector. Otherwise two detectors would be needed, introducing new issues about adding the signals coherently or incoherently and introducing two sources of detector noise. Our specific examples use a set of 20 aligned dielectric disks (1 mm thick, refractive index $n = 5$), providing enough degrees of freedom to make our point, yet few enough to

handle them with relative ease. Our benchmark frequency is $\nu = 25$ GHz ($m_a = 103.1\,\mu$eV), corresponding to a vacuum wavelength of $\lambda_0 = 1.20$ cm and a wavelength in the dielectric of $\lambda_\epsilon = \lambda_0/n = 0.24$ cm, i.e., there is no special relation between the disk thickness and chosen central frequency. We will then provide an example using 80 dielectric disks, in order to demonstrate the validity of the Area Law extrapolation and explore velocity effects.

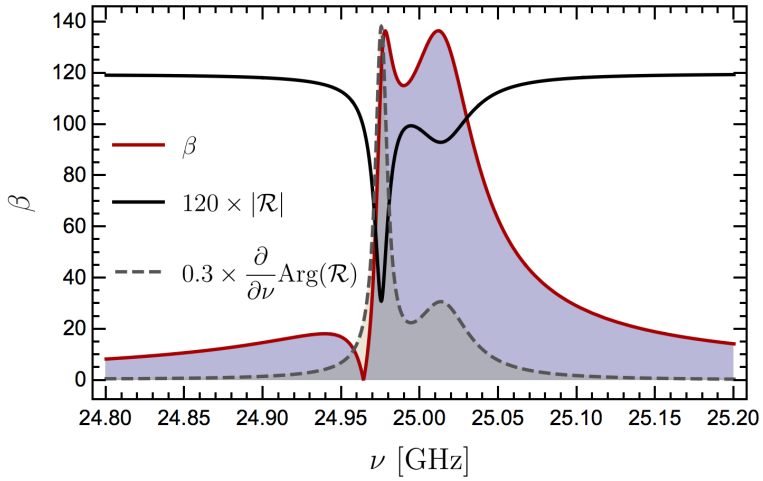

Figure 7.1: Boost factor β (red), reflectivity $|\mathcal{R}|$ (black) and group delay $\frac{\partial}{\partial\nu}\mathrm{Arg}(\mathcal{R})$ (dashed gray) as a function of frequency ν for our configuration B50 (20 disks, 1 mm thick, refractive index $n = 5$, mirror on one side, bandwidth 50 MHz centred on 25 GHz). The reflectivity is illustrated for exaggerated dielectric losses ($\tan\delta = 5 \times 10^{-3}$) to show the non-trivial structure. The reflectivity and group delay have been scaled by the factors 120 and 0.3, respectively.

7.2 20 disk configurations

7.2.1 Configuration with 50 MHz bandwidth

For a first example, termed configuration B50 (B for broadband), we choose a bandwidth of 50 MHz, which is quite broad in comparison to the axion line width $\Delta\nu_a = \mathcal{O}(10\text{ kHz})$. We seek a response function which covers this bandwidth as uniformly as possible, i.e., which comes close to a top-hat shape. To achieve a desired signal-to-noise ratio across this range, the lowest boost factor in this interval is the critical figure of merit. To find the optimal disk positions, we sample a set of frequencies ν_i in the chosen interval using a random walk in the 20 dimensional parameter space to find the configuration that maximises the minimal value $\mathrm{Min}\,[\beta(\nu_i)]$. Our best configuration reaches $\mathrm{Min}\,[\beta(\nu_i)] \sim 115$. The frequency-dependent boost factor is shown in figure 7.1. It has approximately rectangular shape, but in detail shows two distinct peaks.

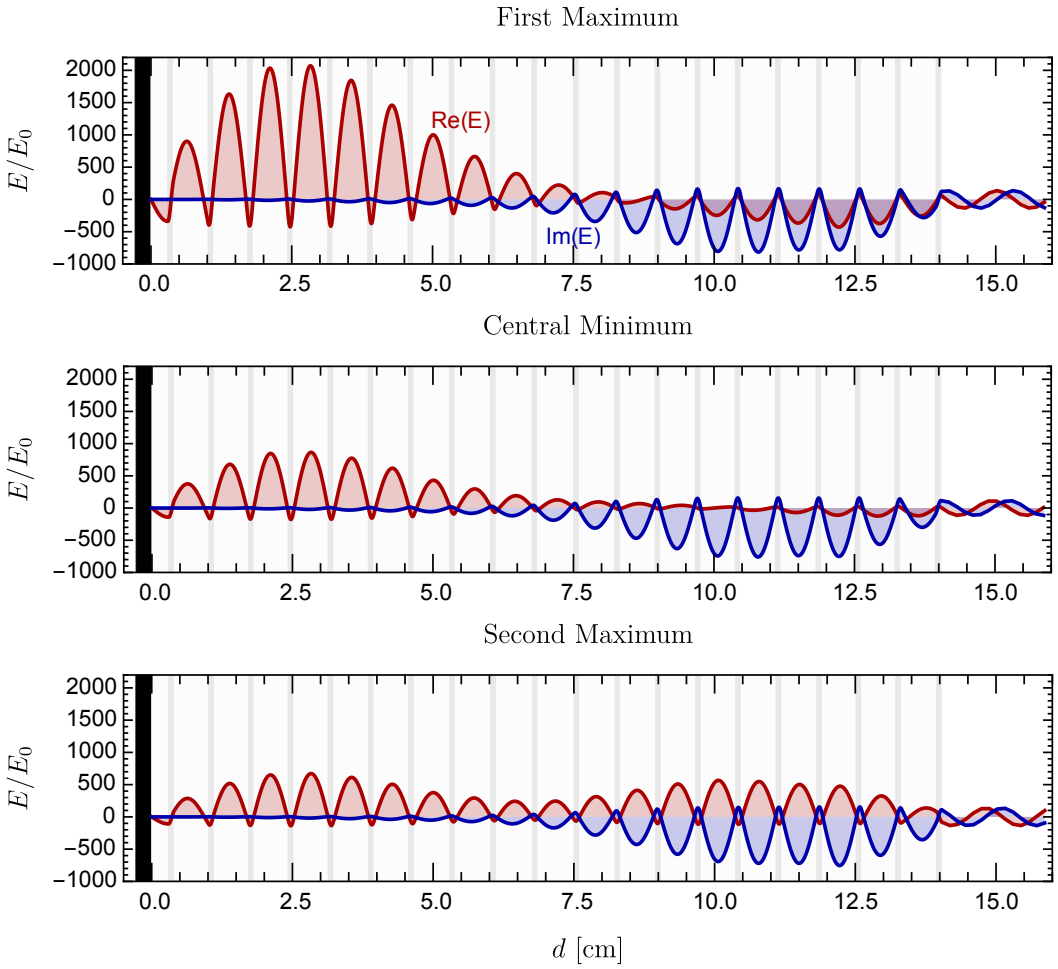

Figure 7.2: E-field distribution as a function of distance d from the mirror in our B50 configuration of a dielectric haloscope. Real part of E in red, imaginary part in blue. As labeled, the panels refer to the frequencies of the first maximum, the minimum, and the second maximum of the boost factor curve shown in figure 7.1. In each panel the locations of the mirror and the dielectric disks are indicated respectively by the black and the light-gray vertical bars.

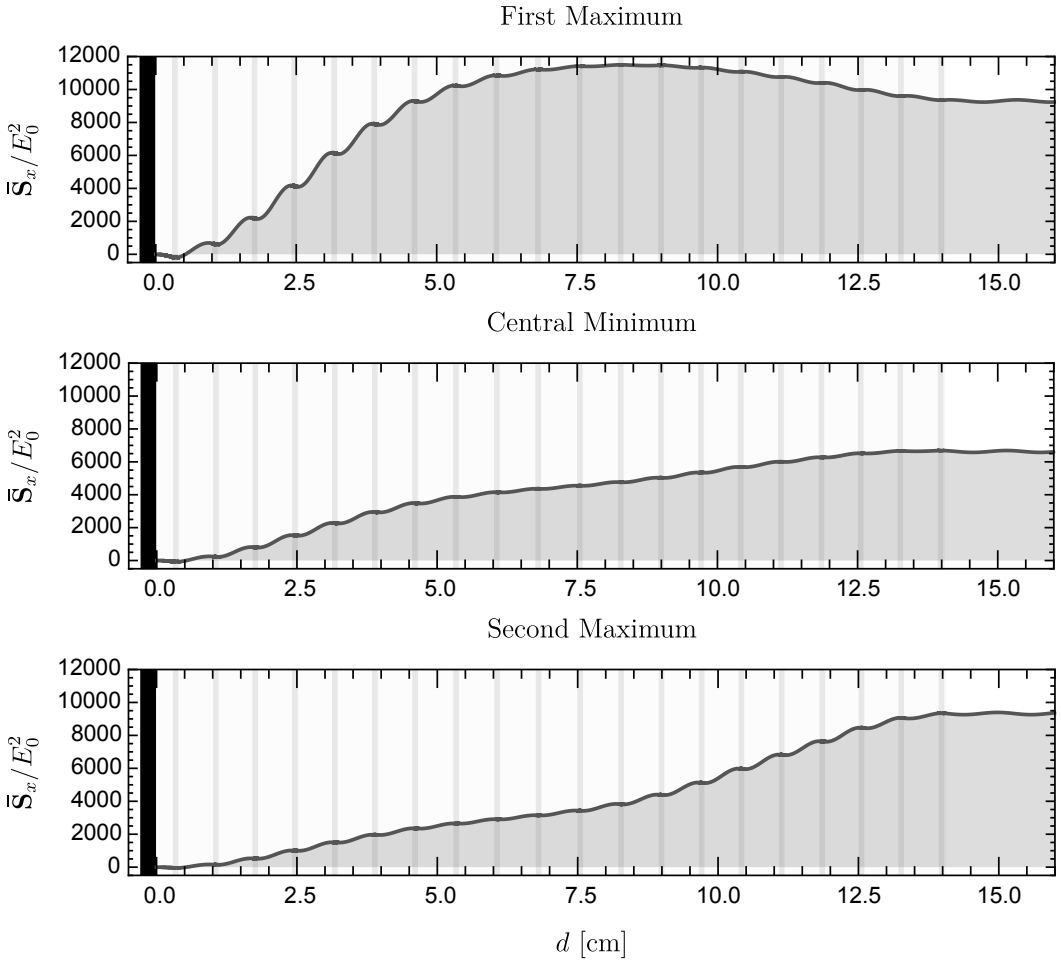

Figure 7.3: Cycle averaged Poynting flow $\bar{\mathbf{S}}_x$ in our B50 haloscope, corresponding to the E-field configurations shown in figure 7.2. Note that the sign of $\bar{\mathbf{S}}_x$ indicates the direction of energy flow. The mirror and dielectric disk locations are indicated as in figure 7.2.

For a heuristic understanding of this shape, we look to the EM response functions. Because our haloscope is closed by a perfect mirror on one end, the transmission coefficient vanishes, whereas the modulus of the reflection coefficient $\mathcal{R}$ is unity. However, the phase of $\mathcal{R}$ carries non-trivial information. While the microwaves are always reflected, the path-length depends on frequency: near frequencies that experience a large number of internal reflections the phase of the reflected radiation must change rapidly. Thus the derivative of this phase, the group delay $\frac{\partial}{\partial\nu}\mathrm{Arg}(\mathcal{R})$, maps out resonances in the system. Of course, $\mathcal{R}$, $\frac{\partial}{\partial\nu}\mathcal{R}$, and $\mathrm{Arg}(\mathcal{R})$ carry the same information, but it is brought out most clearly in the group delay. When losses are included, regions with more internal reflections will experience more damping, so $|\mathcal{R}|$ also maps out the resonant structure, although it does not seem to provide new information over the group delay. We can see this correlation in figure 7.1. While the peaks coming from $\mathcal{R}$ are shifted slightly relative to those in β (and the relative peak heights change), it seems plausible that one could use the group delay to verify the boost factor and correct for errors.

The double peak structure in both β and $\mathcal{R}$ suggests a combination of two resonances. We confirm this interpretation in figure 7.2 by looking at the E-field distribution in the B50 haloscope at the maxima and minimum of the boost-factor curve. Indeed the sharper peak on the lhs seems to correspond to resonant enhancement by the dielectrics close to the mirror, and the rhs peak corresponds to a less pronounced resonance on the side opposite the mirror. This behavior is echoed in $\mathcal{R}$, with the higher peak corresponding to the stronger resonance. The E-field is not simply a standing wave as one would expect in a true resonator, rather both standing wave and significant traveling waves exist. The latter are gleaned from the phase changing spatially throughout the haloscope. Note that the real and imaginary parts of E are not exactly $\pi/2$ out of phase as the axion-induced electric field E_a is included.

Another way to gain more intuition about these coupled resonators is to look at the cycle-averaged Poynting flow that was defined in equation (4.1.9). Figure 7.3 reveals that most of the emergent microwave power is generated in the haloscope region near the mirror for the first resonance, although the entire haloscope contributes. The central minimum and second maximum show less localised power generation.

7.2.2 Shifting the response in frequency space

In a realistic experiment one needs to scan over a much broader frequency range than given by our B50 arrangement. It is one of the main attractions of our approach that one can easily shift the B50 response function from its original center at 25 GHz, for example in steps of 50 MHz to achieve contiguous coverage of a broader search range. In figure 7.4 we show an example of six B50 response functions that seamlessly cover a 300 MHz interval. The disk positions for a shifted configuration are very similar to the previous ones and

indeed we always used the previous configuration as a starting point for finding the next shifted one. Notice that the ability to shift the response function in this way depends on the dielectrics not having a special thickness relative to the chosen frequencies, i.e., they are neither transparent nor fully reflective.

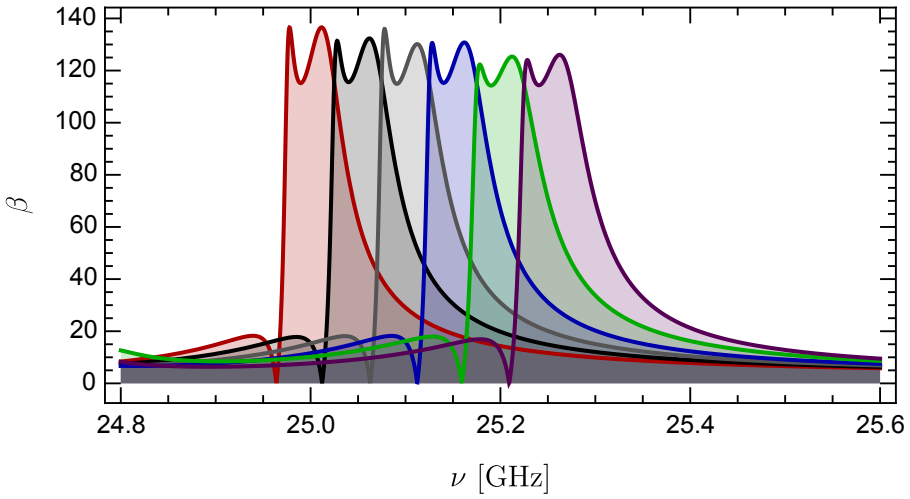

Figure 7.4: Example of a scan across a frequency range of 300 MHz using six B50 configurations with shifted central frequency. The left-most curve is identical with the boost factor of figure 7.1, corresponding to the original case centred on 25 GHz.

Note that we do not quite reach the same boost factor for all configurations, i.e., the central frequency relative to the chosen dielectric thickness is not irrelevant. Indeed with a single set of dielectrics it is not possible to scan all frequencies. When the disks are transparent, as considered in sections 6.2.4 and 6.3.3, $\mathrm{Min}\left[\beta(\nu_i)\right] \leq 2N+1$. Further, as can be seen in section 6.1, the disks do not emit any radiation at $\nu = 2, 4, 6, ... \times \pi/\sqrt{\epsilon}d$. Therefore, a realistic dielectric haloscope will require at least two sets of disks of different thicknesses to avoid such issues.

7.2.3 Varying the number of disks

Starting with the B50 configuration, which has 20 disks, we can use the Area Law to extrapolate these results to settings with a different number N of disks. From the Area Law, equation (A.2), we know that the area under $\beta^2(\nu)$ is due to a sum over the interfaces and so should increase linearly when one adds disks. In figure 7.5 we see that for a wide frequency region surrounding our frequency of interest, the boost factor is dominated by the β peak we optimised for, implying that the Area Law applied to this peak alone gives us a good estimate of the height$^2\times$width of our top-hat boost factor curve.

We consider our B50 configuration, keeping the 50 MHz width fixed, but

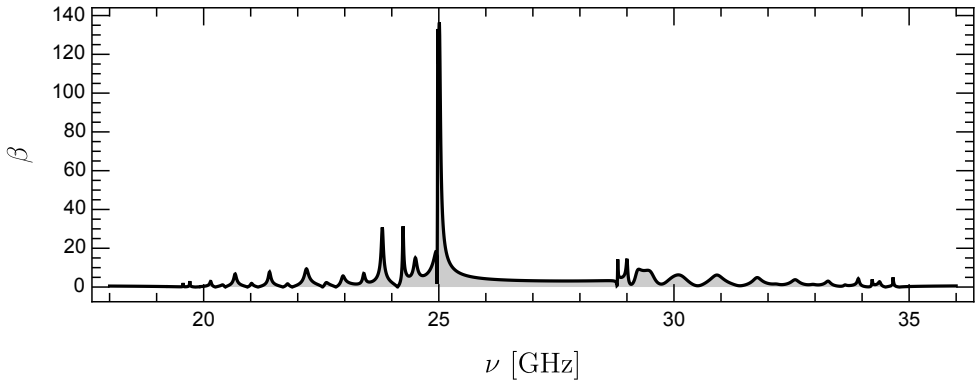

Figure 7.5: Boost factor of the B50 configuration as in figure 7.1 for a broader range of frequencies. The dominant peak appears in the 50 MHz region around the central frequency of 25 GHz.

varying the number N of disks. We perform the same optimization procedure and determine the boost factor $\mathrm{Min}\,[\beta(\nu_i)]$ within the chosen bandwidth. In figure 7.6 we show the result for $N = 15$–25 and find excellent agreement with the predicted linear variation of the squared boost factor with N. We will show an explicit example of an 80 disk setup in the next section, which shows remarkable agreement with the extrapolated trend-line. In other words, we can use the modified number of disks to modify the boost factor in the given frequency band, or we can modify the band while keeping the boost factor fixed.

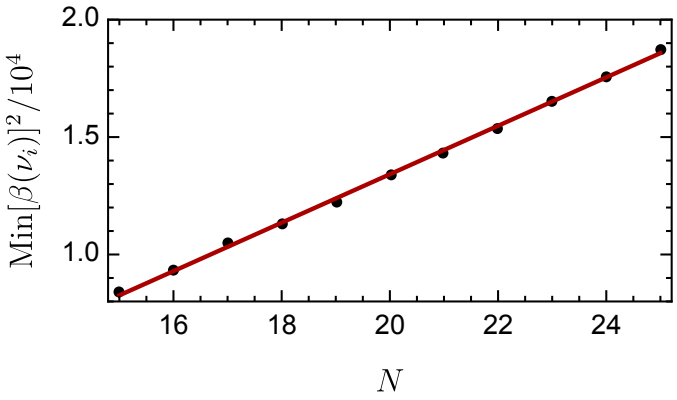

Figure 7.6: Squared boost factor $\mathrm{Min}\,[\beta(\nu_i)]^2$ achieved by our B50 configuration with fixed 50 MHz width, but varying the number N of disks. The variation is indeed approximately linear.

7.2.4 Configuration with 200 MHz bandwidth

We return to our configuration with a fixed number of $N = 20$ disks, but now consider a broader frequency band of 200 MHz while keeping all else fixed: the B200 configuration. We perform an analogous procedure and show in figure 7.7 the corresponding response functions. We recognise that one can indeed trade between bandwidth and boost factor, now reaching $\mathrm{Min}\,[\beta(\nu_i)] \sim 65$. Actually this value is slightly larger than expected from a naive application of the Area Law. The response function is here more rectangular, i.e., the smallest boost factor within the chosen frequency interval does not dip down as far.

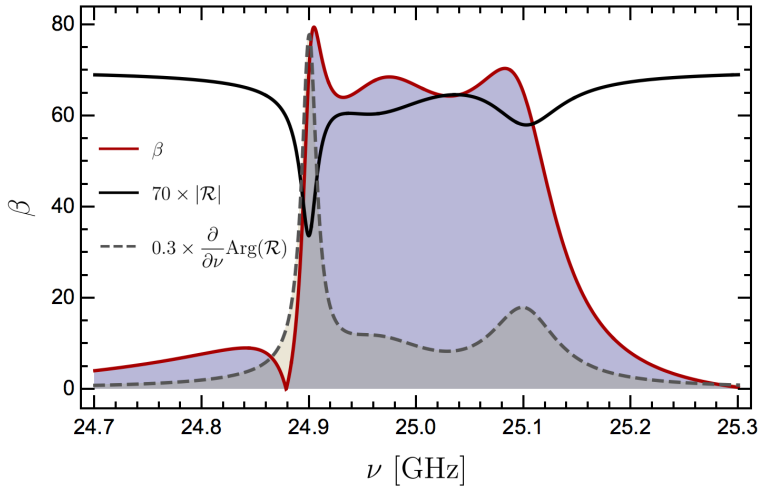

Figure 7.7: Boost factor β (red), reflectivity $|\mathcal{R}|$ (black) and group delay $\frac{\partial}{\partial\nu}\mathrm{Arg}(\mathcal{R})$ (dashed gray) as a function of frequency ν for our configuration B200 (20 disks, 1 mm thick, refractive index $n = 5$, mirror on one side, bandwidth 200 MHz centred on 25 GHz) in analogy to figure 7.1. The reflectivity is illustrated for exaggerated dielectric losses ($\tan\delta = 5 \times 10^{-3}$) to show the non-trivial structure. The reflectivity and group delay have been scaled by the factors 70 and 0.3, respectively.

The same point can be made by comparing the response functions of B50 and B200 directly in figure 7.8. We also compare the numerical responses with idealised top-hat profiles which have the chosen width of 50 and 200 MHz and heights derived from the Area Law applied to the main peak of the B200 configuration. So the broader bandwidth case, being more rectangular, uses the available area more efficiently.

While an analytic understanding of the positions required for these broadband setups is not available at present, we can gain some insight from the numerical results of our B50 and B200 configurations. In figure 7.9 we show the disk separations in these two configurations. Most of the separations are around $\lambda_0/2$, although the dielectric next to the mirror is much closer to it. The configuration with a broader bandwidth (B200, red) shows a greater dispersion of the disk separations, corresponding to this configuration being less

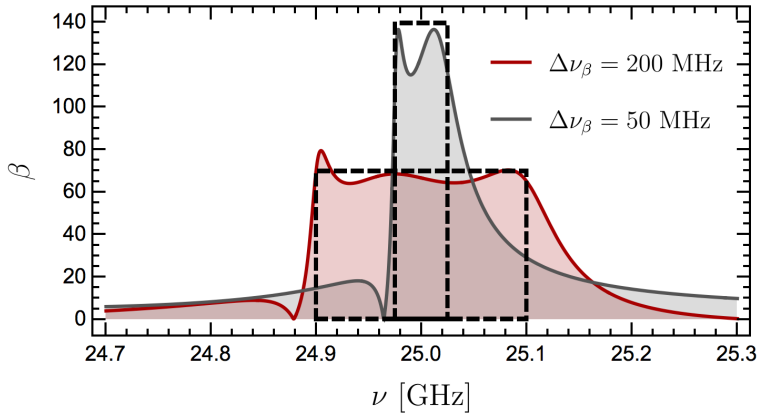

Figure 7.8: Comparison of the B50 (gray) and B200 (red) response functions. These are contrasted with hypothetical ideal top-hat configurations (black dashed) based on what one might expect from the Area Law as applied to the main peak of the B200 configuration.

resonant.

That the behaviour of the B200 configuration is less resonant is indicated in $\mathcal{R}$: the middle peak is not pronounced, suggesting that it does not correspond to strongly resonant behaviour. Figure 7.10 shows the E-fields at the maxima and minima of the boost factor curve in figure 7.7. The sharp cut-off on the lhs of the β curve seems to be due a resonant mode near the mirror, as in the B50 configuration. The interpretation we had of two resonant regions for our B50 configuration is not quite as clear for the B200 configuration: we do not see three obviously distinct resonant modes creating the three-peak structure, although the left and right peaks do seem to correspond to resonances. Again, as can be seen in the significant spatial variation of the phase, traveling waves are present. By looking at the cycle averaged Poynting flow in figure 7.11, one can see that the power is generated more or less evenly throughout the haloscope for the central maximum and is not localised to any one region, unlike the left and right peaks.

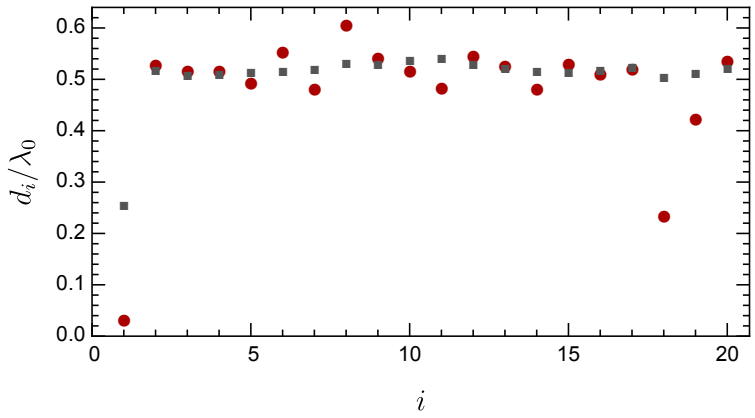

Figure 7.9: Positions of the 20 disks for the B50 (gray) and B200 (red) configurations. We show the distances d_i of disk i relative to disk $i-1$, where for $i = 1$ it is the distance to the mirror which is counted as $i = 0$. We normalise the distances to the wavelength of the central frequency $\lambda_0 = 1.20$ cm.

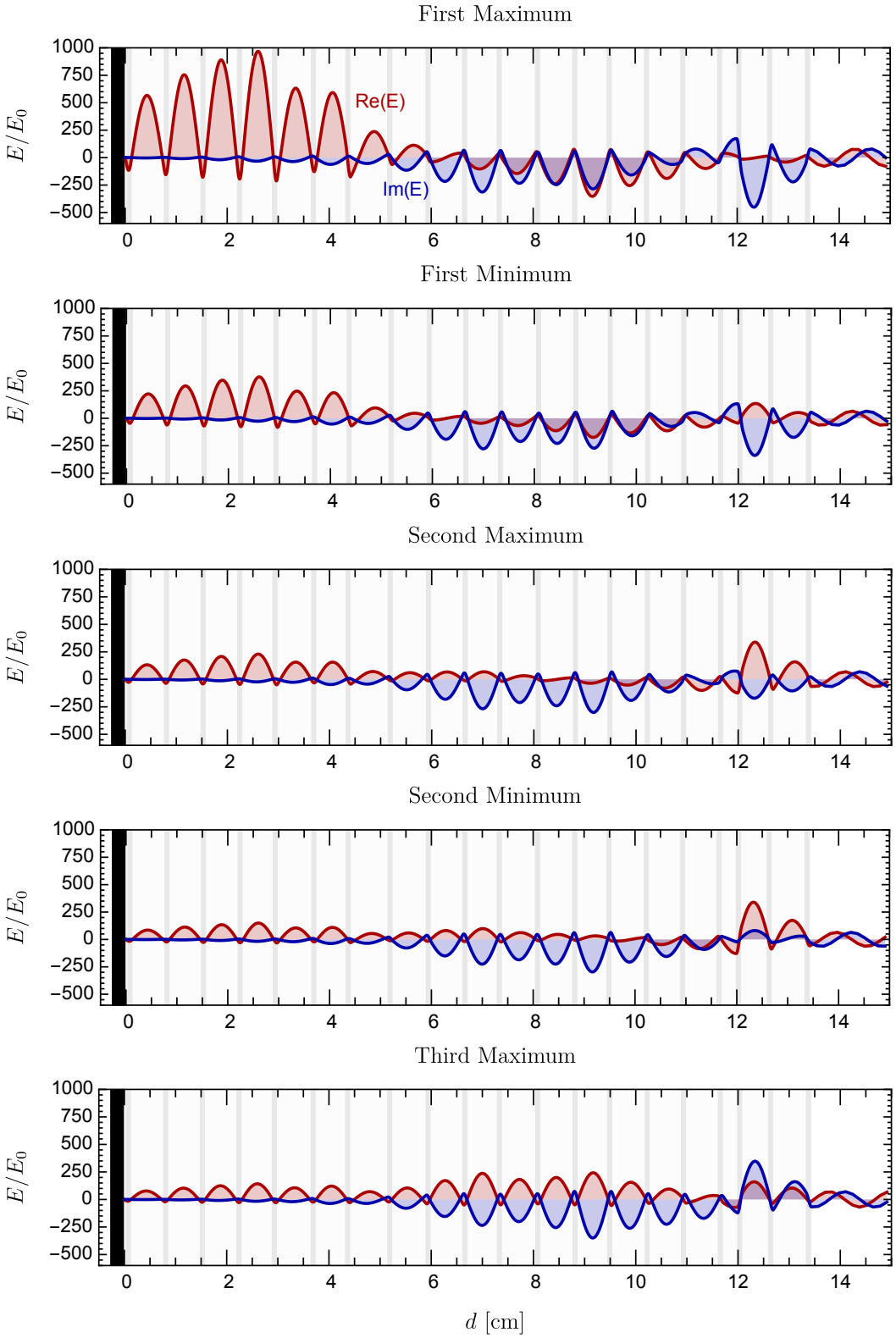

Figure 7.10: E-field distribution as a function of distance d from the mirror in our B200 configuration. Real part of E in red, imaginary part in blue. As labeled, the panels refer to the frequencies of the maxima and minima of the boost-factor curve shown in figure 7.7. The mirror and dielectric disk locations are indicated as in figure 7.2.

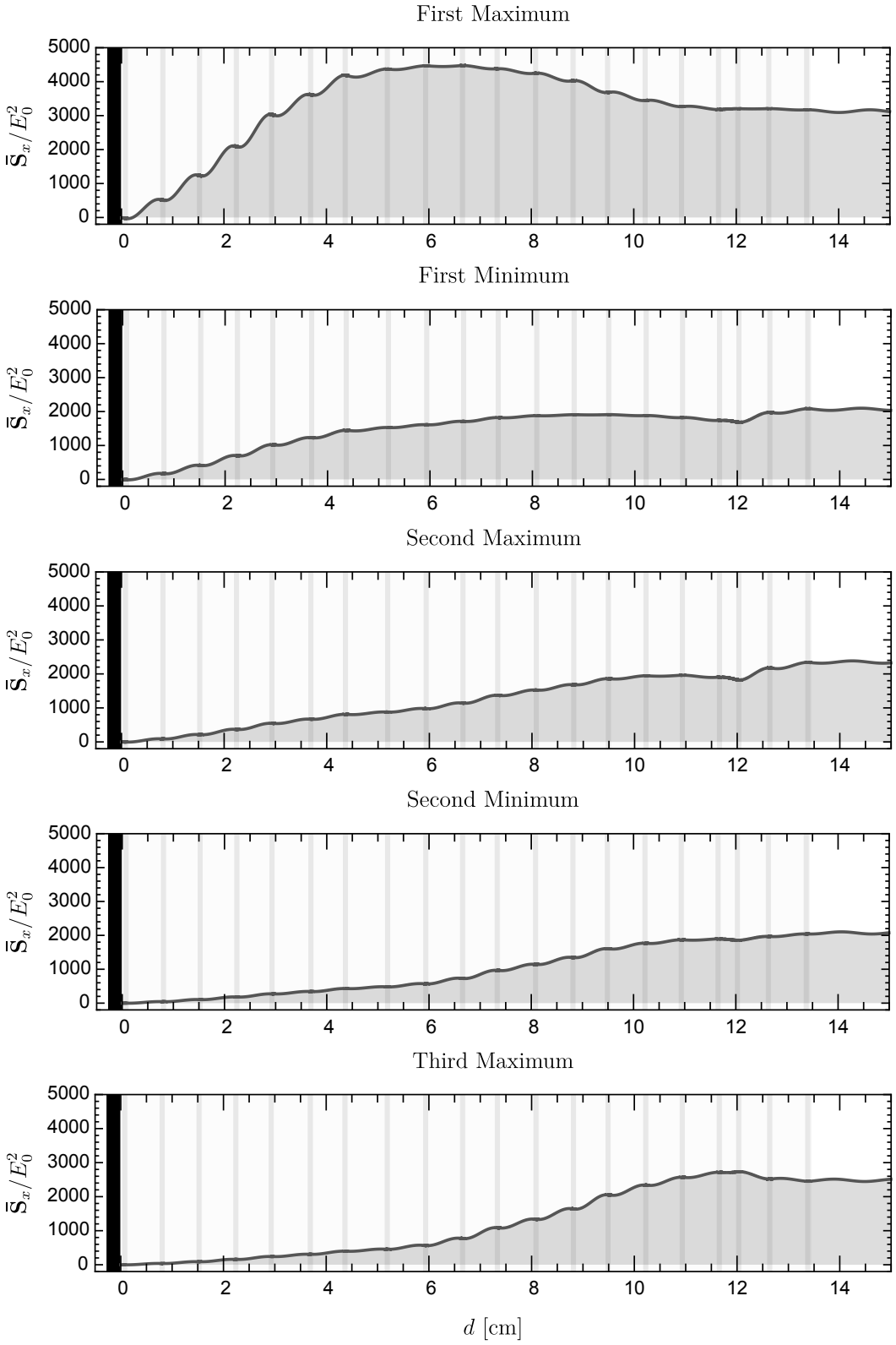

Figure 7.11: Cycle averaged Poynting flow $\bar{\mathbf{S}}_x$ in our B200 configuration, corresponding to the E-field configurations shown in figure 7.10. The mirror and dielectric disk locations are indicated as in figure 7.2.

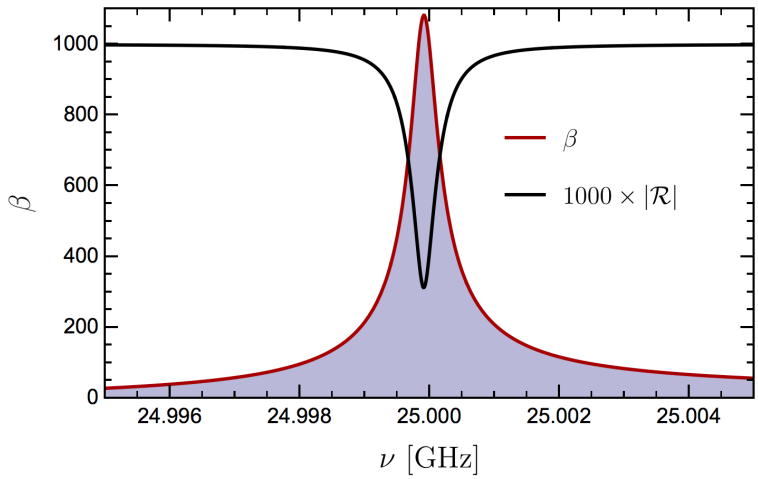

Figure 7.12: Boost factor β (red) and reflectivity $|\mathcal{R}|$ (black) as a function of frequency for our B1 configuration (20 disks, 1 mm thick, refractive index $n = 5$, mirror on one side, bandwidth 1 MHz centred on 25 GHz). The reflectivity is illustrated with exaggerated dielectric losses ($\tan\delta = 2 \times 10^{-4}$) to show non-trivial structure. The reflectivity has been scaled by a factor 1000.

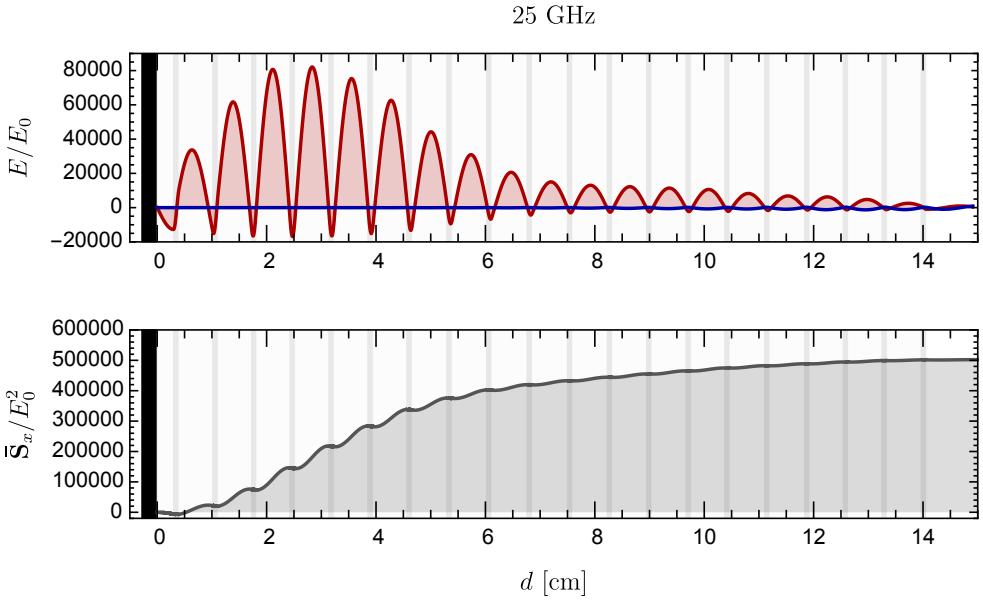

Figure 7.13: E-field distribution (top panel, red: real part, blue: imaginary part) and cycle-averaged Poynting flow $\bar{\mathbf{S}}_x$ (bottom panel) for the B1 configuration at the central frequency of 25 GHz. The mirror and dielectric disk locations are indicated as in figure 7.2.

7.2.5 Configuration with 1 MHz bandwidth

As a final example we consider a configuration with a 1 MHz bandwidth, all else being equal to the previous examples, our B1 configuration. Proceeding in the same way as earlier we find the boost factor curve shown in figure 7.12 which reaches $\mathrm{Min}\left[\beta(\nu_i)\right] \sim 600$. The shape is now far from rectangular—qualitatively it looks more like a Lorentzian. If it were more rectangular, the Area Law would suggest $\mathrm{Min}\left[\beta(\nu_i)\right] \sim 800$. While the boost factor at the central frequency is much larger than for B200 or B50, an even larger value of $\beta \gtrsim 10^4$ at 25 GHz can be achieved by judicious disk positioning. In this sense, the B1 configuration still qualifies as "broadband," although it really consists of a single resonance as one can also see from $\mathcal{R}$. From the E-field distribution and cycle-averaged Poynting flow shown in figure 7.13 we can see that that this single resonance is much stronger than any in B50 and B200. Unlike in the previous two examples there are no significant traveling waves in the haloscope.

7.3 80 disk dielectric haloscope

While the 20 disk examples were very useful for exploring broad behaviour of dielectric haloscopes, and the Area Law should allow us to extrapolate to higher numbers of disks, it is important to check that this is the case. One must check that the boost factor behaves as expected, as well as that the system is not overly sensitive to non-zero axion velocities. Finally, we can also use this opportunity to see how sensitive a full experimental setup would be to mispositioning errors.

We use the same 1 mm disks as in the 20 disk cases, simply adding disks. We will optimise for a 50 MHz bandwidth, calling this configuration B8050. The boost factor β, reflectivity $|\mathcal{R}|$ and group delay $\frac{\partial}{\partial\nu}\mathrm{Arg}(\mathcal{R})$ can be seen in figure 7.14. The B8050 configuration gives a power boost (β^2) within 5% of the prediction made in section 7.2.3 using the Area Law. Increasing the number of disks increases the number of boundary conditions that must be satisfied, leading to configurations containing a more "rippling" structure than the 20 disk configuration of the same width shown (B50). Similar substructure can also be seen if one looks at the reflectivity of the setup. The group delay maps out resonances and reveals a similar rippling structure to β. In addition, assuming that the dielectrics are lossy, with $\mathrm{Im}(n) = 10^{-3}$, $|\mathcal{R}|$ maps out resonant structure within the haloscope. To show this structure clearly, in figure 7.14 the losses were exaggerated an order of magnitude when compared to a realistic dielectric such as $LaAlO_3$ at low temperatures.

Reassuringly, we see that the Area Law is a good predictor for behaviour of the boost factor. From our analytic considerations in chapter 6, we expect that there is only a weak dependence on the velocity of the axion. We can check this by assuming a monochromatic axion with a non-zero velocity. This

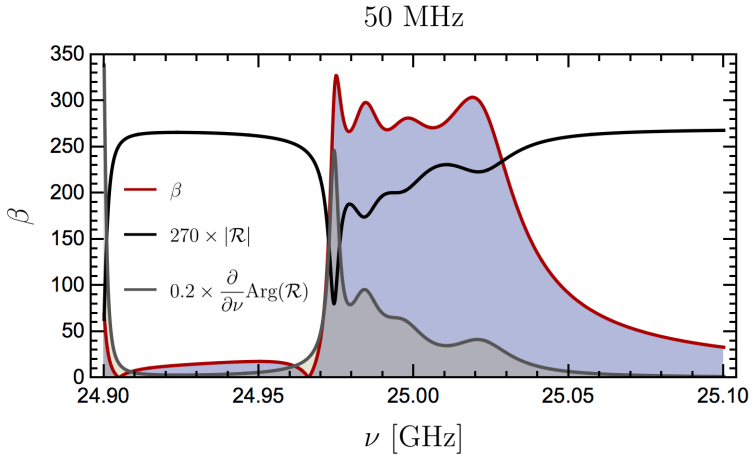

Figure 7.14: Boost factor $\beta(\nu)$ (red curve), reflectivity $|\mathcal{R}(\nu)|$ (black curve) and group delay $\frac{\partial}{\partial\nu}\mathrm{Arg}(\mathcal{R})$ (gray curve) for 80 disks optimised for a bandwidth of 50 MHz, centred on 25 GHz (the B8050 configuration). The reflectivity has been plotted assuming lossy dielectrics, with $\tan\delta \sim \text{few}\times 10^{-4}$. More specifically, we assume $\mathrm{Im}(n) = 10^{-3}$.

is shown by plotting $\beta_{v=10^{-3}} - \beta_{v=0}$ as a function of frequency in the bottom panel of figure 7.15. The difference is entirely negligible, with less than a percent level change in the region of interest (as seen in the top panel of figure 7.15). This dependence is actually somewhat less than one would expect from studying the transparent mode. As the spacing between each disk is close to $\lambda/2$, 80 disks in transparent mode (as shown in the top left panel of figure 6.18) should be comparable with our 80 disk broadband configuration. However, the transparent setup is actually more prone to velocity effects than the realistic configurations. Most likely this sensitivity is because of the large levels of symmetry present in the transparent mode; destructive and constructive effects occur coherently. That being said, the size of the distortion is similar enough to conclude that the scale at which velocity effects becomes important depends only weakly on the configuration as long as the total size of the haloscope remains constant. Thus dielectric haloscopes of the size considered for a search experiment in the next chapter are free to neglect the 1D effects of a finite axion velocity without negative consequence.

Note that errors in the disk placement made when readjusting the disks between measurements will likely result in larger changes to β than the axion velocity. While the exact sensitivity to mispositioning errors depends on the distribution function of these errors, from numerical simulation we can see that one will require $\mathcal{O}(\mu\mathrm{m})$ placement position to keep the change in β at the 10% level. One can see an example assuming a top hat error function with a width of $5\,\mu$m in figure 7.16. Such an error function gives deviations in β of order 10–20%, which should be acceptable an experiment. Note that this is

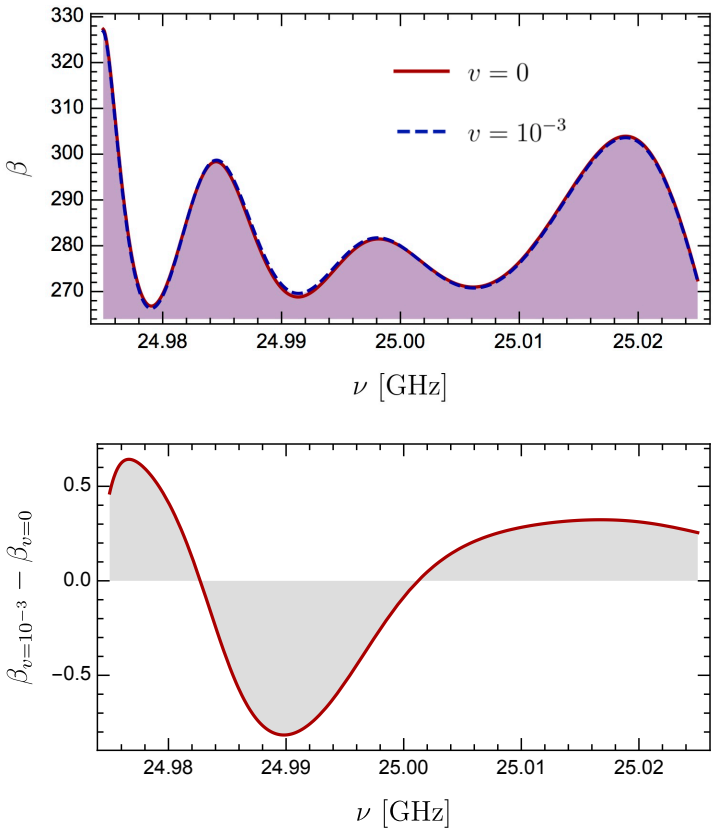

Figure 7.15: *Top:* Boost factor $\beta(\nu)$ for 80 disks optimised for a bandwidth of 50 MHz, centred on 25 GHz. Both $\beta_{v=0}$ and $\beta_{v=10^{-3}}$ are plotted as red and dotted blue curves, respectively. *Bottom:* Difference between β for $v = 10^{-3}$ and $v = 0$ as a function of frequency. Inside the region of interest (the shown 50 MHz bandwidth), this difference corresponds to a less than percent level effect.

somewhat more than one would expect from the purely analytic calculations in section 6.4, being more restrictive by an order of magnitude. Further, one can see that the reflectivity $|\mathcal{R}|$ remains correlated with β, allowing one to gain information about the deviation of β, allowing for errors to be corrected. For example, the large deviation of the gray curve can be seen in both the reflectivity and boost factor. If one observed this one could reposition the disks until an appropriately small distortion of $|\mathcal{R}|$ was obtained. in While the distortion from mispositioning errors is a greater effect than that of non-zero axion velocities, the time-dependence of changes to the axion velocity may allow it to be extracted from a signal.

7.4 Summary

We have seen from these numerical calculations that by controlling the separation between different dielectrics one has considerable control over the shape of the boost factor. One can scan through frequencies as well as change the relative width and height of the emitted power, both very important traits for practical experiments. The Area Law seems to provide an excellent predictor for the behaviour of the experiment, with extrapolations up to 80 dielectric disks matching very well. The reflective properties of the system remain closely matched to the boost factor, giving a very plausible mechanism for insuring the system is behaving correctly, and could be used to help correctly position the dielectric disks. The kinds of setups we will consider for a practical search experiment seem free of any deleterious effects of a non-zero axion velocity.

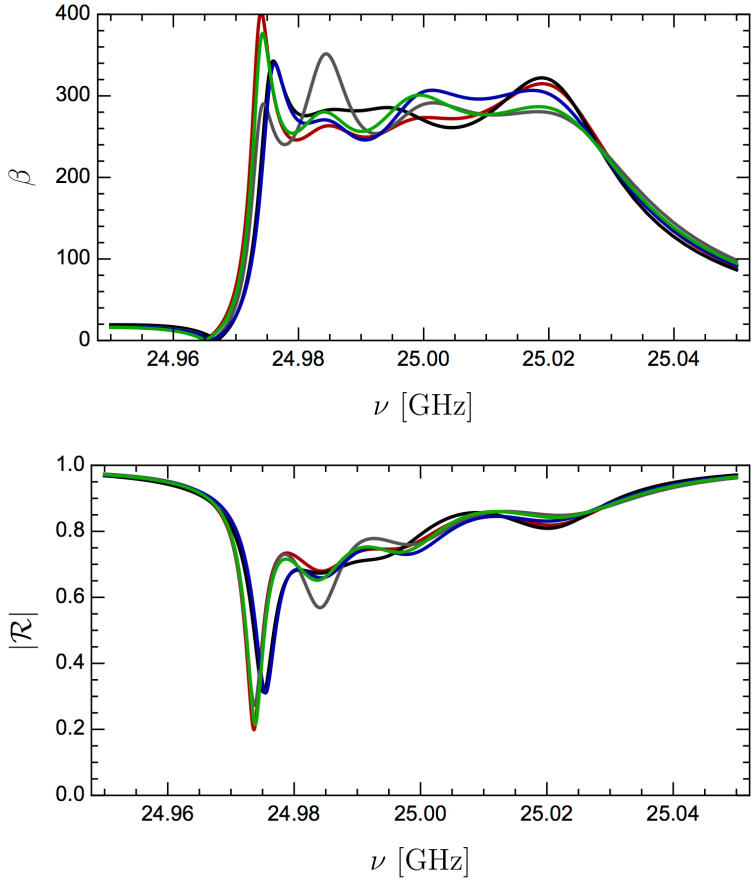

Figure 7.16: Boost factor $\beta(\nu)$ (top) and reflectivity $|\mathcal{R}(\nu)|$ (bottom) for 80 disks optimised for a bandwidth of 25 MHz, centred on 25 GHz. Five configurations are shown, with each disk perturbed from the configuration shown in figure 7.14 by a top hat error function with width $5\,\mu$m. For the reflectivity we assume losses exaggerated by an order of magnitude over the realistic value for visual comparison, with $\mathrm{Im}(n) = 10^{-3}$. Losses are neglected for the boost factor.

Chapter 8

Axion Detection

Now that we have a good understanding of the underlying behaviour of a dielectric haloscope, we can at last turn our attention to what might be possible with an experiment. In this section we will focus on dielectric haloscopes operating in the microwave regime, though it is also possible to operate dielectric haloscopes at optical frequencies [193]. First we will explore the discovery potential of a realistic experiment, with the primary study being an 80 disk haloscope as planned in the upcoming MADMAX experiment [21]. We also discuss possible upgrades, including a 200 disk experiment. We will then briefly turn our attention to the hypothetical case where the axion has been discovered. In such a scenario, one would wish to gain as much information as possible about the DM field. We note that dielectric haloscopes with a strong sensitivity to the axion velocity would be ideal to learn directional information about the axion.

8.1 Searching for the axion

We now turn to the discovery potential of dielectric haloscopes for axion DM. Unlike what is generally assumed for cavity haloscopes, we operate under the assumption that the limiting factor to the scanning rate is not how large a boost factor one can achieve, but rather by the time required to adjust the spacings between dielectrics from one configuration to the next. The broadband nature of the dielectric-haloscope response can compensate for this limitation, allowing one to scan across most of the unexplored high-mass axion parameter space.

When searching for axions, the velocity effects must be small, i.e., the boost factor $\beta(v)$ should be approximately independent of the axions velocity v. To see why we must require v independence, notice that the generated power at a given axion momentum $\mathbf{p}$ is

$$P(\mathbf{p}) \propto |a(\mathbf{p})|^2 \beta^2(\mathbf{p}). \tag{8.1.1}$$

Note $P(\mathbf{p})$ is our only observable: as we do not know the velocity distribution

of the axion $a(\mathbf{p})$ a priori, one cannot disentangle $a(\mathbf{p})$ from $\beta(\mathbf{p})$, unless $\beta(\mathbf{p})$ is independent of v. Consider if an experiment had a strongly $\mathbf{p}$ dependent β. When no signal is seen in a given measurement, we could not tell whether there were no axions present, or if there were DM axions with an unexpected velocity distribution giving a different boost factor than expected. In other words, the experiment does not distinguish between $a(\mathbf{p}) \sim 0$ and $\beta(\mathbf{p}) \sim 0$, so no limits can be easily set. Thus, a design requirement for a search experiment is that $\beta(\mathbf{p}) = \beta(m_a)$. Hence for our discovery potentials we will simply assume a zero velocity axion.

As we saw in chapter 6, velocity effects become relevant when the haloscope is on the order of 20% of the axion de Broglie wavelength. This gives us a limit on the potential size of the device, corresponding to several hundred disks, as can be seen from considering the transparent mode in section 6.3. Ultimately, due to the Area Law, velocity dependence will provide a (very high) limit on the possible boost factor/bandwidth achievable by a search experiment type dielectric haloscope. To go beyond this limit, one would have to devise a search strategy so that regardless of the assumed velocity distribution, no parameter space is missed.

8.1.1 Example 80 disk experiment

For a realistic setup, we assume a device consisting of a mirror and 80 disks of refractive index $n = 5$ and area $\mathcal{S} = 1\ \mathrm{m}^2$, contained inside a 10 T magnetic field. We also assume a conservative full day of downtime between measurements (readjustment time $t_{\mathrm{R}} = 1$ day). As there are $\mathcal{O}(10^6)$ channels in our search region, we require $S/N \sim 5$ to reduce the number of false positives to an acceptable amount. Depending on the ease of rescanning false positives, in particular depending on t_{R}, it may be more efficient to allow for more false positives and rescan more frequently.

In order to find the time taken for a single measurement, one can use equation (4.1.18), searching $\Delta\nu_\beta/\Delta\nu_a$ channels in each measurement. Naively, one might expect that a narrow resonance is most efficient: the Area Law implies that $P\Delta\nu_\beta \sim$ const and from equation (4.1.18) we see that the scanning rate scales as $P^2\Delta\nu_\beta$, so one gains by a factor P. But this argument ignores the time t_{R} necessary to reposition the disks—as shown in appendix D an optimal scanning rate requires $t_{\mathrm{R}} = \Delta t$. To compensate for a relatively long t_{R} one can use a broadband response to measure a larger frequency range in each measurement.

With some simplifications, the time taken to optimally measure some frequency range ν_2–ν_1 can be found analytically, as in appendix D. If the boost factor required to obtain $\Delta t = t_{\mathrm{R}}$ at ν_2 is β_2, then the optimal overall scanning time t_{o} is

$$t_{\mathrm{o}} \sim \frac{2t_{\mathrm{R}}}{2p+1}\,\frac{\beta_2^2}{K}\nu_2\,, \tag{8.1.2}$$

where $K = \Delta\nu\beta^2$ is an (approximate) constant given by the Area Law and the constant p contains the dependence of $T_{\rm sys}$ on ν: specifically, $\beta_2 \propto \nu_2^p$. Explicitly,

$$\begin{aligned}\beta_2 &= 430 \left(\frac{\rm day}{t_{\rm R}}\right)^{1/4} \left(\frac{\nu_2}{25\ {\rm GHz}}\right)^{1/4} \left(\frac{\rm S/N}{5}\right)^{1/2} \\ &\quad \times \left(\frac{1\,{\rm m}^2}{\mathcal{S}}\right)^{1/2} \left(\frac{T_{\rm sys}}{8\,{\rm K}}\right)^{1/2} \left(\frac{10\,{\rm T}}{B_{\rm e}}\right) \left(\frac{0.8}{\eta}\right)^{1/2} C_{a\gamma}^{-1} f_{\rm DM}^{-1/2}\,. \quad (8.1.3)\end{aligned}$$

The idealised HEMT (high-electron-mobility-transistor) amplifier with constant $T_{\rm sys}$ has $p = 1/4$, whereas quantum-limited amplifiers ($T_{\rm sys} = \omega$) have 3/4. Interestingly, to first approximation the measurement time depends only on ν_2, with $t_o \propto \nu_2^{2p+1}$. Further, $\beta_2 \propto C_{a\gamma}^{-1}$, so the measurement time decreases with the square of $C_{a\gamma}$, rather than the forth power as one might expect from Dicke's formula (4.1.18).

Note that one could be more conservative, and assume that one could only optimise the relative width and height over some longer period, such as six months. As the required β varies very slowly with frequency, both procedures give similar results, especially as we are only concerned with simple estimates.

To estimate the power generated for a given bandwidth, we extrapolate our 25 GHz configurations using the Area Law. Explicitly, we use the trend line from figure 7.6 to get an idea of the boost factor for an 80 disk haloscope, i.e., $\beta \sim 275$ across $\Delta\nu_\beta = 50\,{\rm MHz}$. Due to the Area Law being a good approximation, one gets a similar answer by using the explicit 80 disk solution. While the exact β one can achieve depends on the frequency (even when using a few different sets of dielectrics one will not achieve a uniform result), our method should give a reasonable estimate. Of course, as in every case for a projected experiment all values should be taken with a grain of salt. For consistency with other DM detection forecasts, we assume $f_{\rm DM} = 1$, i.e., $\rho_a = 0.3\ {\rm GeV/cm}^3$.

In figure 8.1 we show the discovery potential of an 80 disk experiment with a run time of three years. In this figure we adopted the more conservative approach and assumed that one was optimising the bandwidth vs boost factor on a half yearly basis, rather than optimising the bandwidth for every measurement. In other words, each half-year period uses the same boost factor. This estimate assumes 80% power efficiency and quantum-limited detection ($T_{\rm sys} \sim m_a$). One would be able to search a large fraction (40–230 μeV) of the high-mass parameter space for $|C_{a\gamma}| = 1$, and 40–180 μeV for $|C_{a\gamma}| = 0.746$. The lower limit is not a true lower bound: we simply restricted the range to coincide with the upper limit of CULTASK. In practise the true lower limit depends on the exact length of the magnetised volume, and even then one could extend the limit by using fewer disks. This range would cover most of the mass range predicted by Scenario B. If the Peccei–Quinn symmetry is not restored after inflation (Scenario A), this range corresponds to initial misalign-

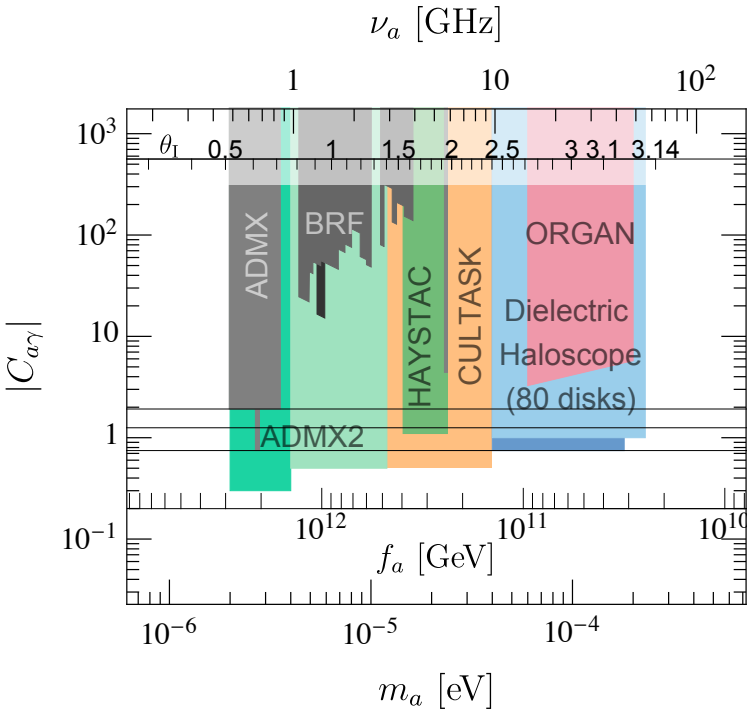

Figure 8.1: Two examples of the discovery potential (light and dark blue) of our dielectric haloscope using 80 disks ($n = 5$, $\mathcal{S} = 1\,\mathrm{m}^2$, $B_\mathrm{e} = 10\,\mathrm{T}$, $\eta = 0.8$, $t_\mathrm{R} = 1\,\mathrm{day}$) with quantum-limited detection in a 3-year campaign. We also show exclusion limits (gray) and sensitivities (coloured) of current and planned cavity haloscopes [128, 132, 140–146]. The upper inset shows the initial misalignment angle θ_I required in Scenario A [60]. The lower inset depicts the f_a value corresponding to a given m_a, and the three black lines denote $|C_{a\gamma}| = 1.92$, 1.25 and 0.746. Note that Scenario B predicts $25\,\mu\mathrm{eV} \lesssim m_a \lesssim 200\,\mu\mathrm{eV}$ [76, 78, 81].

ment angles $2.4 \lesssim \theta_\mathrm{I} \lesssim 3.12$. Figure 8.1 compares this forecast with existing limits and forecasts from planned cavity haloscopes [128, 132, 140–145].

It is conceivable to use a two-stage search strategy, using a mixture of commercially available HEMT amplifiers and quantum-limited detection. Using HEMT amplifiers with $T_\mathrm{sys} = 8\,\mathrm{K}$, in a five year campaign one could scan $m_a \lesssim 120\,\mu\mathrm{eV}$ reaching $|C_{a\gamma}| = 1$ or $m_a \lesssim 100\,\mu\mathrm{eV}$ for $|C_{a\gamma}| = 0.746$. One could then upgrade to quantum-limited detection for an additional two-year scan to cover the high-mass range, $m_a \lesssim 230$ or $180\,\mu\mathrm{eV}$.

Note that the target $|C_{a\gamma}|$ depends on ones search strategy. One always has a choice between scanning deeper into parameter space, i.e., smaller $|C_{a\gamma}|$, or scanning a wider frequency range. For example, in Scenario B KSFZ models are more favoured than DFSZ models, which tend to suffer from a domain wall problem as discussed in section 2.1.3. One could also do something more similar to ADMX and CULTASK, and aim for $|C_{a\gamma}| = 0.5$. In this case one

can easily calculate from equation (8.1.2) that one would cover 40–130 μeV in a three year quantum limited scan, covering a log scale similar to CULTASK.

8.1.2 Possible upgrades

In general, there are six ways to improve a dielectric haloscope, as can be seen by equation (8.1.2). Three of them would be by lowering the required β_2: reducing the system noise $T_{\rm sys}$, increasing the surface area $\mathcal{S}$ or increasing the external magnetic field $B_{\rm e}$. One could also increase the accessible bandwidth $\Delta\nu|_{\nu_2}$ by adding more dielectrics, or reduce the time required to reposition the dielectrics $t_{\rm R}$. Finally, one could simply run the experiment for longer. By doing some combination of these upgrades one could either reach lower $C_{a\gamma}$ or scan a larger range of m_a (or both). Scanning becomes increasingly difficult at higher frequencies (i.e., there is a non-linear relation between ν_2 and $t_{\rm o}$), but not nearly as rapidly as in the case of a cavity haloscope.

Note that one must be a bit careful extending our analysis beyond $\sim 250\,\mu$eV if one uses $1\,\mathrm{m}^2$ dielectric disks. At this point, the axion is not spatially homogeneous across the surface of the disk due to the relatively small de Broglie wavelength, and the inhomogeneities are on the same scale as the disk dimensions. These subtleties are not fully captured in our treatment, as with other boundary effects. One could avoid the issue by either measuring each area of the haloscope in a way independent of the relative phase, or simply by reducing the size of the disks. Either way, it would be certainly possible to push into higher m_a. Adding more dielectrics seems like the most feasible upgrade path, as the linear distance of the system shrinks at higher masses, allowing more dielectrics inside the same magnet volume.

At high masses instead of using a linear amplifier one could instead move towards counting photons. The photon flux is given by

$$\Phi_\gamma = \frac{P_\gamma}{\mathcal{S}\,\omega} = \frac{22}{\mathrm{m}^2\ \mathrm{s}} \left(\frac{\beta}{400}\right)^2 \left(\frac{100\,\mu\mathrm{eV}}{m_a}\right) \left(\frac{B_{\rm e}}{10\,\mathrm{T}}\right)^2 C_{a\gamma}^2 f_{\rm DM}\,. \tag{8.1.4}$$

While due to the suppression by a factor of m_a photon counting appears to be less viable at high frequencies, photon counting has the advantage of avoiding the quantum limit $T_{\rm sys} = m_a$ [194]. While there is still thermal shot noise, this can be reduced by cooling the experiment. At higher frequencies, being able to cool beneath the quantum limit can easily make up for the factor of m_a in Φ_γ. Such a strategy is proposed for an optical dielectric haloscope aiming to detect ALPs and hidden photons in the extremely high mass range 0.1–10 eV [193]. Note that in this mass range the QCD axion is already ruled out by astrophysical bounds [121].

8.1.3 Example 200 disk experiment

To see how upgrades could play a role, let us consider a hypothetical second generation experiment. We will keep the magnetic field and surface area of

the disks fixed, as it would be economical to continue to use the same magnet, which tends to be the primary cost driver. This would be a kind of "MADMAX 2". We will assume that the only changes are made by adding dielectric disks, and reducing the readjustment time t_{R} (which presumably will happen with greater mechanical experience with such devices). Assuming quantum limited detection, we see that

$$\nu_2 \propto \left(\frac{t_{\mathrm{o}} K |C_{a\gamma}|^2}{\sqrt{t_{\mathrm{R}}}} \right)^{\frac{2}{5}} . \tag{8.1.5}$$

To give a concrete example, let us consider a 200 disk setup with $t_{\mathrm{R}} = 6\,\mathrm{hours}$, changing none of the other parameters from our 80 disk example. In figure 8.2 we see that in a three year quantum limited scan one could scan up to $255\,\mu\mathrm{eV}$ axions down to couplings of $|C_{a\gamma}| = 0.5$. With an additional two years, one could scan even up to $315\,\mu\mathrm{eV}$. At higher axion masses, the initial misalignment angle θ_{I} in Scenario A becomes increasingly tuned. For example, $\sim 250\,\mu\mathrm{eV}$ corresponds to $\theta_{\mathrm{I}} = 3.14 \sim \pi$. Further, higher masses lie outside the usual prediction for Scenario B [76,78,81]. If one uses this as a guide, going to higher masses becomes increasingly unmotivated. While such a device is certainly not around the corner, it is a very plausible upgrade to the planned MADMAX experiment, with most of the parameter space not requiring any change in the magnet (at lower masses, 200 disks could not fit inside a magnet designed for 80, however the lower masses are much easier to scan, and so could be done with less disks).

Dielectric haloscopes seem uniquely suited to searching for high-mass axions. In this thesis we have made relatively minimal assumptions about the required technologies: like cavity haloscopes it should be possible to extend the natural range of a dielectric haloscope ever further with future technological advances. For example, as m_a increases the quantum limit $T_{\mathrm{sys}} = m_a$ of linear amplifiers becomes increasingly problematic. One would then benefit by moving to photon counting experiments. The ability to use a large transverse area as well as a high boost factor with a broadband search strategy would allow one to search a large fraction of the high-mass parameter space.

8.2 The axion is discovered... now what?

While it is more typical for planned experiments to take the pessimistic approach, and speak of projected exclusion limits and ruling out parameter space, one must also plan for success. Imagine the axion actually lies within the range searched by dielectric haloscopes, and is discovered. Once the champaign and caviar runs out we must set ourselves to the task of extracting as much information as possible. Here, we start to see the benefits of the axion's velocity. Whether or not the axion velocity plays a role depends on the type of experiment under consideration. Broadly speaking, there are two types of experimental setups: a search experiment, i.e., the original experiment which

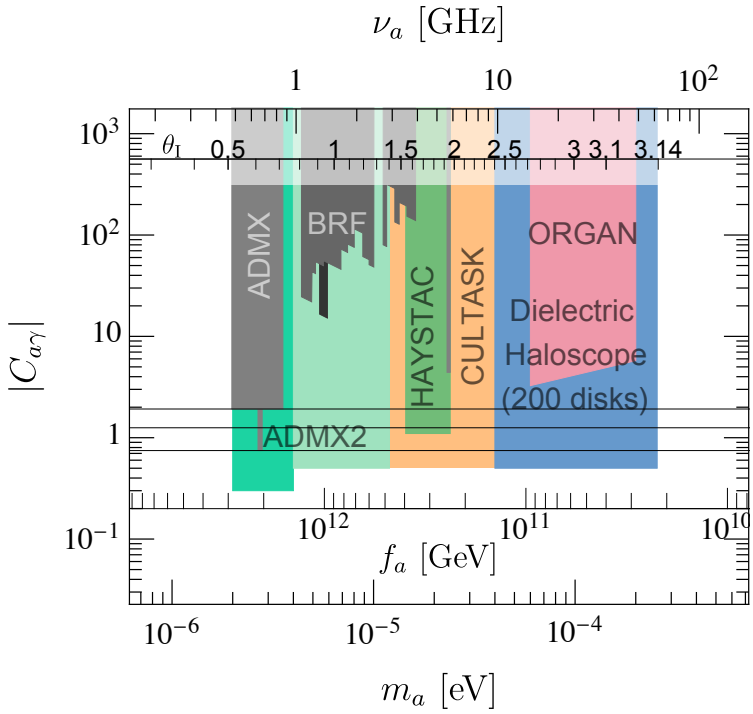

Figure 8.2: Example of the discovery potential (dark blue) of a second generation dielectric haloscope using 200 disks ($n = 5$, $\mathcal{S} = 1\,\mathrm{m}^2$, $B_\mathrm{e} = 10\,\mathrm{T}$, $\eta = 0.8$, $t_\mathrm{R} = 6\,\mathrm{hours}$) with quantum-limited detection in a 3-year campaign. All other curves and features are as described in figure 8.1.

was trying to verify the existence of DM axions, and an "axion telescope", which would try to extract the most astrophysical information possible out a discovered DM signal.

8.2.1 Search experiment

Despite the lack of direct directional sensitivity, there is still a wealth of information that can be extracted after detection. When an axion signal is found, measuring $P(\omega)$ gives immediately the axion power spectrum $|a(\omega)|^2$ from equation (8.1.1), as β would be roughly constant and known by design. Note that P only has a direct directional sensitivity if β does. However, we could easily extract the mass and an angle averaged velocity distribution. We require that the velocity distribution to satisfy

$$1 = \int d\omega f(\omega). \tag{8.2.1}$$

From equation (3.5.10) this gives

$$f(\omega) = \frac{v\omega^4}{V\bar{\rho}_a} \int \frac{d\Omega}{(2\pi)^3} \frac{|a(\mathbf{p})|^2}{2}. \tag{8.2.2}$$

With current receiver technology the number of channels (i.e., energy bins) in a single measurement can easily be $\gtrsim 10^4$; once a signal is detected these can be easily refocused to within the axion linewidth, allowing a very precise measurement of $f(\omega)$. Measuring the angle averaged velocity distribution alone contains significant astrophysical information: for example, if the axion DM forms a Bose-Einstein condensate as proposed in reference [195], we would expect an almost Dirac delta power spectrum rather than say a Maxwell-Boltzmann spectrum, as is often assumed. One could also look for transient phenomena, though detecting substructure such as axion miniclusters [84] and associated tidal streams [196] could take many years of measurement [197]. If found these would give strong hints about the origin and structural formation of axion DM. Recall that we only measure the axion generated E-field (like any other haloscope experiment), which depends on both the coupling $g_{a\gamma}$ and the DM density $\bar{\rho}_a$ given by equation (3.5.10). This degeneracy means that a haloscope experiment cannot determine the absolute local axion DM density and thus the normalisation of $a(\mathbf{p})$. Breaking the degeneracy between $g_{a\gamma}$ and ρ_a requires an independent measurement of $g_{a\gamma}$, an extraordinary challenge in this mass range.

Interestingly, $f(\omega)$ depends on time, due to the relative motion of the experiment with respect to the DM wind. With sufficiently long measurements one could detect annual and diurnal modulation, though the latter would be difficult [181,197,198]. The time dependence of $f(\omega)$ enters via very small shifts in the frequency of the axion, coming from small changes to the relative velocity of the DM with respect to the lab location on Earth. Annual modulation gives a relatively large (5%) change to the velocity, but of course happens over yearly timescales [198, 199]. By contrast diurnal modulation is relatively rapid, but so slight (on the order of 0.1% [198, 199]) that a very large amount of accumulated statistics would be needed to detect it. These measurements will help to confirm the veracity of the signal and give information about the local structure of DM. Measuring annual modulation would confirm the rough direction of the DM wind, as well as potentially detecting some substructure in the halo.

8.2.2 Axion telescope: true directional sensitivity

Once we know the axion mass and $f(\omega)$, we could become much more ambitious and move towards an "axion telescope". In this case, we desire the extra information contained in the axion velocity distribution, the full $a(\mathbf{p})$. To extract more information about $a(\mathbf{p})$ we need an experiment in which the output power is sensitive to $\mathbf{p}$, i.e., we require β to have a strong $\mathbf{p}$ dependence.

To achieve directional dependence one would build an experiment with a size comparable to the axion de Broglie wavelength: from chapters 6 and 7 we know that the generated power is then is highly sensitive to v_x. In this case, we can essentially measure the fraction of DM with a velocity in the x direction

(or a range of velocities, depending on the details of the setup). This is similar to the type of elongated cavity experiments proposed in reference [192], which would also be sensitive to the change in phase of the axion over the device. Using knowledge of the axion mass and power spectrum obtained from the search experiment, the dielectric disks could be placed to provide a very large signal, allowing for shorter measurements. For example, we could measure for a few hours rather than a day as was considered in the last section. These shorter measurements would be sensitive to velocity changes on shorter time scales, giving a more rapid accumulation of statistics.[9]

To see the directional dependence more concretely, note that detectors would in general only be sensitive the total power as a function of frequency,

$$P(\omega) \propto \int \mathrm{d}\Omega_v \, v^2 \beta^2(\mathbf{v}) |a(\mathbf{p})|^2. \tag{8.2.3}$$

From section 5.3.7 we saw that at lowest order we can approximate $\beta^2(\mathbf{v})$ as having either a linear or quadratic dependence on v_x, with the former only occurring for some systems without a mirror or strongly resonant behaviour. To get the optimal sensitivity to the three velocity directions, one could use an experiment consisting of four devices, three with a velocity dependence in a single linearly independent direction x_i, and one that simply measures $f(\omega)$. In this case, for each device the power depends only on v_i or v_i^2, so one can rearrange the measured powers to get

$$\langle v_i(\omega) \rangle = \frac{\int \mathrm{d}\Omega_v \, v_i \, |a(\mathbf{p})|^2}{\int \mathrm{d}\Omega_v \, |a(\mathbf{p})|^2} \tag{8.2.4}$$

for linearly dependent experiments or

$$\langle v_i^2(\omega) \rangle = \frac{\int \mathrm{d}\Omega_v \, v_i^2 \, |a(\mathbf{p})|^2}{\int \mathrm{d}\Omega_v \, |a(\mathbf{p})|^2} \tag{8.2.5}$$

for an experiment with quadratic dependence. In other words, we measure either the first or second moment of the velocity distribution in each direction. One would use the moments to try to reconstruct $a(\mathbf{p})$. With limited information one cannot do so perfectly without any assumptions, however the moments would make it much easier to fit some distribution models.

While the rotation of the Earth only changes the magnitude of the axion velocity by 0.1%, the changing direction gives a sizeable modulation of v_x depending on the alignment of the x-direction of the experiment and the DM wind. The directional modulation of the axion velocity allows each device to probe the axion velocity structure in a 2D plane.[10] As the device would now be

[9] Note that one does not actually have to perform shorter measurements, rather we simply want for the statistics to be accumulated at a faster rate. One could do a single long measurement and break the data down into different times during analysis.

[10] This 2D plane is given by the circle traced out by the x direction of the experiment as the Earth rotates. Note that the traced circle changes over the course of the year, allowing for limited 3D coverage with a single experiment.

the same size as the de Broglie wavelength, there would be an $\mathcal{O}(1)$ variation in the signal power, sensitive to much smaller variations in v_x than the $\mathcal{O}(10^{-9})$ shift in the axion frequency would allow. Directional detection would give a much more detailed map of the local DM than is possible with directionally insensitive devices, hence the name "axion telescope". We could build further evidence for the astrophysical origin of the signal by comparing very precisely the observed directionality of the signal with theory (i.e., the expected DM wind). Unlike a search experiment, any features observed would come with directional information; a search experiment can only infer the direction of DM wind using knowledge of the motion of the Earth. For example, if we see features such as axion miniclusters or tidal streams [197] we would know the direction that these objects came from. When combined with simulations of galaxy formation this directional information could be a test of structure formation.

Directional sensitivity can be partially achieved even with the search experiment. If the axion were discovered at the high-mass end of the scanned range, as the corresponding Compton wavelength λ is small there would be a lot of unused magnet volume. As the spacings between the dielectrics would be roughly $\lambda/2$ during a regular search, as λ decreases the total distance taken up by the haloscope decreases. We could then increase the spacing between the disks to a higher harmonic configuration where the distance is $\sim 3\lambda/2, 5\lambda/2$, etc. instead of $\sim \lambda/2$. In figure 8.3 we show the v_x dependence for an experiment using 80 dielectric disks arranged in a configuration optimised for a 25 GHz axion signal, using spacings of order $5\lambda/2$. For illustrative purposes, we assumed a Dirac delta velocity distribution, and have neglected the effects caused by the $\mathcal{O}(10^{-9})$ change in frequency, i.e., we show only the boost factor dependence. Note that the exact distribution does not significantly change this result: if a Maxwell-Boltzmann distribution is used instead the effect of the directional change is similar. While the exact velocity variation during the Earth's rotation depends on the location and alignment of the experiment, figure 8.3 gives the rough scale of the boost factor modulation. Maximal diurnal modulations can be achieved by aligning the x-direction of the experiment with the DM wind at some time of the day: this point gives the maximum v_x, with the minimum occurring 12 hours later. The power modulation caused by the axion velocity is typically 10%, significantly more pronounced than for the configuration shown in figures 7.14 and 7.15, and potentially detectable.

For most cases the effects of the DM velocity are slight for an experiment of a similar size to the planned MADMAX [21], but in the event that axions are discovered these effects contain a wealth of information about the DM in our universe, and potentially the galactic structure. As dielectric haloscopes are sensitive not only to the overall velocity distribution, but in principle have directional sensitivity, they would be a very powerful tool to study the DM in our galaxy. A study of these effects in detail, along with similar extensions of cavity haloscopes, is currently underway.

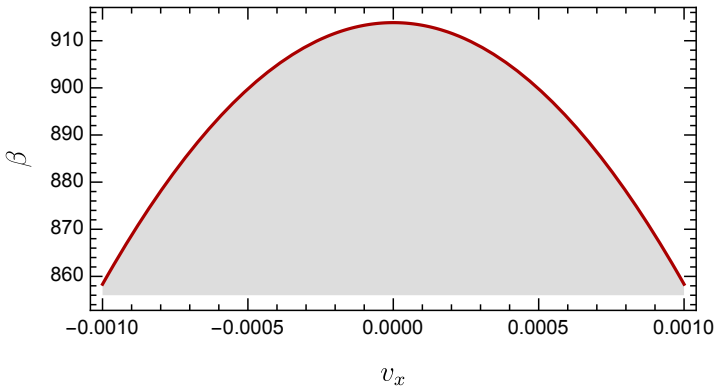

Figure 8.3: Boost factor $\beta(v_x)$ for 80 disks of 1 mm thickness optimised for a 25 GHz axion (with a bandwidth of 1 MHz). The disk spacings have been optimised around $5\lambda/2$. This gives the rough scale of diurnal modulations due to the changing axion velocity. Here we have assumed that $a(\mathbf{p})$ is a delta function.

Chapter 9

Conclusions and Outlook

The nature of DM remains one of the great roadblocks to our understanding of the Universe. The axion was originally introduced to resolve the Strong CP Problem but makes an excellent candidate for DM. If axions exist, they would be produced non-thermally in the early Universe, meaning that at least some fraction of DM would be guaranteed to be axionic. As axions have a unique phenomenology, they require specifically designed experiments to search for them. Very little of the axion parameter space has been experimentally tested, leading to a need for new design concepts to push into untouched, but still well motivated, mass ranges. This thesis explored one such new idea—dielectric haloscopes.

A dielectric haloscope, consisting of a mirror and many dielectric disks with adjustable vacuum gaps between them placed in a strong external B-field, is a unique approach to search for galactic DM axions in the high-mass region of 40–400 μeV. The oscillating axion field drives microwave radiation emitted orthogonally to the dielectric disks that can be picked up by a suitable detector. We have performed a systematic study of the EM response of such an apparatus, providing a firm theoretical foundation for this approach.

To this end we have calculated the microwave production rate and E-fields induced by the axion field at interfaces between different dielectric media, using both a classical transfer matrix formalism and a quantum field overlap integral formalism that allow one to study multilayer systems.

The classical transfer matrix calculation is based on encoding the discontinuous boundary conditions of the axion induced E-field into the regular transfer matrices of EM. These encode each interface and distance as a matrix, allowing for efficient computation of factors such as transmissivity, reflectivity and, with our extension, axion generated EM radiation.

The key point to the quantum field calculation was to use distorted photon wave functions caused by the presence of dielectric interfaces. For Primakoff axion-photon conversion or axion-photon oscillations in large-scale magnetic fields, translational invariance is broken by the external EM field and as such by the interaction term. In contrast for dielectric haloscopes translation invariance

is broken by the photon wave function, regardless of the interaction term. This situation is analogous to transition radiation at dielectric interfaces. We have used the distorted wave functions first introduced by Garibian for a quantum calculation of transition radiation. Our final expression for the production rate involves an overlap integral between the distorted photon wave functions and the magnetic field configuration, assuming a plane-wave initial axion.

Having a clear physical understanding of both pictures gives one greater flexibility to answer questions which may be obscured in one language. Moreover, we have clarified that a classical calculation is equivalent to a traditional first-order perturbative quantum calculation so long as we only ask for the average photon production rate.

By controlling the spacings between the interfaces it is possible to manipulate the frequency-dependent efficiency of microwave production which can be greatly enhanced. Unlike the traditional resonant cavity, it is possible to use a broadband search strategy, which is a key feature of dielectric haloscopes. We have shown that the area under the power boost as a function of frequency is independent of the chosen spacings, but grows linearly with the number of disks. For cavity haloscopes the power output is proportional to the overlap integral between the external B-field and the cavity-mode E-field. We have generalised this formalism to our case, i.e., the transfer matrix approach is equivalent to an overlap integral approach for any setup which converts axions to photons, regardless of resonant conditions. This equivalence allows a more direct comparison between dielectric and cavity haloscopes.

In addition to setting up this theoretical formalism, we have considered some of the practicalities involved in realising such an experiment. We expect the required precision in placing the dielectric disks to be of the order of a few μm. Further, we have seen that the frequency-dependent phase shift of a reflected microwave signal could be used to corroborate the boost factor curve, which potentially allows one to correct for positioning errors.

Lastly, we explored the effects of a non-zero axion velocity. Such a velocity can in principle have non-trivial effects in devices where the linear dimensions are comparable to the axion de Broglie wavelength. We saw that the main influence of the velocity of the axion comes from the change of phase of the axion itself over the haloscope: effects from the transverse velocities and axion induced H-field were always subdominant. With a generalised transfer matrix formalism, we could then study the change to the boost factor in detail. We found that for haloscopes smaller than $\sim$ 15–20% of the axion de Broglie wavelength, the axion's velocity could be safely ignored.

To see velocity effects in realistic setting, we studied an optimised 80 disk setup for the first time. While in normal situations velocity effects were entirely negligible, if one increases the spacing between each disk by odd multiples of $\lambda/2$ it is possible to see a noticeable shift in the boost factor. Such effects could be used in the event of a potential discovery of the axion, allowing one to observe effects such as diurnal modulation. Understanding the velocity dis-

tribution of DM would be both a useful check on the veracity of the signal, as well as allow one to preform astrophysical measurements, such as testing for diurnal modulation with directional sensitivity. A full study of what information one could extract with a directionally sensitive device is currently ongoing.

Developing the theoretical understanding of dielectric haloscopes is not purely for academic purposes. At the beginning of my PhD in 2015 the number of people interested and working on an experimental realisation of this idea was very limited. What would become the MADMAX Collaboration was formed by a handful of people, primarily at the Max Planck Institute for Physics (and in fact it was not yet an offical project inside the Max Planck Institute). Many practical and theoretical details were not known, for example how to extrapolate up to many disks, arrange these disks, or tell if the disks were positioned correctly. No prototype device had been built, and there were still doubts about the validity of the approach. However, at the end of 2017 MADMAX formed into an official and international collaboration with one of the largest particle physics laboratories in the world, DESY, agreeing to host a completed experiment. To go from idea to multi-institute collaboration in such a short period of time is a huge leap forward in high mass axion detection, and speaks to the hard work of many people.

Many of these early feasibility questions have been answered, either experimentally or theoretically. In addition to the theoretical developments discussed in this thesis, there have been considerable experimental efforts to characterise the behaviour of dielectric haloscopes. For example, a device of five disks has already been intensely studied and there exists a prototype capable of holding and positioning 20 sapphire disks, 20 cm in diameter. Such a device would be capable of searching for hidden photons in novel parameter space, though at the time of writing this thesis the main experimental focus is on understanding dielectric haloscopes themselves. There are currently ongoing magnet design studies for a roughly 10 T, 1 m aperture dipole magnet with two world leading institutions (CEA Saclay and Bilfinger Noell). This is not to say that all engineering problems have been solved. How to move and support $1\,\mathrm{m}^2$ dielectric disks inside a high Tesla magnetic field, to create such disks in the first place and the influence of 3D effects are still being studied. Fortunately, the growing size of the collaboration increases our capacity to look into these effects in detail. While there is always the possibility for an engineering or financial showstopper, the MADMAX Collaboration seems likely to realise a full scale experiment.

Further, MADMAX is no longer alone in exploring dielectric haloscopes. Recently a group at the Perimeter Institute in Canada has proposed using photon counting to build a dielectric haloscope in the optical range (searching for ALPS and hidden photons with masses $0.1 - 10\,\mathrm{eV}$) [193]. This proposal provides a great example of how widely applicable the ideas, formalisms and techniques developed in this thesis are. While building separate disks at such

frequencies is extremely difficult, alternating layers of dielectric materials are commonly made (for example, anti-reflective coatings on glasses). Rather than scanning parameter space by changing the positions of the disks, one would need to create many such stacks of materials.

Dielectric haloscopes are an exciting new way to search for high mass axion DM. The formalisms introduced here allow one to perform detailed and systematic studies of these devices. In the growing climate of serious attempts to detect axions, these formalisms should be extremely useful tools.

Appendix A

Proof of the Area Law

In section 4.3.3 we stated the Area Law in the form of equation (4.3.16) which we here prove. We assume the haloscope is described by N independent phase depths forming a vector $\boldsymbol{\delta} = (\delta_1, \ldots, \delta_N)$ where N could be smaller than the total number of $m-1$ dielectric regions between interfaces. In practice we will often use many identical dielectric disks, each of them having the same phase depth. Each phase depth is given as $\delta_j = n_j d_j$ with $\mathbf{d} = (d_1, \ldots, d_N)$ forming the configuration vector. We further assume that $\boldsymbol{\delta}$ consists only of real numbers, meaning that all dielectrics are taken to be lossless.

The boost amplitude $\mathcal{B}$ is constructed from polynomials and powers of all $e^{\pm i\delta_j}$. Overall, in the zero velocity limit $\mathcal{B}$ is 2π periodic in any of the δ_j, so similarly to equation (4.3.18) we may write it as an infinite Fourier series

$$\mathcal{B} = \sum_{\mathbf{k}} u_{\mathbf{k}}\, e^{i\mathbf{k}\cdot\boldsymbol{\delta}}\,, \tag{A.1}$$

where $\mathbf{k} = (k_1, \ldots, k_N)$ is a N-dim vector of positive and negative integers. The sum is over all integers, i.e., each individual k_j runs over integers from $-\infty$ to $+\infty$. There is a complex Fourier amplitude $u_{\mathbf{k}}$ for every $\mathbf{k}$. Notice that even for a finite series of interfaces, the sum runs to infinite k values because, in the expression for $\mathcal{B}$, we divide by a finite polynomial of $e^{ik_j\delta_j}$ expressions, usually leading to an infinite series.

We now consider the Area Law in the sense of $|\mathcal{B}|^2$ averaged over the N-dim space of all phase depths $\boldsymbol{\delta}$,

$$\left\langle |\mathcal{B}|^2 \right\rangle_{\boldsymbol{\delta}} = \langle \mathcal{B}\mathcal{B}^* \rangle_{\boldsymbol{\delta}} = \left(\prod_{j=1}^{N} \int_{-\pi}^{+\pi} \frac{d\delta_j}{2\pi} \right) \sum_{\mathbf{k},\mathbf{k}'} u_{\mathbf{k}} u^*_{\mathbf{k}'}\, e^{i(\mathbf{k}-\mathbf{k}')\cdot\boldsymbol{\delta}} = \sum_{\mathbf{k}} |u_{\mathbf{k}}|^2\,. \tag{A.2}$$

After integration, only those terms have survived which have $\mathbf{k} = \mathbf{k}'$ assuming n does not strongly depend on ω. Therefore, $\left\langle |\mathcal{B}|^2 \right\rangle_{\boldsymbol{\delta}}$ no longer depends either on ω or the configuration vector $\mathbf{d}$. Note that this sum is over interfaces—each $\mathbf{k}$ is associated with a δ and so is given by a corresponding interface. This is seen in, for example, equation (6.3.2).

We may achieve the same result if instead of averaging over $\boldsymbol{\delta}$ space we average over configuration space $\mathbf{d}$ except that we need to choose the integration volume such that each d_j covers a full period. Alternatively, we can average over an infinite volume.

We also get the same answer if we we integrate over frequency alone, replacing the N-dim integral over all phases by a 1-dim $d\omega$-integral, keeping in mind that each $\delta_j = n_j \omega d_j$. Explicitly,

$$\begin{aligned}\left\langle |\mathcal{B}|^2 \right\rangle &= \frac{1}{s_2 - s_1} \int_{s_1}^{s_2} ds \sum_{\boldsymbol{k},\boldsymbol{k}'} u_{\boldsymbol{k}} u^*_{\boldsymbol{k}'}\, e^{i(\boldsymbol{k}-\boldsymbol{k}')\cdot\boldsymbol{\delta}\, s} \\ &= \sum_{\boldsymbol{k}} |u_{\boldsymbol{k}}|^2 + \frac{1}{s_2 - s_1} \int_{s_1}^{s_2} ds \sum_{\boldsymbol{k}\neq\boldsymbol{k}'} u_{\boldsymbol{k}} u^*_{\boldsymbol{k}'}\, e^{i(\boldsymbol{k}-\boldsymbol{k}')\cdot\boldsymbol{\delta}\, s}\,. \end{aligned} \tag{A.3}$$

The second integral over phases vanishes if the integration range is large enough—all relative phases average to zero. In particular, if the relative phase depths δ_j are commensurate (rational fractions of each other), then $\mathcal{B}$ is periodic in ω and we may integrate over one such period, which however could be very large. In general, $\mathcal{B}$ is not periodic and the Area Law strictly applies only for a $d\omega$ integration over an infinite range. In practice, it is useful as an approximation if we integrate over a finite region that contains the main resonance.

Appendix B

Orthogonality of Garibian Wave Functions

To check that the Garibian wave functions used in section 5.3 are the correct free photon wave functions, we must check that they are eigenvalues of the Hamiltonian with the appropriate energy. In particular, for our wave functions we must confirm that [191]

$$\frac{1}{V\sqrt{\omega\omega'}}\int dV\frac{1}{2}\left[\epsilon\mathbf{E}^*(\mathbf{k}')\cdot\mathbf{E}(\mathbf{k})+\mathbf{B}^*(\mathbf{k}')\cdot\mathbf{B}(\mathbf{k})\right]=\omega\delta_{\mathbf{k},\mathbf{k}'}, \tag{B.1}$$

where for simplicity we have assumed that $\mu = 1$ throughout the device, and that ϵ does not depend on ω. Here $\mathbf{k}$ denotes the wavenumber of the incoming/outgoing photon wave function (i.e., the wavenumber outside the device). Recall that throughout this paper we defined $\mathbf{E}$ and $\mathbf{B}$ essentially classically in terms of the unnormalised wave function A_ω; the factor of $1/\sqrt{\omega V}$ must be restored to obtain a finite result from integrating over the Hamiltonian density. While this situation seems much more complicated than the case for plane waves, it will turn out that the contribution from every interface is exactly zero, allowing one to transform this integral into one over simple plane waves.

Consider arbitrary incoming waves of frequencies ω and ω', specified by some R'_0, L'_m and R_0, L_m. The primed coefficients correspond to waves of frequency ω' and the unprimed to waves of frequency ω. The integrals in the y, z directions are trivial, simply pulling out the area $\mathcal{S}$. Using equation (5.3.10) we can write the remaining integral in a piecewise fashion,

$$\begin{aligned}
&\frac{1}{2}\int dx\left[\epsilon E^*(\omega')E(\omega)+B^*(\omega')B(\omega)\right]=\omega\omega'\int_{-L/2}^{x_1}dx\,R'^*_0R_0e^{i\Delta x_0\Delta\omega}+L'^*_0L_0e^{-i\Delta x_0\Delta\omega}\\
&+\omega\omega'\sum_{s=1}^{m-1}n_s^2\int_{x_s}^{x_{s+1}}dx\,R'^*_sR_se^{in_s\Delta x_s\Delta\omega}+L'^*_sL_se^{-in_s\Delta x_s\Delta\omega}\\
&+\omega\omega'\int_{x_m}^{L/2}dx\,R'^*_mR_me^{i\Delta x_m\Delta\omega}+L'^*_mL_me^{-i\Delta x_m\Delta\omega},
\end{aligned} \tag{B.2}$$

where $\Delta\omega = \omega - \omega'$. Fortunately, it is sufficient to consider the evaluation of the integrals at the boundary and the interior integral associated with each interface separately. Ignoring the boundary terms for now, we can rewrite the interior integral as the sum over interfaces,

$$\begin{aligned}
&\omega\omega' \sum_{s=1}^{m-1} n_s^2 \int_{x_s}^{x_{s+1}} dx\, R'^*_s R_s e^{in_s \Delta x_s \Delta\omega} + L'^*_s L_s e^{-in_s \Delta x_s \Delta\omega} \\
=&\frac{i\omega\omega'}{\Delta\omega} \sum_{s=1}^{m} n_s \left[R'^*_s R_s - L'^*_s L_s\right] \\
&- n_{s-1} \left[R'^*_{s-1} R_{s-1} e^{id_{s-1} n_{s-1} \Delta\omega} - L'^*_{s-1} L_{s-1} e^{-id_{s-1} n_{s-1} \Delta\omega}\right], \qquad \text{(B.3)}
\end{aligned}$$

where we have already performed the integration. The first two terms (with a factor of n_s) correspond to the integral being evaluated on the rhs of the interface and the last two terms (with a factor of n_{s-1}) correspond to evaluating the integral on the lhs. To see that all terms in this sum cancel, we can look more closely at the terms coming from the lhs of the interface. From equation (4.3.7), we know that the R and L on the lhs and rhs of an interface between media with different refractive indices are related. More specifically,

$$\begin{pmatrix} R_r \\ L_r \end{pmatrix} = \mathsf{G}_{r-1}\mathsf{P}_{r-1} \begin{pmatrix} R_{s-1} \\ L_{s-1} \end{pmatrix}. \qquad \text{(B.4)}$$

With a little algebra, this allows us to rewrite the lhs interface terms using only quantities from the rhs of the interface,

$$n_{s-1} \left[R'^*_{s-1} R_{s-1} e^{id_{s-1} n_{s-1} \Delta\omega} - L'^*_{s-1} L_{s-1} e^{-id_{s-1} n_{s-1} \Delta\omega}\right] = n_s \left[R'^*_s R_s - L'^*_s L_s\right], \qquad \text{(B.5)}$$

which makes it immediately clear that every term in equation (B.3) vanishes. Thus the only terms contributing to the integral in equation (B.2) are the boundary terms evaluated at the edge of the normalisation volume ($\pm L/2$). To deal with these, we can use that conservation of energy requires the incoming and outgoing waves to be related by SU(2) matrices, and that we can switch left and right moving waves by changing the sign of the integration limits and x. This allows us to rewrite the integral in equation (B.2) as an integration over simple plane waves,

$$\omega\omega' \int_{-L/2}^{L/2} dx \left[R'^*_0 R_0 e^{ix\Delta\omega} + L'^*_m L_m e^{-ix\Delta\omega}\right] = \omega^2 L (R'^*_0 R_0 + L'^*_m L_m) \delta_{\omega,\omega'}, \qquad \text{(B.6)}$$

where the equality holds for very large L due to the oscillatory nature of the integral. Note that our Garibian wave functions are the only solutions that have definite asymptotic values of momentum, i.e., can be associated with a

single traveling photon entering/exiting the haloscope. For these waves, as either $|R_0|= 1$ or $|L_m|= 1$ so equation (B.1) must hold. Thus we see that our Garibian wave functions have the correct orthonormality conditions, and so can be used to quantise the photon field for use in section 5.3.

Appendix C

Transfer Matrix Formalism vs Overlap Integral Formalism

In this paper we have introduced both transfer matrix and overlap integral formalisms in chapters 4 and 5, respectively. While the results were checked to be equal for some simple cases, more work will be required to show that they must agree for all cases. Further, many readers are probably more familiar with the overlap integral formalism introduced by Sikivie to study cavity haloscopes [124]. This integral formalism was written in the language of quality factors and cavity volumes, requiring some reinterpretation to connect to our own formalism. We will check explicitly that the overlap integral formalism developed here agrees with that of Sikivie when restricted to a 1D cavity, in which both apply.

In chapter 5 we developed the overlap integral formalism by using a perturbative quantum field calculation. To show that the transfer matrix formalism, which was developed classically, agrees with the overlap integral approach we will derive the overlap integral formalism directly from transfer matrices. While the transfer matrices in chapter 4 are written as a sum over interfaces, we will thus use matrix identities to reorganise the sum by region rather than by interfaces. This will use only regular transfer matrices. Such an expression can be rewritten as an overlap integral for some E-field, which will turn out to be that given by the Garibian wave functions of chapter 5.

We will then review the overlap integral formalism for a 3D cavity and reduce it to a 1D resonator that may contain layers of dielectric media. We will then show that the Sikivie formalism gives the same result as our overlap integral formalism.

C.1 Overlap integral formalism for dielectric haloscopes: classical calculation

From chapter 5 we know what form the overlap integral must take. To compare with our classical transfer matrix formalism, we must show that one can also derive the overlap integral formalism classically. In particular, we will show that our transfer matrix formalism can be rewritten in the same form. This can be done by performing some matrix transformations and then reinterpreting each interface as contributing two boundary terms to an integral in each region.

C.1.1 Derivation from transfer matrices

For simplicity, throughout this calculation we will neglect the axion's velocity. We will consider a general situation as in section 4.3.1, with the refractive index in a region r being given by n_r. We will take the external magnetic field to be oriented along the z-direction, $\mathbf{B}_{\rm e}(x) = B_{\rm e}(x)\hat{\mathbf{z}}$, and to be piecewise homogeneous. Each region r will thus be characterised by a given $B_{{\rm e},r}$ and n_r. To normalise $B_{\rm e}$ we use

$$b(x) \equiv \frac{B_{\rm e}(x)}{B_{\rm e,max}} \quad \text{and} \quad b_r \equiv \frac{B_{\rm e,r}}{B_{\rm e,max}}. \tag{C.1.1}$$

To see how we might connect an overlap integral formalism, formed by an integral over let us now evaluate the overlap integral of some E-field in the z direction, $\int_{-\infty}^{\infty} dx\, Ab$, in terms of transfer matrices. We will be somewhat more general than chapter 5 and simply assume that A is formed by injecting some arbitrary incoming and outgoing waves to the system. To define A it is sufficient to specify R_0 and L_0. In this case, similar to equation (5.3.10) value of A in each region r is given by

$$A_r(x) = R_r e^{in_r\omega\Delta x_r} + L_r e^{-in_r\omega\Delta x_r}\,, \tag{C.1.2}$$

$\Delta x_r = x - x_r$. Recall that we define these coefficient with reference to the left most interface ($x = x_1$) for the waves on the lhs of the device and rightmost interface ($x = x_m$) for those on the rhs of the device. We can then split the integral by region. Each of the right and left moving waves in these regions is a simple plane wave, so evaluating the integrals simply gives us the boundary terms

$$\begin{aligned}\int_{-\infty}^{\infty} dx\, A(x)b(x) &= b_0\frac{R_0 - L_0}{i\omega n_0} + b_m\frac{L_m - R_m}{i\omega n_m} \\ &+ \sum_{r=1}^{m-1}\frac{b_r}{i\omega n_r}\left[R_r\left(e^{in_r\omega d_r} - 1\right) - L_r\left(e^{-in_r\omega d_r} - 1\right)\right]\end{aligned} \tag{C.1.3}$$

where $d_{r-1} = x_r - x_{r-1}$ is the thickness of each dielectric layer. Again, we have used that the integral at infinity vanishes due to its oscillatory nature. As the fields in each region are connected to the others by transfer matrices, one can rearrange this expression to obtain

$$i\omega \int_{-\infty}^{\infty} dx\, A(x)b(x) = \frac{b_0}{n_0}(R_0 - L_0) + \frac{b_m}{n_m}(L_m - R_m) \tag{C.1.4}$$

$$+ \begin{pmatrix} 1 \\ -1 \end{pmatrix}^T \left[\sum_{r=1}^{m-1} \frac{b_r}{n_r} (\mathsf{P}_r - \mathbb{1}) \mathsf{T}_1^r \right] \begin{pmatrix} R_0 \\ L_0 \end{pmatrix} . \tag{C.1.5}$$

This will be our target form: we must manipulate our generalised transfer matrix formalism to find a similar expression.

In our transfer matrix formalism, the boost amplitudes are given by the matrix equation (4.3.6) in the absence of incoming waves, $R_0 = L_m = 0$,

$$\begin{pmatrix} \mathcal{B}_R \\ 0 \end{pmatrix} = \mathsf{T} \begin{pmatrix} 0 \\ \mathcal{B}_L \end{pmatrix} + \mathsf{M} \begin{pmatrix} 1 \\ 1 \end{pmatrix}, \tag{C.1.6}$$

which solves as

$$\begin{pmatrix} \mathcal{B}_R \\ \mathcal{B}_L \end{pmatrix} = \frac{1}{\mathsf{T}[2,2]} \begin{pmatrix} \mathsf{T}[2,2] & -\mathsf{T}[1,2] \\ 0 & -1 \end{pmatrix} \mathsf{M} \begin{pmatrix} 1 \\ 1 \end{pmatrix}. \tag{C.1.7}$$

Let us focus first on $\mathcal{B}_R$. Note that the top two entries of the matrix multiplying M are the same as those of $\mathrm{Det}[\mathsf{T}]\mathsf{T}^{-1}$. Thus,

$$\mathcal{B}_R = \frac{\mathrm{Det}[\mathsf{T}]}{\mathsf{T}[2,2]} \begin{pmatrix} 1 \\ 0 \end{pmatrix}^T \mathsf{T}^{-1}\mathsf{M} \begin{pmatrix} 1 \\ 1 \end{pmatrix} \quad \text{with} \quad \mathsf{T}^{-1}\mathsf{M} = \sum_{s=1}^{m} \mathsf{S}_{s-1} (\mathsf{T}_0^s)^{-1}, \tag{C.1.8}$$

which is obtained from equation (4.3.8) using $\mathsf{T} = \mathsf{T}_s^m \mathsf{T}_0^s$ and its inverse $\mathsf{T}^{-1} = (\mathsf{T}_0^s)^{-1}(\mathsf{T}_s^m)^{-1}$. Using the Pauli matrix σ_2 that satisfies $\sigma_2^2 = \mathbb{1}$ and $\sigma_2 \mathsf{A}^T \sigma_2 = \mathrm{Det}[\mathsf{A}]\mathsf{A}^{-1}$ for any 2×2 matrix A,

$$\mathcal{B}_R = \frac{\mathrm{Det}[\mathsf{T}]}{\mathsf{T}[2,2]} \begin{pmatrix} i \\ -i \end{pmatrix}^T \sigma_2 \left[\mathsf{T}^{-1}\mathsf{M}\right]^T \sigma_2 \begin{pmatrix} 0 \\ i \end{pmatrix}, \tag{C.1.9}$$

where

$$\sigma_2 \left[\mathsf{T}^{-1}\mathsf{M}\right]^T \sigma_2 = \sum_{s=1}^{m} \mathsf{S}_{s-1} \sigma_2 \left[(\mathsf{T}_0^s)^{-1}\right]^T \sigma_2 = \sum_{s=1}^{m} \mathsf{S}_{s-1} \frac{n_s}{n_0} \mathsf{T}_0^s \tag{C.1.10}$$

with $\mathrm{Det}[(\mathsf{T}_0^s)^{-1}] = 1/\mathrm{Det}[\mathsf{T}_0^s] = n_s/n_0$ according to equation (4.3.9). This gives an expression for the boost amplitude that includes a sum over the interfaces,

$$\mathcal{B}_R = \frac{-\mathrm{Det}[\mathsf{T}]}{\mathsf{T}[2,2]} \begin{pmatrix} 1 \\ -1 \end{pmatrix}^T \sum_{s=1}^{m} \mathsf{S}_{s-1} \frac{n_s}{n_0} \mathsf{T}_0^s \begin{pmatrix} 0 \\ 1 \end{pmatrix}, \tag{C.1.11}$$

We will now rearrange equation (C.1.11) as a sum over the different regions r:

$$\begin{aligned}
\mathcal{B}_R &= \frac{-(n_0/n_m)}{\mathsf{T}[2,2]}\begin{pmatrix}1\\-1\end{pmatrix}^T\sum_{s=1}^{m}\frac{1}{2}\left(\frac{b_s}{n_s^2}-\frac{b_{s-1}}{n_{s-1}^2}\right)\frac{n_s}{n_0}\mathsf{T}_0^s\begin{pmatrix}0\\1\end{pmatrix}\\
&= \frac{-1}{n_m\mathsf{T}[2,2]}\frac{1}{2}\begin{pmatrix}1\\-1\end{pmatrix}^T\left[\left(\frac{b_m}{n_m^2}-\frac{b_{m-1}}{n_{m-1}^2}\right)n_m\mathsf{T}_0^m\right.\\
&\quad\left.+\left(\frac{b_{m-1}}{n_{m-1}^2}-\frac{b_{m-2}}{n_{m-2}^2}\right)n_{m-1}\mathsf{T}_0^{m-1}+\ \ldots\ +\left(\frac{b_1}{n_1^2}-\frac{b_0}{n_0^2}\right)n_1\mathsf{T}_0^1\right]\begin{pmatrix}0\\1\end{pmatrix}\\
&= \frac{-1}{n_m\mathsf{T}[2,2]}\frac{1}{2}\begin{pmatrix}1\\-1\end{pmatrix}^T\sum_{r=1}^{m-1}\frac{b_r}{n_r}\left(\mathbb{1}-\frac{n_{r+1}}{n_r}\mathsf{G}_r\mathsf{P}_r\right)\mathsf{T}_0^r\begin{pmatrix}0\\1\end{pmatrix}\\
&\quad-\frac{1}{n_m\mathsf{T}[2,2]}\frac{1}{2}\begin{pmatrix}1\\-1\end{pmatrix}^T\frac{b_m}{n_m}\mathsf{T}_0^m\begin{pmatrix}0\\1\end{pmatrix}\\
&\quad+\frac{1}{n_m\mathsf{T}[2,2]}\frac{1}{2}\begin{pmatrix}1\\-1\end{pmatrix}^T\frac{b_0n_1}{n_0^2}\mathsf{T}_0^1\begin{pmatrix}0\\1\end{pmatrix}\,,
\end{aligned}\tag{C.1.12}$$

where we have used equation (4.3.5c) with equation (C.1.1), $\mathsf{T}_0^{s+1}=\mathsf{G}_s\mathsf{P}_s\mathsf{T}_0^s$, and equation (4.3.9). We can use

$$\begin{pmatrix}1\\-1\end{pmatrix}^T\mathsf{G}_r=\frac{n_r}{n_{r+1}}\begin{pmatrix}1\\-1\end{pmatrix}^T.\tag{C.1.13}$$

to rewrite this as

$$\begin{aligned}
\mathcal{B}_R &= \frac{1}{n_m\mathsf{T}[2,2]}\frac{1}{2}\begin{pmatrix}1\\-1\end{pmatrix}^T\sum_{r=1}^{m-1}\frac{b_r}{n_r}\left(\mathsf{P}_r-\mathbb{1}\right)\mathsf{T}_0^r\begin{pmatrix}0\\1\end{pmatrix}\\
&\quad+\frac{1}{2n_m}\left[\left(1-\frac{\mathsf{T}[1,2]}{\mathsf{T}[2,2]}\right)\frac{b_m}{n_m}-\frac{1}{\mathsf{T}[2,2]}\frac{b_0}{n_0}\right].
\end{aligned}\tag{C.1.14}$$

This now looks reassuringly similar to (C.1.5). If one chooses $R_0=0$ and $L_0=1/\mathsf{T}[2,2]$, then from (4.3.10) $R_m=\mathsf{T}[1,2]/\mathsf{T}[2,2]$ and $L_m=1$. From (C.1.5) we see that

$$\mathcal{B}_R=i\frac{\omega}{2n_m}\int dx\,A_Rb\,,\tag{C.1.15}$$

where we have defined A_R as the field given by inserting a left moving wave of amplitude 1 on the rhs of the device (i.e, $R_0=0$, $L_m=1$). Note that the amplitude being 1 is due to the boost amplitude being a dimensionless quantity, meaning that the A-field is also dimensionless, as in chapter 5. If one wishes to avoid this, one can restore A_R as a dimensional quantity by

dividing by the initial amplitude. This is precisely one of the Garibian wave functions found in chapter 5, albeit if the medium m is non-zero there are some subtleties with the normalisation. Note that if one calculates the power of an electromagnetic wave in a medium, there is an extra factor of n^2, meaning that the same power is being dissipated from the axion as the case where no medium is present.

To get the boost amplitude on the other side we can simply substitute 0 and m and rearrange the terms

$$\begin{aligned}\mathcal{B}_L &= \frac{1}{2n_0}\begin{pmatrix}1\\-1\end{pmatrix}^T \sum_{r=1}^{m-1}\frac{b_r}{n_r}\left(\mathsf{P}_r - \mathbb{1}\right)\mathsf{T}_0^r \begin{pmatrix}1\\ -\frac{\mathsf{T}[1,2]}{\mathsf{T}[2,2]}\end{pmatrix} \\ &\quad + \frac{1}{2n_0}\left[-\frac{\mathrm{Det}\mathsf{T}}{\mathsf{T}[2,2]}\frac{b_m}{n_m} + \left(1+\frac{\mathsf{T}[2,1]}{\mathsf{T}[2,2]}\right)\frac{b_0}{n_0}\right]. \end{aligned} \tag{C.1.16}$$

So we find that

$$\mathcal{B}_{L,R} = i\frac{\omega}{2n_{0,m}}\int dx\, A_{L,R} b\,, \tag{C.1.17}$$

where $A_{L,R}$ is the complex field amplitude given by shining a wave of magnitude 1 in from either the 0 or mth layer (left and right hand sides, respectively) in the absence of axions. I.e., we have recovered the Garibian wave functions used in Section 5 and proven (5.3.8). Note that without the quantum calculation these wave functions have no physical interpretation: they are just a mathematical trick. This formalism is fully general—it can be applied to a completely open system, even when there is no resonant behaviour.

We have successfully transformed the transfer matrix formalism into an overlap integral formalism as derived in Section 5. Thus we see that the two agree in all cases. To see this correspondence in practice, we compare the two formalisms in figure C.1 for the B50 configuration of section 7.2.1. The two methods give very good agreement for the boost factor even off resonance (this agreement is not perfect, as the integral was done numerically, and so not over all space). However, the overlap integral method is more computationally involved as one must first find $E_{L,R}$ and then integrate them.

C.2 Sikivie's overlap integral formalism

The physical picture of the original overlap integral formalism is that of the axion field acting as a source inside the cavity, which feeds the resonance so that a steady state is reached where power exiting the cavity is balanced with the power injected by the axion field. If the cavity quality factor Q is very large, the field strength $\mathbf{E}_\alpha$ of the relevant resonant mode far exceeds the source fields which are neglected.

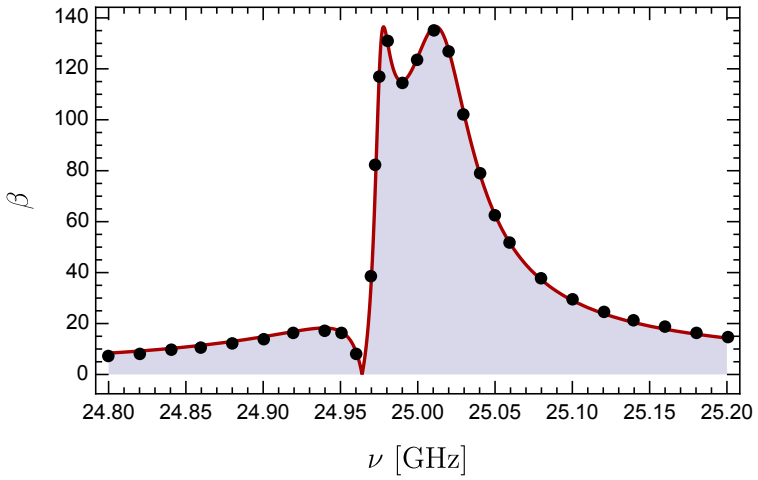

Figure C.1: Comparison of the boost factor β calculated by the generalised overlap integral formalism (black dots) and the transfer matrix formalism (red curve). We plot $\beta(\nu)$ for the B50 configuration of section 7.2.1, i.e., a dielectric haloscope consisting of 20 disks, 1 mm thick, refractive index $n = 5$, mirror on one side, optimised for bandwidth of 50 MHz centred on 25 GHz (as shown in figure 7.1).

C.2.1 3D cavity

With good approximation, the resonant mode is a standing wave with a time-dependent electric field configuration of the form $\mathbf{E}_\alpha(\mathbf{x})\sin(\omega t)$, where the eigenfrequency ω on resonance corresponds to the axion mass m_a. For a homogeneous external field $\mathbf{B}_\mathrm{e}$, the power extracted from a 3D cavity is [124]

$$P_\mathrm{cav} = \kappa \mathcal{G} V \frac{Q}{m_a} \rho_a g_{a\gamma}^2 B_\mathrm{e}^2, \tag{C.2.1}$$

where V is the cavity volume and

$$\mathcal{G} = \frac{\left(\int dV\, \mathbf{E}_\alpha \cdot \mathbf{B}_\mathrm{e}\right)^2}{V B_\mathrm{e}^2 \int dV\, \mathbf{E}_\alpha^2} \tag{C.2.2}$$

is the geometry factor. Moreover,

$$Q = -\omega\, U/\dot{U}_l \tag{C.2.3}$$

is the loaded quality factor, where U is the energy stored in the cavity in mode α and $\dot{U}_l$ is the rate with which energy is lost. Some of this loss is simply dissipation, whereas some part is the extracted signal $\dot{U}_s$, defining the cavity coupling factor

$$\kappa = \dot{U}_s/\dot{U}_l\,. \tag{C.2.4}$$

On resonance, electric and magnetic fields contribute equally to the energy content U so that

$$U = \frac{1}{4}\int dV \left(\mathbf{E}_\alpha^2 + \mathbf{B}_\alpha^2\right) = \frac{1}{2}\int dV\, \mathbf{E}_\alpha^2\,, \tag{C.2.5}$$

where $\mathbf{B}_\alpha$ is the B-field of mode α. Notice that one factor $1/2$ in these expressions derives from the cycle average. When computing P_{cav} given by equation (C.2.1), this integral will cancel with that in the denominator of $\mathcal{G}$. We use equation (3.5.10) with $m_a = \omega$ to introduce

$$E_0^2 = g_{a\gamma}^2 B_{\text{e}}^2 |a_0|^2 = \frac{g_{a\gamma}^2 B_{\text{e}}^2}{\omega^2}\omega^2 |a_0|^2 = \frac{g_{a\gamma}^2 B_{\text{e}}^2}{\omega^2} 2\rho_a\,. \tag{C.2.6}$$

We can now recast equation (C.2.1) in the form

$$P_{\text{cav}} = -\frac{\dot{U}_s}{2(\dot{U}_l)^2}\frac{m_a^2\left(\int dV\, \mathbf{E}_\alpha \cdot \mathbf{B}_{\text{e}}\right)^2}{B_{\text{e}}^2}\frac{E_0^2}{2}\,. \tag{C.2.7}$$

This form will allow us to more easily compare Sikivie's calculation with the language used in this thesis. That (C.2.1) can be reduced so much is due to significant degeneracy between the various terms, which are written in that way to seperate out quantities that are easily described experimentally.

C.2.2 1D cavity

Now let us consider a 1D cavity made of reflecting walls and several regions r with different refractive indices n_r based on the same arrangements as in section 4.3.1. The setup is shown in figure C.2 and is a special case of the

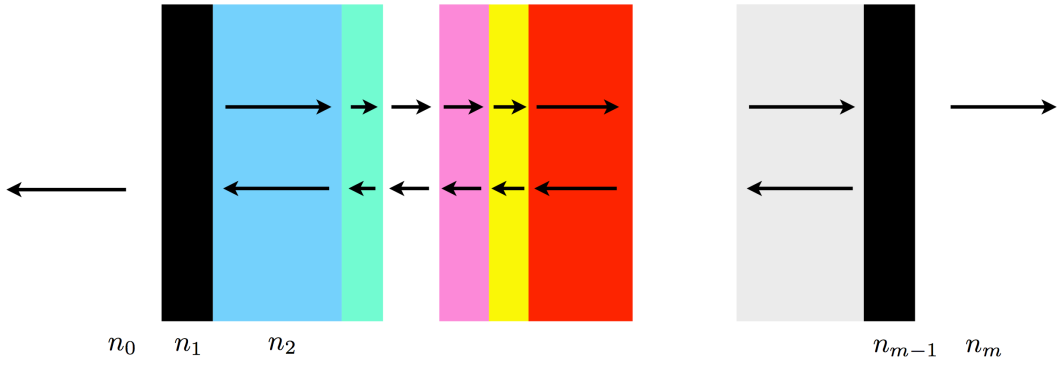

Figure C.2: A 1D cavity consisting of several dielectric regions r with different refractive indices n_r represented by different colors. Regions 1 and $m-1$ are the cavity walls, made of extremely reflective materials with a high refractive index, and regions 0 and m the vacuum space outside of the cavity. Left and right moving EM waves are represented by the corresponding arrows.

one in figure 4.4: Regions 0 and m are the vacuum space outside of the cavity

($n_0 = n_m = 1$), regions 1 and $m-1$ the cavity walls made of reflective materials with a large refractive indices n_1 and n_{m-1}, and regions 2 to $m-2$ the ones inside the cavity. The optical thickness of each region r is $\delta_r = \omega n_r(x_{r+1} - x_r)$. The arrows illustrate left and right moving EM waves in each homogeneous region.

In the following we will consider a leaky cavity as well as the limit of a closed one. In the leaky case, some EM waves travel away from the mirrors in regions 0 and m as illustrated in figure 4.4. The refractive indices of the mirrors n_1 and n_{m-1} are large but finite and we assume phase depths $\sin\delta_1 = \sin\delta_{m-1} = 1$, i.e., maximal reflectivity, although other values of $\sin\delta_1$ and $\sin\delta_{m-1}$ can be chosen. For increasing n_1 and n_{m-1}, the physical thickness of the mirrors would have to be chosen ever smaller. Moreover, $n_2/n_1 \ll 1$ and $n_{m-2}/n_{m-1} \ll 1$ is assumed which implicitly avoids the possibility of transparent cavity walls via a simple combination of two adjacent $\lambda/4$ layers of material with the same refractive index n_r. For a closed (perfect) cavity, we assume $n_1 \sin\delta_1 \to \infty$ and $n_{m-1}\sin\delta_{m-1} \to \infty$.

We will consider modes with the electric field oriented in the z-direction, $\mathbf{E}_\alpha = i\omega A(x)\,\hat{\mathbf{z}}$, where mode subscripts will be suppressed to simplify our notation from here on. We consider a piecewise homogeneous magnetic field such as given by (C.1.1). Then we express the overlap integral in the form

$$\frac{\left(\int dV\, \mathbf{E}_\alpha \cdot \mathbf{B}_\mathrm{e}\right)^2}{B_{\mathrm{e,max}}^2} = \omega^2 \mathcal{S}^2 \left(\int dx\, Ab\right)^2 , \tag{C.2.8}$$

where $\mathcal{S}$ is the transverse area considered. Note that as the modes of a cavity are standing waves we can treat A as real.

We can track the fields inside the cavity by using (C.1.2). We assume that there are no incoming waves outside of the cavity walls, i.e., $R_0 = L_m = 0$. For a perfect cavity, the outgoing waves vanish as well ($L_0 = R_m = 0$), whereas they take small nonvanishing values in the leaky cavity case.

In the leaky cavity case, the energy loss per unit area results from the waves exiting the cavity into the external media (regions 0 and m in figure C.2) and from internal losses, which we define by unit area $\dot{U}_\mathrm{int} \equiv -\omega^2 \Gamma \mathcal{S}/2$ in terms of a damping rate $\omega^2\Gamma$,

$$\dot{U}_l = -\omega^2 \mathcal{S}\left(\frac{L_0^2}{2} + \frac{R_m^2}{2} + \frac{\Gamma}{2}\right). \tag{C.2.9}$$

We take the signal from only one side of the device, $\dot{U}_{s,m} = \omega^2 \mathcal{S} R_m^2/2$ or $\dot{U}_{s,0} = \omega^2 \mathcal{S} L_0^2/2$, in analogy with our boost factor considerations, e.g., in equations (4.3.11a) and (4.3.11b). The corresponding power per unit area is

$$\frac{P_m}{\mathcal{S}} = \frac{R_m^2}{\left(R_m^2 + L_0^2 + \Gamma\right)^2}\omega^2 \left(\int dx\, Ab\right)^2 \frac{E_0^2}{2}, \tag{C.2.10a}$$

$$\frac{P_0}{\mathcal{S}} = \frac{L_0^2}{\left(R_m^2 + L_0^2 + \Gamma\right)^2}\omega^2 \left(\int dx\, Ab\right)^2 \frac{E_0^2}{2}. \tag{C.2.10b}$$

These expressions allow us to identify the respective boost factors with

$$\beta_m = \frac{R_m}{R_m^2 + L_0^2 + \Gamma}\,\omega \int dx\, Ab\,, \tag{C.2.11a}$$

$$\beta_0 = \frac{L_0}{R_m^2 + L_0^2 + \Gamma}\,\omega \int dx\, Ab\,. \tag{C.2.11b}$$

Notice that in this derivation we have taken A and the amplitudes R_m and L_0 to be real, which is approximately possible because the resonance configuration forms an approximate standing wave in the cavity and the emerging waves traveling away are in phase with the cavity at the surface. Note that as they are standing waves, the cavity modes can be chosen to be purely real.

C.2.3 Field configurations inside a closed 1D cavity

To evaluate the overlap integral in equation (C.2.11), the electric field configurations of the cavity modes are required. We will now determine these field configurations in the limit of a perfect cavity. When returning to the case of a leaky cavity in section C.2.4 below, we will assume that the small losses to regions 0 and m will modify these field configurations in a negligible way.

The boundary conditions for a perfect cavity are simply given by $A^{(2)}(x_2) = 0$ and $A^{(m-2)}(x_{m-1}) = 0$ because the fields vanish inside perfect mirrors, $A^{(1)} = A^{(m-1)} = 0$. These conditions require the corresponding R_r and L_r components to be equal in magnitude and opposite in phase,

$$\begin{pmatrix} R_2 \\ L_2 \end{pmatrix} = R_2 \begin{pmatrix} 1 \\ -1 \end{pmatrix} \quad \text{and} \quad \begin{pmatrix} R_{m-2}^D \\ L_{m-2}^D \end{pmatrix} = R_{m-2}^D \begin{pmatrix} 1 \\ -1 \end{pmatrix}, \tag{C.2.12}$$

where the superscript D denotes fields at the rhs of the region r, i.e., at $x = x_{r+1}$. To specify the electric field that we are integrating over, one can simply specify the field at any point and then use the regular EM transfer matrices to calculate the field everywhere inside the cavity. (We will neglect settings with disconnected configurations, i.e., completely independent cavities.) For example, using the transfer matrices T_b^a given in equation (4.3.7), all $A^{(r)}(x)$ inside the cavity can be built from the boundary condition at x_2 via

$$\begin{pmatrix} R_r \\ L_r \end{pmatrix} = \mathsf{T}_2^r \begin{pmatrix} R_2 \\ L_2 \end{pmatrix} = \mathsf{T}_2^r \begin{pmatrix} 1 \\ -1 \end{pmatrix} R_2\,. \tag{C.2.13}$$

C.2.4 Leaky cavity

We now return to the case of the leaky cavity. As long as the fields leaking to the vacuum regions are much smaller than those inside the cavity the distortion of the perfect-cavity modes will be small. Indeed, we use now the

approximation that this distortion is negligible so that the leaking fields can be related to fields in regions $r = 2$, $m - 2$ in the form

$$\begin{pmatrix} R_2 \\ L_2 \end{pmatrix} = \quad \mathsf{T}_0^2 \begin{pmatrix} 0 \\ L_0 \end{pmatrix} = \frac{in_1}{2n_2} \begin{pmatrix} 1-\varepsilon_1 \\ -1-\varepsilon_1 \end{pmatrix} L_0 \,, \tag{C.2.14a}$$

$$\begin{pmatrix} R_{m-2}^D \\ L_{m-2}^D \end{pmatrix} = \quad \mathsf{T}_m^{m-2} \begin{pmatrix} R_m \\ 0 \end{pmatrix} = -\frac{1}{n_{m-2}} \frac{in_{m-1}}{2} \begin{pmatrix} 1+\varepsilon_{m-1} \\ -1+\epsilon_{m-1} \end{pmatrix} R_m \,, \tag{C.2.14b}$$

with the transfer matrices (for vacuum outside the cavity, i.e., $n_{0,m} = 1$)

$$\mathsf{T}_0^2 \;=\; \frac{in_1}{2n_2} \begin{pmatrix} 1+\varepsilon_1 & 1-\varepsilon_1 \\ -1+\varepsilon_1 & -1-\varepsilon_1 \end{pmatrix} , \tag{C.2.15a}$$

$$\mathsf{T}_{m-2}^m \;=\; \frac{in_{m-1}}{2} \begin{pmatrix} 1+\varepsilon_{m-1} & 1-\varepsilon_{m-1} \\ -1+\varepsilon_{m-1} & -1-\varepsilon_{m-1} \end{pmatrix} . \tag{C.2.15b}$$

We have introduced the small parameters $\varepsilon_{m-1} \equiv n_{m-2}/n_{m-1}$ and $\varepsilon_1 \equiv n_2/n_1$, not to be confused with the dielectric constants. Neglecting terms $\propto \varepsilon_{1,m-1}$, the boundary conditions (C.2.12) hold for

$$R_2 = \frac{in_1}{2n_2} L_0 \equiv Z_0 L_0 \quad \text{and} \quad R_{m-2}^D = -\frac{in_{m-1}}{2n_{m-2}} R_m \equiv Z_m R_m \,. \tag{C.2.16}$$

Here one can see that the electric fields in the cavity are larger by one power of the large factors $n_{1,m-1}$ with respect to the fields outside. Indeed, the factors $Z_{0,m}^2 \propto n_{1,m-1}^2/4$ play a role similar to the quality factor of the cavity (in absence of dissipation).

We can now substitute equation (C.1.5) into (C.2.10) and apply (C.2.16) to find the emerging power in the form

$$\frac{P_m}{A} = \quad Z_0^2 \frac{R_m^2 L_0^2}{\left(R_m^2 + L_0^2 + \Gamma\right)^2} \left| \begin{pmatrix} 1 \\ -1 \end{pmatrix}^T \left[\sum_{r=2}^{m-2} \frac{b_r}{in_r} (\mathsf{P}_r - \mathbb{1}) \mathsf{T}_2^r \right] \begin{pmatrix} 1 \\ -1 \end{pmatrix} \right|^2 \frac{E_0^2}{2} \,, \tag{C.2.17a}$$

$$\frac{P_0}{A} = \quad Z_0^2 \frac{L_0^4}{\left(R_m^2 + L_0^2 + \Gamma\right)^2} \left| \begin{pmatrix} 1 \\ -1 \end{pmatrix}^T \left[\sum_{r=2}^{m-2} \frac{b_r}{in_r} (\mathsf{P}_r - \mathbb{1}) \mathsf{T}_2^r \right] \begin{pmatrix} 1 \\ -1 \end{pmatrix} \right|^2 \frac{E_0^2}{2} \,. \tag{C.2.17b}$$

Note the the terms coming from integrating outside to the cavity have been neglected, as in this formalism we are only integrating over the interior of the cavity. We have successfully expressed the overlap integral in terms of a sum over transfer matrices, which will allow us to make a direct comparison to our overlap integral formalism.

C.2.5 Direct comparison with Sikivie's formalism

Conceptually both Sikivie and our formalisms must agree, but it is still useful to check this. In particular, we must check that one integrates the same electric field in both cases and that the normalisations of the integrals agree. In our generalised overlap integral formalism, the normalisation comes from the transmissivity, whereas in the original formalism this comes from, in part, the quality factor and coupling factor.

Instead of considering a situation where the cavity has already had some power input from an unspecified (axion) source, in this transfer matrix inspired picture we are inserting the power externally. However, due to the presence of the cavity walls these are equivalent: a resonant standing wave looks the same regardless of how it is excited. To recover exactly the same formula, assuming a cavity setup as in section C.2.4 we can use $\mathsf{T}_0^r = \mathsf{T}_2^r \mathsf{T}_0^2$, so

$$\mathsf{T}_0^2 \begin{pmatrix} R_0 \\ L_0 \end{pmatrix} = (R_0 + L_0) Z_0 \begin{pmatrix} 1 \\ -1 \end{pmatrix} \tag{C.2.18}$$

and we can write

$$\mathcal{B}_R \simeq Z_0 \frac{1}{\mathsf{T}[2,2]} \frac{1}{2} \begin{pmatrix} 1 \\ -1 \end{pmatrix}^T \sum_{r=2}^{m-2} \frac{1}{n_r} \left(\mathsf{P}_r - \mathbb{1}\right) \mathsf{T}_2^r \begin{pmatrix} 1 \\ -1 \end{pmatrix}, \tag{C.2.19a}$$

$$\mathcal{B}_L \simeq Z_0 \left(1 - \frac{\mathsf{T}[1,2]}{\mathsf{T}[2,2]}\right) \frac{1}{2} \begin{pmatrix} 1 \\ -1 \end{pmatrix}^T \sum_{r=2}^{m-2} \frac{1}{n_r} \left(\mathsf{P}_r - \mathbb{1}\right) \mathsf{T}_2^r \begin{pmatrix} 1 \\ -1 \end{pmatrix}, \tag{C.2.19b}$$

which has exactly the same structure we found in the cavity case, cf. equation (C.2.17): the same electric fields are integrated in both cases. Again we have neglected the fields inside the cavity walls. To complete the comparison we must confirm that the normalisations of the integrals agree, i.e., that

$$\frac{1}{\mathsf{T}[2,2]} = \frac{2R_m L_0}{R_m^2 + L_0^2 + \Gamma}, \tag{C.2.20a}$$

$$1 - \frac{\mathsf{T}[1,2]}{\mathsf{T}[2,2]} = \frac{2L_0^2}{R_m^2 + L_0^2 + \Gamma}, \tag{C.2.20b}$$

where we are implicitly assuming the absolute values of all the quantities. To show the validity of equation (C.2.20), we must restrict ourselves to the case of a cavity on resonance, without which (C.2.1) does not apply. From equation (C.2.19) we know R_m and L_0. They are the same up to factors of $1/\mathsf{T}[2,2]$ and $1 - \mathsf{T}[1,2]/\mathsf{T}[2,2]$. Further, as we assume a resonance forming a standing wave, $\mathsf{T}[1,2]/\mathsf{T}[2,2]$ is real, i.e., a standing wave does not experience

a phase shift. Because of this we have

$$\begin{aligned}\frac{2R_mL_0}{R_m^2+L_0^2+\Gamma} &= 2\frac{\frac{1}{\mathsf{T}[2,2]}\left(1-\frac{\mathsf{T}[1,2]}{\mathsf{T}[2,2]}\right)}{\left(\frac{1}{\mathsf{T}[2,2]}\right)^2+\left(1-\frac{\mathsf{T}[1,2]}{\mathsf{T}[2,2]}\right)^2+\Gamma} \\ &= \frac{1}{\mathsf{T}[2,2]}\frac{2\left(1-\frac{\mathsf{T}[1,2]}{\mathsf{T}[2,2]}\right)}{\left(\frac{1}{\mathsf{T}[2,2]}\right)^2+\left(\frac{\mathsf{T}[1,2]}{\mathsf{T}[2,2]}\right)^2+1-2\frac{\mathsf{T}[1,2]}{\mathsf{T}[2,2]}+\Gamma} \\ &= \frac{1}{\mathsf{T}[2,2]}, \end{aligned} \tag{C.2.21}$$

where we have used that $1/\mathsf{T}[2,2]^2 + (\mathsf{T}[1,2]/\mathsf{T}[2,2])^2 = 1-\Gamma$ (conservation of energy). As $L_0/R_m = \mathsf{T}[2,2]-\mathsf{T}[1,2]$ we can similarly prove equation (C.2.20b).

So the generalised overlap integral formalism developed here agrees with that of Sikivie for a resonant cavity, as one would expect. Indeed, we can make the connection more apparent by rearranging expression (C.1.17) to get

$$P_{L,R} = \mathcal{G}_{\mathrm{d},L,R}V\frac{Q_{\mathrm{d},L,R}}{m_a}\rho_a g_{a\gamma}^2 B_{\mathrm{e}}^2, \tag{C.2.22a}$$

$$\mathcal{G}_{\mathrm{d},L,R} = \frac{\left|\int dx\, E_{L,R}B_{\mathrm{e}}\right|^2}{LB_{\mathrm{e}}^2U_{L,R}}, \tag{C.2.22b}$$

$$Q_{\mathrm{d},L,R} = m_a\frac{1}{4}\frac{U_{L,R}}{E_{\mathrm{in}}^2}, \tag{C.2.22c}$$

where L is the length of the haloscope, $V=\mathcal{S}L$ and

$$U_{L,R} = \frac{1}{2}\int dx\,\epsilon(x)|E_{L,R}|^2+|B_{L,R}|^2. \tag{C.2.23}$$

As L factors out of P, the actual value of L is irrelevant. Here $E_{L,R}(x) = A_{L,R}(x)E_{\mathrm{in}}$, i.e., simply turning our $A_{L,R}$ into E-fields which are injected into the system with a magnitude E_{in}, with $B_{L,R}$ being the associated B-field. Note that $Q_{\mathrm{d},L,R}$ are not true quality factors: rather than giving the generic response of the system to any input, it depends on the input wave (i.e., $Q_{\mathrm{d},L} \neq Q_{\mathrm{d},R}$ in general). The cavity coupling κ (where applicable) is built into our choice of electric fields and the loss tangents of the media.

While the overlap integral formalism can be extended to non-resonant cases, the usual physical interpretation cannot. For a resonant cavity, the axion excites the same resonant mode that is integrated over. For a general dielectric haloscope, the integrated electric field is different from the one generated by the axion field. For example, when one side is a mirror, our integrated electric field is a standing wave. However, when the axion field is included, traveling waves are also present, as can seen in, for example, figure C.3. Thus, the

generalised overlap integral formalism is more of a mathematical tool than a physical picture.

In this language, one sees that the main concept behind a dielectric haloscope is to use dielectrics to increase the volume and geometry factor of a haloscope while maintaining the flexibility to use resonant and non-resonant setups. This flexibility distinguishes dielectric haloscopes from the more limited cases studied in references [133,138], which propose enhancing the volume and geometry factor of a strictly resonant cavity by either modifying the magnetic field or by using dielectrics.

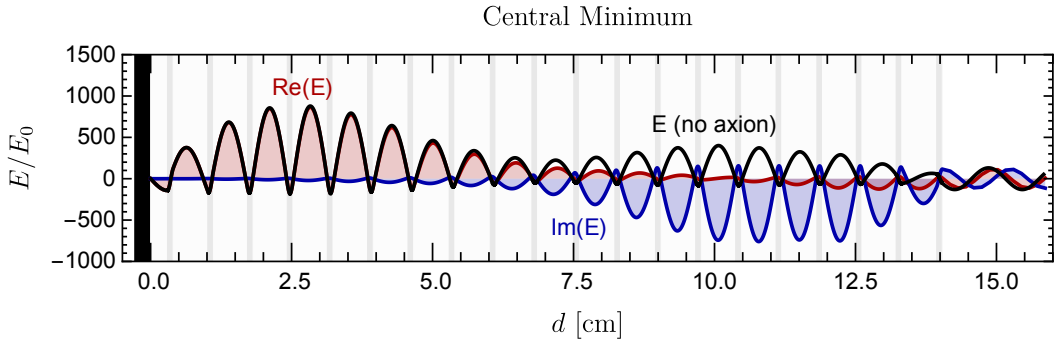

Figure C.3: Real and imaginary parts of the electric field produced by the axion (red and blue) and the electric field in the absence of axions (black) as a function of distance from the mirror d inside a dielectric haloscope for our B50 configuration (20 disks, 1 mm thick, refractive index $n = 5$, mirror on one side, bandwidth of 50 MHz centred on 25 GHz). The electric field in the absence of axions has been scaled so that it matches the one produced by axions near the mirror. While there is a correlation between the two, they are different in general. The agreement generally seems to be better on resonance. We consider the frequency associated with the central minimum in figure 7.1.

Appendix D

Scan Optimisation

Any experiment to search for dark-matter axions needs to scan over a large frequency range. For a dielectric haloscope, this means to re-adjust the disk spacings for every search channel i centred on some frequency ν_i, an operation that requires a re-adjustment time t_{R}. Note that as described in chapter 8 by design a search experiment will be insensitive to the axion velocity, so we will neglect it throughout this discussion. For a given set of disks, we seek the optimal channel width $\Delta\nu_i$ to minimise the overall search time

$$t = \sum_i \left(\Delta t_i + t_{\mathrm{R}}\right) , \tag{D.1}$$

where we take t_{R} to be independent of channel i. In section 8.1 we assumed that $\Delta\nu_i$ should be chosen such that $\Delta t_i = t_{\mathrm{R}}$. We here prove this intuitive assumption to be exact.

A given set of dielectric disks allows us to cover a certain frequency range ν_1 to ν_2 by re-adjusting the spacings alone. We need to find the optimal frequency channels ν_i (width $\Delta\nu_i$ and boost factor β_i) to cover the search range $\sum_i \Delta\nu_i = \nu_2 - \nu_1$. In order to achieve the desired signal-to-noise in a given channel, the relation between measurement time and boost factor is given by equation (4.1.18) to be $\Delta t_i = a_i/\beta_i^4$ with

$$\begin{aligned} a_i \sim 400^4 \times 1.3\,\mathrm{days} &\left(\frac{\mathrm{S/N}}{5}\right)^2 \left(\frac{1\,\mathrm{m}^2}{\mathcal{S}}\right)^2 \left(\frac{m_a}{100\ \mu\mathrm{eV}}\right) \left(\frac{T_{\mathrm{sys}}}{8\,\mathrm{K}}\right)^2 \\ &\times \left(\frac{10\,\mathrm{T}}{B_{\mathrm{e}}}\right)^4 \left(\frac{0.8}{\eta}\right)^2 C_{a\gamma}^{-4} f_{\mathrm{DM}}^{-2} , \end{aligned} \tag{D.2}$$

where $m_a = 2\pi\,\nu_i$ in terms of the search frequency ν_i. The scanning speed is then

$$\frac{d\nu}{dt} = \frac{\Delta\nu_i}{\Delta t_i} = \frac{K_i/\beta_i^2}{a_i/\beta_i^4} . \tag{D.3}$$

We have here used the Area Law in the form $\Delta\nu_i\beta_i^2 = K_i$, where K_i is approximately constant for a given set of disks, but in detail depends weakly on frequency ν_i and boost factor β_i.

The width and required boost factor varies slowly with i because of the large number of channels, so instead of summing over all channels i, we integrate over frequency ν to obtain the overall measurement time. So for the first term in equation (D.1) we can write

$$\sum_i \Delta t_i \to \int_{\nu_1}^{\nu_2} \frac{d\nu}{d\nu/dt} = \int_{\nu_1}^{\nu_2} \frac{d\nu}{K\beta^2/a} \tag{D.4}$$

and for the second term

$$\sum_i t_{\rm R} \to \int_{\nu_1}^{\nu_2} \frac{d\nu}{\Delta\nu} t_{\rm R} = \int_{\nu_1}^{\nu_2} \frac{d\nu}{K/\beta^2}\, t_{\rm R}\,, \tag{D.5}$$

where K depends weakly on ν and β, whereas a can depend more strongly on ν (at least a linear dependence coming from m_a). Thus the quantity we need to minimise with an appropriate choice of β_ν is

$$t = \int_{\nu_1}^{\nu_2} \frac{d\nu}{K_{\nu,\beta}} \left(\frac{a_\nu}{\beta_\nu^2} + t_{\rm R}\beta_\nu^2 \right) , \tag{D.6}$$

where we show the dependencies on parameters as subscripts. To minimise the integral we differentiate the integrand with respect to β

$$\frac{d}{d\beta}\left[\frac{1}{K_{\nu,\beta}} \left(\frac{a_\nu}{\beta_\nu^2} + t_{\rm R}\beta_\nu^2 \right) \right] = \frac{2}{K}\left(-\frac{a}{\beta^3} + t_{\rm R}\beta \right) + \frac{1}{K^2}\frac{dK}{d\beta}\left(\frac{a}{\beta^2} + t_{\rm R}\beta^2 \right) = 0\,. \tag{D.7}$$

As the Area Law is generally a good approximation, $dK/d\beta$ is small which implies an optimal boost factor

$$\beta_{\rm o}(\nu) \simeq \left(\frac{a_\nu}{t_{\rm R}} \right)^{1/4} \tag{D.8}$$

or explicitly

$$\begin{aligned} \beta_{\rm o}(\nu) = 430 &\left(\frac{\rm day}{t_{\rm R}} \right)^{1/4} \left(\frac{\nu}{25\ {\rm GHz}} \right)^{1/4} \left(\frac{\rm S/N}{5} \right)^{1/2} \\ &\times \left(\frac{1\,{\rm m}^2}{\mathcal{S}} \right)^{1/2} \left(\frac{T_{\rm sys}}{8\,{\rm K}} \right)^{1/2} \left(\frac{10\,{\rm T}}{B_{\rm e}} \right) \left(\frac{0.8}{\eta} \right)^{1/2} C_{a\gamma}^{-1} f_{\rm DM}^{-1/2}\,. \end{aligned} \tag{D.9}$$

The ν dependence is relatively weak, but generally a higher frequency requires a larger boost factor. $T_{\rm sys}$ can also depend on ν, typically increasing for higher ν.

Inserting the optimal boost factor (D.7) in the expression for the search time in equation (D.6) reveals that the two terms in brackets are equal, confirming $\Delta t = t_{\rm R}$ for each frequency channel. The minimal scanning time becomes

$$t_{\rm o} = 2t_{\rm R} \int_{\nu_1}^{\nu_2} \frac{d\nu}{K_\nu}\, \beta_{\rm o}^2(\nu) = 2\sqrt{t_{\rm R}} \int_{\nu_1}^{\nu_2} \frac{d\nu}{K_\nu}\, \sqrt{a_\nu}\,, \tag{D.10}$$

depending only on $\sqrt{t_{\mathrm{R}}}$. If one improves the re-adjustment time, the optimal strategy requires also a shorter measurement time Δt. To achieve the same sensitivity, one needs a larger boost factor and, according to the Area Law, a narrower channel width and thus more measurement channels. By the same token, t_{o} decreases only with $C_{a\gamma}^{-2}$ rather than the fourth power.

The cases used in section 8.1 are both examples of the boost factor obeying a power law $\beta \propto \nu^p$ for some p. The idealised HEMT amplifier with constant T_{sys} had $p = 1/4$, whereas the quantum-limited amplifiers ($T_{\mathrm{sys}} = \omega$) had $p = 3/4$. In this case the integrals are easy to evaluate explicitly if we take K to be constant. We write $\beta_{\mathrm{o}}(\nu) = \beta_2(\nu/\nu_2)^p$, where $\beta_2 \equiv \beta_{\mathrm{o}}(\nu_2)$ and find

$$\begin{aligned} t_{\mathrm{o}} &= \frac{2t_{\mathrm{R}}}{K}\int_{\nu_1}^{\nu_2} d\nu \beta_{\mathrm{o}}^2(\nu) = \frac{2t_{\mathrm{R}}}{2p+1}\,\frac{\beta_2^2}{K\nu_2^{2p}}\left(\nu_2^{2p+1} - \nu_1^{2p+1}\right) \\ &\sim \frac{2t_{\mathrm{R}}}{2p+1}\,\frac{\beta_2^2}{K}\nu_2 = \frac{2t_{\mathrm{R}}}{2p+1}\,\frac{\nu_2}{\Delta\nu|_{\nu_2}}\,, \end{aligned} \tag{D.11}$$

where $\Delta\nu|_{\nu_2}$ is the bandwidth of β_2 at ν_2. Notice that this bandwidth for the optimal search contains a factor $1\sqrt{t_{\mathrm{R}}}$, i.e., $t_{\mathrm{o}} \propto \sqrt{t_{\mathrm{R}}}$ as discussed earlier. Interestingly, to first approximation the measurement time depends only on ν_2 and scales in a manner that is invariant under the exact choice of p. As K is a linear function of the number of disks, we see that the frequency range measured in a given amount of time is also linear.

Bibliography

[1] **MADMAX Working Group** Collaboration, A. Caldwell, G. Dvali, B. Majorovits, A. Millar, G. Raffelt, J. Redondo, O. Reimann, F. Simon, and F. Steffen, "Dielectric haloscopes: a new way to detect axion dark matter," *Phys. Rev. Lett.* **118** (2017) 091801, arXiv:1611.05865.

[2] A. J. Millar, G. G. Raffelt, J. Redondo, and F. D. Steffen, "Dielectric haloscopes to search for axion dark matter: theoretical foundations," *JCAP* **1701** (2017) 061, arXiv:1612.07057.

[3] A. N. Ioannisian, N. Kazarian, A. J. Millar, and G. G. Raffelt, "Axion-photon conversion caused by dielectric interfaces: quantum field calculation," *JCAP* **1709** (2017) 005, arXiv:1707.00701.

[4] A. J. Millar, J. Redondo, and F. D. Steffen, "Dielectric haloscopes: sensitivity to the axion dark matter velocity," *JCAP* **1710** (2017) 006, arXiv:1707.04266.

[5] S. Knirck, A. J. Millar, C. A. O'Hare, J. Redondo, and F. D. Steffen, "Directional axion detection," *in preparation* (2018) [MPP-2018-56].

[6] F. Zwicky, "Die Rotverschiebung von extragalaktischen Nebeln," *Helv. Phys. Acta* **6** (1933) 110–127. [Gen. Rel. Grav. **41** (2009) 207 (english translation)].

[7] J. L. Feng, "Dark matter candidates from particle physics and methods of detection," *Ann. Rev. Astron. Astrophys.* **48** (2010) 495–545, arXiv:1003.0904.

[8] J. Frieman, M. Turner, and D. Huterer, "Dark energy and the accelerating universe," *Ann. Rev. Astron. Astrophys.* **46** (2008) 385–432, arXiv:0803.0982.

[9] J. L. Feng, "Naturalness and the status of supersymmetry," *Ann. Rev. Nucl. Part. Sci.* **63** (2013) 351–382, arXiv:1302.6587.

[10] J. M. Cline, "Baryogenesis," in *Les Houches summer school - session 86: particle physics and cosmology: the fabric of spacetime Les Houches, France, July 31-August 25, 2006*. arXiv:hep-ph/0609145.

[11] S. F. King, "Neutrino mass models," *Rept. Prog. Phys.* **67** (2004) 107–158, arXiv:hep-ph/0310204.

[12] R. P. Woodard, "How far are we from the quantum theory of gravity?," *Rept. Prog. Phys.* **72** (2009) 126002, arXiv:0907.4238.

[13] C. A. Baker *et al.*, "An improved experimental limit on the electric dipole moment of the neutron," *Phys. Rev. Lett.* **97** (2006) 131801, arXiv:hep-ex/0602020.

[14] J. M. Pendlebury *et al.*, "Revised experimental upper limit on the electric dipole moment of the neutron," *Phys. Rev. D* **92** (2015) 092003, arXiv:1509.04411.

[15] R. D. Peccei, "The Strong CP Problem and axions," in *Axions: theory, cosmology, and experimental searches. Proceedings, 1st Joint ILIAS-CERN-CAST axion training, Geneva, Switzerland, November 30-December 2, 2005*. arXiv:0607268. [*Lect. Notes Phys.* **741** (2008) 3–17].

[16] J. E. Kim and G. Carosi, "Axions and the Strong CP Problem," *Rev. Mod. Phys.* **82** (2010) 557–602, arXiv:0807.3125.

[17] **Particle Data Group** Collaboration, C. Patrignani *et al.*, "Review of particle physics," *Chin. Phys. C* **40** (2016) 100001.

[18] P. Sikivie, "Experimental tests of the invisible axion," *Phys. Rev. Lett.* **51** (1983) 1415–1417. [Erratum: *ibid* **52** (1984) 695].

[19] I. G. Irastorza and J. Redondo, "New experimental approaches in the search for axion-like particles," arXiv:1801.08127.

[20] inSPIRE. https://inspirehep.net.

[21] **MADMAX interest Group** Collaboration, P. Brun *et al.*, "A new experimental approach to probe QCD axion dark matter in the mass range above 40 eV,". https://www.mpp.mpg.de/fileadmin/user_upload/Forschung/MADMAX/madmax_white_paper.pdf.

[22] S. Weinberg, "The U(1) Problem," *Phys. Rev. D* **11** (1975) 3583–3593.

[23] G. 't Hooft, "Symmetry breaking through Bell-Jackiw anomalies," *Phys. Rev. Lett.* **37** (1976) 8–11.

[24] G. 't Hooft, "Computation of the quantum effects due to a four-dimensional pseudoparticle," *Phys. Rev. D* **14** (1976) 3432–3450. [Erratum: *ibid* **18**, 2199 (1978)].

[25] C. Cao and A. Zhitnitsky, "Axion detection via topological Casimir effect," *Phys. Rev. D* **96** (2017) 015013, arXiv:1702.00012.

[26] J. E. Kim, "Light pseudoscalars, particle physics and cosmology," *Phys. Rept.* **150** (1987) 1–177.

[27] I. B. Khriplovich and S. K. Lamoreaux, *CP violation without strangeness: Electric dipole moments of particles, atoms, and molecules*. Springer: Berlin, Germany (1997).

[28] J. A. Sánchez-Monroy and C. Quimbay, "Some classical properties of the non-abelian Yang-Mills theories," *Rev. Mex. Fis. E* **56** (2010) 172–176, arXiv:hep-ph/0702173.

[29] V. Baluni, "CP violating effects in QCD," *Phys. Rev. D* **19** (1979) 2227–2230.

[30] R. J. Crewther, P. Di Vecchia, G. Veneziano, and E. Witten, "Chiral estimate of the electric dipole moment of the neutron in quantum chromodynamics," *Phys. Lett. B* **88** (1979) 123. [Erratum: *ibid* **91** (1980) 487].

[31] M. Pospelov and A. Ritz, "Theta vacua, QCD sum rules, and the neutron electric dipole moment," *Nucl. Phys. B* **573** (2000) 177–200, arXiv:hep-ph/9908508.

[32] F. K. Guo, R. Horsley, U. G. Meissner, Y. Nakamura, H. Perlt, P. E. L. Rakow, G. Schierholz, A. Schiller, and J. M. Zanotti, "The electric dipole moment of the neutron from 2+1 flavor lattice QCD," *Phys. Rev. Lett.* **115** (2015) 062001, arXiv:1502.02295.

[33] C. Alexandrou, A. Athenodorou, M. Constantinou, K. Hadjiyiannakou, K. Jansen, G. Koutsou, K. Ottnad, and M. Petschlies, "Neutron electric dipole moment using $N_f = 2 + 1 + 1$ twisted mass fermions," *Phys. Rev. D* **93** (2016) 074503, arXiv:1510.05823.

[34] E. Shintani, T. Blum, T. Izubuchi, and A. Soni, "Neutron and proton electric dipole moments from $N_f = 2 + 1$ domain-wall fermion lattice QCD," *Phys. Rev. D* **93** (2016) 094503, arXiv:1512.00566.

[35] M. Abramczyk, S. Aoki, T. Blum, T. Izubuchi, H. Ohki, and S. Syritsyn, "Lattice calculation of electric dipole moments and form factors of the nucleon," *Phys. Rev. D* **96** (2017) 014501, arXiv:1701.07792.

[36] D. B. Kaplan and A. V. Manohar, "Current mass ratios of the light quarks," *Phys. Rev. Lett.* **56** (1986) 2004–2007.

[37] T. Banks, Y. Nir, and N. Seiberg, "Missing (up) mass, accidental anomalous symmetries, and the Strong CP Problem," in *Yukawa couplings and the origins of mass. Proceedings, 2nd IFT Workshop, Gainesville, USA, February 11-13, 1994*. International Press: Cambridge, USA (1994) 26–41. arXiv:hep-ph/9403203.

[38] G. Grilli di Cortona, E. Hardy, J. Pardo Vega, and G. Villadoro, "The QCD axion, precisely," *JHEP* **01** (2016) 034, arXiv:1511.02867.

[39] M. Pospelov and A. Ritz, "Electric dipole moments as probes of new physics," *Annals Phys.* **318** (2005) 119–169, arXiv:hep-ph/0504231.

[40] R. D. Peccei and H. R. Quinn, "CP conservation in the presence of instantons," *Phys. Rev. Lett.* **38** (1977) 1440–1443.

[41] S. Weinberg, "A new light boson?," *Phys. Rev. Lett.* **40** (1978) 223–226.

[42] F. Wilczek, "Problem of Strong P and T invariance in the presence of instantons," *Phys. Rev. Lett.* **40** (1978) 279–282.

[43] M. Dine, W. Fischler, and M. Srednicki, "A simple solution to the Strong CP Problem with a harmless axion," *Phys. Lett. B* **104** (1981) 199–202.

[44] A. R. Zhitnitsky, "On possible suppression of the axion hadron interactions," *Sov. J. Nucl. Phys.* **31** (1980) 260. [*Yad. Fiz.* **31** (1980) 497].

[45] J. E. Kim, "Weak interaction singlet and Strong CP invariance," *Phys. Rev. Lett.* **43** (1979) 103.

[46] M. A. Shifman, A. I. Vainshtein, and V. I. Zakharov, "Can confinement ensure natural CP invariance of Strong interactions?," *Nucl. Phys. B* **166** (1980) 493–506.

[47] J. E. Kim, "Calculation of axion–photon–photon coupling in string theory," *Phys. Lett. B* **735** (2014) 95–100, arXiv:1405.6175. [Erratum: *ibid* **741** (2014) 327].

[48] L. Di Luzio, F. Mescia, and E. Nardi, "Redefining the axion window," *Phys. Rev. Lett.* **118** (2017) 031801, arXiv:1610.07593.

[49] L. Di Luzio, F. Mescia, and E. Nardi, "Window for preferred axion models," *Phys. Rev. D* **96** (2017) 075003, arXiv:1705.05370.

[50] S. W. Hawking, "Quantum coherence down the wormhole," *Phys. Lett. B* **195** (1987) 337.

[51] G. V. Lavrelashvili, V. A. Rubakov, and P. G. Tinyakov, "Disruption of quantum coherence upon a change in spatial topology in quantum gravity," *JETP Lett.* **46** (1987) 167–169. [*Pisma Zh. Eksp. Teor. Fiz.* **46** (1987) 134].

[52] S. B. Giddings and A. Strominger, "Baby universes, third quantization and the cosmological constant," *Nucl. Phys. B* **321** (1989) 481–508.

[53] L. F. Abbott and M. B. Wise, "Wormholes and global symmetries," *Nucl. Phys. B* **325** (1989) 687–704.

[54] S. R. Coleman and K.-M. Lee, "Wormholes made without massless matter fields," *Nucl. Phys. B* **329** (1990) 387–409.

[55] R. Kallosh, A. D. Linde, D. A. Linde, and L. Susskind, "Gravity and global symmetries," *Phys. Rev. D* **52** (1995) 912–935, arXiv:hep-th/9502069.

[56] D. J. E. Marsh, "Axion cosmology," *Phys. Rept.* **643** (2016) 1–79, arXiv:1510.07633.

[57] **Planck** Collaboration, P. A. R. Ade *et al.*, "Planck 2015 results. XIII. Cosmological parameters," *Astron. Astrophys.* **594** (2016) A13, arXiv:1502.01589.

[58] P. Fox, A. Pierce, and S. D. Thomas, "Probing a QCD string axion with precision cosmological measurements," arXiv:hep-th/0409059.

[59] G. G. Raffelt, "Astrophysical axion bounds," in *Axions: theory, cosmology, and experimental searches. Proceedings, 1st Joint ILIAS-CERN-CAST axion training, Geneva, Switzerland, November 30-December 2, 2005*. arXiv:hep-ph/0611350. [*Lect. Notes Phys.* **741** (2008) 51–71].

[60] S. Borsanyi *et al.*, "Calculation of the axion mass based on high-temperature lattice quantum chromodynamics," *Nature* **539** (2016) 69–71, arXiv:1606.07494.

[61] A. D. Linde, "The new inflationary universe scenario," in *The very early universe*. Cambridge University Press: Cambridge, United Kingdom (1993).

[62] A. D. Linde, "The inflationary universe," *Rept. Prog. Phys.* **47** (1984) 925–986.

[63] A. D. Linde, "Eternally existing self-reproducing chaotic inflationary universe," *Phys. Lett. B* **175** (1986) 395–400.

[64] F. Wilczek, "A model of anthropic reasoning, addressing the dark to ordinary matter coincidence," *Universe or multiverse?* (2004) 151–162, arXiv:hep-ph/0408167.

[65] M. Tegmark, A. Aguirre, M. Rees, and F. Wilczek, "Dimensionless constants, cosmology and other dark matters," *Phys. Rev. D* **73** (2006) 023505, arXiv:astro-ph/0511774.

[66] M. P. Hertzberg, M. Tegmark, and F. Wilczek, "Axion cosmology and the energy scale of inflation," *Phys. Rev. D* **78** (2008) 083507, arXiv:0807.1726.

[67] T. W. B. Kibble, "Topology of cosmic domains and strings," *J. Phys.* **A9** (1976) 1387–1398.

[68] T. Hiramatsu, M. Kawasaki, K. Saikawa, and T. Sekiguchi, "Production of dark matter axions from collapse of string-wall systems," *Phys. Rev. D* **85** (2012) 105020, arXiv:1202.5851. [Erratum: *ibid* **86** (2012) 089902].

[69] P. Sikivie, "Of axions, domain walls and the early universe," *Phys. Rev. Lett.* **48** (1982) 1156–1159.

[70] G. B. Gelmini, M. Gleiser, and E. W. Kolb, "Cosmology of biased discrete symmetry breaking," *Phys. Rev. D* **39** (1989) 1558.

[71] S. E. Larsson, S. Sarkar, and P. L. White, "Evading the cosmological domain wall problem," *Phys. Rev. D* **55** (1997) 5129–5135, arXiv:hep-ph/9608319.

[72] H. M. Georgi, L. J. Hall, and M. B. Wise, "Grand unified models with an automatic Peccei-Quinn Symmetry," *Nucl. Phys. B* **192** (1981) 409–416.

[73] A. Ringwald and K. Saikawa, "Axion dark matter in the post-inflationary Peccei-Quinn symmetry breaking scenario," *Phys. Rev.* **D93** (2016) 085031, arXiv:1512.06436. [Addendum: *ibid* **94** (2016) 049908].

[74] G. Lazarides and Q. Shafi, "Axion models with no domain wall problem," *Phys. Lett. B* **115** (1982) 21–25.

[75] K. Choi and J. E. Kim, "Domain walls in superstring models," *Phys. Rev. Lett.* **55** (1985) 2637.

[76] G. Ballesteros, J. Redondo, A. Ringwald, and C. Tamarit, "Unifying inflation with the axion, dark matter, baryogenesis and the seesaw mechanism," *Phys. Rev. Lett.* **118** (2017) 071802, arXiv:1608.05414.

[77] G. Ballesteros, J. Redondo, A. Ringwald, and C. Tamarit, "Standard Model—axion—seesaw—Higgs portal inflation. Five problems of particle physics and cosmology solved in one stroke," *JCAP* **1708** (2017) 001, arXiv:1610.01639.

[78] M. Kawasaki, K. Saikawa, and T. Sekiguchi, "Axion dark matter from topological defects," *Phys. Rev. D* **91** (2015) 065014, arXiv:1412.0789.

[79] L. Fleury and G. D. Moore, "Axion dark matter: strings and their cores," *JCAP* **1601** (2016) 004, arXiv:1509.00026.

[80] V. B. Klaer and G. D. Moore, "How to simulate global cosmic strings with large string tension," *JCAP* **1710** (2017) 043, arXiv:1707.05566.

[81] V. B. Klaer and G. D. Moore, "The dark-matter axion mass," *JCAP* **1711** (2017) 049, arXiv:1708.07521.

[82] S. Al Kenany *et al.*, "Design and operational experience of a microwave cavity axion detector for the 20–100 μeV range," *Nucl. Instrum. Meth. A* **854** (2017) 11–24, arXiv:1611.07123.

[83] E. Nardi and E. Roulet, "Are exotic stable quarks cosmologically allowed?," *Phys. Lett. B* **245** (1990) 105–110.

[84] C. J. Hogan and M. J. Rees, "Axion miniclusters," *Phys. Lett. B* **205** (1988) 228–230.

[85] I. I. Tkachev, "On the possibility of Bose star formation," *Phys. Lett. B* **261** (1991) 289–293.

[86] E. W. Kolb and I. I. Tkachev, "Axion miniclusters and Bose stars," *Phys. Rev. Lett.* **71** (1993) 3051–3054, arXiv:hep-ph/9303313.

[87] E. W. Kolb and I. I. Tkachev, "Nonlinear axion dynamics and formation of cosmological pseudosolitons," *Phys. Rev. D* **49** (1994) 5040–5051, arXiv:astro-ph/9311037.

[88] E. Braaten, A. Mohapatra, and H. Zhang, "Dense axion stars," *Phys. Rev. Lett.* **117** (2016) 121801, arXiv:1512.00108.

[89] L. Visinelli, S. Baum, J. Redondo, K. Freese, and F. Wilczek, "Dilute and dense axion stars," *Phys. Lett. B* **777** (2018) 64–72, arXiv:1710.08910.

[90] E. W. Kolb and I. I. Tkachev, "Large amplitude isothermal fluctuations and high density dark matter clumps," *Phys. Rev. D* **50** (1994) 769–773, arXiv:astro-ph/9403011.

[91] M. Fairbairn, D. J. E. Marsh, and J. Quevillon, "Searching for the QCD axion with gravitational microlensing," *Phys. Rev. Lett.* **119** (2017) 021101, arXiv:1701.04787.

[92] M. Fairbairn, D. J. E. Marsh, J. Quevillon, and S. Rozier, "Structure formation and microlensing with axion miniclusters," *Phys. Rev. D* **97** (2018) 083502, arXiv:1707.03310.

[93] Paredes, D. Novoa, and D. Tommasini, "Self-induced mode mixing of ultraintense lasers in vacuum," *Phys. Rev. A* **90** (2014) 063803, arXiv:1412.3390.

[94] S. Villalba-Chávez, "Laser-driven search of axion-like particles including vacuum polarization effects," *Nucl. Phys. B* **881** (2014) 391–413, arXiv:1308.4033.

[95] T. Hasebe, K. Homma, Y. Nakamiya, K. Matsuura, K. Otani, M. Hashida, S. Inoue, and S. Sakabe, "Search for sub-eV scalar and pseudoscalar resonances via four-wave mixing with a laser collider," *PTEP* **2015** (2015) 073C01, arXiv:1506.05581.

[96] D. A. Burton and A. Noble, "Plasma-based wakefield accelerators as sources of axion-like particles," arXiv:1710.01906.

[97] K. Homma and Y. Toyota, "Exploring pseudo-Nambu–Goldstone bosons by stimulated photon colliders in the mass range 0.1 eV to 10 keV," *PTEP* **2017** (2017) 063C01, arXiv:1701.04282.

[98] Y. Nakamiya, K. Homma, T. Moritaka, and K. Seto, "Probing vacuum birefringence under a high-intensity laser field with gamma-ray polarimetry at the GeV scale," *Phys. Rev. D* **96** (2017) 053002, arXiv:1512.00636.

[99] J. Redondo, *Can the PVLAS particle be compatible with the astrophysical bounds?* PhD thesis, Barcelona, Autonoma U., 2007. arXiv:0807.4329.

[100] B. Döbrich, J. Jaeckel, F. Kahlhoefer, A. Ringwald, and K. Schmidt-Hoberg, "ALPtraum: ALP production in proton beam dump experiments," *JHEP* **02** (2016) 018, arXiv:1512.03069.

[101] F. Hoogeveen and T. Ziegenhagen, "Production and detection of light bosons using optical resonators," *Nucl. Phys. B* **358** (1991) 3–26.

[102] G. Mueller, P. Sikivie, D. B. Tanner, and K. van Bibber, "Detailed design of a resonantly-enhanced axion-photon regeneration experiment," *Phys. Rev. D* **80** (2009) 072004, arXiv:0907.5387.

[103] F. Caspers, J. Jaeckel, and A. Ringwald, "Feasibility, engineering aspects and physics reach of microwave cavity experiments searching for hidden photons and axions," *JINST* **4** (2009) P11013, arXiv:0908.0759.

[104] J. E. Moody and F. Wilczek, "New macroscopic forces?," *Phys. Rev. D* **30** (1984) 130.

[105] J. K. Hoskins, R. D. Newman, R. Spero, and J. Schultz, "Experimental tests of the gravitational inverse square law for mass separations from 2-cm to 105-cm," *Phys. Rev. D* **32** (1985) 3084–3095.

[106] D. J. Kapner, T. S. Cook, E. G. Adelberger, J. H. Gundlach, B. R. Heckel, C. D. Hoyle, and H. E. Swanson, "Tests of the gravitational inverse-square law below the dark-energy length scale," *Phys. Rev. Lett.* **98** (2007) 021101, arXiv:hep-ph/0611184.

[107] R. S. Decca, D. Lopez, E. Fischbach, G. L. Klimchitskaya, D. E. Krause, and V. M. Mostepanenko, "Novel constraints on light elementary particles and extra-dimensional physics from the Casimir effect," *Eur. Phys. J.* **C51** (2007) 963–975, arXiv:0706.3283.

[108] A. A. Geraci, S. J. Smullin, D. M. Weld, J. Chiaverini, and A. Kapitulnik, "Improved constraints on non-Newtonian forces at 10 microns," *Phys. Rev. D* **78** (2008) 022002, arXiv:0802.2350.

[109] A. O. Sushkov, W. J. Kim, D. A. R. Dalvit, and S. K. Lamoreaux, "New experimental limits on non-Newtonian forces in the micrometer range," *Phys. Rev. Lett.* **107** (2011) 171101, arXiv:1108.2547.

[110] G. L. Smith, C. D. Hoyle, J. H. Gundlach, E. G. Adelberger, B. R. Heckel, and H. E. Swanson, "Short range tests of the equivalence principle," *Phys. Rev. D* **61** (2000) 022001.

[111] S. Schlamminger, K. Y. Choi, T. A. Wagner, J. H. Gundlach, and E. G. Adelberger, "Test of the equivalence principle using a rotating torsion balance," *Phys. Rev. Lett.* **100** (2008) 041101, arXiv:0712.0607.

[112] A. Arvanitaki and A. A. Geraci, "Resonantly detecting axion-mediated forces with nuclear magnetic resonance," *Phys. Rev. Lett.* **113** (2014) 161801, arXiv:1403.1290.

[113] A. A. Geraci *et al.*, "Progress on the ARIADNE axion experiment," 2017. arXiv:1710.05413.

[114] G. G. Raffelt, "Astrophysical axion bounds diminished by screening effects," *Phys. Rev. D* **33** (1986) 897.

[115] **CAST** Collaboration, S. Andriamonje *et al.*, "An improved limit on the axion-photon coupling from the CAST experiment," *JCAP* **0704** (2007) 010, arXiv:hep-ex/0702006.

[116] I. G. Irastorza *et al.*, "Towards a new generation axion helioscope," *JCAP* **1106** (2011) 013, arXiv:1103.5334.

[117] K. Barth *et al.*, "CAST constraints on the axion-electron coupling," *JCAP* **1305** (2013) 010, arXiv:1302.6283.

[118] G. G. Raffelt, Stars as laboratories for fundamental physics. University Press: Chicago, USA (1996). http://wwwth.mpp.mpg.de/members/raffelt/mypapers/199613.pdf.

[119] K. Zioutas *et al.*, "A decommissioned LHC model magnet as an axion telescope," *Nucl. Instrum. Meth. A* **425** (1999) 480–489, arXiv:astro-ph/9801176.

[120] **CAST** Collaboration, K. Zioutas *et al.*, "First results from the CERN Axion Solar Telescope (CAST)," *Phys. Rev. Lett.* **94** (2005) 121301, arXiv:hep-ex/0411033.

[121] **IAXO** Collaboration, I. Irastorza *et al.*, "The International Axion Observatory IAXO. Letter of intent to the CERN SPS committee,". http://cds.cern.ch/record/1567109.

[122] W. Buchmuller and F. Hoogeveen, "Coherent production of light scalar particles in Bragg scattering," *Phys. Lett. B* **237** (1990) 278–283.

[123] E. A. Paschos and K. Zioutas, "A proposal for solar axion detection via Bragg scattering," *Phys. Lett. B* **323** (1994) 367–372.

[124] P. Sikivie, "Detection rates for 'invisible' axion searches," *Phys. Rev. D* **32** (1985) 2988. [Erratum: *ibid* **36** (1987) 974].

[125] **ADMX** Collaboration, G. Rybka, "Direct detection searches for axion dark matter," in *Proceedings, 13th international conference on Topics in Astroparticle and Underground Physics (TAUP 2013): Asilomar, California, September 8-13, 2013.* [*Phys. Dark Univ.* **4** (2014) 14–16].

[126] **HAYSTAC** Collaboration, L. Zhong *et al.*, "Results from phase 1 of the HAYSTAC microwave cavity axion experiment," arXiv:1803.03690.

[127] H. Zheng, M. Silveri, R. T. Brierley, S. M. Girvin, and K. W. Lehnert, "Accelerating dark-matter axion searches with quantum measurement technology," arXiv:1607.02529.

[128] W. Chung, "Launching axion experiment at CAPP/IBS in Korea," in *Proceedings, 12th Patras workshop on axions, WIMPs and WISPs: Jeju Island, South Korea, June 20-24, 2016*. DESY: Hamburg, Germany (2017) 30–34. http://inspirehep.net/record/1644238/files/fulltext.pdf.

[129] D. S. Kinion, *First results from a multiple microwave cavity search for dark matter axions*. PhD thesis, UC, Davis, 2001. http://wwwlib.umi.com/dissertations/fullcit?p3019020.

[130] J. Jeong, S. Youn, S. Ahn, C. Kang, and Y. K. Semertzidis, "Phase-matching of multiple-cavity detectors for dark matter axion search," *Astropart. Phys.* **97** (2018) 33–37, arXiv:1707.05925.

[131] O. K. Baker, M. Betz, F. Caspers, J. Jaeckel, A. Lindner, A. Ringwald, Y. Semertzidis, P. Sikivie, and K. Zioutas, "Prospects for searching axion-like particle dark matter with dipole, toroidal and wiggler magnets," *Phys. Rev. D* **85** (2012) 035018, arXiv:1110.2180.

[132] B. T. McAllister, G. Flower, E. N. Ivanov, M. Goryachev, J. Bourhill, and M. E. Tobar, "The ORGAN Experiment: an axion haloscope above 15 GHz," *Phys. Dark Univ.* **18** (2017) 67–72, arXiv:1706.00209.

[133] G. Rybka, A. Wagner, A. Brill, K. Ramos, R. Percival, and K. Patel, "Search for dark matter axions with the Orpheus experiment," *Phys. Rev. D* **91** (2015) 011701, arXiv:1403.3121.

[134] M. Goryachev, B. T. Mcallister, and M. E. Tobar, "Axion detection with cavity arrays," arXiv:1703.07207.

[135] J. Jeong, S. Youn, S. Ahn, J. E. Kim, and Y. K. Semertzidis, "Concept of multiple-cell cavity for axion dark matter search," *Phys. Lett. B* **777** (2018) 412–419, arXiv:1710.06969.

[136] A. Melcón *et al.*, "Axion searches with microwave filters: the RADES project," arXiv:1803.01243.

[137] B. T. McAllister, G. Flower, L. E. Tobar, and M. E. Tobar, "Tunable supermode dielectric resonators for axion dark-matter haloscopes," *Phys. Rev. Applied* **9** (2018) 014028, arXiv:1705.06028.

[138] D. E. Morris, "An electromagnetic detector for relic axions," *Unpublished LBL Report* (1984) . https://www.osti.gov/servlets/purl/6446664.

[139] B. Phillips, "The Electric Tiger Experiment: a proof-of-concept for the periodic dielectric loaded resonator," *Talk given at the 2nd Workshop on Microwave Cavities and Detectors for Axion Research* (2017) . https://indico.fnal.gov/event/13068/contribution/8/material/slides/0.pdf.

[140] W. Wuensch, S. De Panfilis-Wuensch, Y. K. Semertzidis, J. T. Rogers, A. C. Melissinos, H. J. Halama, B. E. Moskowitz, A. G. Prodell, W. B. Fowler, and F. A. Nezrick, "Results of a laboratory search for cosmic axions and other weakly coupled light particles," *Phys. Rev. D* **40** (1989) 3153.

[141] C. Hagmann, P. Sikivie, N. S. Sullivan, and D. B. Tanner, "Results from a search for cosmic axions," *Phys. Rev. D* **42** (1990) 1297–1300.

[142] **ADMX** Collaboration, S. J. Asztalos *et al.*, "A SQUID-based microwave cavity search for dark-matter axions," *Phys. Rev. Lett.* **104** (2010) 041301, arXiv:0910.5914.

[143] K. van Bibber, "Status of the ADMX-HF experiment," in *Proceedings, 11th Patras workshop on axions, WIMPs and WISPs: Zaragoza, Spain, June 22-26, 2015*. DESY: Hamburg, Germany (2015). http://axion-wimp2015.desy.de/sites/sites_conferences/site_axion-wimp2015/content/e13847/e16320/Proc_11thPatras.pdf.

[144] B. M. Brubaker *et al.*, "First results from a microwave cavity axion search at 24 μeV," *Phys. Rev. Lett.* **118** (2017) 061302, arXiv:1610.02580.

[145] G. Carosi, "Cavity-based searches for relic axions," *Talk given at Bethe Forum on Axions and the Low Energy Frontier* (2016) . http://bctp.uni-bonn.de/bethe-forum/2016/axions/talks/Carosi.pdf.

[146] **ADMX** Collaboration, N. Du *et al.*, "A search for invisible axion dark matter with the Axion Dark Matter Experiment," *Phys. Rev. Lett.* **120** (2018) 151301, arXiv:1804.05750.

[147] D. Horns, J. Jaeckel, A. Lindner, A. Lobanov, J. Redondo, and A. Ringwald, "Searching for WISPy cold dark matter with a dish antenna," *JCAP* **1304** (2013) 016, arXiv:1212.2970.

[148] J. D. Jackson, *Classical electrodynamics*. Wiley: New York, USA (1998).

[149] B. Döbrich *et al.*, "The FUNK search for hidden photon dark matter in the eV range," in *Photon 2015: international conference on the structure and interactions of the photon and 21th international workshop on photon-photon collisions and international workshop on*

high energy photon linear colliders Novosibirsk, Russia. arXiv:1510.05869.

[150] J. Suzuki, T. Horie, Y. Inoue, and M. Minowa, "Experimental search for hidden photon CDM in the eV mass range with a dish antenna," *JCAP* **1509** (2015) 042, arXiv:1504.00118.

[151] **BRASS** Collaboration, "BRASS: Broadband Radiometric Axion SearcheS." http://www.iexp.uni-hamburg.de/groups/astroparticle/brass/brassweb.htm.

[152] J. Jaeckel and J. Redondo, "Resonant to broadband searches for cold dark matter consisting of weakly interacting slim particles," *Phys. Rev. D* **88** (2013) 115002, arXiv:1308.1103.

[153] B. Cabrera and S. Thomas, "Detecting string-scale QCD axion dark matter," *Talk give at at Axions 2010, University of Florida, Gainesville* (2010) .

[154] P. Sikivie, N. Sullivan, and D. B. Tanner, "Proposal for axion dark matter detection using an LC circuit," *Phys. Rev. Lett.* **112** (2014) 131301, arXiv:1310.8545.

[155] Y. Kahn, B. R. Safdi, and J. Thaler, "Broadband and resonant approaches to axion dark matter detection," *Phys. Rev. Lett.* **117** (2016) 141801, arXiv:1602.01086.

[156] S. Chaudhuri, P. W. Graham, K. Irwin, J. Mardon, S. Rajendran, and Y. Zhao, "Radio for hidden-photon dark matter detection," *Phys. Rev. D* **92** (2015) 075012, arXiv:1411.7382.

[157] S. Chaudhuri, K. Irwin, P. W. Graham, and J. Mardon, "Fundamental limits of electromagnetic axion and hidden-photon dark matter searches: part I - the quantum limit," arXiv:1803.01627.

[158] M. Silva-Feaver *et al.*, "Design overview of DM Radio pathfinder experiment," in *Proceedings, applied superconductivity conference (ASC 2016): Denver, Colorado, September 4-9, 2016.* arXiv:1610.09344. [*IEEE Trans. Appl. Supercond.* **27** (2016) 1400204].

[159] L. Krauss, J. Moody, F. Wilczek, and D. E. Morris, "Calculations for cosmic axion detection," *Phys. Rev. Lett.* **55** (1985) 1797–1800.

[160] L. M. Krauss, "Axions: the search continues," in *Proceedings, theoretical advanced study institute in elementary particle physics new haven, Connecticut, June 9-July 5, 1985.* 1985. https://lib-extopc.kek.jp/preprints/PDF/1986/8604/8604139.pdf.

[161] R. Barbieri, M. Cerdonio, G. Fiorentini, and S. Vitale, "Axion to magnon conversion: a scheme for the detection of galactic axions," *Phys. Lett. B* **226** (1989) 357–360.

[162] D. Budker, P. W. Graham, M. Ledbetter, S. Rajendran, and A. Sushkov, "Proposal for a Cosmic Axion Spin Precession Experiment (CASPEr)," *Phys. Rev. D* **X4** (2014) 021030, arXiv:1306.6089.

[163] P. W. Graham and S. Rajendran, "Axion dark matter detection with cold molecules," *Phys. Rev. D* **84** (2011) 055013, arXiv:1101.2691.

[164] R. Barbieri, C. Braggio, G. Carugno, C. S. Gallo, A. Lombardi, A. Ortolan, R. Pengo, G. Ruoso, and C. C. Speake, "Searching for galactic axions through magnetized media: the QUAX proposal," *Phys. Dark Univ.* **15** (2017) 135–141, arXiv:1606.02201.

[165] F. Wilczek, "Two applications of axion electrodynamics," *Phys. Rev. Lett.* **58** (1987) 1799.

[166] S. Das, P. Jain, J. P. Ralston, and R. Saha, "Probing dark energy with light: propagation and spontaneous polarization," *JCAP* **0506** (2005) 002, arXiv:hep-ph/0408198.

[167] S. Das, P. Jain, J. P. Ralston, and R. Saha, "The dynamical mixing of light and pseudoscalar fields," *Pramana* **70** (2008) 439, arXiv:hep-ph/0410006.

[168] A. K. Ganguly, P. Jain, and S. Mandal, "Photon and axion oscillation in a magnetized medium: a general treatment," *Phys. Rev. D* **79** (2009) 115014, arXiv:0810.4380.

[169] L. Visinelli, "Axion-electromagnetic waves," *Mod. Phys. Lett. A* **28** (2013) 1350162, arXiv:1401.0709.

[170] M. C. Huang and P. Sikivie, "The structure of axionic domain walls," *Phys. Rev. D* **32** (1985) 1560.

[171] G. Raffelt and L. Stodolsky, "Mixing of the photon with low mass particles," *Phys. Rev. D* **37** (1988) 1237.

[172] A. Dobrynina, A. Kartavtsev, and G. Raffelt, "Photon-photon dispersion of TeV gamma rays and its role for photon-ALP conversion," *Phys. Rev. D* **91** (2015) 083003, arXiv:1412.4777. [Erratum: *ibid* **95** (2017) 109905].

[173] J. Galán *et al.*, "Exploring 0.1–10 eV axions with a new helioscope concept," *JCAP* **1512** (2015) 012, arXiv:1508.03006.

[174] R. Catena and P. Ullio, "A novel determination of the local dark matter density," *JCAP* **1008** (2010) 004, arXiv:0907.0018.

[175] L. E. Strigari and R. Trotta, "Reconstructing WIMP properties in direct detection experiments including galactic dark matter distribution uncertainties," *JCAP* **0911** (2009) 019, arXiv:0906.5361.

[176] M. Weber and W. de Boer, "Determination of the local dark matter density in our galaxy," *Astron. Astrophys.* **509** (2010) A25, arXiv:0910.4272.

[177] J. Bovy and S. Tremaine, "On the local dark matter density," *Astrophys. J.* **756** (2012) 89, arXiv:1205.4033.

[178] F. Nesti and P. Salucci, "The dark matter halo of the milky way, AD 2013," *JCAP* **1307** (2013) 016, arXiv:1304.5127.

[179] N. Bozorgnia, R. Catena, and T. Schwetz, "Anisotropic dark matter distribution functions and impact on WIMP direct detection," *JCAP* **1312** (2013) 050, arXiv:1310.0468.

[180] J. I. Read, "The local dark matter density," *J. Phys.* **G41** (2014) 063101, arXiv:1404.1938.

[181] J. W. Foster, N. L. Rodd, and B. R. Safdi, "Revealing the dark matter halo with axion direct detection," arXiv:1711.10489.

[182] R. H. Dicke, "The measurement of thermal radiation at microwave frequencies," *Rev. Sci. Instrum.* **17** (1946) 268.

[183] J. Redondo, "Photon-axion conversions in transversely inhomogeneous magnetic fields," in *Proceedings, 5th Patras workshop on axions, WIMPs and WISPs: Durham, UK, July 13-17, 2009*. DESY: Hamburg, Germany (2010). arXiv:1003.0410.

[184] J. Jaeckel and J. Redondo, "An antenna for directional detection of WISPy dark matter," *JCAP* **1311** (2013) 016, arXiv:1307.7181.

[185] J. Jaeckel and S. Knirck, "Directional resolution of dish antenna experiments to search for WISPy dark matter," *JCAP* **1601** (2016) 005, arXiv:1509.00371.

[186] V. L. Ginzburg and V. N. Tsytovich, "Several problems of the theory of transition radiation and transition scattering," *Phys. Rept.* **49** (1979) 1–89.

[187] V. L. Ginzburg and V. N. Tsytovich, *Transition radiation and transition scattering*. Hilger: New York, USA (1990).

[188] G. M. Garibian, "Phenomenological quantum electrodynamics in the case of two media," *Sov. Phys. JETP* **12** (1961) 1138. [*J. Exptl. Theoret. Phys.* (U.S.S.R.) **39** (1960) 1630].

[189] G. Garibian and C. Yang, *X-ray transition radiation*. Armenian Science Academy Press: Yerevan, Armenia (in Russian), 1983.

[190] **CAST** Collaboration, V. Anastassopoulos *et al.*, "New CAST limit on the axion-photon interaction," *Nature Phys.* **13** (2017) 584–590, arXiv:1705.02290.

[191] W. Grimus and H. Neufeld, "Transition radiation of ultrarelativistic neutral particles," *Phys. Lett. B* **344** (1995) 252–258, arXiv:hep-ph/9410245.

[192] I. G. Irastorza and J. A. Garcia, "Direct detection of dark matter axions with directional sensitivity," *JCAP* **1210** (2012) 022, arXiv:1207.6129.

[193] M. Baryakhtar, J. Huang, and R. Lasenby, "Axion and hidden photon dark matter detection with multilayer optical haloscopes," arXiv:1803.11455.

[194] S. K. Lamoreaux, K. A. van Bibber, K. W. Lehnert, and G. Carosi, "Analysis of single-photon and linear amplifier detectors for microwave cavity dark matter axion searches," *Phys. Rev. D* **88** (2013) 035020, arXiv:1306.3591.

[195] P. Sikivie and Q. Yang, "Bose-Einstein condensation of dark matter axions," *Phys. Rev. Lett.* **103** (2009) 111301, arXiv:0901.1106.

[196] P. Tinyakov, I. Tkachev, and K. Zioutas, "Tidal streams from axion miniclusters and direct axion searches," *JCAP* **1601** (2016) 035, arXiv:1512.02884.

[197] C. A. J. O'Hare and A. M. Green, "Axion astronomy with microwave cavity experiments," *Phys. Rev. D* **95** (2017) 063017, arXiv:1701.03118.

[198] M. S. Turner, "Periodic signatures for the detection of cosmic axions," *Phys. Rev. D* **42** (1990) 3572–3575.

[199] F.-S. Ling, P. Sikivie, and S. Wick, "Diurnal and annual modulation of cold dark matter signals," *Phys. Rev. D* **70** (2004) 123503, arXiv:astro-ph/0405231.